Microfabrication of hard x-ray lenses

Stöhr, Frederik; Hansen, Ole; Jensen, Flemming; Poulsen, Henning Friis

Publication date:
2015

Document Version
Publisher's PDF, also known as Version of record

Microfabrication of hard x-ray lenses

Frederik Stöhr

Supervised by:

Prof. Ole Hansen, Assoc. Prof. Flemming Jensen and Prof. Henning Friis Poulsen

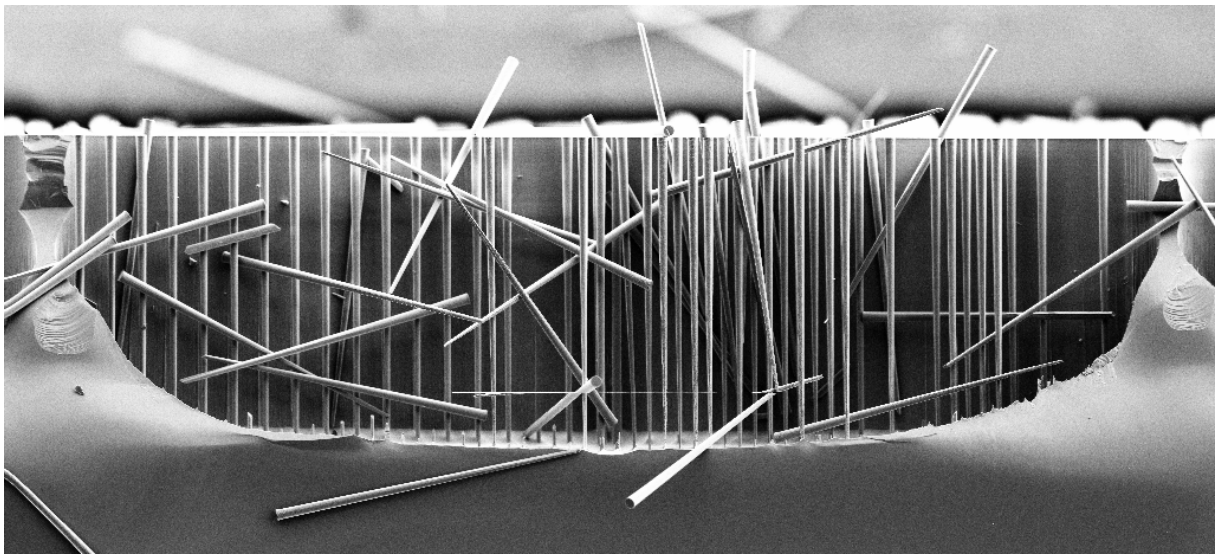

PhD Thesis

Technical University of Denmark

Kgs. Lyngby, Denmark 2015

Summary

Microfabrication of hard x-ray lenses

This thesis deals with the development of silicon compound refractive lenses (Si-CRLs) for shaping hard x-ray beams. The CRLs are to be fabricated using state of the art microfabrication techniques. The primary goal of the thesis work is to produce Si-CRLs with considerably increased structure heights and improved uniformity compared to what is currently available. To this end, established fabrication procedures are improved and the toolbox used for lens development is enriched.

The central theme of this thesis is x-ray microscopy (XRM). As a spearhead of today's materials research it provides characterization details that cannot be obtained by other means. The respective x-ray techniques largely benefit from continuously improved x-ray sources, x-ray detectors and x-ray optics. For instance, some techniques aiming for structural investigation of poly-crystalline materials directly benefit from more intense and wider line beams with narrower waists.

The thesis starts with a review of alternative x-ray lenses. Si-CRLs are identified as valuable optical components that allow shaping hard x-rays efficiently and creating beam waists that are clearly in the nanometer range. They stand out by their potential for compact integration, which makes them cost-effective, easy to handle and stable on-axis optics.

A Si-CRL comprises multiple bi-parabolic cylindrical cavities. The bi-parabolic patterns are defined lithographically and vertically transferred into the Si substrate using deep reactive ion etching (DRIE). Based on a theoretical framework for CRLs, stringent requirements on the pattern transfer are found. Most crucially, the sidewalls of the cavities must be strictly parallel. Already slight deviations from the ideal parabolic shapes result in non-uniform and broadened waists of focused x-ray beams.

Two strategies are demonstrated, which guarantee shape fidelity, while the heights of etched lenses can be increased. Both are based on defining the bi-parabolic cavities at their perimeter by trenches of uniform width, where one trench wall is comprised of sacrificial material. The two strategies differ in the way the unwanted sacrificial material inside the cavities is removed subsequent to DRIE. While the first strategy utilizes etching of the trenches through the entire thickness of the wafer for releasing the sacrificial portions, the second strategy relies on thin sacrificial structures that can be completely oxidized and removed by selective etching. Both strategies have proven to be equally successful in achieving a substantial increase of the heights of Si-CRLs and to facilitate accurate sidewall profile control necessary for uniform x-ray focusing.

A precise manufacture in turn asks for highly precise metrology. Therefore, a mix of techniques including optical profilometry and atomic force microscopy (AFM) has been used to obtain reliable information about the detailed three-dimensional shapes of the lenses. Adequate sample preparation and measuring procedures have been developed. Inverse replica molding in PDMS of the CRLs was established as an effective way to circumvent the limitations AFM probes have when concave surfaces need to be characterized, e.g. due to the finite lengths of AFM probes.

Four different x-ray optical components have been designed, manufactured and characterized with respect to their shape. Their optical performances were tested at the European Synchrotron Radiation Facility (ESRF). Two 1D-focusing Si-CRLs suitable as condensers in hard-XRM were developed utilizing the aforementioned two different strategies. The first Si-condenser showed focusing of a 56 keV x-ray beam into a 310 μm wide line and a waist of 980 nm (FWHM, full width at half maximum) at a focal length of 1.3 m. The second Si-condenser allowed the focusing of 17 keV x-rays into a 180 μm-wide line with a waist of 430 nm (FWHM) at a focal length of 0.215 m. Both systems leave plenty of space for sample surroundings and ensure low-divergent and wide x-ray beams with narrow waists. Both results are substantial improvements to what was available at the start of this thesis work.

The challenge of making x-ray objectives in silicon by interdigitation of lenslets alternately focusing in the vertical and horizontal directions was addressed. A functioning prototype of a 2D silicon objective for use in a bright-field hard-XRM was demonstrated. The results are promising; showing acceptably low aberration and performance close to theoretical expectations. A resolution of 300 nm with 17 keV x-rays and a focal length of 300 mm was achieved. By harnessing the potential for making more compact objectives and avoiding shape defects, one could significantly improve the focusing power, transmission and numerical aperture.

Polymer injection molding was explored as a novel route for x-ray lens manufacture. A Si-CRL template was used as a master for obtaining nickel mold inserts. CRLs made of polyethylene have proven to be promising highly efficient x-ray optics. A 55 μm long line focus with a minimal waist of 770 nm (FWHM) at a focal length of 350 mm was obtained with 17 keV x-rays. A final production rate larger than 10 pieces per hour indicates the economic value of injection molded x-ray lenses, which may have applications in more readily available small laboratory x-ray instruments or medical devices.

In each case, observed non-uniformities of the shaped x-ray beams were investigated and found to be in agreement with the lens shape measurements. In iterative steps the lenses have been improved and the most recent results allow yet another whole range of improvements to be made. The fundamentals for an advanced fabrication of silicon CRLs are laid out, which will contribute to their future use in novel applications.

Resumé

Mikrofabrikation af linser til hård røntgenstråling

Denne afhandling omhandler udvikling af silicium baserede "compound refractive lenses" (sammensatte refraktive linser, forkortet CRL) til brug for formgivning af strålebundter af hård røntgenstråling. CRL-komponenterne vil blive fremstillet ved brug af "state-of-the-art" mikrofabrikationsteknikker. Det primære formål med projektet er at fremstille Si-CRL-komponenter med væsentlig større strukturhøjder og forbedrede egenskaber sammenlignet med, hvad der er tilgængeligt i dag. Til det formål er allerede etablerede fremstillingsmetoder blevet forbedret og udvalget af teknikker til udvikling af linser udbygget i det foreliggende arbejde.

Det centrale tema for projektet er røntgenmikroskopi (XRM). Røntgenmikroskopi er et frontforskningsområde der indenfor materialeforskning leverer karakteriseringsresultater, som ikke kan opnås med andre metoder. Som eksempel kan nævnes teknikker indenfor strukturelle undersøgelser af polykrystalinske materialer, som direkte drager nytte af stadig mere intense og brede røntgenstrålebundter med stadig smallere strålebundtstaljer.

Afhandlingen starter med et overbliksbillede af de alternative typer af røntgen linser, der er til rådighed. Si-CRL komponenter identificeres som en central løsning, der muliggør effektiv formgivning af hård røntgenstråling og realisering af strålebundtstaljer med dimensioner i nanometerområdet. De adskiller sig ved deres potentiale for kompakt integration, hvilket gør dem økonomisk attraktive, nemme at håndtere, og da de er parallelle med den optiske akse er systemet stabilt.

En Si-CRL komponent består af en række bi-parabolske cylindriske hulrum. De bi-parabolske mønstre bliver defineret med en litografisk metode og derefter overført til silicium-substratet ved hjælp af dyb reaktiv ion ætsning (DRIE). De strikse fremstillingskrav til CRL komponenterne er blevet udledt fra en teoretisk model for linserne. Det er af afgørende betydning, at sidevæggene i disse hulrum er fuldstændigt parallelle. Små afvigelser fra den ideelle parabolske form vil resultere i en uensartet og bredere strålebundts-talje for det fokuserede røntgenstrålebundt.

To strategier, der muliggør en forøgelse af højden (ætsedybden) af linserne og samtidig sikrer en nøjagtig gengivelse af deres form, er blevet demonstreret. Begge er baseret på at definere kanten af de bi-parabolske hulrum ved hjælp af en grøft med en ensartet bredde, hvor den ene af grøftens vægge er en "offerstruktur". De to strategier adskiller sig fra hinanden ved måden, det overflødige materiale i hulrummene fjernes på efter DRIE-processen. Medens den første strategi udnytter gennemætsning af grøften og hele skiven og dermed frigørelse af det overflødige materiale, beror den anden strategi på tynde "offer-strukturer", som efterfølgende kan oxideres fuldstændigt og til sidst fjernes med selektiv ætsning af oxiden. Begge strategier er vellykkede og har resulteret i en væsentlig forøgelse af højden på de fremstillede Si-CRL komponenter

sammenlignet med tidligere ”state-of-the-art” og muliggjort den nødvendige nøjagtige kontrol af sidevægsprofilen til at opnå ensartet fokusering af røntgenstrålebundtet.

Udvikling af en nøjagtig fremstillingsproces nødvendiggør at meget præcise målinger kan foretages. Derfor er en række forskellige teknikker, herunder optisk profilometri og atomar kraft mikroskopi (AFM), blevet bragt i anvendelse for at opnå detaljeret information om linsernes tredimensionale form. Detaljerede procedurer for prøveforberedelse og målinger er blevet udviklet. Negative afstøbninger i PDMS af CRL komponenterne viste sig at være en effektiv metode til at omgå de begrænsninger, som AFM proberne har ved måling af konkave overflader, blandt andet på grund af AFM probernes endelige længde.

Fire forskellige røntgenoptiske komponenter er blevet designet, fremstillet og karakteriseret med hensyn til deres form. Deres optiske egenskaber blev testet ved European Synchrotron Radiation Facility (ESRF). To 1-D-fokuserende Si-CRL komponenter, som er velegnede som kondensatorer i hård-røntgen XRM, blev udviklet ved hjælp af begge de to førnævnte strategier. Den første Si-kondensator fokuserede et 56 keV røntgenstrålebundt til en 310 µm bred linje med en talje på 980 nm (FWHM, fuld bredde i halv maksimum) ved en fokallængde på 1,3 m. Den anden Si-kondensator fokuserede et 17 keV røntgenstrålebundt til en 180 µm bred linje med en talje på 430 nm (FWHM) ved en fokallængde på 0,215 m. Begge systemer efterlader god plads til prøveomgivelserne og sikrer lav-divergente, brede røntgenstrålebundter med smalle strålebundtstaljer. Begge resultater udgør væsentlige forbedringer i forhold til de løsninger, der var tilgængelige ved starten af dette arbejde.

Udfordringen ved at konstruere silicium-baserede røntgenobjektiver ved sammenfletning af linseelementer, som skiftevis fokuserer i vertikal og horisontal retning, blev taget op. I denne sammenhæng blev en fungerende prototype af et 2D siliciumobjektiv til brug i et ”bright-field” hård-røntgen XRM demonstreret. Resultaterne er lovende, idet de viser en acceptabel lav aberration og egenskaber tæt på de teoretisk forventede. For et 17 keV røntgenstrålebundt blev en opløsning på 300 nm og en fokallængde på 300 mm opnået. Ved at udnytte potentialet til at fremstille mere kompakte objektiver og undgå formdefekter er det muligt at opnå en væsentlig forbedring af fokuseringsstyrke, transmission og numerisk apertur.

Sprøjtestøbning af polymer-materiale blev undersøgt som en ny vej til fremstilling af røntgenlinser. Her blev en Si-CRL-form benyttet som form til fremstilling af en nikkelsprøjtestøbeindsats. Sprøjtestøbte CRL komponenter fremstillet af polyethylen har her vist sig lovende som meget effektive røntgenlinser. Med et 17 keV røntgenstrålebundt blev en 55 µm bred linjefokus med en minimal taljebredde på 770 nm (FWHM) opnået ved en fokallængde på 350 mm. Det økonomiske potentiale for sprøjtestøbte røntgenlinser, der kan finde anvendelser i lettere tilgængelige, mindre laboratorieudgaver af røntgeninstrumenter eller medicinsk udstyr, understreges af en fremstillingsrate på mere end 10 stk. pr time.

I alle tilfælde blev de observerede forvrængninger af røntgenstrålebundterne diskuteret og fundet i overensstemmelse med målingerne af linsernes form. Gennem en række iterative trin er linserne blevet forbedret og de nyeste resultater åbner for en række nye muligheder for yderligere forbedringer. Afhandlingen etablerer grundlaget for en avanceret fabrikation af silicium-baserede CRL komponenter, der vil bidrage til deres fremtidige brug i nye anvendelser.

Preface

This PhD thesis has been submitted to the Department of Physics at the Technical University of Denmark in partial fulfillment of the requirements for acquiring the PhD degree. The research providing the foundation for the thesis has been conducted over a period of three years from December 15th, 2012, to December 14th, 2015. It has been carried out partly at the Danish National Center for Micro- and Nanofabrication (DTU Danchip) and partly at the Department of Physics (DTU Physics), both located at the Technical University of Denmark (DTU). It has been supervised by Prof. Henning Friis Poulsen and co-supervised by Prof. Ole Hansen and Assoc. Prof. Flemming Jensen. The thesis work was publicly funded by a DTU internal institute stipend.

Frederik Stöhr
Kongens Lyngby, Denmark, December 2015

Acknowledgements

My acknowledgements go to the Technical University of Denmark (DTU), DTU Danchip, DTU Physics, DTU Nanotech, the European Synchrotron Radiation Facility (ESRF), Danish Fundamental Metrology (DFM) and my family.

I am grateful to my official PhD supervisors, Henning Friis Poulsen, Flemming Jensen and Ole Hansen for the opportunity to work in a vibrant environment striving for a fundamental understanding of today's technological needs and delivering innovative solutions. I thank Jörg Hübner for providing the resources necessary to conduct my research and the freedom I was given to pursue my goals.

I thank Henning for allocating enough beamtime at the ESRF for lens testing. I thank Hugh Simons, currently Post Doc at DTU Physics, for intellectual exchange, his ideas, and dedication to the experiments performed at the ESRF. I thank the ESRF for providing beamtime, instrumentation and experimental support. In particular, I thank Carsten Detlefs, beamline responsible at ID06, Jonathan Wright, beamline responsible at ID11, and Wolfgang Ludwig, researcher at the ESRF, for their assistance and discussions. I thank Anatoly Snigirev for disclosing me the world of x-ray optics at the early stage of my PhD project.

I thank Jørgen Garnæs from DFM for his collaboration, providing AFM usage and important insights into metrology. I thank DTU Nanotech for laboratory usage and in particular Klaus Bo Mogensen for sharing expertise on PDMS casting.

I am grateful to the full personnel of DTU Danchip for maintaining a state of the art research and development facility. In particular, I am endlessly thankful to Roy Cork and Peter Windmann for keeping my workhorse etching tool up and running, while providing invaluable technical details. I thank Berit Herstrøm and Jonas Michael Lindhard for coming along with me during my PhD project.

I thank DTU for administering my PhD, Jane Hvolbæk Nielsen for her interest in my project, my teachers from DTU, Murat Kulahci, Per Dannemand Andersen, Peter Vesborg, Jens Juul Rasmussen, Søren Schmidt, and Niels Bech Christensen, as well as my external instructors Joe Boyle and Poul Albæk.

I thank the International Association for the Exchange of Students for Technical Experience (IAESTE) for support and hospitality upon my arrival in Denmark. I thank Anders Jørgensen and Jesper Hanberg for the original chance to become part of the Danish ecosystem and giving me as a trainee in the Danchip customer support team responsibility from early on.

I thank my family and friends for moral support and their indirect contributions to this thesis work.

Contents

Summary iii

Resumé v

Preface vii

Acknowledgements ix

1 Introduction 3

1.1 Motivation 3

1.2 Objectives of the thesis 10

1.3 Thesis outline 11

2 X-ray refractive lenses 13

2.1 Historical note 13

2.2 Lens theory 13

2.3 Lens manufacture 26

2.4 Lens imperfections 29

2.5 Summary 35

3 Microfabrication 37

3.1 Standard process flow 37

3.2 Mask design 38

3.3 Lithography 39

3.4 Hard mask preparation 39

3.5 Deep reactive ion etching 41

3.6 Surface smoothing 54

3.7 Packaging 54

3.8 Summary 56

4 Advanced Si-CRL manufacture 57

4.1 Sidewall profile control 57

4.2 Strategy A: Through wafer etching 59

4.3 Strategy B: Sacrificial oxidation and selective etching 63

4.4 Summary 69

5 Metrology 71

5.1 Characterization tasks 71

5.2 Top 2D analysis 73

5.3 Cross sections 74

5.4 Optical profilometry 75
5.5 Atomic force microscopy & replica molding 79
5.6 Optical performance 87
5.7 Summary 91
6 Results and discussion 93
6.1 Strategy A: Deep 1D Si lenses 93
6.2 Strategy A: Interdigitated Si objective 105
6.3 Strategy B: Polymeric 1D lenses 111
6.4 Strategy B: Kinoform 1D Si lenses 120
6.5 Summary 127
7 Conclusion 129
7.1 Recapitulation 129
7.2 Achievements 130
7.3 Outlook 135
7.4 Final remarks 138
References 141
A Publications based on this thesis I
B Conferences and workshops III
C Abbreviations V

1 Introduction

This thesis deals with the development of silicon compound refractive lenses for shaping hard x-ray beams; the compound refractive lenses (CRLs) are to be fabricated using state of the art microfabrication techniques. The primary goal of the thesis work is to produce silicon CRLs with considerably increased structure heights and improved uniformity compared to what is currently available. This is achieved by improving established fabrication procedures and by enriching the toolbox used for lens development. The toolbox enhancements include innovative pattern designs and new shape characterization capabilities.

X-ray microscopy is a spearhead of today's materials research since it provides characterization details that cannot be obtained by other means. The respective x-ray techniques largely benefit from continuously improved x-ray sources, x-ray detectors and x-ray optics. For instance, some techniques aiming for structural investigation of poly-crystalline materials directly benefit from more intense line beams with narrower waists. To produce such intense well focused beams, CRLs are valuable optical components, which allow efficient focusing of hard x-rays and delivery of beams with sizes that are clearly in the nanometer range. Below, the background and objectives of this thesis are presented in more detail.

1.1 Motivation

1.1.1 X-rays

The discovery of x-rays by Wilhelm Röntgen in 1895 enabled the development of a plethora of techniques for the nondestructive investigations of opaque samples. X-ray analyses are most commonly known from medical diagnosis where techniques such as radiography and x-ray computed tomography allow to see inside human bodies without the need for time-consuming surgeries. Likewise, x-rays gain more and more importance in the industry, where they are similarly used to study specimens of all kinds at various length scales. X-rays allow the nondestructive testing of products, facilitate airport security, enable non-intrusive cargo scanning and assist machine wear monitoring. Obviously, x-rays play a crucial role in applied and fundamental research on the understanding of material properties and the development of novel materials or devices.

X-ray radiation is high energetic light and covers a broad range in the electromagnetic spectrum starting from the deep ultraviolet at 100 eV reaching into gamma radiation at 100 keV, corresponding to wavelengths of 10 nm to 10 pm. It is able to excite core level electrons of all atoms across the periodic table and to probe interatomic distances, which are typically in the order of a few ångströms. Therefore, x-rays are well suited to analyze samples regarding their elemental composition and chemical states utilizing x-ray absorption and fluorescence

spectroscopy, to retrieve structural information of partially ordered materials using x-ray scattering techniques, or to determine the structure of crystalline samples using x-ray diffraction [1–7].

X-ray characterization techniques benefit largely from developments of brighter and novel x-ray sources. While bulk, thin, rotating, or molten metal targets bombarded with energetic electrons produce x-rays in home laboratories [8,9], the brightest x-rays are generated at large scale facilities [10–12]. Today, third generation synchrotron radiation sources routinely produce intense x-ray beams that are tunable over a broad energy spectrum.[1] Third generation sources utilize electrons circulating with relativistic speeds in storage rings, while the electrons periodically traverse bending magnets and insertion devices. Undulators force the electrons to execute small-amplitude oscillations, thereby creating intense and partially coherent x-rays. So-called diffraction-limited storage rings with better control over the shape and divergence of the circulating electron beam are currently being built and will create more brilliant x-rays [13]. Free electron lasers currently in operation deliver coherent x-ray pulses with durations in the order of femtoseconds with even higher peak brightness and new facilities are under construction that will deliver x-rays >12 keV [14,15].

1.1.2 X-ray microscopy

X-ray microscopy (XRM) is a collective term for a variety of techniques exploiting x-rays for mapping local micro- and nanoscale spatial variations in material properties [16–24]. Its advantages include structural sensitivity, elemental sensitivity, high penetration depth and small wavelength. Thereby it complements optical, electron, or probe based microscopic techniques, which are mainly surface-sensitive and may require samples that are transparent or very thin. Various modalities of XRM may be systemized by differentiating contrast mechanisms and methodologies. The contrast mechanisms include

1. photo absorption (attenuating the transmitted beam),
2. photon or electron emission (generating particles that may be detected),
3. refraction (imposing a phase shift on the transmitted beam), and
4. coherent elastic scattering of photons (diffracting x-rays apart from the direct beam).

Respective methodologies may be divided into those that

1. illuminate the specimen with a parallel beam and use a high spatial resolution detector placed close to the specimen to determine the spatial distribution of x-rays exiting the specimen (radiography),
2. use a focusing system between sample and detector to direct exiting x-rays to different points on the detector according to their points of origin in the specimen (full-field imaging),
3. use a focusing system between source and sample to create a secondary source, while putting the sample into the diverging x-ray beam and recording the spatial distribution of exiting x-rays (projection imaging, cf. Figure 1.1),

[1] http://www.lightsources.org/ (Dec 2015).

4. use a focusing system between source and sample to create a locally defined probe beam that is raster-scanned over the sample, while recording exiting x-rays (scanning microscopy),
5. analyze the interference patterns formed by exiting coherently scattered x-rays, permitting accurate location of the coherent scattering sites without a corresponding requirement for high-accuracy detectors or optics (diffraction microscopy),
6. analyze a part of the interference pattern by using a focusing system between sample and detector (dark-field imaging),
7. analyze the intensity and energy of secondary electrons or photons by a variety of means (photoelectron and fluorescence spectroscopy).

Different methodologies favor certain contrast mechanisms and offer different compromises of spatial resolution, field-of-view, acquisition time and sensitivity. Acquiring tomographic datasets then allows the three-dimensional inner structure and composition of a specimen to be reconstructed [25–28].

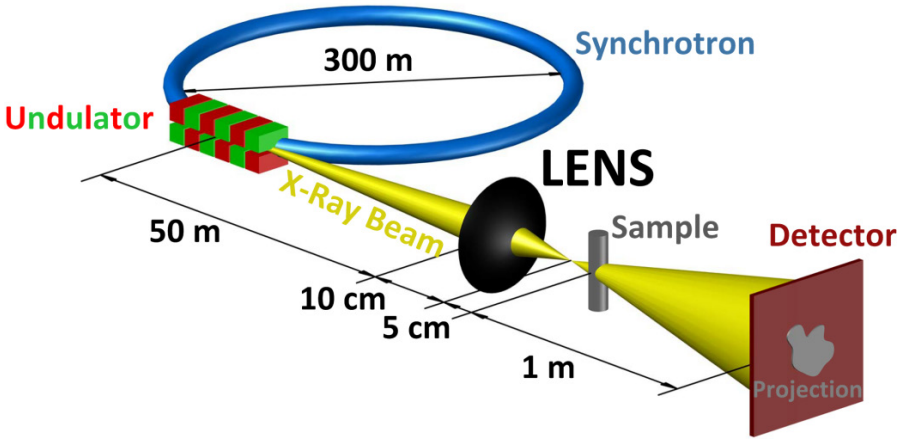

Figure 1.1. Conceptual drawing of a typical projection microscope using synchrotron radiation highlighting the importance of x-ray lenses. X-rays are generated by relativistic electrons circulating in a storage ring and traversing an undulator. After a free propagation the x-ray source is imaged using a lens and high de-magnification ratio, thereby generating a small secondary source. The sample is put shortly after the x-ray focus into the diverging beam. After free propagation a magnified shadow of the sample is recorded on a spatially resolved detector. The achievable resolution is ultimately limited by the size of the secondary source. The sketched dimensions are typical values, but may vary. The drawing is not to scale and essential components in the beam path may be missing.

While soft x-rays with photon energies lower than 5 keV are particularly suited to study thin biological samples with resolutions as fine as 30 nm [29], thick samples or samples composed of heavier elements require hard x-rays with energies higher than 5 keV [18,24,30]. For example the penetration depth[2] of 10 keV x-rays through aluminum is ~150 µm and that of 30 keV x-rays is ~3.3 mm. Often it is desirable to be able to study embedded structures of millimeter thick samples, since such samples resemble materials we regularly cope with in our daily lives.

[2] The penetration depth is defined as the depth at which the x-ray intensity inside the material falls to 1/e (about 37%) of its original value at the surface.

Metals, ceramics and semiconductors are important materials that are crystalline and tend to be composed of elements such as grains and domains that are structured hierarchically in a complex manner on several length scales. Studying structural dynamics inside crystalline materials on multiple length scales and in three dimensions (3D) is currently of major research interest [31]. Experimental insights will serve the validation of material models that predict the evolution of the entire material structure during important materials transformations such as processing or failure.

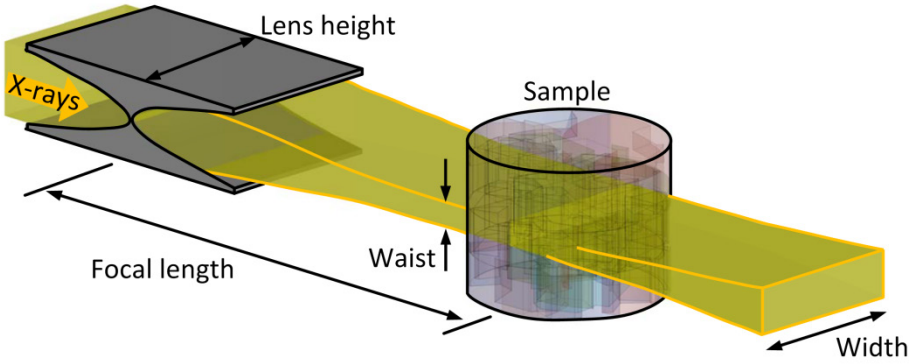

Figure 1.2. Conceptual drawing of a sample being illuminated by a one-dimensionally focused line beam.

While full-field imaging with an objective is relevant as its efficiency enables real-time imaging of complex processes, techniques for grain/domain mapping, such as 3D x-ray diffraction [32–39], high-energy diffraction microscopy [40–42], topo-tomography [43,44], or variants of diffraction contrast tomography [45–49] benefit from using an x-ray line focus to study a two dimensional (2D) slice through a sample (cf. Figure 1.2). This approach simplifies reconstruction problems from 3D to 2D since the slices can be 'stacked' layer-by-layer to give the 3D volume. It is a scanning approach, which facilitates the data analysis by avoiding diffraction spot overlaps. It necessitates scanning in one direction only and is thereby faster than procedures based on scanning the sample with respect to a point beam. Additionally, focused line beams increase the spatial and angular resolution, as well as improve the signal-to-noise ratio.

Optimal line foci should be wide but with a narrow waist in order to illuminate a broad 2D slice of a specimen while maximizing the 3D spatial resolution of the analysis (cf. Figure 1.2). The width of a line beam is naturally determined by the height of a line-focusing lens, whereas the minimum waist is limited by the optical configuration (source demagnification), the numerical aperture of the lens (diffraction limit) and lens imperfections (optical aberrations).

1.1.3 X-ray optics

A large variety of optical components capable of shaping x-ray beams exist [17,18,22–24,50–56]. They may be categorized primarily by the type of physical phenomena they exploit for manipulating the x-ray wavefront and secondly by the techniques used for their fabrication. The three basic principles upon which x-ray lenses may be built are reflection, diffraction and refraction. There is an ongoing international race in the development of x-ray lenses to produce

ever smaller and more intense probe beams, as well as more efficient objectives that allow imaging with higher spatial resolution. Improvements of existing and the development of new technology make this race possible and theoretical limits of x-ray lenses are still under debate, while the general aim is to obtain single-nanometer resolution with hard x-ray techniques [57–61].

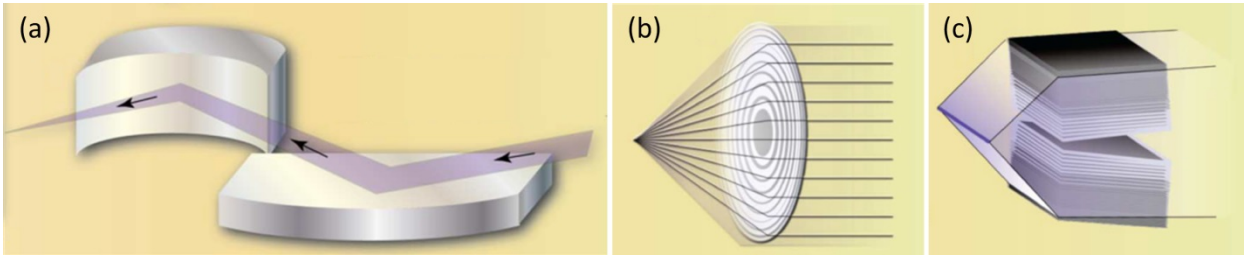

Figure 1.3. Reflective and diffractive x-ray optical components. (a) Kirkpatrick-Baez optics focus x-rays by sequential focusing with crossed elliptical x-ray mirrors. (b) Zone plates are designed with different path lengths from each zone, so x-rays add constructively at the focus. (c) Multilayer Laue lenses use multilayer technologies to produce high-aspect-ratio 1D zone plates. Adapted from [51].

X-ray optics is a complex field of research and the general challenge is to precisely manipulate radiation which per se only weakly interacts with matter. Today, the most abundant optics found in x-ray microscopes capable to deliver sub-micrometer spot sizes or imaging resolutions are KB-mirrors, Fresnel zone plates, multilayer Laue lenses and compound refractive lenses. Each system has its own advantages and faces different technological challenges.

KB-mirrors (named after the inventors Kirkpatrick and Baez [62–64]) are based on total external reflection or on Bragg's law, if single layer coatings or multilayer coatings are used, respectively. The mirrors are typically elliptically shaped for point to point imaging. Horizontal and vertical imaging is performed on independent mirrors for the sake of higher flexibility and accuracy (cf. Figure 1.3(a)). Incidence angles are very small (~mrad) and result in large foot prints on the mirrors (~cm), whereas angles decrease with an increase in x-ray energy. Mirrors are fabricated by a mixture of grinding, polishing, and coating techniques, which may be combined with in-situ metrology [65–72]. Alternatively to mirror figuring, flat polished and optionally coated mirrors may be bent into the proper shape inside the beamline [73–79]. Slope errors (~0.1 µrad) and surface roughness (~Å) need to be minimized. Mirrors are very sensitive with respect to misalignments in the beamline. Glancing angles (~mrad), rotations (~µrad) and the perpendicularity of the mirror pair must be aligned with high precision. Thermal drifts and vibrations need to be controlled. Sub-10 nm focusing was previously demonstrated using an additional grazing-incidence piezo-controlled deformable mirror for in situ error compensation [80–82]. In-line figuring techniques are being developed striving for ultimate resolution [83,84]. KB-mirrors are particularly attractive, because they are highly efficient and most importantly achromatic. High-quality mirrors are expensive and they require efficient cooling, a stable environment and high accuracy alignment systems. KB-mirrors for shaping >20 keV x-rays become very long. A drawback of mirrors is that they are off-axis optical components, meaning that their focusing direction is apart the direct beam direction. In setups that require rapid changes in beam shape (e.g. switching between the focused and the direct beam) the change in the beam direction is catastrophic.

Fresnel zone plates (FZPs) are based on diffraction and consist of a series of concentric rings with radially increasing diameters and decreasing width (cf. Figure 1.3(b), [85]). FZPs either alternate between transparent and opaque zones (amplitude zone plate suitable for low x-ray energies) or introduce alternately a phase shift of π (phase zone plate suitable for high x-ray energies). X-rays from different zones interfere constructively in common on axis positions. An order selecting aperture (OSA) then selects one focus and blocks rays from other orders, which would otherwise result in unwanted background radiation. Since interference is involved, FZPs are chromatic devices. The spot size achievable with an FZP is approximately equal to the width of the outermost zone. Their optical efficiency is limited by absorption and diffraction into unwanted orders and is typically <40 % for binary FZPs. The biggest challenge is to fabricate the outermost zones and in particular to achieve high aspect-ratios. Especially if used with high energy x-rays, FZPs must be considerably thick. Obtaining a 40 nm small focus with 8 keV x-rays necessitated a 900 nm thick and 45 nm wide outermost zone, corresponding to an aspect-ratio of 20, which is challenging to achieve [86]. A variety of manufacturing routes have been conceived. Fresnel zones may be defined by lithography in combination with electro plating [86–101], etching [102–112], or atomic layer deposition [113–117]. An alternative route is via thin film deposition onto thin wires combined with focused ion beam milling [118–121]. The later technique resulted in a multilayer zone plate creating a point focus with sub-5 nm features when combined with pre-focusing by a KB-mirror at 8 keV [119]. FZPs for x-rays >20 keV have rarely been reported [106].

Multilayer Laue lenses (MLLs) are a derivative of Fresnel zone plates as they share the same working principle (cf. Figure 1.3(c), [122]). MLLs are exclusively fabricated by thin film deposition onto flat substrates, e.g. by magnetron sputtering or pulsed laser deposition, followed by sectioning using e.g. ion beam milling [123–125]. To obtain reasonable thick stacks of layers, deposition times may be a couple of days, which puts high demands on controlling the stability of the deposition process. Since one MLL focuses in one direction only, two MLLs need to be arranged in crossed geometry to obtain point focusing. The big advantage of MLLs over FZPs is the ease of which narrow outermost zones may be obtained, which are necessary for focusing hard x-ray beams. In contrast to (thin) FZPs, dynamic diffraction inside the multi layers need to be considered and all layers need to obey Bragg's law [60,125]. As a result, individual layers must not be flat, but need to be curved in order to obtain ultimate resolution. Again, various international players successfully participate in the race for the ultimate resolution [126–142]. Today MLLs achieved focusing of 12 keV x-rays to a 11 nm narrow (FWHM) and 10 μm wide line focus at a focal length of 4.2 mm [132], while 1 nm resolution is expected to be within reach for 17 keV x-rays [139]. MLLs may deliver millimeter wide line beams and have high physical apertures, which make them very promising future devices for shaping hard x-ray beams.[3]

Compound refractive lenses (CRLs) are the subject of this thesis and will be discussed in detail in Chapter 2. As the name suggests, these devices are based on refraction just as lenses used for shaping visible light. The main characteristics of refractive x-ray lenses are their weak refractive power, high absorption, and a reverse shape with respect to visible light lenses. Instead of

[3] Notably, MLLs need to be supplemented by their "second halves" with high precision [142].

convex shapes, x-ray CRLs need to have concave shapes, which is due to the fact that the refractive index of materials for x-rays is smaller than unity.[4] Since the refractive index of a given material is energy dependent, CRLs are chromatic devices. The weak refraction of CRLs implies that the lens radii must be very small, namely in the micrometer range. Therefore, CRLs are composed of multiple single lens elements (lenslets), hence the term 'compounded'. The number of lenslets may exceed 100 and therefore CRLs may be 'extremely' long (~m) [143]. Long CRLs mean that x-rays need to pass a lot of material in order to get efficiently focused, which results in high absorption losses. Therefore CRLs are typically built out of materials with low-*Z* elements such as beryllium, aluminum or silicon.

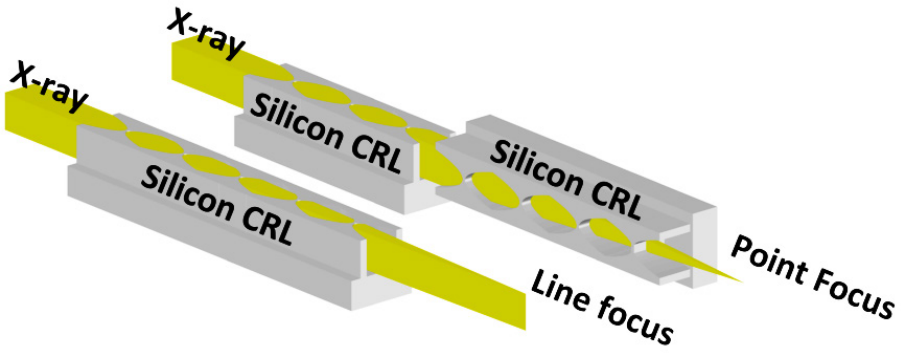

Figure 1.4. Planar compound refractive lenses (CRLs). Multiple lenslets put into series allows focusing with decent focal lengths (< 1 m). While one planar CRL focuses in one direction only, two planar CRLs may be arranged in crossed geometry to obtain a point focus.

By optimizing the manufacture and choosing the right materials for the right x-ray energies, efficient CRLs may be obtained that allow focusing to spots with 125 nm (FWHM) diameter at focal distances of 250 mm using 8.2 keV x-rays generated by a free electron laser [144]. Microfabrication techniques are very attractive for realizing the small radii required for CRLs. Lithography in combination with deep reactive ion etching of silicon wafers allows the integration of multiple CRLs on single chips. It avoids the necessity for high precision assembly of individually manufactured lenslets, allows compact lens systems to be obtained and facilitates their handling in the x-ray beam. So-called silicon nano-focusing lenses (NFLs) allowed 50 nm foci (FWHM) to be obtained at focal distances of ~5 mm using 21 keV synchrotron radiation [145]. Notably, NFLs focus in one direction only and two NFLs must be arranged in crossed geometry to create a point focus (cf. Figure 1.4). CRLs are particularly advantageous with respect to their convenient handling and their ease of alignment. CRLs produce sharp foci with superb signal-to-noise ratios, because they work in transmission (unlike mirrors) and no higher-order maxima exist, thereby avoiding OSAs (unlike diffractive optics). CRLs are on axis components whose focal lengths can be easily adapted to different x-ray energies by changing e.g. the number of lenslets. Likewise, the size of the beam waist may be easily controlled. While

[4] The energy of x-rays is much larger than the binding energies of most atomic electrons and electrons must therefore be considered as if they are essentially free when interacting with x-rays. In contrast, for visible light electrons are bound by the nucleus. This implies that in the x-ray case there is a phase shift of π between the incident and scattered fields, which results in a refractive index less than unity. While the phase velocity inside the material is larger than the speed of light c, the group velocity is less than c, in agreement with the theory of special relativity [1].

CRLs heavily absorb at low x-ray energies, they are excellent devices for energies above 10 keV and probably the perfect choice for energies above 50 keV.

In summary, a variety of optical components for shaping x-rays exist. While KB-mirrors are achromatic devices, they suffer from being off-axis devices and being delicate with respect to their alignment in the x-ray beam. Fresnel zone plates have superb imaging capabilities in the lower x-ray spectrum but are inefficient at higher x-ray energies. Multilayer Laue lenses are the very latest devices and are recently subject to large development efforts, because 1 nm focal spots seem to be within reach and they are suitable for shaping high energy x-rays. Compound refractive lenses have matured and are found today in many synchrotron beamlines. Generally speaking, a main advantage of x-ray refractive lenses is that they are cost-effective on-axis optics, relatively easy to align and have tunable focal lengths by varying the number of lens elements or the radii of curvature. Moreover they can readily be used for shaping x-rays with energies >20 keV.

1.2 Objectives of the thesis

This thesis is on the microfabrication of compound refractive lenses for the purpose of shaping hard x-ray beams. While developed lenses may be used in conjunction with any technique that requires focused x-ray beams, the design and dimensions of lenses in this thesis are tailored towards their use as condensers in techniques such as three-dimensional x-ray diffraction (3DXRD) and dark-field microscopy for the illumination of samples with typical sample sizes in the order of 0.3-1 mm. For such applications it is relevant to

1. maximize the length and uniformity of the incoming x-ray line beam, preferably to the point where an entire sample cross-section is illuminated,
2. minimize the waist of the line beam to improve the spatial resolution of the resulting 3D maps,
3. maximize the peak intensity for signal-to-noise reasons, implying a large effective aperture of the CRL, and
4. obtain a relatively long focal length in order to minimize divergence, to have a long focal depth, and to provide ample space for sample surroundings.[5]

Combining full field absorption and phase contrast tomography measurements with high resolution grain mapping studies permits a more complete picture of microstructures to be determined. The use of inline optics allows the beam size to be rapidly changed for these experiments without moving the sample, simply by inserting or removing the lenses from the beam path. The primary aim is to apply deep reactive ion etching (DRIE) for the fabrication of 1D-focusing Si-CRLs with the emphasis on increasing the heights of the lenses in order to obtain wider line beams. Si-CRLs are currently limited in height due to difficulties associated with DRIE in achieving parallel and straight surface profiles. Due to the required complex bi-parabolic shapes of CRLs, Si lenses are today typically not higher than 50 μm [145,146]. Lenses being etched deeper than 50 μm are typically non-uniform, resulting in a blurred or non-uniform

[5] Achieving the ultimate resolution with CRLs is explicitly not the purpose of this thesis. Creating 200 μm long line foci with <500 nm waist for x-ray energies >15 keV would be a major step forward and improve currently achievable resolutions with 3DXRD.

beam waist [147]. It is anticipated that the utilization of sacrificial structures geometrically establishes more uniform etch characteristics. Expectedly, accurate control of the etch profile will thereby be facilitated, which enables parallel and straight sidewalls to be obtained. Design criteria and strategies for efficiently removing those sacrificial structures in the final devices need to be found. Respective process flows and routines need to be developed.

Following the rationale "you cannot manufacture what you cannot measure", adequate characterization techniques need to be qualified and applied. Respective capabilities and limits need to be identified and possible complementary techniques may be invented. Standard 2D microscopic techniques may be complemented by 3D measuring techniques such as optical profilometry and atomic force microscopy (AFM). Inverse replica molding is conceived to avoid certain shortcomings associated with the finite lengths of AFM probes.

Recognizing that Si-CRLs inherently suffer from high absorption in the low to medium x-ray energy range (E = 5 – 20 keV), silicon may be chosen as a material to fabricate masters, from which then lenses made of different materials can be obtained. Thermoplastic polymers are easy to mold and injection molding is an established process for cheap mass production of polymeric parts. It needs to be investigated how well polymer injection molding is suited for fabricating CRLs.

Full-field x-ray microscopy using x-ray objectives has become a mainstay of the biological and materials sciences. CRLs are ideal to be used as objectives at high x-ray energies which may not be served by Fresnel zone plates. Si-CRLs have today solely been used as efficient optics for sample illumination and for creating fine probe beams used in scanning x-ray microscopy. It needs to be investigated how Si-CRLs may function as objectives, while minimizing optical aberrations.

The optical performances of lenses developed in this thesis need to be measured. The obtained data from these measurements needs to be analyzed and carefully interpreted in order to draw conclusions about potential improvements in the manufacture and to verify the shape characterizations performed during the fabrication. In an iterative process the manufacture needs to be improved to yield more efficient, more uniform and higher x-ray lenses producing smaller x-ray beams.

1.3 Thesis outline

This thesis covers the basic theory of CRLs that is necessary for designing the lenses to be developed (cf. Chapter 2). Previous achievements with respect to the development of refractive x-ray lenses with a strong emphasis on their manufactures are reviewed in detail (cf. Chapter 2.3). The stringent requirements on the shape of CRLs are discussed (cf. Chapter 2.4). The processes involved in the microfabrication are outlined, whereas DRIE using the Bosch process as the most crucial one is discussed in great detail (cf. Chapter 3). Two strategies are presented, which are sought to permit the profile control necessary for obtaining higher and more uniform Si-CRLs (cf. Chapter 4). Methods that guarantee sufficient process control and assessing the 3D shape of lenses are introduced and verified (cf. Chapter 5). The acquired techniques and processes are applied in the manufacture of 300 µm high Si-CRLs (cf. Chapter 6.1), the manufacture of a 2D-focusing Si objective (cf. Chapter 6.2), the demonstration of injection

molded polymeric CRLs (cf. Chapter 6.3), and the fabrication of 200 μm high Si-CRLs with a kinoform design (cf. Chapter 6.4). The work is summarized, critically reviewed and spotted for potential improvements and future developments (cf. Chapter 7).

Individual chapters are sought to be readable independently, while cross-references are given whenever needed. Large parts of this thesis have been published in peer-reviewed journals [148–152], while supplements and unpublished data, as well as more details about individual processing steps and additional background information are presented here.

2 X-ray refractive lenses

This chapter presents refraction as a means to shape hard x-ray beams. The shape of lenses necessary to focus x-rays is discussed, including essential design parameters. The concept of a compound lens is introduced and relevant formulas describing its optical performance are given. The theory presented is very basic and tailored towards its actual application. Hence it does not go beyond what has been previously reported in literature. X-ray absorption is described as one of the most crucial material specific lens properties. Modified lens designs and means to visualize beam paths are presented. Previous techniques for manufacturing x-ray lenses are reviewed. Lens imperfections relevant for this thesis are briefly discussed.

2.1 Historical note

X-ray refraction is very weak. Combined with strong x-ray absorption, its exploitation for efficient x-ray optics was regarded as impractical for almost 100 years since the discovery of x-rays. Wilhelm Röntgen could not observe any indication for x-ray refraction during his early studies [153,154]. In 1918 Albert Einstein suggested that the refractive index may be smaller than one [155]. The feasibility of shaping x-rays by using lenses in the very same way as lenses have been commonly used for shaping visible light was denied in 1948 by Kirkpatrick and Baez, who were two pioneers in the field of x-ray optics and the inventors of the KB-mirrors [156,157]. In the early 90's the discussion about x-ray refractive lenses was taken up again [158,159], which culminated in an article by Yang that discussed the requirements of x-ray lenses in more detail [160]. Tomie sought to overcome technological challenges related to the manufacture of x-ray lenses and proposed to drill multiple cylindrical holes along a straight line in a suitable substrate, which he first applied for a patent in 1994 [161,162]. In 1996 x-ray focusing by refraction was first demonstrated by Snigirev et al. at the European Synchrotron Radiation Facility [163], which at that time was the first high brightness hard x-ray source. Since this first demonstration, advances in technology gave a boost to the manufacture of x-ray lenses and further improvements of their optical quality made them widely-used in hard x-ray instruments. Today, optics based on refraction are found in various beamlines at synchrotron radiation facilities [164], free electron lasers [144] and laboratory x-ray sources [165].

2.2 Lens theory

First demonstrations of x-ray focusing and imaging by refractive lenses went along with the development of a theoretical framework to describe these novel devices [166–176]. One of the first comprehensive studies of compound refractive lenses was given by Lengeler et al. [170]. Of central interest in such theoretical treatises are the possibilities to predict the optical performance of a given lens in an arbitrary optical setup, to optimize the lens dimensions for a

given application and to explore the theoretical limits of refractive x-ray lenses in general [58,177,178]. Key figures of the lens optical performance are the focal length, the x-ray transmission, and the achievable minimal focal spot size or imaging resolution. Theoretical studies need to consider the operating x-ray energy and the lens material properties, since refraction and absorption are material and energy dependent. Indeed, finding the right combinations between x-ray energies, lens materials, optical specifications, and lens dimensions, while using the right technologies, were the keys for extending the success of refractive lenses from the visible light to the x-ray regime.

2.2.1 X-ray refraction

Like in the case of visible light, x-ray refraction takes place at the interface between two different media of different refractive indices n_1 and n_2, and is governed by Snell's law:

$$n_1 \cos\theta_1 = n_2 \cos\theta_2, \tag{1}$$

where θ_1 is the incident angle of a light ray and θ_2 the angle of the refracted ray as specified in Figure 2.1 [1].

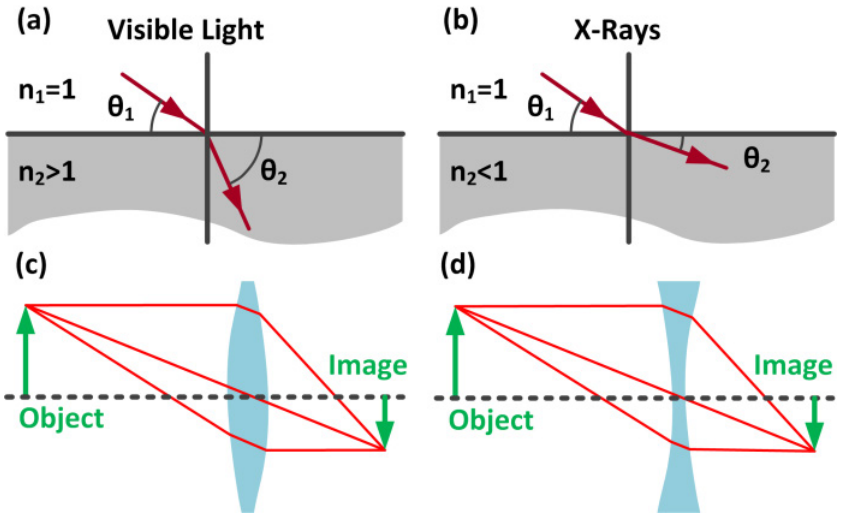

Figure 2.1. The difference in refraction between visible light (a) and x-rays (b), and the respective consequence for the shapes of imaging lenses (c) and (d).

Visible light incident on an air-glass interface ($n_1 = 1$, $n_2 = 1.5$) is refracted towards the surface normal (Figure 2.1(a)). Therefore, a focusing lens for visible light must have a convex shape (Figure 2.1(c)). X-rays, however, are refracted away from the surface normal (Figure 2.1(b)), since n_2 is generally smaller than unity. Therefore, an x-ray focusing lens must have a concave shape (Figure 2.1(d)).

When dealing with x-rays traveling through media, it is crucial to consider x-ray attenuation (generally referred to as absorption), which originates from the photoelectric effect, Compton (inelastic) and Rayleigh (elastic) scattering. It can be accounted for by defining a complex refractive index

$$n = 1 - \delta + i\beta, \tag{2}$$

where the decrement δ specifies its real part and the extinction coefficient β its imaginary part [179]. The strength of refraction is described by δ, whereas β describes attenuation. Away from atomic resonances (absorption edges), δ may be calculated by

$$\delta = \frac{N_A}{2\pi} r_0 \lambda^2 \rho \frac{Z}{A}, \tag{3}$$

where the atomic number Z, the molar mass A, and the mass density ρ are material specific properties, N_A is Avogadro's number,[6] r_0 the classical electron radius,[7] and λ the wavelength of the x-rays. Figure 2.2 shows δ and β for various materials as a function of x-ray energy,[8] where δ values were calculated from Equation (3) and β values were taken from the NIST database.[9] The material properties are detailed in Table 2.1. The jump of β in case of nickel at E = 8.33 keV is due to the absorption edge of K-shell electrons.

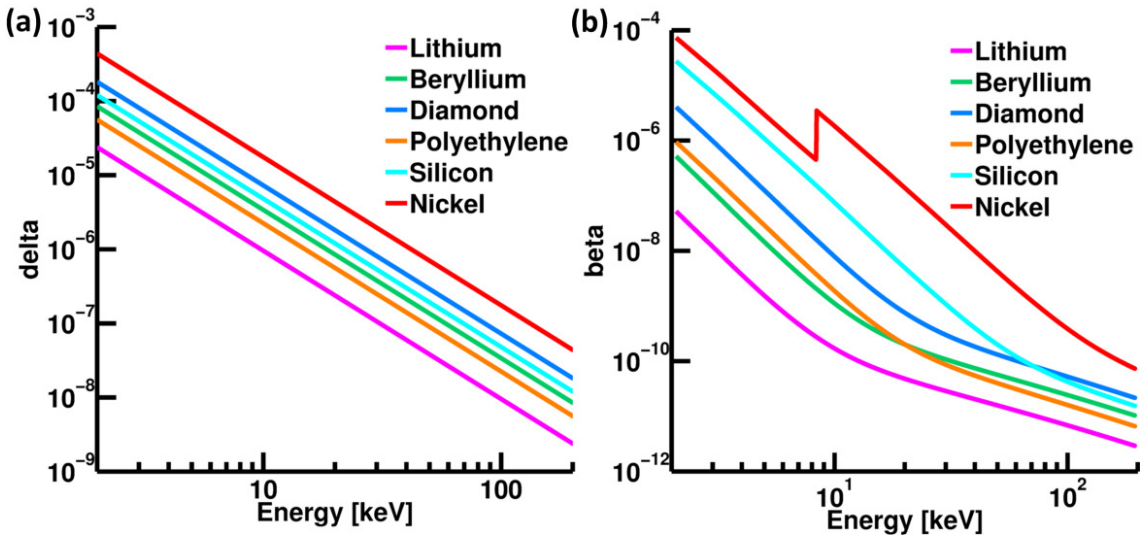

Figure 2.2. The complex refractive index for different elements as a function of x-ray energy. (a) Real part, δ. (b) Imaginary part, β. Note the logarithmic axes. Delta for Nickel at the absorption edge is not correct according to the Kramers-Kronig relations.

Table 2.1. Material specific properties.

Material	Z	A [g/mol]	ρ [g/cm^3]
Lithium (Li)	3	6.94	0.53
Beryllium (Be)	4	9.01	1.85
Diamond (C)	6	12.0	3.5
Polyethylene (C_2H_4)	16	28.1	0.95
Silicon (Si)	14	28.1	2.32
Nickel (Ni)	28	58.7	8.88

[6] $N_A = 6.022\times10^{23}$ mol^{-1}
[7] $r_0 = 2.818\times10^{-15}$ m
[8] X-ray wavelength λ and energy E can be related to each other by $E = 12.398$ keV Å$\times 1/\lambda$.
[9] http://physics.nist.gov/PhysRefData/FFast/html/form.html (Dec 2015).

Instead of beta, it is more convenient to think in terms of the attenuation length μ^{-1}, which corresponds to the characteristic length, where the x-ray intensity entering a medium has been attenuated to $1/e = 37\%$:

$$\mu^{-1} = \frac{\lambda}{4\pi\beta}. \tag{4}$$

In the context of refractive lenses it is useful to illustrate the ratio δ/μ, since the optical performance of the lens is generally better, if the refractive power is high (large δ) and the absorption is low (large μ^{-1}). Figure 2.3 shows this ratio, where it is clearly visible that

1. for every element exists a photon energy where δ/μ is maximized,
2. δ/μ for different elements converges at high energies, and
3. low-Z elements or compounds are generally the preferred lens materials.

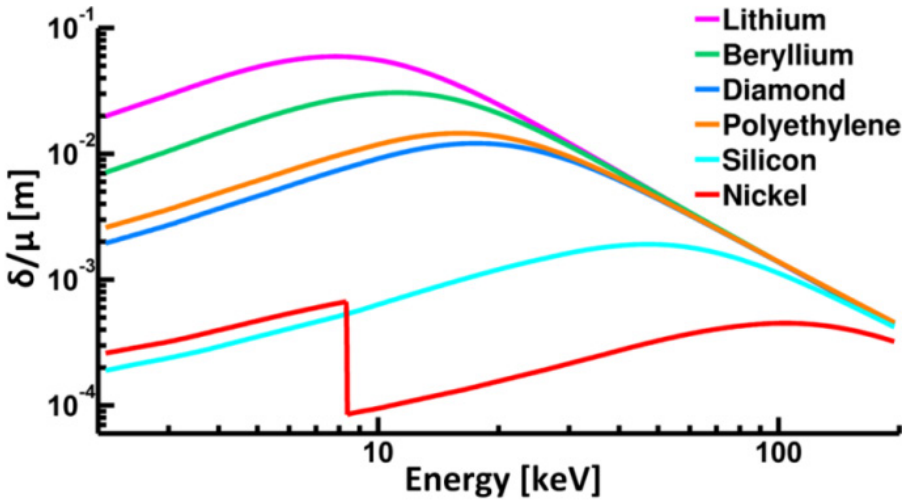

Figure 2.3. Characteristic ratio δ/μ for different elements as a function of x-ray energy.

2.2.2 The ideal lens shape

Lenses for shaping visible light are typically spherically shaped. This is due to convenience in their manufacture, since it is easier and cheaper to grind and polish spheres in contrast to e.g. ellipses. However, a sphere may not be the ideal lens shape. If an incoming parallel beam is considered, it can be shown that rays refracted at different regions across the aperture of a spherical lens do not coincide in a common focus; this is commonly known as spherical aberration. In fact, more advanced optical lenses in hand-held cameras have aspherical shapes to avoid this type of aberration. Generally, the required shape of a lens depends on the required optical quality, on the incoming light field and the desired output. For example, the incoming beam must not necessarily be strictly parallel (collimated), but can be convergent or divergent. Hence, in order to create a point focus, the ideal lens shape needs to adapt accordingly.

The ideal lens shape to produce perfect point-to-point focusing is a Cartesian oval as was recently studied in the context of focusing in x-ray beamlines [180]. Cartesian ovals may be approximated by ellipses [181], which may be approximated by parabolas [182], which may be approximated by spheres [163]. For the present thesis it is regarded sufficient to work with

parabolic lens shapes. This is justified by the small difference between a parabola and an ellipse, given the small apertures of our lenses relative to their radii of curvature. Additionally, the focal lengths found in this thesis are considerably larger than the lengths of the lenses used. Further, a perfectly collimated incoming beam is assumed for simplicity (which is justified by a large source-lens distance) and the paraxial approximation is used, according to which light rays are always considered parallel to the optical axis (which is justified by small refracting angles). In the following the parabolic shape is motivated using Fermat's principle [183].

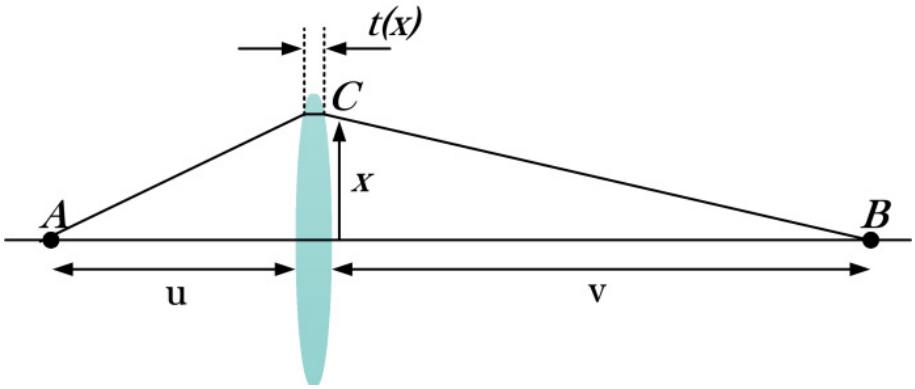

Figure 2.4. Sketch of point-to-point imaging.

According to Fermat's principle, waves traveling from a point A to a point B interfere constructively at B, if they travel on equally long optical paths. We consider rays originating at A, propagating in vacuum with $n = 1$, traversing at C a medium with thickness $t(x)$ and $n = 1-\delta$, and continue in vacuum to B (cf. Figure 2.4). The axial distances are $\overline{AC} = u$ and $\overline{CB} = v$. C is located at a distance x from the optical axis and the axial thickness of the lens is $t(0)$. Given a physical length l, the optical path length is $\mathrm{OPL} = nl$. The complete OPL from A to B via C is

$$\overline{AB} = \sqrt{u^2 + x^2} + \sqrt{v^2 + x^2} + t(0) - t(x) + (1-\delta)t(x), \tag{5}$$

which needs to be constant for all x. Expansion by the binomial theorem to first order $\sqrt{1+x} \approx 1 + x/2$, yields

$$\overline{AB} = \mathrm{const} \approx u + v + \frac{1}{2}x^2\left[\frac{1}{u} + \frac{1}{v}\right] + t(0) - \delta t(x). \tag{6}$$

Replacing u by infinity (assuming a parallel beam) and v by the single-lens focal length f_S, its solution found by differentiation and integration is

$$t(x) = t(0) + \frac{x^2}{2\delta f_S}. \tag{7}$$

By defining the radius of curvature of the parabola $R = 2\delta f_S$ and assuming a bi-concave lens with web thickness T_0 as illustrated in Figure 2.5, the shape of one lens surface is given by

$$y(x) = \frac{x^2}{2R}. \tag{8}$$

According to this, a single lens element has a focal length

$$f_S = \frac{R}{2\delta} \tag{9}$$

and a total thickness T_S

$$T_S = T_0 + \frac{R_0^2}{R}, \tag{10}$$

where $2R_0$ is the physical lens aperture (which needs to be distinguished from the effective lens aperture discussed in Chapter 2.2.4).

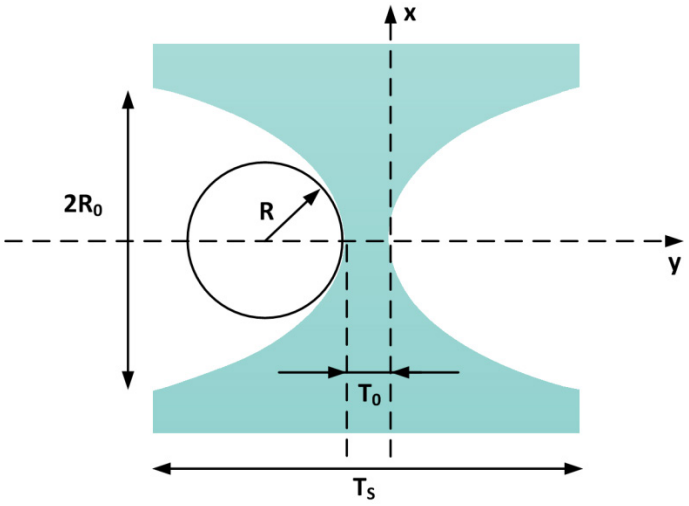

Figure 2.5. Geometry of a single bi-concave parabolic lens element.

Practical focal lengths in x-ray microscopy range from a few hundreds of micrometers to tens of meters and generally depend on the actual application. Some applications require very strong focusing for ultimate resolution and some require merely weak focusing for collimating the x-ray beam. A typical focal length is one meter; it allows decent focusing to micrometer sized spots and provides ample space for sample surroundings. According to Figure 2.2, δ for x-rays is typically in the order of 10^{-8} to 10^{-4}, which is in strong contrast to visible light, where δ is typically in the order 10^{-1} (considering e.g. glass). According to Equation (9), lenses for focusing visible light at a focal length of 1 m must have a radius of curvature in the order of 1 m, which is readily achievable by mechanical techniques such as grinding and polishing. For x-rays, however, the radius of curvature needs to be in the order of 10^{-8} m to 10^{-4} m, where traditional mechanical techniques are no longer adequate.

2.2.3 Compound refractive lens

To relax the requirements on too extreme radii of curvature, multiple lenses may be stacked in series to build a compound refractive lens (CRL, Figure 2.6). The idea is that the x-ray beam is successively focused by individual weakly focusing lenslets, thereby achieving practical focal lengths with technologically realizable radii of curvature.

Using the thin lens approximation, valid if the focal length is considerably larger than the lens thickness, the focal length f_0 of a compound lens consisting of N single lens elements (lenslets) is similar to Equation (9) and given by

$$f_0 = \frac{f_S}{N} = \frac{R}{2N\delta} \propto E^2 \tag{11}$$

with the total CRL thickness T

$$T = NT_0 + \frac{NR_0^2}{R}. \tag{12}$$

According to Equation (11), CRLs are achromatic, meaning that the focal length strongly depends on the x-ray energy being used. In order to obtain a clear focus without background, CRLs should be used with monochromatic x-rays, e.g. $\Delta E/E \leq 10^{-3}$.[10] Alternatively, a CRL combined with a pair of slits or a pinhole may be efficiently used as a monochromator [184].

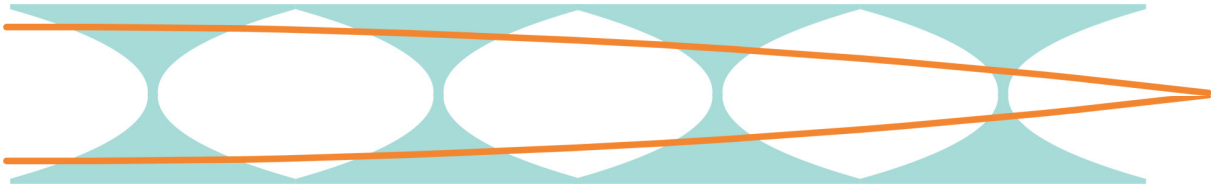

Figure 2.6. Schematical drawing of a compound refractive lens.

A more thorough analysis of the compound system shows that the focal length measured from the middle of the CRL may be better approximated by

$$f = f_0 + T/6, \tag{13}$$

which accounts for the successive convergence of the beam inside the finite thickness of the CRL [172,177].

2.2.4 X-ray absorption

To give an example, let's assume a photon energy E = 17 keV and a desired focal length f = 300 mm. We choose a technically feasible radius of curvature R = 50 µm and a reasonable web thickness T_0 = 10 µm. Further, we chose a lens aperture $2R_0$ = 500 µm to initially capture sufficient incoming photons. Using Equation (11) we can calculate the required number of lenslets to achieve f (approximately due to N being an integer). Table 2.2 lists δ, μ^{-1}, and N for various lens materials.

Table 2.2. Required number of lenslets N with R = 50 µm and $2R_0$ = 500 µm for various elements at a photon energy E = 17 keV. The effective aperture D_{eff}, transmission TX, diffraction limited spot size B_{diff}, spot size accounting for source demagnification B, and the depth of focus DOF are also listed.

Material	δ [×10^{-6}]	μ^{-1} [mm]	N	T [mm]	D_{eff} [µm]	TX [%]	B_{diff} [nm]	B [nm]	DOF [mm]
Lithium (Li)	0.33	95.5	252	116	260	47.0	84	146	0.34
Beryllium (Be)	1.18	21.2	71	32.7	252	41.7	87	148	0.35
Diamond (C)	2.52	4.80	33	15.2	214	28.2	102	158	0.44
Polyethylene (C_2H_4)	0.79	18.6	107	49.2	225	31.2	97	155	0.41
Silicon (Si)	1.67	0.63	50	23.0	70.9	4.01	308	331	2.8
Nickel (Ni)	6.09	0.02	14	6.44	25.4	0.01	842	850	20

Given the required number of lenses, the total CRL thickness T may be calculated using

[10] The required degree of monochromaticity depends on the optical configuration, in particular on the depth of focus and hence on the focal length (cf. Chapter 2.2.6).

Equation (12) and one sees that T may exceed μ^{-1} several times such that particularly rays propagating at the edges of the CRL are mostly absorbed, as is illustrated in Figure 2.7.

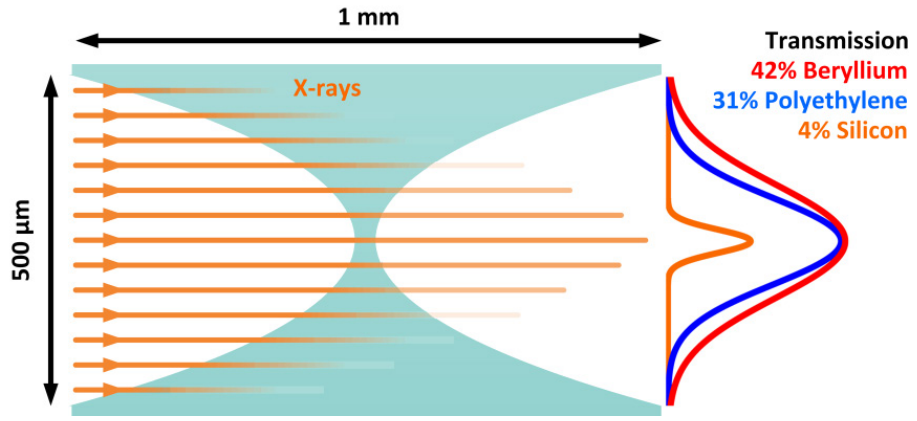

Figure 2.7. X-ray transmission through a CRL. The transmission profiles are to scale and where calculated using Equation (14) and the lens properties listed in Table 2.2.

The transmitted intensity I(x) of a ray impinging at a position x with intensity I_0 at the lens aperture may be approximated by using Beer–Lambert's law

$$I(x) = I_0 \exp\left(-\mu\left(T_0 + 2y(x)\right)N\right) = I_0 \exp\left(-\mu T_0 N\right)\exp\left(-\mu\frac{x^2}{R}N\right) \tag{14}$$

and the total transmission through a lens is thus given by

$$TX = \frac{I}{I_0} = \exp\left(-\mu T_0 N\right)\frac{1}{2R_0}\int_{-R_0}^{R_0}\exp\left(-\mu\frac{x^2}{R}N\right), \tag{15}$$

where the term $\exp\left(-\mu T_0 N\right)$ describes absorption due to the finite web thickness T_0. The values TX are listed in Table 2.2 and the Gaussian transmission profiles for beryllium, polyethylene and silicon are illustrated in Figure 2.7. In case of silicon, it is clear that most parts of the lens do not contribute to the focus. Therefore one may reduce $2R_0$ and thus T to a size where noticeable transmission happens, while essentially not sacrificing the total efficiency. A material specific absorption limited aperture D_{eff} can be calculated by the $1/e^2$ width of the intensity transmission profile by solving Equation (14) according to

$$I\left(D_{\text{eff}}/2\right) \overset{!}{=} \frac{I_0}{e^2}. \tag{16}$$

Neglecting the web thickness T_0 it is well approximated by

$$D_{\text{eff}} = \sqrt{\frac{8R}{\mu N}} = \sqrt{\frac{16f\delta}{\mu}} \tag{17}$$

and Figure 2.8 shows D_{eff} for various lens materials as a function of x-ray energy at a fixed focal length of 300 mm. This formula justifies the ratio δ/μ as a figure of merit concerning the choice of lens materials (cf. Figure 2.3).

A more precise treatment of D_{eff} and TX for arbitrary lens dimensions performed in [170,177], which considers also the RMS roughness σ of the lens surface yields

$$D_{\text{eff}}^{\text{Lengeler}} = 2R_0\sqrt{1-\exp\left(-a_{\text{p}}\right)/a_{\text{p}}}\,, \tag{18}$$

$$TX^{\text{Lengeler}} = \exp\left(-\mu T_0 N\right)\frac{1}{2a_{\text{p}}}\left[1-\exp\left(-2a_{\text{p}}\right)\right], \tag{19}$$

$$\text{with}\quad a_{\text{p}} = \frac{\mu N R_0^2}{2R} + \frac{4\pi^2\delta^2\sigma^2 N R_0^2}{R^2\lambda^2}. \tag{20}$$

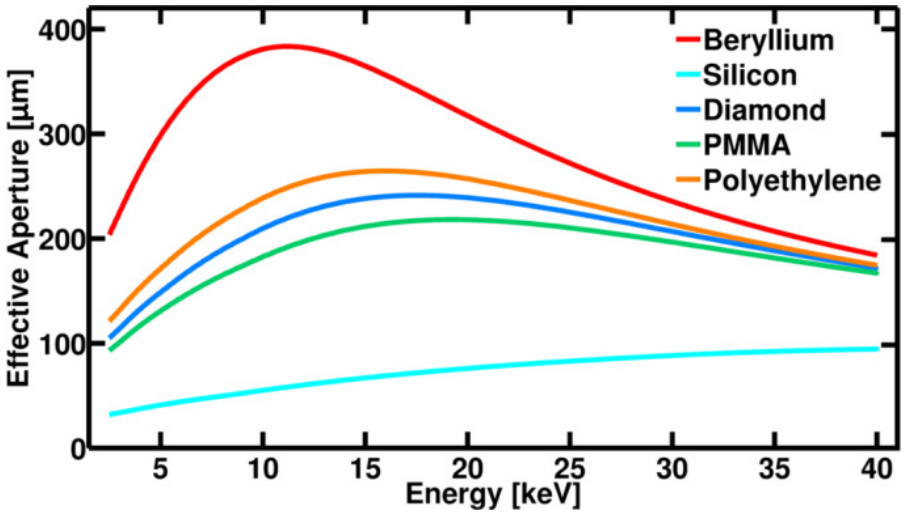

Figure 2.8. Material specific effective apertures of lenses with focal lengths of 300 mm as a function of x-ray energy.

2.2.5 Spot size

The achievable spot size created by a focusing lens is particularly important, because it significantly determines the achievable spatial resolution in an experiment. Besides inherent lens imperfections and respective optical aberrations the focal spot is limited by the geometry of the optical setup and diffraction by the finite lens aperture.

A focal spot is always an image of the source being used. Essential dimensions are the size of the x-ray source d_{Source}, the source to lens distance L_1 and the imaging distance L_2, as specified in Figure 2.9. The imaging distance L_2 is essentially determined by L_1 via

$$L_2 = fL_1/\left(L_1 - f\right), \tag{21}$$

where L_2 converges to f for sufficiently large L_1. The size of the demagnified source B_{demag} is given by

$$B_{\text{demag}} = d_{\text{Source}}\, L_2/L_1\,. \tag{22}$$

Typically focal spots are expressed in terms of the full width at half maximum (FWHM), which may be obtained by using the FWHM of the source

$$d_{\text{Source}}^{\text{FWHM}} = 2\sqrt{2\ln(2)}\,\sigma_v = 2.355\,\sigma_v, \tag{23}$$

where σ_{v} is the Gaussian RMS width (standard deviation) of the intensity distribution, sometimes provided in technical overviews of beamlines.

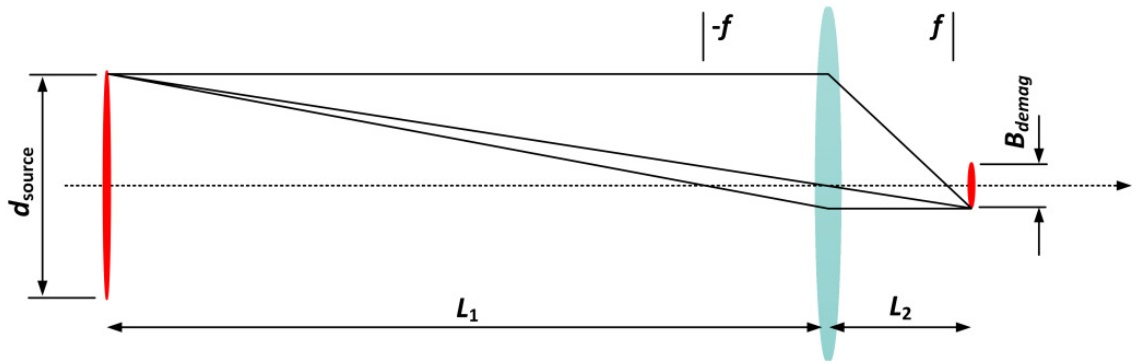

Figure 2.9. Source demagnification.

Besides source demagnification the achievable spot size is limited by diffraction, which merely depends on the wavelength λ and the numerical aperture NA of the lens specified by

$$\mathrm{NA} = n\sin\varphi = n\sin\left[\arctan\left(\frac{D_{\mathrm{eff}}}{2f}\right)\right] \approx \frac{D_{\mathrm{eff}}}{2f}, \tag{24}$$

where D_{eff} is the (effective) aperture of the lens and f its focal length (cf. Figure 2.10). If the spot size is no longer determined by source demagnification, but solely by the Abbe resolution limit, the spot is regarded as being diffraction-limited. Diffraction-limited-focusing takes place if the source can be regarded as being point like (very small), L_1 being large and L_2 small. The size of the diffraction limited spot B_{diff} is taken to be the FWHM of the Airy disk, which is the bright region in the center of the diffraction pattern generated by the uniform illumination of a circular aperture of diameter D_{eff} at a distance f [183]:

$$B_{\mathrm{diff}} \approx \frac{\lambda f}{D_{\mathrm{eff}}} = \frac{\lambda}{2\mathrm{NA}}. \tag{25}$$

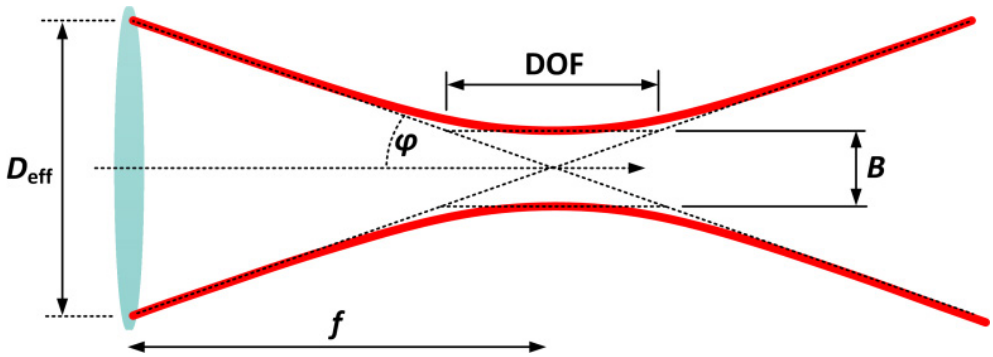

Figure 2.10. Diffraction limited focusing and depth of focus.

Diffraction limited focusing and source demagnification may be united by building the root of the sum of both squares considering that both the x-ray source and transmission function of the lens are Gaussian:

$$B = \sqrt{\left(B_{\mathrm{mag}}\right)^2 + \left(B_{\mathrm{diff}}\right)^2}. \tag{26}$$

Table 2.2 lists B_{diff} and B for the aforementioned lens dimensions and typical specifications of a beamline at a third generation synchrotron, d_{Source} = 20 µm and L_1 = 50 m. This ideal spot size is typically blurred by various aberrations (cf. Chapter 2.4).

2.2.6 Depth of focus

In an experiment, the specimen to be studied is typically positioned at the focus of the generated x-ray beam (e.g. in scanning microscopy or focused illumination). This necessitates knowing the longitudinal extension of the focus, hereafter referred to as the depth of focus (DOF). It may be defined by twice the length of the region along the optical axis where the diffraction-limited spot diameter is equal the geometrical diameter of a cone extending from the aperture of the lens to the focus (cf. Figure 2.10, [183]), yielding

$$\mathrm{DOF} = \frac{2f}{D} B \approx \frac{\lambda}{2\mathrm{NA}^2} \approx 2\lambda \frac{f^2}{D_{\mathrm{eff}}^2} \approx f \frac{\lambda}{8} \frac{\mu}{\delta}, \tag{27}$$

where the last three expressions consider diffraction limited focusing only. Table 2.2 lists DOF for the aforementioned lens specifications.

2.2.7 Kinoform lenses

The high x-ray absorption is largely limiting the optical performance of refractive lenses. On the one hand, x-ray absorption naturally limits x-ray transmission, which negatively affects counting times or signal to noise ratios in an experiment. On the other hand, it limits the numerical aperture of the lens and thus the achievable resolution. To overcome this limitation, optically passive lens material, which is not essential to the refractive lens behavior and merely causes a wavefront phase shift of 2π or multiples thereof, may be removed (cf. Figure 2.11). Such 'kinoform' lens designs in conjunction with CRLs became first feasible by utilizing lithographic techniques [181,185–206] and were used in this thesis (cf. Chapter 6.4).

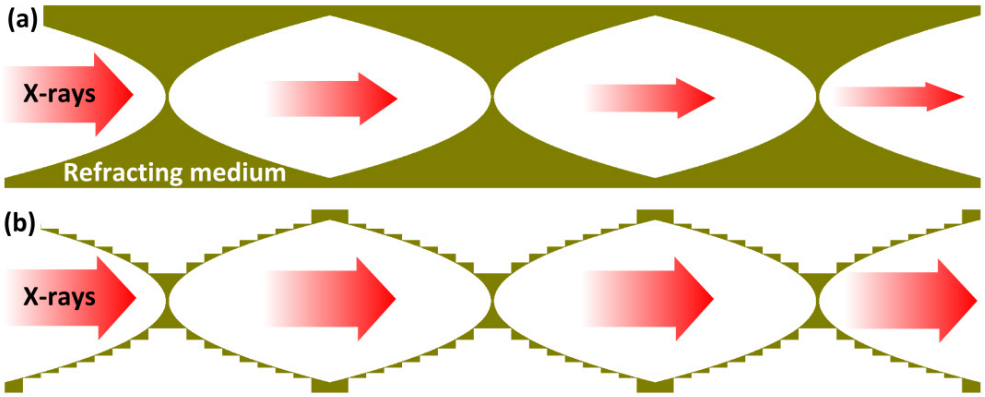

Figure 2.11. X-ray CRL designs. (a) Standard CRL. (b) Kinoform CRL: absorbing material merely causing a 2π phase shift is removed from the light path.

2.2.8 Adiabatic design

As illustrated in Figure 2.6 the x-ray beam converges already inside a CRL by the successive focusing of the consecutively arranged refracting lenslets. The aperture of the lenslet at the exit of the CRL thus may not be fully used, as opposed to the entrance aperture of the CRL. Hence,

the apertures of individual lenslets may be adapted to the progressively decreasing size of the x-ray beam inside the CRL, which would reduce the CRL total length, while leaving the optical performance essentially unaffected [58,202]. Such a design is called 'adiabatic' and especially in the case of strongly focusing CRLs with very short focal lengths it has a significant effect. Ultimately, it allows to maximize the refractive power per unit length for obtaining the ultimate achievable resolution possible with CRLs, which is expected to be well below 10 nm [58]. In the present thesis adiabatic designs were essential when combined with kinoform designs (cf. Chapter 2.2.10).

2.2.9 Simulations

Sometimes it is useful to visualize the x-ray beam modified by an optical system. For that purpose sophisticated software packages are available, which are based on wavefront propagation [207–212], ray-tracing [213–215], or a combination of both [216,217]. In the course of this thesis McXtrace [215] was used to visualize the x-ray beam of parabolic CRLs with non-uniform lens profiles or varying lens dimensions (adiabatic designs). Most beneficial, the effect of a realistic Gaussian-shaped divergent source and a finite energy bandwidth of the x-ray beam may be taken into account. Lens efficiencies, focal lengths and spot sizes were of particular interest. The software allows defining the characteristics of the source and the positions of individual optical components. Multiple 'monitors' or 'detectors' may be placed within the optical path to obtain data, which can be analyzed subsequently. McXtrace uses Monte Carlo algorithms, which allow tracing 10^6 rays that interact with 100 single lens elements, while getting 1D intensity profiles with 2^{13} values of intensity at 100 positons along the optical axis within a couple of minutes.

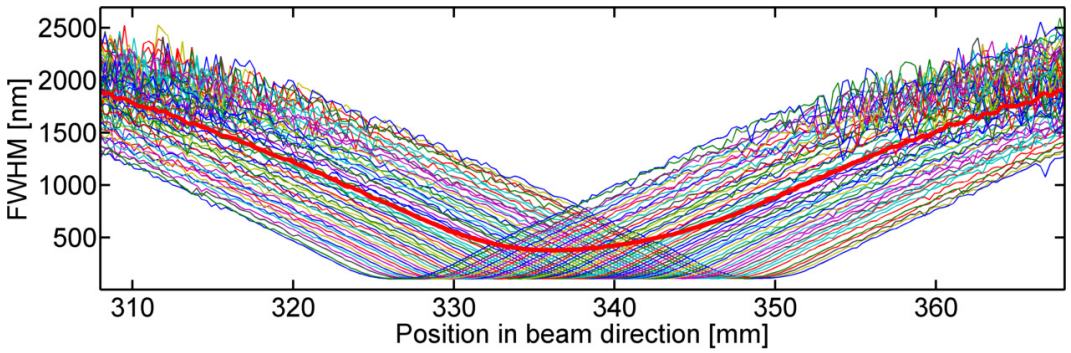

Figure 2.12. Simulated x-ray beam focused by a non-uniform 1D silicon lens. The individual thin beam profiles correspond to lenses with different radii of curvature, while the thick profile is the average of all individual profiles.

For example, the effect of a non-uniform lens was simulated. A non-ideal manufacture results in 1D lenslets with varying radii of curvature along the height of the lenslets. Beam profiles were obtained for lenses with different radii of curvature R, these profiles were overlapped, and the average of the profiles was calculated (cf. Figure 2.12). The lens material was silicon, R ranged from 45 µm to 48 µm in increments of 0.05 µm, $N = 40$, $L_1 = 51$ m, $\sigma_v = 8.6$ µm, the vertical source divergence was 2.8 µrad, $E = 17$ keV, and $\Delta E = 0.03$ keV. The waist of the average profile was 380 nm, the total lens transmission was 8%, which compares favorably well with

calculations using above analytical formulas. The DOF of the simulated beam can be estimated to be ~5 mm. However, caution needs to be payed to the fact that ray-tracing does not account for diffraction and obtained spot sizes may therefore be too optimistic. A future improvement to McXtrace could be to allow simulating arbitrarily shaped lens profiles, i.e. deviations from the ideal parabolic shape.

2.2.10 Matrix formalism

For special needs it may be useful to write a dedicated code in Matlab, e.g. utilizing the ray transfer-matrix method [175,183,218,219]. It uses the paraxial approximation and an individual ray is represented by vectors specifying its positon r_0 from and its angle w_0 with the optical axis. Free space propagation or refraction of rays and combinations thereof are described by successively applying matrices to the vectors. Rays propagating through a CRL may be described by

$$\begin{bmatrix} r_N \\ w_N \end{bmatrix} = \left(\begin{bmatrix} 1 & L_1/2 \\ 0 & 1 \end{bmatrix} \begin{bmatrix} 1 & 0 \\ -2/f_S & 1 \end{bmatrix} \begin{bmatrix} 1 & L_2/2 \\ 0 & 1 \end{bmatrix} \begin{bmatrix} 1 & 0 \\ -2/f_S & 1 \end{bmatrix} \begin{bmatrix} 1 & L_3/2 \\ 0 & 1 \end{bmatrix} \right)^N \begin{bmatrix} r_0 \\ w_0 \end{bmatrix}, \tag{28}$$

where a lenslet is represented by propagation from the entrance of the lenslet to the first lens surface, refraction, propagation to the second lens surface, refraction, and propagation to the exit of the lenslet (cf. Figure 2.13).

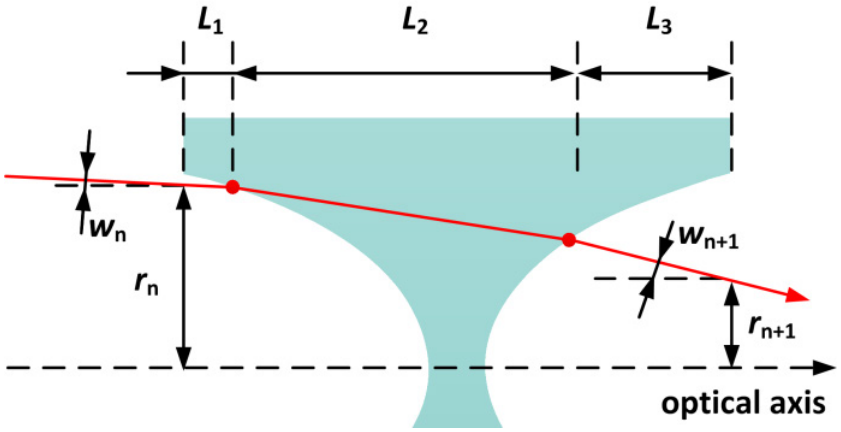

Figure 2.13. Propagation of a ray through a lenslet.

In this thesis the matrix formalism was used to illustrate the precise path of a ray through kinoform lenses and to facilitate optimizing their design with respect to photon transmission. As illustrated in Figure 2.14 the x-ray beam converges inside the lens. This may cause that individual rays travelling through the CRL change propagation between thicker and thinner parts of the lens material, i.e. cross over between different kinoform steps. Maximal transmission, however, is obtained, if individual rays constantly propagate through the 'same step' in each lenslet, i.e. rays entering the lens at a thinner portions of the lens keep propagating through thinner parts until they exit of the CRL and vice versa. This can be obtained by adapting the dimensions of individual lenslets, e.g. by adjusting R_n (i.e. using an adiabatic design, cf. Chapter 2.2.8). Additionally, such illustrations show rays hitting the surfaces that are parallel to

the optical axis. Such crossovers result in total external reflection, which is catastrophic and renders such rays as essentially lost (cf. Chapter 6.4).

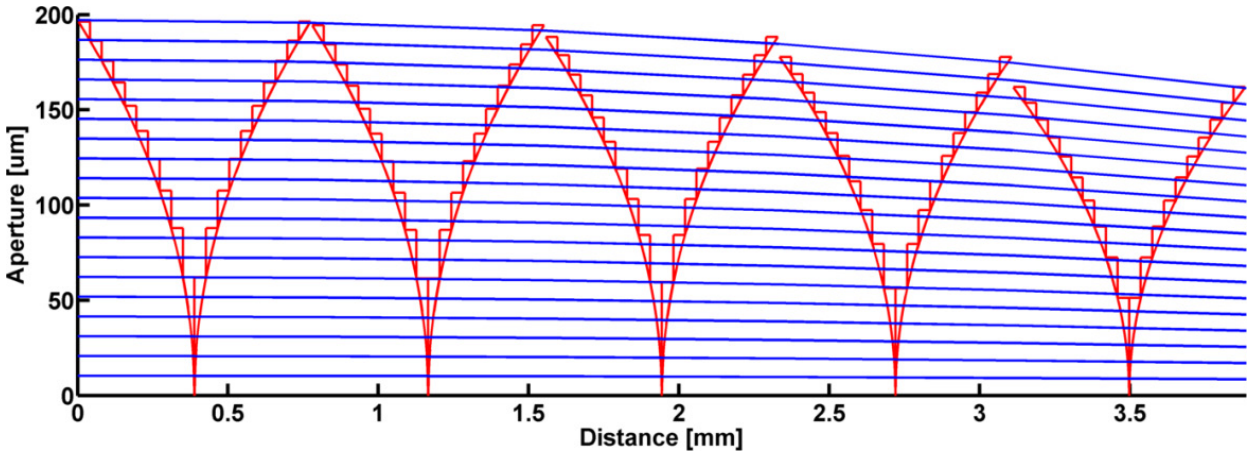

Figure 2.14. Simulated path of rays through a kinoform lens. The refractive power is strongly exaggerated to demonstrate the convergence of the beam inside the lens.

Figure 2.15 shows a real world example, where a kinoform CRL comprising 80 lenslets has been optimized for maximal efficiency. The x-ray transmission may be obtained by tracking the total length an individual ray has passed through lens material, applying Beer–Lambert's law and integration. The total transmission through the lens considered here is 10.4%, in contrast to 4.0% for an equivalent non-kinoform lens.

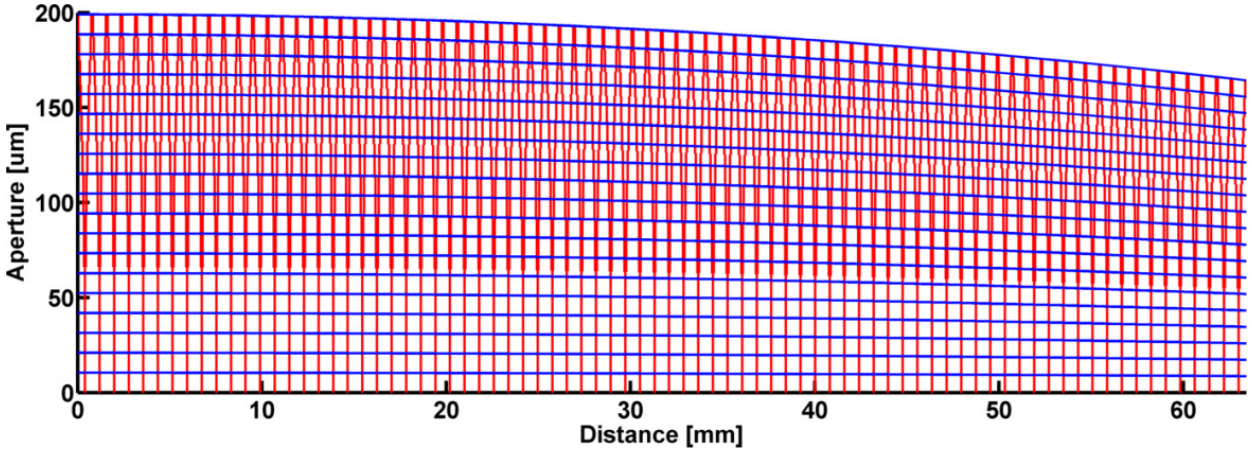

Figure 2.15. Simulated path of rays through a kinoform lens. Real world example with $N = 80$, $E =$ 17 keV and R varies from 50 µm at the lens entrance to 34.3 µm at its exit, $d = 6$, and $f \sim 220$ mm.

2.3 Lens manufacture

2.3.1 Drilling

Since the invention of CRLs, various technologies have been used to manufacture them. As originally suggested in Tomie's patent, refractive focusing was first demonstrated using parallel hollow cylinders mechanically drilled into a single piece of substrate [161]. By using an aluminum-copper alloy as a substrate with 30 cylindrical holes of 300 µm radius drilled into it,

Snigirev et al. achieved focusing 14 keV x-rays from a bending magnet at ESRF's D-5 to a 8 µm narrow line (FWHM) and a photon gain of 3. Experiments were repeated at ESRF's ID6 using undulator radiation and lenses made of beryllium and pyrocarbone [220] and at SPring-8 using beryllium and aluminum [221]. Point-focusing CRLs were manufactured by crossed drilling into substrates [167,169] and a range of alternative materials such as boron nitride or various polymers were tested as well [169,222,223].

2.3.2 Embossing

Parabolic rotational symmetric CRLs made by embossing ductile materials such as aluminum demonstrated by Lengeler et al. were game-changing in the sense that they enabled imaging with a spatial resolution of 345 nm using 25 keV x-rays, which is well suited for microscopy of thick opaque samples [182]. One of today's standard x-ray optical components are 1D- and 2D-focusing CRLs made by embossing beryllium [143,224–226], which are commercially available with radii of curvature down to 50 µm.[11] CRLs made by embossing nickel were also developed, which are particularly useful for shaping x-rays with energies as high as 175 keV [227]. Single lenslets are manufactured individually and subsequent high precision alignment is mandatory. Respective alignment errors were investigated in [228]. Since lenslets are separated from each other, they can be individually moved in and out of the x-ray beam. So-called transfocators enable the focal length to be easily adjusted or the number of lenses adapted to a given photon energy [229]. Embossing (or compression molding) was also explored to fabricate lenses made of lithium [230–232], polyimide (Kapton), or Mylar ($C_5H_4O_2$) [233–237].

Metal lenses can withstand high heat loads and are therefore very well suited to be used in the primary x-ray beam at synchrotrons or free electron lasers [144,238–240]. Beryllium lenses are expensive (~1500 Euro/lenslet). High demands are put on pressing tools, which are typically made by diamond-turning. Tools may degrade with every coined lenslet, resulting in dull apexes and non-parabolic shapes. The grain structure of metals generates a heterogeneous plastic response and thus a non-ideal shape. The poly-crystallinity of metals cause small angle scattering that increase the beam waist and the bulk material may contain voids due to its manufacture by powder metallurgy [241,242].

2.3.3 X-ray lithography

A very powerful tool for fabricating linear (1D-) focusing x-ray lenses is deep x-ray lithography (DXRL) using synchrotron sources [243–247]. The synchrotron radiation is highly collimated, which allows the directional transfer of 2D-patterns present on suitable masks into underlying substrates of substantial thicknesses (100 µm – 2 mm) [248–252]. Typically, polymers such as PMMA are used as substrates, where x-ray induced chemical bond breakage (chain-scission) renders illuminated areas soluble in a suitable solvent [253–255]. Alternatively, photoactive resins such as SU-8 may be used, where x-rays activate photo-initiators, which cross-link exposed resist upon a temperature treatment; unexposed areas remain soluble in a suitable solvent [256–263]. PMMA and SU-8 act as a positive and negative resist, respectively. The sensitivity of PMMA to x-rays is low, because its constituents (carbon and oxygen) have small

[11] http://www.rxoptics.de/index.html (Dec 2015).

x-ray absorption cross sections. The sensitivity of SU-8 is ~100 times higher, partially because one activated photo-molecule cascades multiple crosslinks and partially because photo-initiators contain heavy atoms with high x-ray absorption cross sections [259,264]. Commercially available SU-8 contains up to 10 weight percent of mixed triaryl-sulfonium antimonate photoacid generator,[12] improving the lithography, but considerably degrading the optical performance of the final x-ray lens. CRLs made of SU-8 lenses are considered to be more stable focusing devices due to the presence of aromatic groups, whereas PMMA is considered to structurally degrade after absorbing sufficiently high x-ray doses [245,254].

CRL manufacture using DXRL usually necessitates the manufacture of two lithography masks [245,265–267]. A first mask made by e.g. e-beam lithography into PMMA and subsequent electroplating of ~2 µm thick gold. This mask is then used to fabricate a 'working mask' by x-ray lithography and electroplating of ~20 µm thick gold. The thick gold layer is necessary to obtain sufficient contrast between exposed and unexposed areas during DXRL. Gold structures need to be supported by x-ray transparent membranes, such as beryllium or thin titanium. These membranes are subject to flexure due to gravity and heating during DXRL, which needs to be accounted for and ideally avoided [245,267–269].

As-obtained polymeric structures may be used without further processing as CRLs. Alternatively, DXRL may be used to obtain inverted lens structures, which are used as molds for subsequent electroplating with e.g. nickel [270,271]. This type of process combined with a molding technique, e.g. polymer injection molding, is known as the LIGA technique (German acronym for lithography, electro plating and molding) and may be used in the future for a low-cost mass production of x-ray lenses (cf. Chapter 6.3,).

Point-focusing CRLs using DXRL can be manufactured by exposing the resist layer two times, once at an angle of -45° and once at an angle of +45°. Thereby crossed (interdigitated) linear focusing lenses can be obtained which mimic rotational parabolic lenses, and are useful for distortion free imaging [269,272–274]. The smallest measured focal spot was ~70 nm (FWHM) in both directions using 18.6 keV x-rays at a working distance of 2 mm [247]. Today's developments using DXRL strive to develop more reproducible, sensitive, selective, and radiation stable photoresists showing less x-ray absorption, as well as optimizing the x-ray exposure and resist development to obtain CRLs with higher accuracy [267,275–277].

2.3.4 Lithography & pattern transfer

Microlithographic techniques are well suited to define the required parabolic shapes in 2D with high precision. Radii of curvature considerably below 50 µm can readily be realized using standard UV-lithography and for radii down to 100 nm e-beam lithography may be used. Two dimensional patterns may be directionally transferred into substrates by reactive ion etching (RIE) to obtain linear (1D-) focusing lenses. Deep reactive ion etching (DRIE) using the Bosch process was early recognized as a powerful technique to manufacture CRLs made of silicon [278–280]. Generally, silicon CRLs are less transparent than e.g. beryllium or polymer lenses. However, this route of manufacture is very attractive, because of the possibility to realize extreme radii, dimensional compactness of Si-CRL chips, relatively easy manufacture, cheap

[12] Antimony $Z = 51$.

substrates and easier access to relevant processing equipment. These benefits resulted in ongoing efforts to improve the manufacture of silicon CRLs and ultimately striving for maximal resolution and minimal spot sizes [145–147,281–287]. The electronic grade silicon being used is a very pure material and mono-crystalline, which means that no grain boundaries exist, which would cause detrimental small x-ray scattering. Similar to metal lenses, Si can withstand high heat loads [240]. Integrated lens systems comprising multiple CRLs may be fabricated in parallel on single wafers. More advanced lens patterns may be realized, which facilitate the manufacture [288] or result in CRLs with less absorption (cf. Chapter 2.2.7). The compactness of Si-CRLs enables very short focal lengths and thereby diffraction limited focusing (cf. Chapter 2.2.5). Schroer et al. reported a spot size of ~50 nm (FWHM) obtained by silicon CRLs realized by e-beam lithography and DRIE; the lenses had a structure height of 60 µm, a focal length of ~5 mm and were operated at 21 keV [145]. Recently, a focus with 17 nm features was demonstrated using adiabatic Si lenses and 20 keV x-rays [289]. Silicon CRLs are particularly useful at x-ray energies higher than 30 keV, where the x-ray transmission is similar to that of beryllium and equivalent beryllium lenses would be very long and thus very expensive. Details about the manufacture of Si-CRLs will be discussed more thoroughly in Chapter 3.

Lithography combined with pattern transfer by RIE was also used to obtain CRLs made of boron or diamond, however, for the time being only with limited success with respect to the surface finish and the heights of the lenses [193,290–295]. Recently, inverted lens structures in silicon were used as molds for nano-crystalline diamond deposited by PECVD also facing technological limitations with respect to achievable lens heights [296–299].

2.3.5 Others

The parabolic lens shape may be approximated by multiple prisms, thereby facilitating the manufacture [300–303]. These multi-prism lenses were manufactured by anisotropic wet etching of crystalline silicon [304–306], mechanical milling [307,308], DXRL [206,264,309–313], or RIE [314,315]. Silicon multi-prism structures may be used as templates for pattern transfer into lithium [316], beryllium [301], diamond [305], or polymers [165,301,317]. Interestingly, structured thin polymer films may be rolled to obtain large aperture point-focusing lenses [266,318–321]. Multi-prism lenses ease the manufacture and increase the lens transmission; however, they face technological challenges if sub-micron focusing is required [322–325].

For the sake of completeness, some alternative methods should be mentioned as well. CRLs may be fabricated by direct etching of polymers using x-rays [326–328], photo-anodic etching of silicon [329], or laser milling of diamond [330–332]. Dudchik et al. exploited surface tension of viscous polymer inside glass capillaries upon introducing air bubbles to develop so called ‘bubble lenses’ [333–336]. Pavlov et al. used a photo-curable polymer combined with a tool used for embossing metals to obtain rotationally symmetric lenses [337], resulting in long production times and similar problems with respect to the lens shape as with beryllium lenslets.

2.4 Lens imperfections

This thesis is on the fabrication of line-focusing lenses using the basic process steps of 2D lithography and pattern transfer by DRIE into silicon wafers. Most crucial for efficient focusing

are the parabolic shapes of the lenses. Ideally, the etched cavities have the shapes of parabolic cylinders, meaning that the lithographically defined 2D parabolic shapes are vertically transferred into the substrate by DRIE. The parabolic profile must be strictly constant along the depth of the lenses in order to obtain uniform focusing. Unfortunately, deviations from this ideal lens shapes occur.

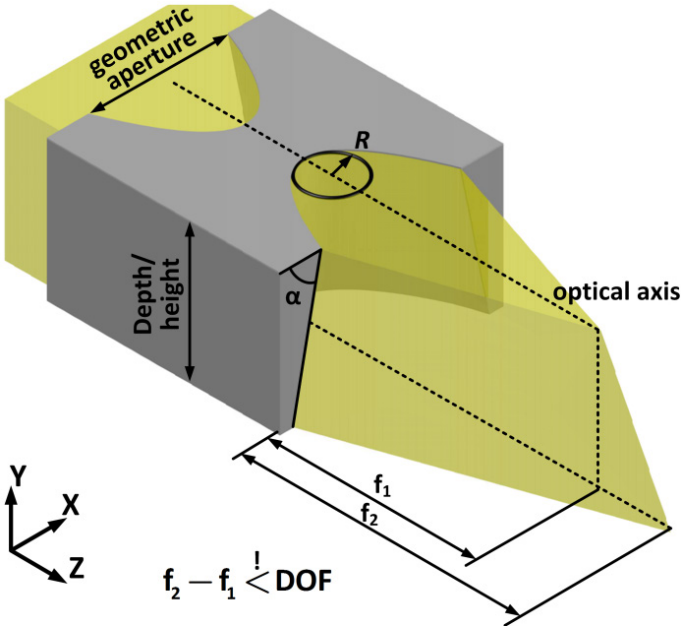

Figure 2.16. Illustration of the effect of a non-uniform cavity shape on the optical performance. In particular, a tapered lens sidewall results in a slanted focal plane and for optimal optical performance the variation of focal lengths need to be smaller than the depth of focus (DOF).

The lithographically defined 2D shape typically widens slightly in the course of the manufacture due to

1. overexposure or overdevelopment during the lithography,
2. mask undercut encountered during DRIE, and
3. surface smoothing steps (cf. Chapter 3).

This type of shape deviation affects the cylindrical shape uniformly along the depth of the cavities and it may be compensated for at the very beginning of the manufacture. It can be accounted for by defining slightly tighter shapes in the original mask design, which widen in the course of the various processing steps and at the end of the manufacture result in close to ideal parabolic shapes (cf. Chapter 5.2).

Additional to a uniform structural widening, DRIE usually results in an over-depth shape variation of the etched cavities (cf. Chapter 3.5). This variation generally results in non-uniform focusing along the depth of a CRL. The reason is DRIE being a complex process, which does not necessarily result in a strictly vertical pattern transfer, but cause sidewall profiles that are typically slightly positively or negatively tapered (cf. Chapter 3.5 and Chapter 4.1). Figure 2.16 illustrates the effect of a negative sidewall profile, which causes a structural widening of the cavity along its depth, resulting in a deviation from the ideal parabolic shape and ultimately in a slanted focal plane.

The compensation of uniform shape deviations and the optimization of DRIE may be possible only to a limited extent. In order to guide the manufacture and predict the optical performance, it is important to understand the consequences of shape deviations from the ideal parabolic cylinders. If the dimension of a structure is properly chosen (cf. Chapter 3.6), DRIE can be well controlled to yield profiles that differ from the vertical less than 1 µm per 100 µm etch depth. Uniform widening may be compensated for with an accuracy of ± 200 nm or better.

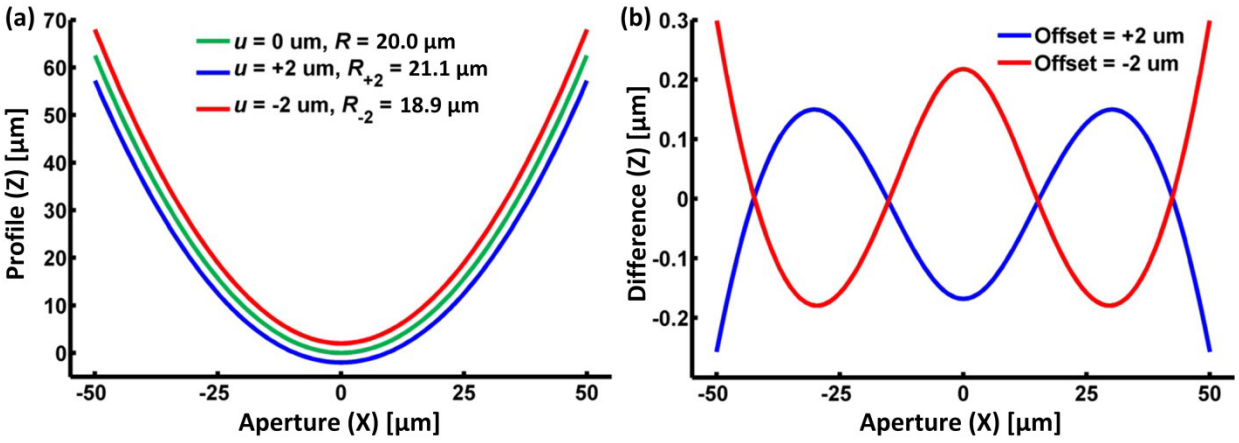

Figure 2.17. Effect of linear offsets to a parabola. The nominal radius of curvature is 20 µm. (a) Parallel parabolas. (b) Differences from parabolic fits.

To first order, the shape variations may be approximated by linear offsets corresponding to parallel curves to parabolas. This is justified as long as the offset is considerably smaller than the radius of curvature of the parabola. A parallel curve to a parabola is parametrically described by:

$$\vec{g}(t)=\begin{pmatrix}X\\Z\end{pmatrix}=\begin{pmatrix}t\\f(t)\end{pmatrix}+\frac{u}{\sqrt{f'(t)^2+1}}\begin{pmatrix}f'(t)\\-1\end{pmatrix}, \tag{29}$$

where $f(t)=t^2/2R$ is the parabolic function and u the offset (or undercut). Figure 2.17(a) shows a parabola with R = 20 µm and its parallel curves with u = ± 2 µm. Notably, the parallel curves are no parabolas anymore, but may be fitted to parabolic functions. Figure 2.17(b) shows the differences in Z between the parallel curves and their respective parabolic fits. The fitting parameter is the radius of curvature and it is R_{+2} = 21.1 µm and R_{-2} = 18.9 µm for u = + 2 µm and u = - 2 µm, respectively. Consequently, positive offsets, corresponding to widened parabolic cavities, result in longer focal lengths. Vice versa, negative offsets, which correspond to tightened parabolic cavities, result in shorter focal lengths.

Generally, parabolas with smaller radii are stronger affected by offsets than are parabolas with larger radii. For this reason, it is generally easier to manufacture CRLs with larger radii than to manufacture CRLs with smaller radii. However, a CRL composed of large radii lenslets need to be composed of more of those lenslets in order to achieve the same focal length. A larger number of lenslets corresponds to respective larger number of lens surfaces the x-ray beam needs to intersect. More severely, the beam needs to pass through a larger number of webs, thereby increasing absorption. Therefore, a compromise must be struck between the achievable accuracy of the manufacture and required number of lenslets. The CRLs illustrated in Figure

2.18 are basically equivalent with respect to their focal lengths; however, they differ in absorption and ease of manufacture.

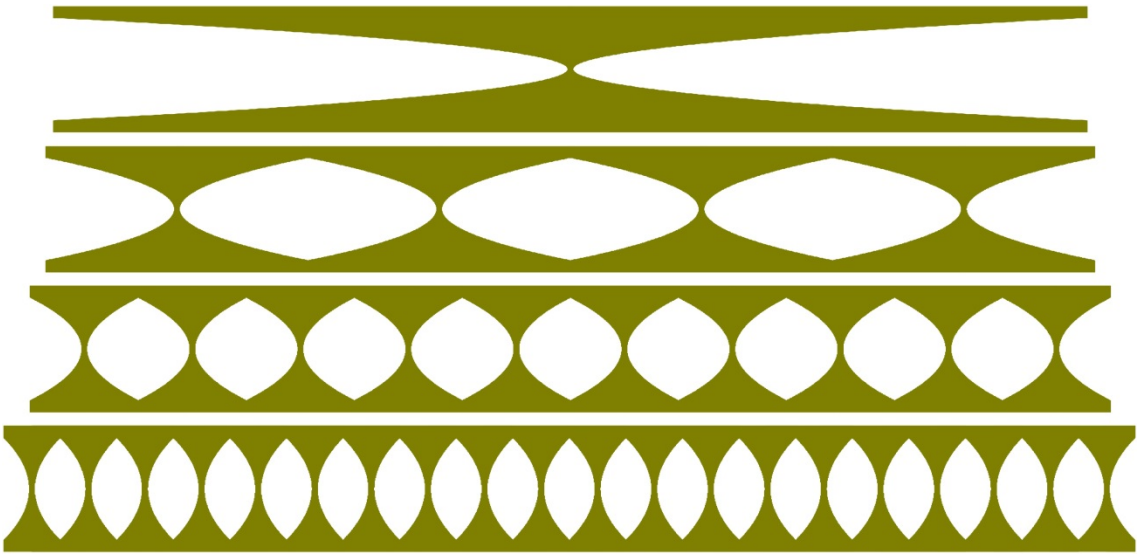

Figure 2.18. CRLs with equivalent focal lengths but varying radii. From top to bottom: $N = 1$, $R = 5$ µm; $N = 4$, $R = 20$ µm; $N = 10$, $R = 50$ µm; $N = 20$, $R = 100$ µm. $2R_0 = 200$ µm, $d = 10$ µm.

Using a code written in Matlab, Figure 2.19 shows rays being refracted at lens surfaces that are subject to offsets. A thin CRL at $Z = 0$ mm is illuminated by a parallel beam and refraction is calculated using Snell's law ($R = 20$ µm, $N = 50$, $d = 5$ µm, $E = 56$ keV, cf. Chapter 2.2.3). Absorption was accounted for by using Equation (14). Predicted spot sizes are generally too small, because we do not account for diffraction. The diffraction limited spot size for this configuration is ~200 nm (cf. Chapter 2.2.5). However, this simple model shows some trends. Slight aberration is already visible for the case of $u = 0$ µm, which is due to the fact that a parabola is not the ideal lens shape, nevertheless a good approximation (cf. Chapter 2.2.2). The Z position of the best focus matches favorably well with Equation (11). Behind the focus, a double peak is visible. A negative offset of -2 µm reduces the focal length by 10% and stretches the focus. A positive offset of +2 µm increases the focal length by 7% and causes a double peak in front of the focus as well as additional peaks at the position behind the best focus. This analysis suggests that in terms of minimal spot size it is generally better to have a negative offset, i.e. an overcorrected lens. This is in agreement with earlier analyses using a wave-optical approach [293].

Another interesting case to consider is a lens not being perfectly aligned parallel to the incoming beam, but being rotated by ϕ around the symmetry axis of the lens (cf. Figure 2.20). Besides the aperture of the lens effectively being reduced, the spot size and position are affected. Figure 2.20 shows the intensity plots around the best focus of slightly rotated lenses. Usually, motorized stages allow lenses to be aligned considerably better than 0.01°. In Chapter 6.1 slight misalignment is utilized to compensate for shape imperfections.

Another scenario involves lenses with dull apexes, which may be the result of a non-optimal manufacture (cf. Chapter 6.1). A dull apex essentially means that the beam is not refracted properly. For the sake of simplicity we assume that the lenses are flat within a region $\pm b$ around

the apex, i.e. x-rays transmit the lens in this region without being refracted. This does not affect the focal position, however causes a double peak to appear in front of the focus as is shown in Figure 2.21.

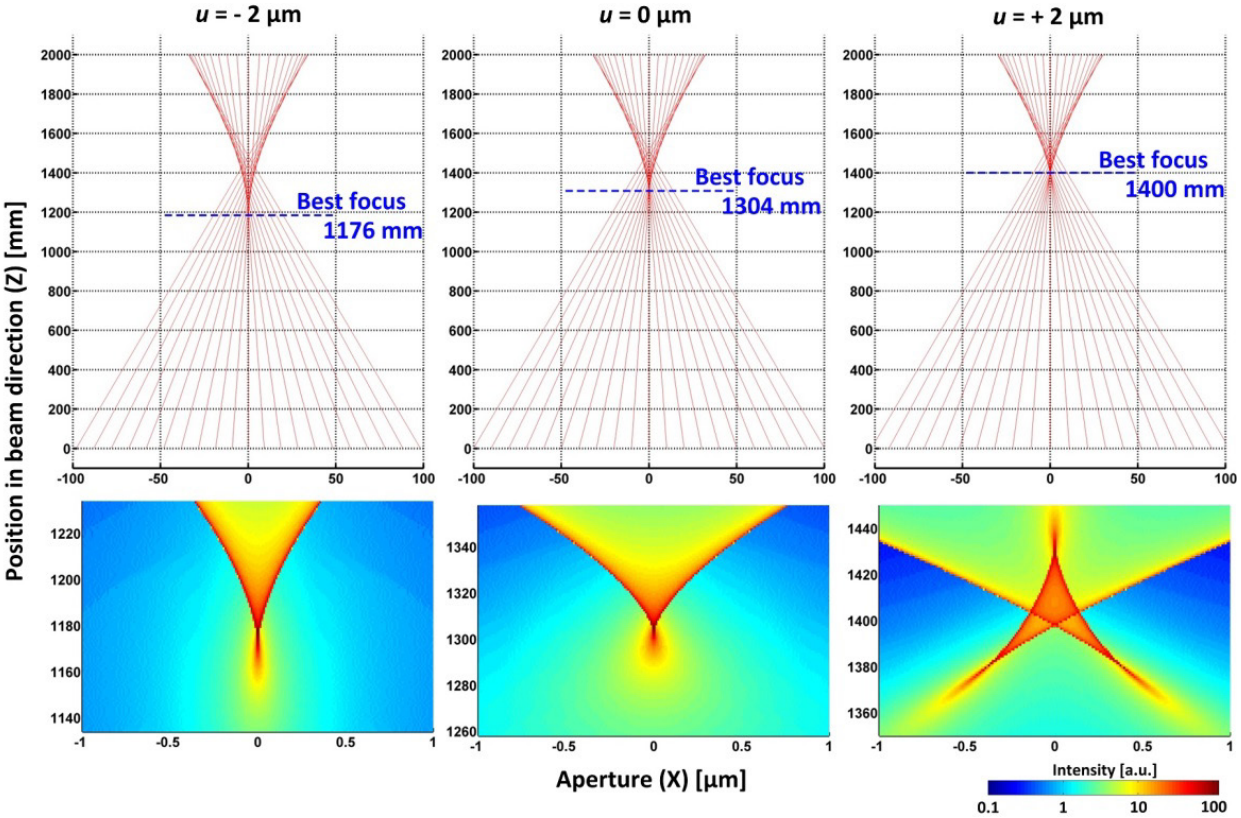

Figure 2.19. Ray tracing of a parallel beam being refracted by a thin lens with varying offsets of the parabolic shape. $R = 20$ µm, $N = 50$, $d = 5$ µm, $E = 56$ keV. Note the logarithmic scale in the surface intensity plots.

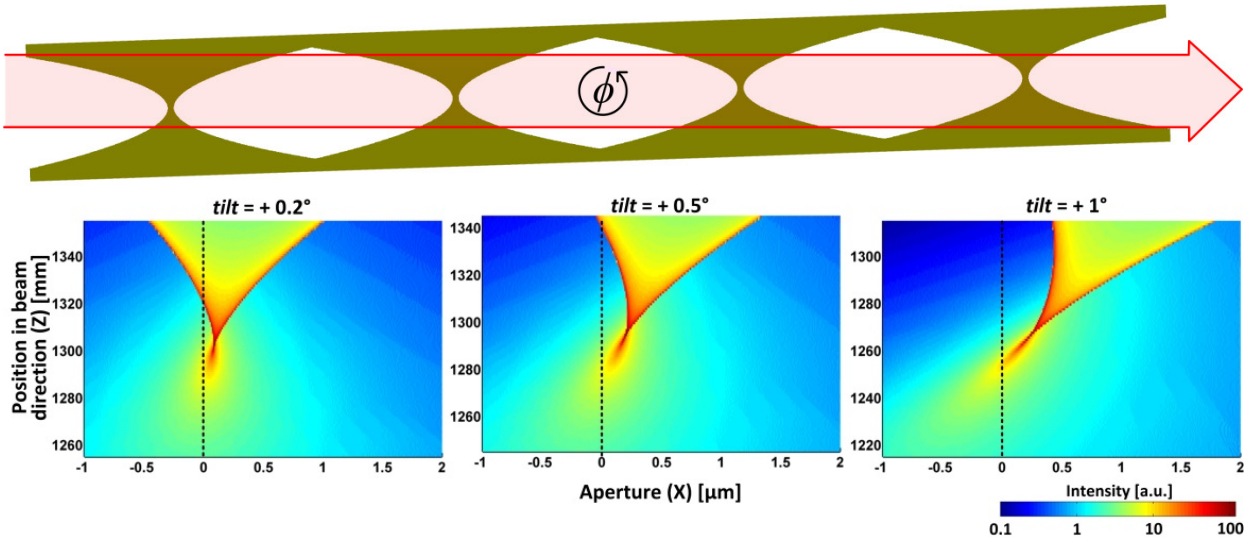

Figure 2.20. Schematical drawing of a CRL being misaligned with respect to the incoming beam by a rotation around the symmetry axis of the lens. Effect of rotation of a lens around its symmetry axis. The optical axis is indicated by a dashed line.

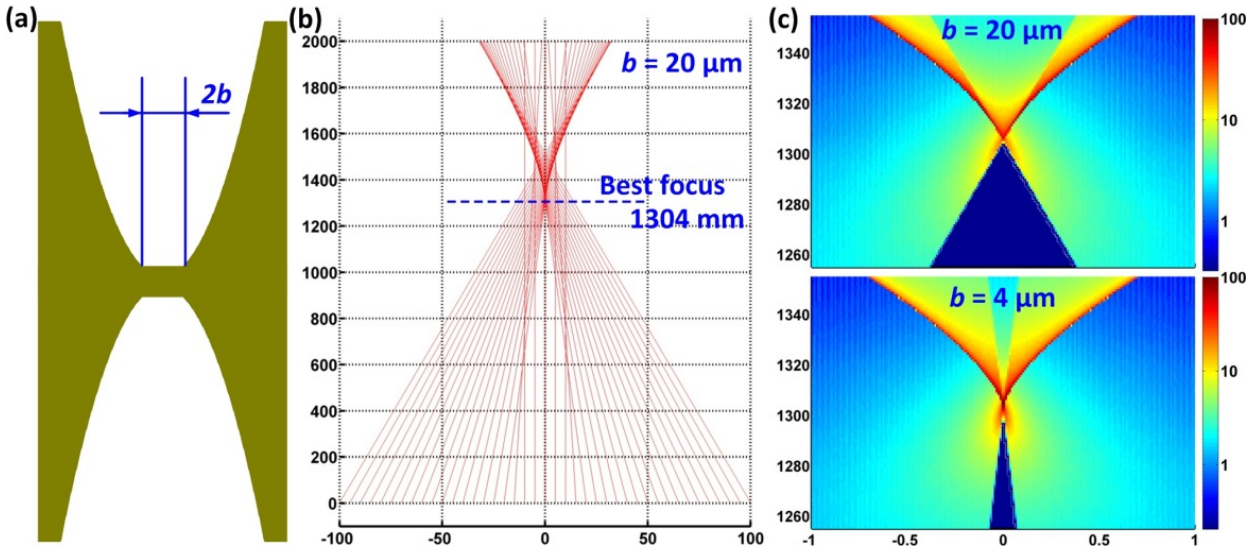

Figure 2.21. Effect of dull apexes on the focusing performance. (a) Schematic of a dull lenslet. (b) Ray tracing. (b) Intensity plots around the best focus.

Other lens defects are surface roughness and the regular scallops imposed on the surface in the course of the Bosch process used for the pattern transfer (cf. Chapter 3.5.1). In contrast to x-ray mirrors, CRLs are considerably less sensitive to surface roughness [170]. As long as the RMS roughness is well below 1 µm, roughness has no notable influence on the spot size (cf. Chapter 2.2.5, [293]). Scallops along the depth of the lens correspond to a periodic widening and tightening of the parabolic shape. Scallops with amplitudes in the order of 1 µm therefore need to be dealt with. However, scallops encountered in this thesis had amplitudes less than 100 nm and were effectively removed by surface smoothing steps (cf. Chapter 3.6.).

In this thesis, the optical performance of manufactured lenses was for the most part limited by a non-vertical etching. As was mentioned before, a tapered etch profile essentially alters the parabolic shape and the effective radius of curvature of the profile, which in turn results in varying focal lengths and ultimately in a slanted focal plane. This effect is tremendous, considering that an offset of ±2 µm on a parabola with R = 20 µm causes effectively a change $\Delta R = \pm 1\,\mu\text{m} = 5\%$ and hence $\Delta f = \Delta R/(2N\delta) = 5\%$. The effect of multiple beams being focused at different positions is illustrated in Figure 2.12. In a typical real experiment a sample is placed into the minimum of the average of these beams, meaning that some parts of the sample are within, but most parts of the sample are out of focus. Obviously, the x-ray flux density varies as well. In order to illuminate a sample with a uniformly focused beam, the focal lengths need to match within the depth of focus (cf. Chapter 2.2.6). For the example given above (cf. Figure 2.19) $\text{DOF} = 7\text{ mm}$, or 0.5 % of the focal length, which requires $\Delta R = \pm 0.1\,\mu\text{m}$ or a maximum offset of the parabola $u = \pm 0.2\,\mu\text{m}$. Especially for deeply etched lenses these are very challenging targets in terms of what is technologically feasible. For this reason heights of etched Si lenses reported in literature typically did not exceed 50 µm (cf. Chapter 2.3.4).

The variation of R is essentially determined by the parallelism of the lens sidewalls as illustrated in Figure 2.16. Assuming a lens depth of 300 µm, a widening $u = +0.2\,\mu\text{m}$ corresponds to a

sidewall angle α of less than 0.1°. In general, the requirement on sidewall verticality increases when shorter focal lengths are needed, the lens radius of curvature is decreased, or when operating at higher x-ray energies.

2.5 Summary

This chapter introduced refractive lenses as relatively novel optical devices for the x-ray regime. Refraction is very weak for hard x-rays, which necessitates lenses with extreme radii of curvature. Compound lenses may be built to facilitate their manufacture. X-ray absorption plays a crucial role for the efficiency of lenses as well as achievable spot sizes. Low-Z materials are preferred for x-ray lenses. However, a compromise must be struck between their focusing power and machinability. Silicon is a good candidate for photon energies higher than 30 keV. Simple formulas for describing the optical performance of CRLs have been presented. For almost two decades CRLs have been developed by various techniques. Two-dimensional lithography combined with pattern transfer using etching techniques remains a viable route for the manufacture of high-quality 1D-focusing CRLs. It allows realizing extreme radii and defining required parabolic lens shapes with high repeatability and precision. It turned out that the uniformity of the lens along its entire depth is most crucial with respect to its optical performance. More precisely, the parabolic shape needs to be constant along the lens depth and – depending on the actual lens dimension and optical configuration – it must not deviate by more than 200 nm, corresponding to sidewall profile angles of ±0.1°.

3 Microfabrication

This chapter presents the main steps involved in the manufacture of silicon compound refractive lenses (CRL). The process flow traditionally used is outlined and demonstrated. Deep reactive ion etching (DRIE) is discussed in great detail, including its parameter space and the peculiarities of the machine used throughout this thesis. A selection of relevant DRIE specific features is presented.

3.1 Standard process flow

Figure 3.1 illustrates schematically the basic process flow for fabricating 1D-focussing Si-CRLs.[13] The main steps are lithography and pattern transfer.[14] Lithography is done by exposing a photo-sensitive polymeric layer with UV light through a mask containing the lens patterns and subsequent developing the polymer in a suitable solvent. Typically, the polymeric pattern is transferred into another thin layer such as silicon dioxide, which is more resistant against erosion during the process used to structure the bulk silicon. The resulting patterned SiO_2 then serves as a hard mask for DRIE of the silicon using the Bosch process. Optionally, the sidewalls are smoothed in additional process steps. The structured silicon wafers need to be diced into suitable chips, which may be used as optical devices without further processing.

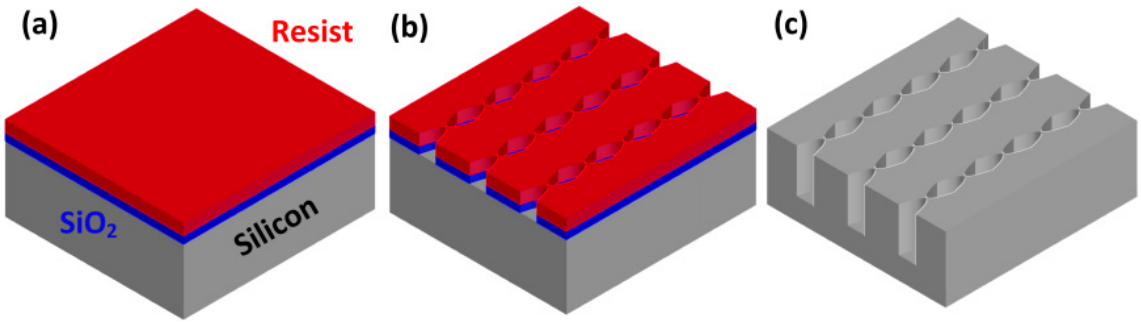

Figure 3.1. A typical process flow for fabricating 1D-focussing silicon CRLs. (a) The starting material is a silicon wafer covered with SiO_2 and photo resist. (b) The resist and SiO_2 are patterned by UV-lithography and reactive ion etching, respectively. (c) Deep reactive ion etching of silicon.

Compared to other processes feasible with modern micro- and nanotechnology, CRL manufacture is rather simple, not least because the dimensions of the lenslets can be considered

[13] Hereafter, CRL always refers to silicon CRL, if not otherwise mentioned.
[14] All microfabrication in this thesis work was performed at DTU Danchip, which is the National Center for Micro- and Nanofabrication located at the Technical University of Denmark. It operates and maintains advanced processing equipment within a 1350 m^2, class 10-100, ISO 9001-certified cleanroom. www.danchip.dtu.dk (Dec 2015).

to be relatively large and only one single lithographic step is required. However, the tolerances on the three dimensional shape of the lens cavities are rather strict and therefore DRIE needs to be pushed to its very limits. Additionally, a manufacturing method is always just as good as the techniques of its characterization. Therefore, respective procedures for measuring the shapes of CRLs need to be developed (cf. Chapter 4).

3.2 Mask design

The manufacture of CRLs starts with designing the lithographic mask. Prior to the design, the x-ray energies E and the desired focal lengths f need to be known. Thus, CRL manufacture is typically tailored towards specific applications. The radius of curvature R, lens aperture $2R_0$ and number of lenslets N may be specified given E and f, as well as considerations regarding the desired height (or depth) of the lenses.

A first version of CRLs (called XOPTIX4) was designed for E = 17 keV, variable focal lengths, R = 6 µm, $2R_0$ = 50 µm, d = 2 µm, N = 1 – 50 (cf. Chapter 2.2). Throughout this thesis AutoCAD is used for mask drawing. The parabolic lens shapes are generated in Matlab and imported into AutoCAD via coordinates of polygon lines. Individual lenslets are combined to CRLs and the CRLs are arranged on chips with dimensions that allow easy handling and fit holders of stages in the beamline (cf. Figure 3.2). Simple trenches for alignment, identification of individual CRLs and various labels may be included. Multiple chips can be arranged on single wafers to increase throughput (cf. Figure 3.3). Individual chips may differ. For example in XOPTIX4 every second chip is a ‘dummy chip’, where CRLs with N = 50 are arranged such that during inspection every wafer cleavage yields cross sections for the purpose of process control and characterization (cf. Chapter 4). Hence, dummy chips facilitate the characterization of the manufacture. Additionally, chips differ by the degree of compensation for shape widening due to overexposure, mask undercut during DRIE, or surface smoothing steps (cf. Chapter 2.4).

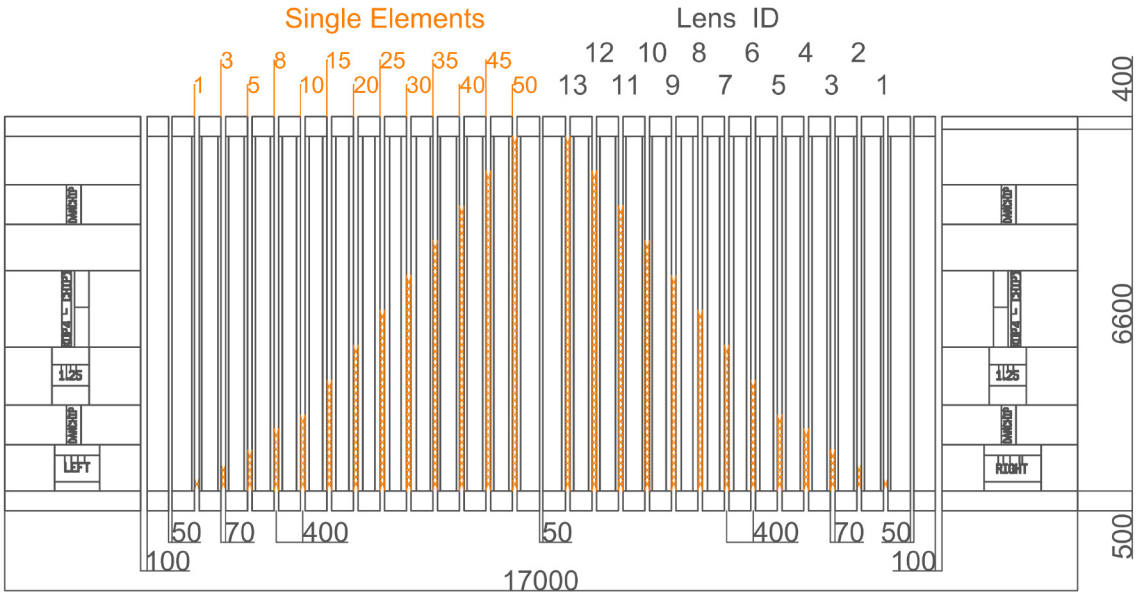

Figure 3.2. Technical drawing of a lens chip XOPTIX4. The dimensions are given in units of micrometers.

In the course of the manufacture using a former mask design (XOPTIX3) it was found that the shape widens by approximately u = 1.1 µm. Therefore in XOPTIX4 lenslets were drawn with parabolas of u = -0.95 µm to u = -1.25 µm in steps of Δu = 0.05 µm, such that the chips with the least shape deviations may be found subsequent to the manufacture. The whole design included 48 chips, half of them dummies, with each 26 CRLs with up to 50 single lens elements. The total number of lenslets on a 4-inch wafer is thus ~40000 and highlights one of the advantages of the technology being used.

AutoCAD drawings are saved as DXF-files and imported into Clevin were the files are converted into CIF-files, which can then be sent to a mask supplier, which typically delivers within 1-2 weeks.[15] The ordered masks are Quartz plates with a thin film of chromium that has been structured by laser writing into a photoresist layer, development and etching.

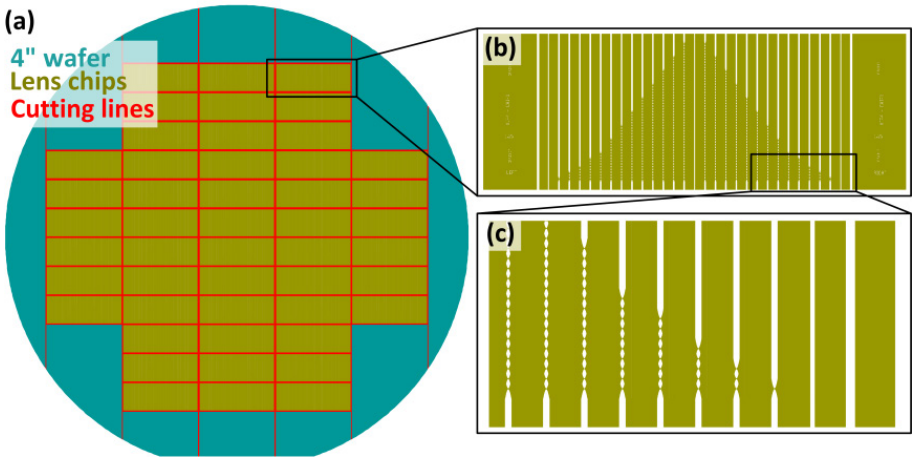

Figure 3.3. Schematics of wafer design XOPTIX4. (a) A full 4-inch wafer. (b) A lens chip. (c) A zoom in of the chip.

3.3 Lithography

Throughout this thesis standard UV lithography was used. Therefore wafers were typically spin coated with 1.5 µm or 2.2 µm thick resist layers (AZ5214E), prebaked at 90°C and exposed with broadband UV light from a mercury-vapor lamp with an EVG620 mask aligner (exposure times 3-4 sec, I-line exposure dose 20-30 mJ/cm^2). Exposed wafers are immersed in a developer (AZ351B) for 60-70 sec and spin dried. Prior to applying the photo resist, wafers may be primed by an HMDS treatment or a bottom-anti-reflective coating (BARC) to promote resist adhesion. Especially, BARC was essential when isolated features <8 µm were needed (cf. Chapter 4.3.).

3.4 Hard mask preparation

The patterned photo resist may be directly used as a mask for DRIE. However, during DRIE not only silicon is being etched, but also the mask. In this context the ratio between the etch rates of silicon and the mask is important, the selectivity. For the DRIE process used throughout this thesis the selectivity of photoresist was ~35. For Si etching deeper than 100 µm, thermally

[15] http://www.deltamask.nl/ (Dec 2015).

grown SiO_2 or Al_2O_3 deposited by atomic layer deposition (ALD) with etch selectivities of ~100 and >10000, respectively, were better suited [338]. Both, SiO_2 and Al_2O_3 were pattered using reactive ion etching based on a plasma-chemistry composed of C_4F_8, He, and H_2 combined with a relatively high ion impact guaranteed by applying a platen power of 200 W (SPTS, Advanced Oxide Etcher, SiO2_res). SiO_2 was patterned with an etch rate of 150 nm/min, while Al_2O_3 was patterned with an etch rate of 15 nm/min. For structuring 3 µm SiO_2, 2.2 µm thick photo resist was used. If thicker SiO_2 layers need to be etched, a pre-structured chromium layer may be used. Al_2O_3 was tested as a hard mask for DRIE, but caused large striations on the sidewalls of etched cavities (cf. Chapter 6.2). Therefore, SiO_2 was preferred for Si etching beyond depths of 70 µm. Figure 3.4 shows some obtained patterns in SiO_2 and Al_2O_3 on Si substrates. Most sidewalls are vertical, but characterized by striations along the etching direction; however, their amplitudes are estimated to be well below 100 nm and were of no further concern. After structuring the hard mask, the remaining photo resist is typically removed by an oxygen-plasma treatment.

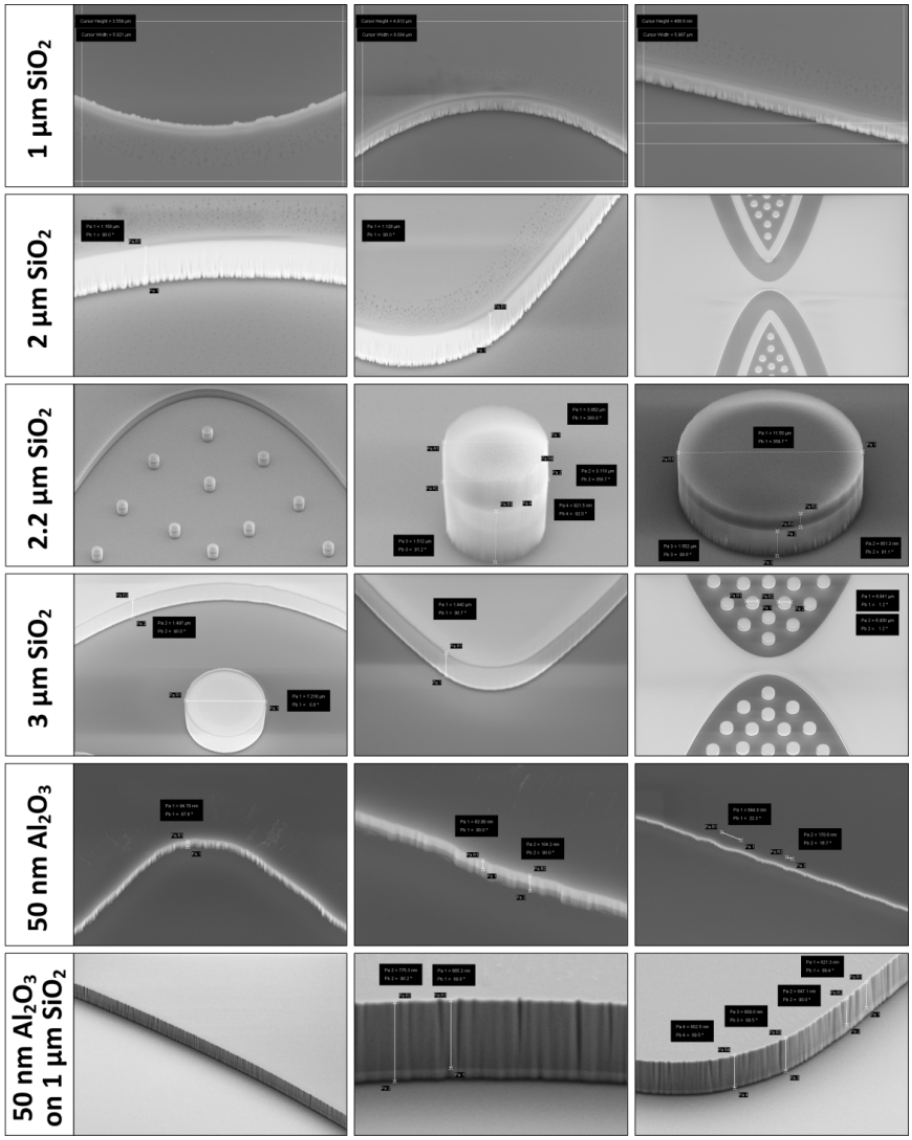

Figure 3.4. Collage of SEM images of patterned hard masks used for DRIE. In the images with 2.2 µm SiO_2, the photo resist layer is still visible.

3.5 Deep reactive ion etching

Silicon CRLs are obtained by defining their 2D parabolic shapes and transfer them vertically into the substrates. Etching can generally be categorized by its anisotropy (cf. Figure 3.5, [339–343]). Most chemical etchants etch isotropically, i.e. in all directions equally fast. The exceptions to this are those which are sensitive to crystallographic orientation, such as a potassium hydroxide solution (KOH). However these crystallographic dependent etchants are not suited for CRL manufacture, because of their complex shapes. Physical etching typically happens in dry environments, i.e. under vacuum using ion bombardment. Ions are created by applying oscillating high electric fields to gases inside low-pressure systems. Electrons and ions are accelerated, causing ionization and dissociation of gas molecules and atoms, thereby maintaining a plasma. Ionic species may be chemically inert to the substrate (e.g. He^+ or Ar^+); however, if they are accelerated towards the substrate by an electric field (so-called bias) and bombard the substrate surface they cause sputtering. Pure physical etching is typically slow and shows similar etch rates for various materials. Neutral species that were subject to dissociation may become reactive, such as atomic fluorine present in plasma fed with SF_6. Exposed to silicon, it etches isotropically. Reactive neutral species and ions may act in a synergetic fashion resulting in so-called ion-enhanced etching [344].

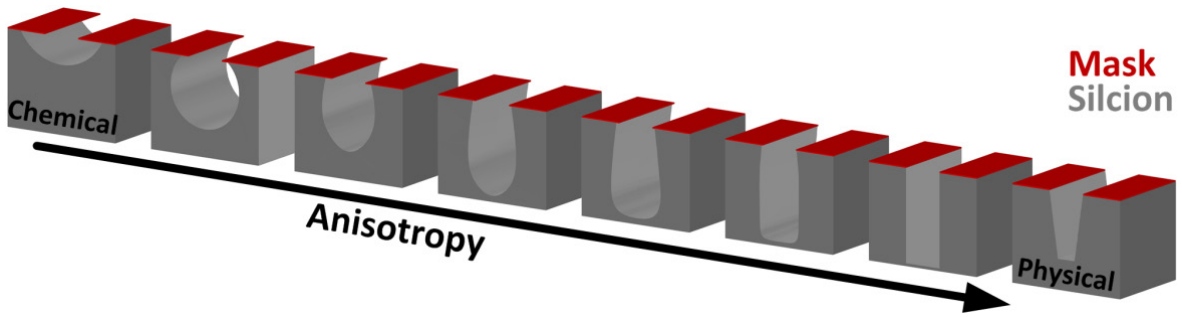

Figure 3.5. Schematics of the transition of silicon structuring from chemical to physical.

3.5.1 The Bosch process

Strict directional etching may be achieved by continuous or a sequential processes (sometimes called switched, time-multiplexed or pulsed processes) [345]. In a continuous process the plasma chemistry and bias remains constant throughout the process. Typically, a mixture of two gases is used. One of the gases forms a uniform layer all over the wafer including sidewalls of already etched cavities, which inhibits spontaneous chemical etching. The other gas supplies the radical species. An applied wafer bias results in a continuous ion bombardment normal to the wafer surface causing directional sputtering, leaving vertical sidewalls essentially unaffected. Thus, the inhibiting layer is locally removed thereby enabling chemical etching by the radical etching species. Since sidewalls remain protected, etching pursues normal to the wafer surface. A typical gas used for etching silicon is SF_6 and the inhibiting gas may be O_2 (preferable for low temperature processing) or a fluorocarbon such as C_4F_8 (well suited up to room temperature processing) [345–348].

In a switched process the deposition of the inhibiting layer, the local sputtering of this layer and the (ion-enhanced) etching are separated in time (cf. Figure 3.6). Typically, a strong polymer-

building fluorocarbon is used as the etch-inhibiting gas, e.g. C_4F_8 building Teflon-like films. The sputtering and etching steps are usually combined, resulting in alternating passivation and etching phases – a technique commonly known as the Bosch process [349–353]. Improvements to this method and optimizations of etching systems today allow achieving etch rates of 10 µm/min, near-vertical sidewalls with angles considerably less than 0.5°, aspect ratios approaching 100 and etch depths beyond 1 mm [354–356].

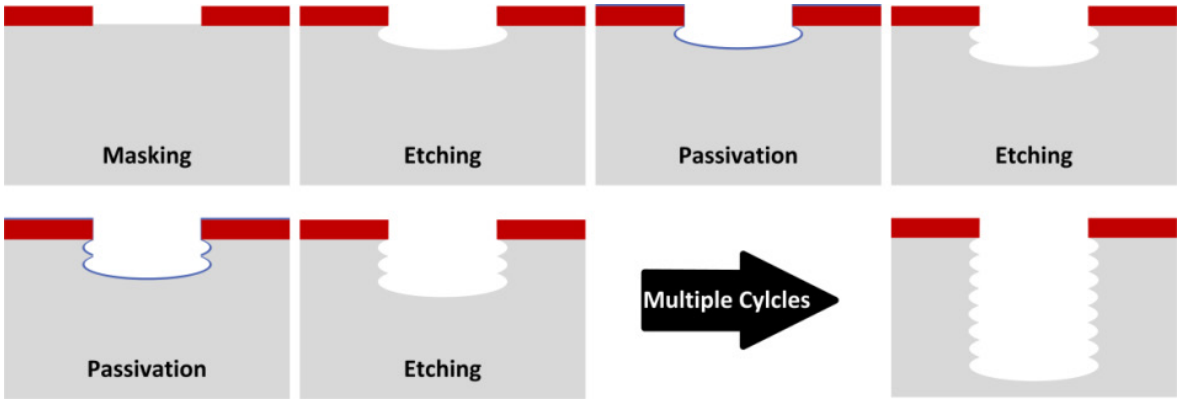

Figure 3.6. Schematic of the Bosch process for the anisotropic etching of silicon.

One of the most distinct features of the Bosch process is the scalloping of the sidewalls of etched features (cf. Figure 3.7(a)). It results from the cyclic nature of the process. The shape of these scallops – most particularly their pitch and amplitude – is determined by the actual process parameters (cf. Chapter 3.5.3). Generally, the longer and the more intense the etching phases are, the more pronounced are the scallops. Consequently, higher etch rates typically result in larger scallops. Optionally, scallops may be reduced in steps subsequent to DRIE (cf. Chapter 3.6, Figure 3.7(b)).

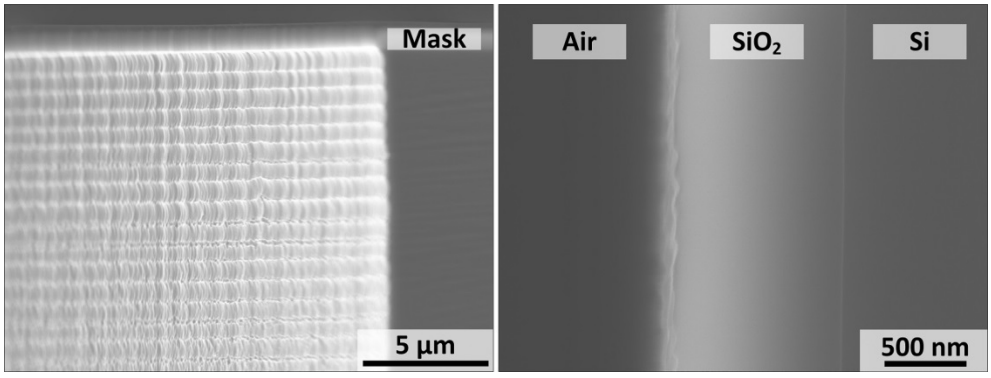

Figure 3.7. Scalloped surface upon DRIE. (a) Scallop pitch = 416 nm. Remaining SiO_2 mask thickness = 500 nm. (b) Thermally grown oxide subsequent to DRIE. Thickness = 1 µm.

3.5.2 The etching tool

System configuration

Figure 3.8(a) shows a schematical drawing highlighting the main components and features of a modern plasma etching system, very similar to that used throughout this thesis (SPTS, Pegasus).

Our system is equipped with a massive turbo pump with a pumping speed of 1000 l/s (Leybold Mag 2000 CT), which together with a backing pump establishes a base pressure of ~10^{-7} mBar.[16] This pressure typically rises to ~10^{-2} mBar during processing, which is sufficient to enable transfer of etchants into and etch products out of deep micro- or nanostructures. The strong pumping guarantees an efficient gas transport through the whole machine and hence enables short cycle times (<10 sec). Between the turbo pump and the processing chamber is a large valve that regulates the exhaust and thereby the processing pressure. It can be controlled either manually by specifying its position or automatically by specifying a chamber pressure (using automatic pressure control, APC).

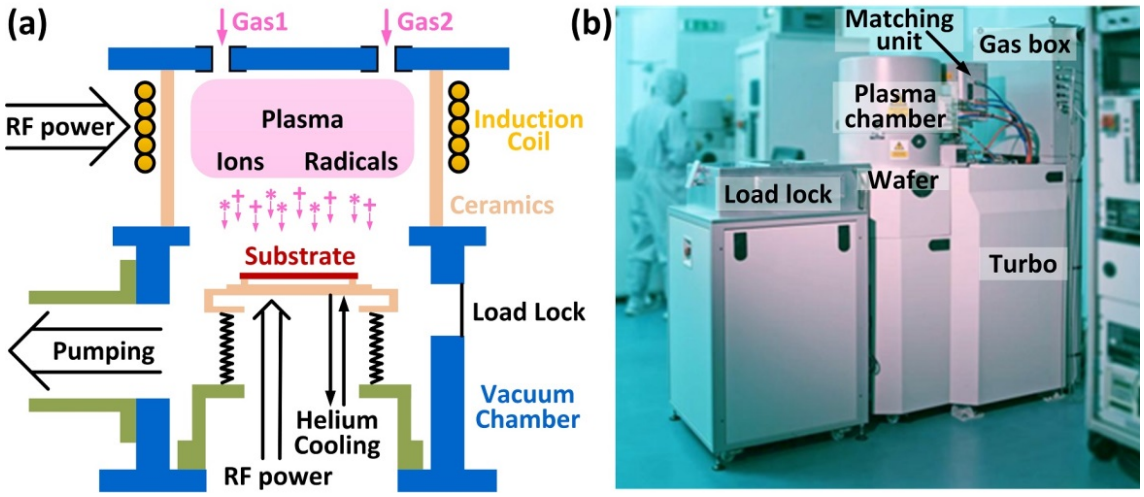

Figure 3.8. Etching tool used in this thesis. (a) Schematics adapted from [357]. (b) Photograph of an SPTS Pegasus copied from [358].

Single wafers are loaded into the chamber via a load lock and an automatic handling system without breaking the vacuum in the main processing chamber. A robot may be used, which can handle a whole wafer cassette with up to 25 wafers automatically. The wafer is located horizontally on a ceramic chuck and the wafer position is fixed using electrostatic clamping. On the surface of the chuck are small grooves that are filled from the backside through holes with helium gas with pressures up to 20 Torr, which combined with a chiller allows cooling of wafers down to -20°C during processing.

Above the wafer surface is the plasma chamber, which is surrounded by a water-cooled electromagnetic coil. Our system is equipped with an additional coil inside the vessel, which increases the uniformity of the plasma guided to the substrate, thereby effectively increasing the etch uniformity. To couple an electromagnetic field into the plasma chamber, its walls are ceramic. The rest of the vacuum chamber is typically milled from a single block of stainless steel to avoid issues with temperature gradients, which in the long run may cause vacuum leakages. Some aluminum parts may be present as well and various valves, gauges, etc. are connected using O-rings most made of expensive Kalrez. The whole chamber is constantly heated to ~140°C to maintain constant processing conditions and to avoid excessive polymeric built-up on the chamber walls.

[16] 20 mTorr = 2.67×10^{-2} mBar.

Processing gases are introduced from above through a plate with multiple small holes (so-called showerhead), which guarantees a uniform gas transport. Mass flow controllers (MFCs) are located very close to the gas inlets in order to guarantee an efficient and fast switching of process gases. Our system supports SF_6, C_4F_8, Ar and O_2.

The electromagnetic coil is coupled by a matching unit to an RF generator, which works at the standard frequency 13.56 MHz and supplies a power up to 5 kW (MKS QL6513). Underneath the ceramic chuck is a platen electrode, which by separate generators may be supplied with RF or optionally LF power, up to 300 W or 500 W, respectively. This platen power accelerates ionic species towards the wafer surface. The wafer is remote from the plasma generation zone and a ~20 cm long funnel is used to direct the plasma towards the wafer.

Malfunctioning parts and process drifts

A DRIE system is a relatively complicated system with a lot of single electrical, mechanical and pneumatic components that are prone to failure. In the course of the three years thesis work, several incidents caused major process drifts. For example a capacitor in the matching unit was defect and needed to be replaced by a new one. At the same time the RF generator for the coil was replaced and the chamber was cleaned from polymeric residues etc. After the machine has been repaired, developed processes gave considerably different results and hence needed to be readjusted. Malfunctioning of parts is unavoidable and a necessary replacement or repair may or may not result in changed processing characteristics. Other than malfunctions, various parts may be subject to drift. E.g. the operation of pressure gauges, MFCs, or the APC valve may vary over time (weeks, months, or years). This can be counteracted by monitoring potential drift on a regular basis, regular calibration procedures, or resetting parts in a systematic fashion. Generally, destructive incidents or drift need to be taken into account and it is advisable to e.g. block optimization studies in order to minimize the chance of their occurrence.

Maintenance and cleaning

A DRIE system needs to be serviced on a regular basis to guarantee stable processing conditions. This includes cleaning of the chamber walls and replacing vacuum sealings. As mentioned before, the passivation gas also condenses on the chamber walls. This polymeric layer grows in the course of the up-time of the machine, forming flakes that may detach from the walls and end up e.g. on the wafer surface, thereby causing major defects. This polymeric layer sometimes must be removed by e.g. sand-blasting and one can imagine that this considerably changes the general condition of the system. Not only the wafer consumes radials or CF-species, but so does the whole system. If the chamber properties are changed, so is its affinity to consume species from the plasma, which necessarily affects the etching of the wafer. However, process drifts of such kind have not been investigated systematically. Nevertheless, awareness for potential drifts is advisable and the system needs ideally to be tested before and after services using reliable procedures.

Conditioning

The sensitivity of processes on the conditions of the chamber walls is also embodied in the fact that processes can depend on the immediately preceding process. For example, I once experienced that a process resulted in effective Si etching only if another slightly different

process was run before. However, if a standard oxygen-clean was applied instead, no etching was observed at all, but instead excessive passivation on the wafer occurred. In industry, machines are typically dedicated for one single process, which runs 24/7. In such a case it is relatively easy to guarantee stable processing conditions. However, our machine is part of a multi-user facility, which by nature hosts multiple users working on various projects and running various processes. In order to guarantee stable machine conditions every user is advised to run oxygen-plasma cleans regularly (i.e. after every processed wafer for a duration of 10% of the processing time), followed by a final 10 min long oxygen-plasma clean prior to the next user. Literature on chamber conditioning procedures is available and it may be advised for the future to coat the chamber walls with a polymer film prior to every process additional to foregoing oxygen-plasma cleaning [359–361]. However laborious systematic studies may be required to establish a more advanced conditioning procedure that is not disadvantageous in other aspects. Another important point is warm-up of the machine in the course of long processing recipes, which may also alter processing conditions.

Change of configuration

Intentional changes to the configuration of the machine are another source for process variations. These may include a change of the turbo pump to obtain more efficient pumping, change of pressure gauges to obtain more accurate values or change of MFCs to allow faster or more reliable switching. In the course of the three years we intentionally changed the showerhead following an expert advice. The original showerhead had ~20 holes ~5 mm long with ~100 µm diameter. It was anticipated that these holes significantly limit the gas flow and more severely the minimum gas switching frequency. Upon opening the holes to 1 mm diameter gas transport seemed to be more efficient, resulting in over passivation in some switched processes. The benefit of this change was the feasibility of faster switching times. The drawback was that some process needed readjustments. Fortunately, the uniformity of the etching across the wafer did not suffer. Hence, intentional changes may be beneficial. However, awareness of potential consequences is advisable.

3.5.3 DRIE parameters space

DRIE using the Bosch method[17] is a complex process, which involves a lot of variables that need to be adjusted in order to achieve optimal results. However, optimizing the process can be largely simplified, if the effects of relevant parameters have been properly understood [345].

Timing

DRIE is a cyclic process and therefore timing plays a crucial, if not the most crucial role. Both, the length of a cycle and the time ratio between the etching and passivation phases are variables. The length of the passivation phase determines the amount of passivation, while the length of the etching phase determines the amount of Si being etched. During the etch phase both must happen: the bottom removal of the passivation layer and the actual etching of silicon. Si etching occurs, if the etching phase lasts at least until the bottom passivation layer has been completely removed. Lateral etching may be prevented by a passivation phase, which lasts at least until a

[17] Hereafter, DRIE always refers to DRIE using the Bosch method, unless otherwise noted.

uniform polymer film all over the sidewalls of structures has been built. The etching phase does to some degree also consume sidewall passivation. Therefore, the duration of the etch phase must be limited at the point where the etching gas would start to attack the Si sidewalls, i.e. the onset of sidewall passivation break-through. All other parameters left constant, maximal etch rate is achieved if the etch phase lasts as long as the sidewall passivation is intact. In such a case a process is typically called 'balanced'.

Chamber pressure, main valve position, gas flows and coil powers

The chamber pressure is a function of pumping efficiency, gas flows, and coil powers. The pumping efficiency is controlled by the position of the main valve between the pump and the processing chamber. It also controls the gas residence time and thereby influences the timing and mixing of gases. In principal, the higher the gas flows, the higher the amount of passivating molecules and etchants, hence the stronger the passivation and the etching. However, gases need to undergo dissociation and ionization to become effective. Therefore, the flows of gases need to be in balance with the coil power. If there is too much gas or too little coil power, not all of the gas undergoes dissociation. Vice versa, using larger coil power than necessary to dissociate all the gas is not efficient either. Notably, dissociation and ionization compete with recombination and neutralization, respectively. Hence, below or above a certain pressure, amount of gas, or coil power no plasma is generated or maintained. Due to dissociation of molecules the chamber pressure generally rises if a plasma is generated.

The pressure determines the mean free paths of species, hence the efficiency of etchants or etching products entering or leaving narrow structures. If structures with high-aspect ratios need to be etched, it is therefore necessary to work in a low pressure regime. Additionally, the mean free path determines the angular distribution of ions that are accelerated towards the substrate.

The RF matching unit assures an effective energy delivery from the power generator to the plasma. The matching unit is equipped with mechanically driven variable vacuum capacitors, which are automatically controlled in some sort of closed-loop to match the impedance of the generator and the machine. In order to keep the power delivery stable within and between cycles, it is advantageous to strive for using the same settings of the matching unit during both, the etching and the passivation phases. Therefore, the coil powers and respective gas flows need to be matched, such that the system always has the same impedance.

Platen power

The platen power determines the energy of the ions impinging on the substrate as well as the ion angular distribution (IAD). Generally the IAD should be narrow, if directional etching is required. The energy of the ions determines the efficiency of sputtering of the bottom passivation layer. Simultaneously, it controls the consumption of the etching mask. Therefore a compromise must be struck between the IAD, the mask consumption, and the bottom passivation removal.

Platen temperature and helium pressure

The polymer deposition efficiency is strongly determined by the temperature of a surface, where a lower temperature generally causes higher sticking coefficients and deposition rates [362]. To prevent polymer deposition and detrimental effects or even damage, the plasma and processing

chambers, as well as the turbo pump are constantly heated. Contrary, substrates are cooled to increase the efficiency of the passivation. The spontaneous silicon etch rate is only marginally dependent on the substrate temperature [345]. Crucially, the erosion of the masking and the sidewall passivation layer is more pronounced at higher temperatures. Therefore, the temperature of the wafer should generally be minimized. Notably, spontaneous Si etching is an endothermic process and produces heat that needs to be dissipated. A high helium pressure increases the heat conduction. Backside He may leak into the chamber during processing and dilute the processing gases. Therefore, a He-leak-up test is performed prior to every process and wafers showing too much bowing should not be processed.

Process trends

A change of one DRIE parameter may give multiple responses, which complicates optimizations. One important among many responses is the etch rate. In the context of the present thesis the sidewall profile is the main response to optimize. However, other responses such as the mask selectivity, the etch uniformity, or the sidewall roughness also need to be controlled. Figure 3.9 summarizes process trends as encountered in the course of the project. Some responses are very sensitive to slight changes of some parameters, whereas other responses are rather indifferent.

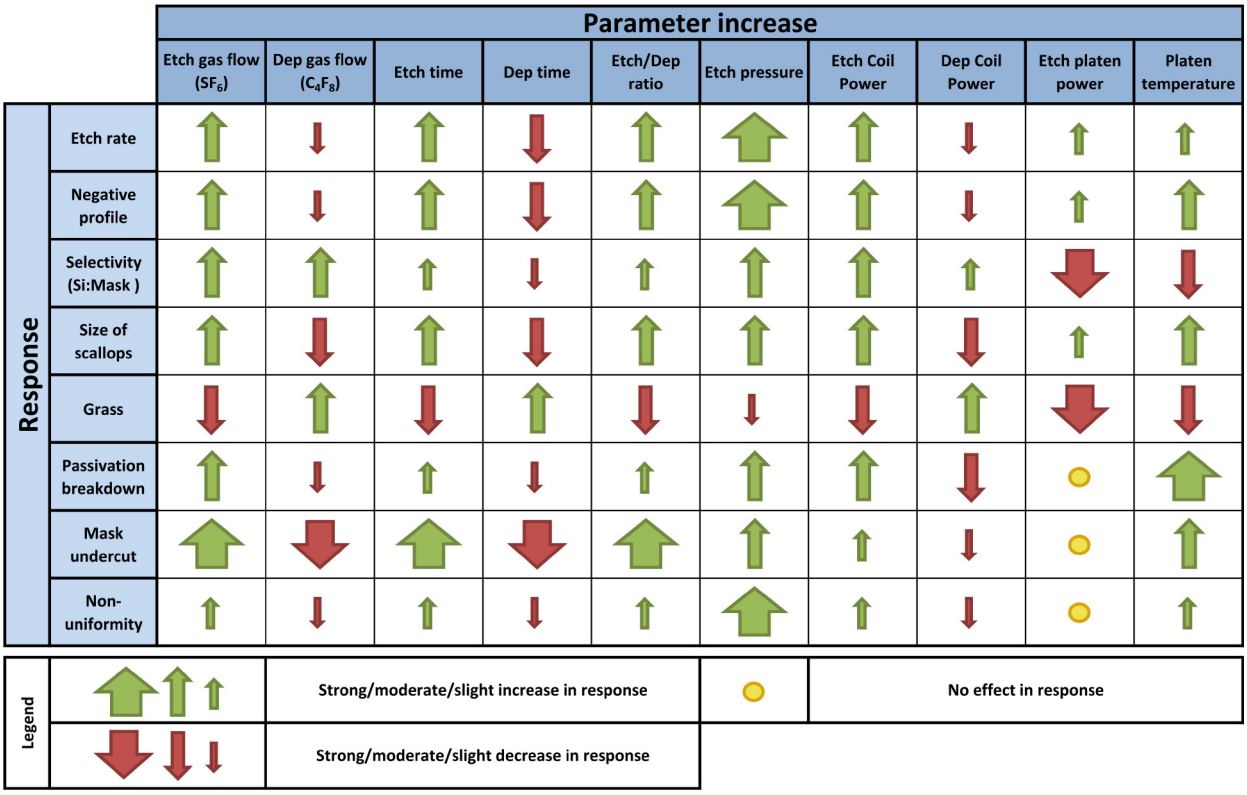

Figure 3.9. Bosch process trends adapted from a document provided by SPTS Technologies.

A particular process must not be designed from scratch, since a couple of standard processes are typically provided by the constructor of the etching machine, colleagues or peers. These standard processes may be tailored to specific needs. Figure 3.9 as well as conducting relevant literature facilitates optimizing processes [363–370]. In the context of the present thesis a recipe

must be used which works at a relatively low pressure (in order to narrow the IAD and allow vertical etching), has a relatively short cycle time (in order to decrease the scallops and obtain smooth sidewalls), while potentially allows high aspect ratio etching up to depths of 1 mm.

Table 3.1 summarizes the main parameters of an optimized etching recipe. Eventually it was subject to slight modifications here and there, but essentially stayed the same throughout this thesis. Oxygen is used as an additive in the etch phase to improve the sidewall roughness, although maybe at the cost of slightly reduced etch rate [371–373]. The chuck-temperature was set to its minimum value of -19 °C and the backside helium gas cooling pressure to 10 Torr, which increased the efficiency of sidewall passivation and the mask-selectivity. Operating at a relatively low pressure of <30 mTorr narrowed the angular distribution of ionic species during etching and facilitated efficient gas transport in trenches with aspect ratios up to 17. A total of 800 cycles were sufficient to etch through a wafer of 350 µm thickness.

Table 3.1. Optimized DRIE recipe used throughout the thesis.

Parameter	Passivation	Etch
Time (sec)	1	3.3
Pressure (mTorr)	20	26
C_4F_8 (sccm)	150	---
SF_6 (sccm)	---	275
O_2 (sccm)	---	15
RF coil (W)	2000	2500
RF platen (W)	---	35

3.5.4 Etch effects

ARDE

DRIE is largely determined by the efficiency of ion sputtering of the bottom passivation layer, the transport of reactive fluorine to the opened silicon and the transport of etch products out of cavities and away from the wafer [374]. The amount of ions reaching the bottom, as well as the efficiency of the gas transport largely depends on the dimensions of structures to be etched. Due to collisions of ions with other species and their thermal motion, accelerated ions are not perfectly collimated toward the substrate. Instead, they have a finite ion angular distribution (IAD) [375,376]. Moreover, as ions enter trenches or holes, ion deflection (ID) toward the sidewalls occurs [377–379] e.g. by a distorted plasma sheath [380,381] or by the attraction of ions by their image charges [382]. Depending on the ratio between the width and the depth of a structure, substantial fractions of ions may be lost by wall collisions, known as shadowing [383]. Consequently, the ion flux available for bottom passivation removal and ion etch assistance is decreased, ultimately reducing etch rates. Generally, the etch rate will be inversely proportional to the aspect ratio, i.e. the ratio between the depth and width of a structure. This phenomenon is commonly known as the RIE-lag or aspect ratio dependent etching (ARDE) [384–387], and it is of great importance for this thesis since it also effects the sidewall profile angles. The RIE-lag may be reduced or even eliminated by carefully balancing etch and deposition times [387].

Figure 3.10(a) shows a cross section of trenches of variable widths after 450 cycles using the optimized recipe given in Table 3.1. Surface smoothing steps were applied after DRIE (cf. Chapter 3.6), hence the nominal trench widths widened due to silicon consumption. This effectively removed the scallops inherent to DRIE. Figure 3.10(b) plots the etch depths as a function of trench widths and a clear correlation is visible.

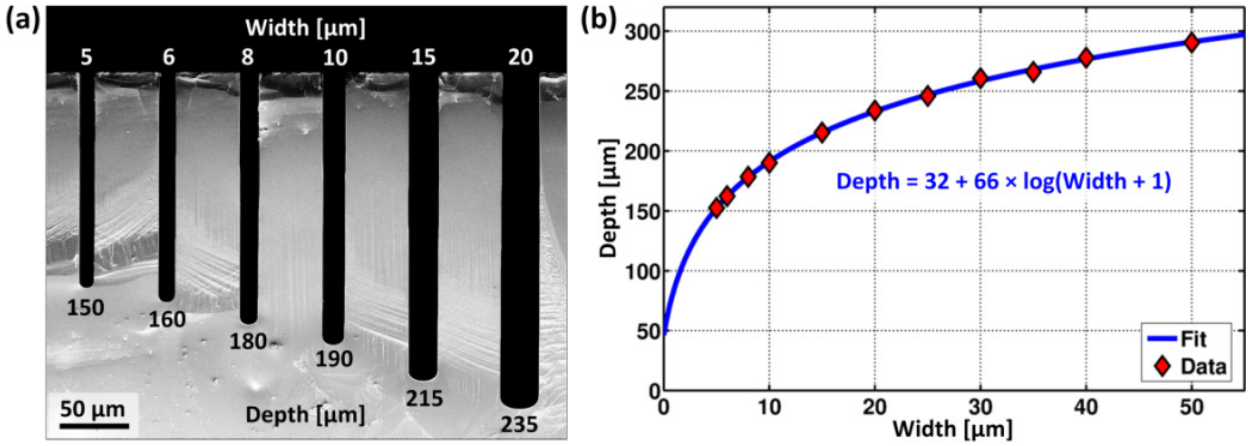

Figure 3.10. Aspect ratio dependent etching. (a) SEM of a cross section of trenches of various widths after 30 min of DRIE. (b) Etch depth over trench width diagram.

An un-collimated ion bombardment promotes ion/wall collisions resulting in local sputtering of the passivation layer, partial protection breakthrough, a finite lateral etch rate and non-vertical sidewalls. Sidewalls of large trenches are usually negatively tapered, i.e. they have a sidewall angle $\alpha < 90°$ since they are exposed to the full IAD independent of the etch depth reached, while narrower trenches show local sidewall features such as barreling or bowing [368,369,388] (cf. Figure 3.11). Close inspection of Figure 3.10(a) also reveals a slight positive tapering of the profiles ranging from 90.4° to 90.2°, for a trench width of 5 µm and 20 µm, respectively. Hence, profile control is possible by dimensioning the widths of trenches, albeit at the cost of reducing the etch rate, and it will be utilized to increase the uniformity of Si-CRLs as discussed in more detail in Chapter 4.

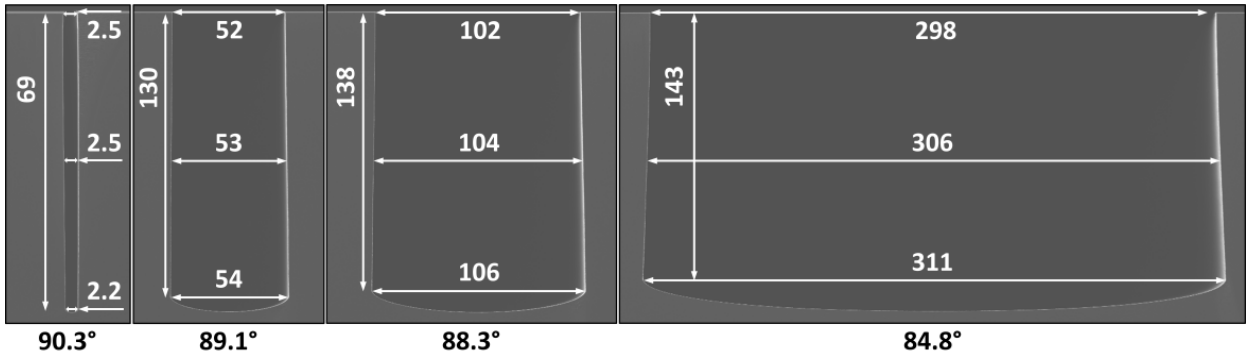

Figure 3.11. Dependence of the sidewall angle α on the trench width. Features were on one and the same wafer. Note that the etch depths varies substantially. Dimensions are given in micrometers.

As can be seen in Figure 3.12, the etch rate depends on the aspect ratio and not on the depth or the width alone. While etch rates are similar between trenches of different widths after initial

etching, they start to largely differ after prolonged etching. Thus, ARDE must be taken into account when designing wafers with openings of variable widths.

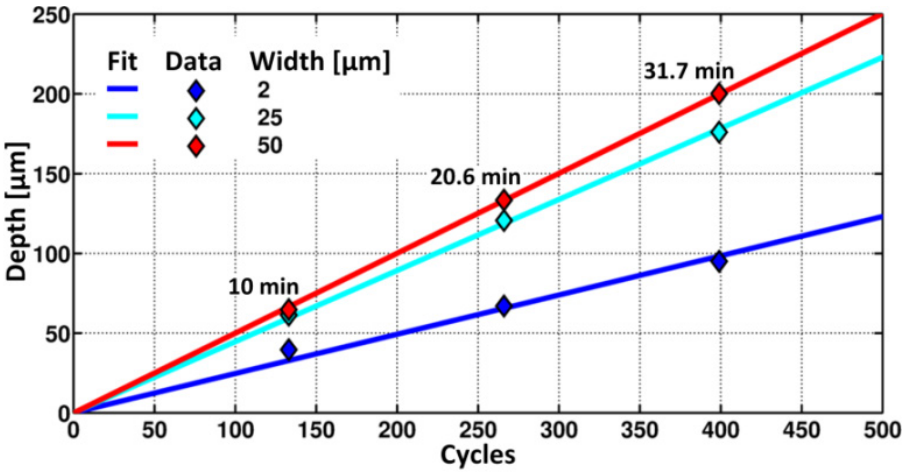

Figure 3.12. Etch depth of trenches with different widths for different etch times.

Micro- and macroloading

Other important effects that need to be considered in wafer design are micro- and macroloading, which both have their origin in the (local) depletion of the available radical fluorine [389–392]. The macroloading concerns the overall open area of a wafer (opposed to the overall masked area) and is typically specified in percentage of the total area of the wafer [389]. The microloading concerns the local opening percentage and typically affects etching within a limited area, which may be specified by a characteristic radius [392]. Generally, the plasma provides a limited number of fluorine radicals. The more open silicon area exists, the higher is the consumption of etchants. Etchants may be depleted locally, while on different areas of the wafer plenty still exist. Hence, while etching is diffusion limited on one area, it continues on the rest of the wafer. In order to guarantee maximal control of the etching it was aimed to keep total wafer loads below 10% and locally leave plenty of masked area around large openings.

Grass

Silicon grass or ‘black silicon’ as it is visible in Figure 3.13 is a sign for the onset of over-passivation [393]. It is caused by micro-masking due to insufficient removal of the bottom passivation. It may occur only in a small processing window and be used to find the sweet spot in continuous processes where passivation has been removed without causing additional lateral etching [394,395]. It is more likely to occur in wide structures or close to sidewalls and it is typically accompanied by rough sidewalls. It may be avoided by increasing the etching or decreasing the passivation by adjusting relevant parameters. However, it may also be caused by sputtering and re-deposition of masking material, which may be compensated by adjusting the platen power or wafer temperature, or using a different masking material.

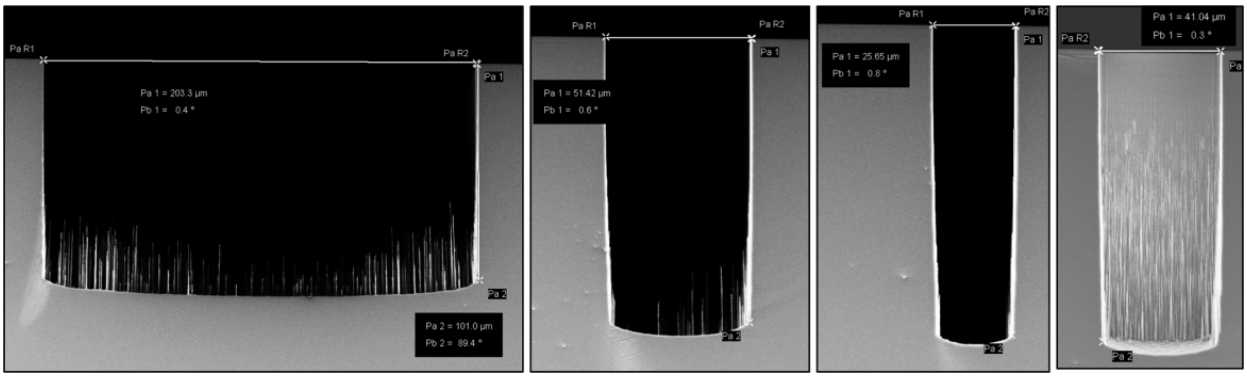

Figure 3.13. Silicon grass caused by slight over-passivation.

Passivation build-up

The main etch product $4F + Si \rightarrow SiF_4$ is volatile, while sputtered fluorocarbons may be non-volatile and remain inside structures [396]. These fluorocarbons may accumulate as can be seen at the top of the sidewalls in Figure 3.14. These deposits locally cause additional masking, which results in vertical striations on the sidewall. They could be effectively removed by an oxygen-plasma after DRIE. To prevent these residues, the standard Bosch process may be interrupted and regular oxygen-cleaning steps added to remove accumulated polymers. Subsequently, sidewalls would need to be re-passivated for continuing with DRIE [397,398].

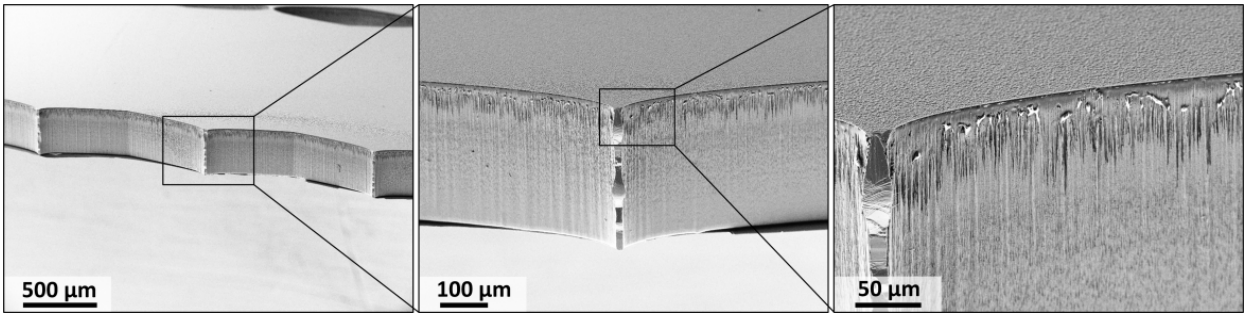

Figure 3.14. Passivation built-up at the top of the sidewalls in the course of 85 min DRIE through a silicon wafer.

Passivation break-through

Ideally, sidewall passivation lasts until the end of the etch phase upon which it needs to be renewed. In order to avoid over-passivation, which would effectively cause micro-masking and stop the etching, passivation needs to be limited. Establishing a perfect balance between both phases is difficult, especially during long and deep etching. Optimal results need to tolerate slight break-through of the sidewall passivation as can be seen in Figure 3.15. It does not harm, as long as it is not excessive and the etch profiles are not significantly affected.

Break-through is the cause for mask undercut as shown in Figure 3.16 and Figure 3.17 [399]. It can and should be avoided in order to guarantee the dimensional integrity of the structures (cf. Chapter 2.4). One strategy is to strengthen the passivation by increasing the passivation phase time, gas flows, pressure, or coil power. Alternatively, the etching may be weakened by respective adjustments. Local undercut may happen due to slightly different geometries as can

be seen in Figure 3.17. As long as it does not result in a complete structural collapse, it is of no concern, since the pillars will be removed in the course of further processing (cf. Chapter 4.3).

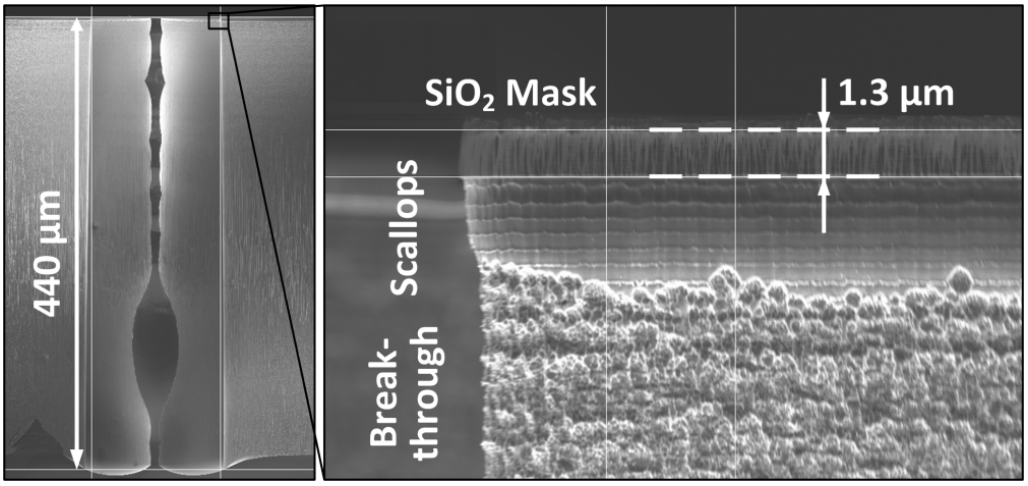

Figure 3.15. Passivation break-through in the course of 80 min DRIE.

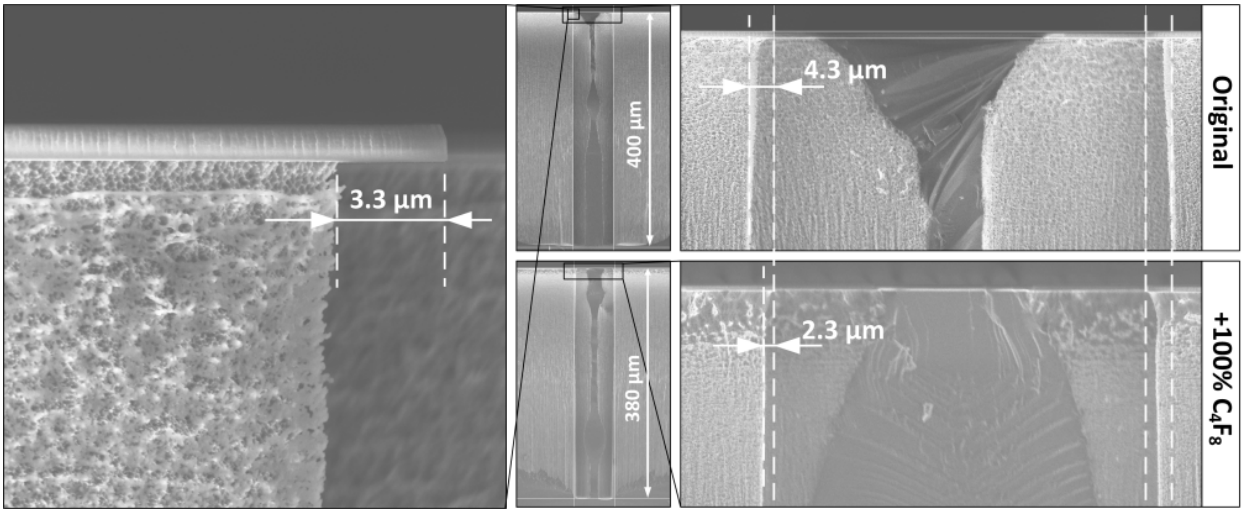

Figure 3.16. Excessive mask undercut, which occurred after the configuration of the machine had been changed.

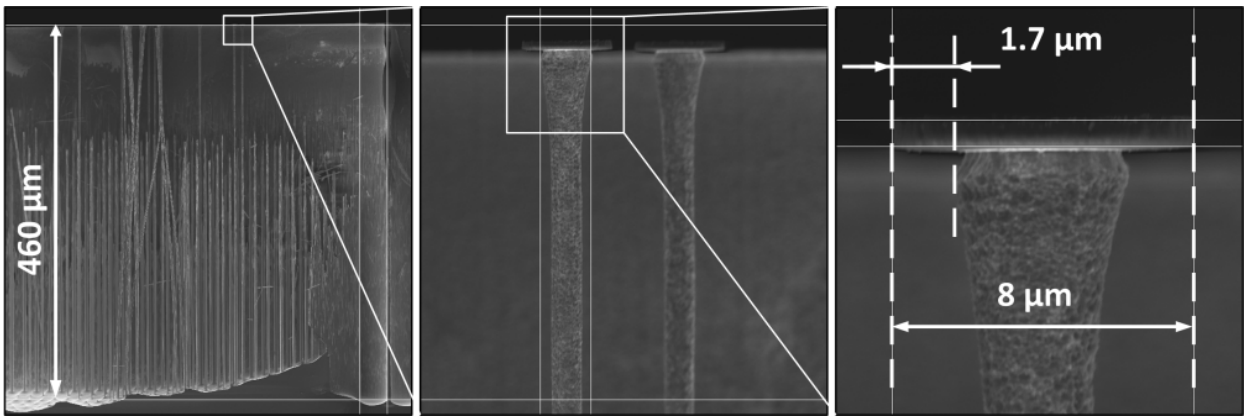

Figure 3.17. Local mask undercut of sacrificial structures.

Notching

DRIE may continue until a dielectric has been reached at the bottom of structures. Such a dielectric could be a buried SiO_2 layer as it is found in silicon-on-insulator substrates (SOI wafers) or a SiO_2 membrane on the backside of substrates. Dielectrics charge up when bombarded with ions, which results in ions being deflected towards the sidewalls, local sputtering of the sidewall passivation, and ultimately in lateral etching of silicon at the bottom of structures. It may be utilized for the release of sacrificial structures [400–403]. It can be avoided by using an LF instead of the usually used HF power, however, at the cost of a broadened IAD [404,405]. A solution would be to switch from an RF to an LF platen power, once the dielectric has been exposed and then finish the etching.

Mask erosion

The SiO_2 or Al_2O_3 used as masking materials are consumed during DRIE. The mask selectivity is mostly affected by the applied platen power (cf. Figure 3.9). Al_2O_3 is almost chemically inert to fluorine etching and hence a very attractive masking material [338]. In this thesis Al_2O_3 deposited by ALD was used. It was observed that while using a relatively low platen power (~30 W) the selectivity is indeed very high, it sharply drops when using higher platen powers (~100 W). When using Al_2O_3 surface roughness and vertical striations were considerably more pronounced than when using SiO_2, which is visible in comparing Figure 3.15 with Figure 3.18 and Figure 3.19. Its origin may be due to sputtering and re-deposition during DRIE causing micro-masking, or due to insufficient clearance of open silicon upon structuring Al_2O_3 by RIE. Using Al_2O_3 on top of SiO_2 did not improve DRIE. Al_2O_3 as a masking material was not further investigated and instead SiO_2 was used.

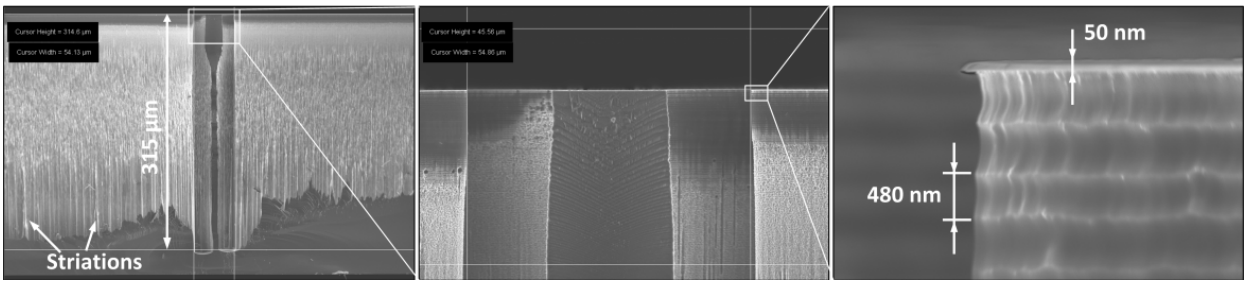

Figure 3.18. 50 nm thick aluminum oxide patterned by 3 min RIE used as a mask for 70 min DRIE.

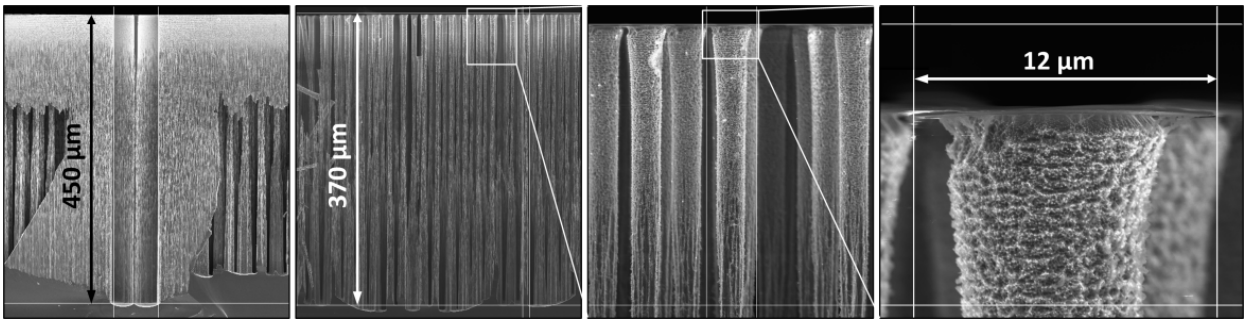

Figure 3.19. 50 nm thick Al_2O_3 patterned by 3 min RIE used as a mask for 100 min DRIE.

3.6 Surface smoothing

The sidewall finish can be controlled by adjusting relevant parameters [406–408]. A DRIE post-process including thermal oxidation in combination with subsequent etching of the grown SiO_2 layer may be used to further smooth sidewalls [409,410]. General roughness, surface corrugations, scallops, and vertical striations can be reduced, with varying efficiencies. Since thermal oxidation of silicon is diffusion limited, sharp surface features oxidize faster than flat surfaces [411]. Subsequent etching of the grown oxide layer then removes more corrugations than smooth areas, thereby effectively creating a smoother surface. Oxidation and SiO_2 etch steps may be repeated several times, however, the first step is the most effective one. The oxide thickness should at least equal twice the amplitude of the features to be removed, since a growth of t thick oxide, consumes ~t/2 thick silicon. The more oxide is grown, the smoother the surface will become. Silicon consumption needs to be accounted for in the initial design of the lithography mask and may also be utilized to control the final parabolic shape of the lenses.
Prior to surface smoothing, residuals from the passivating layers were typically removed in an oxygen-plasma for ~1 hr (PVA TePla, 300) followed by stripping of remaining masking material in buffered hydrofluoric acid (bHF) and wafer cleaning using a standard RCA procedure. Figure 3.20 shows examples of surface smoothing. Figure 3.21 shows the smoothing of optimized CRL cavities (XOPTIX4), which were used to perform actual x-ray experiments [31] and are characterized in more detail below (cf. Chapter 4, Figure 3.22). Alternatively, thermal annealing in hydrogen may be used to reduce sidewall roughness [412].

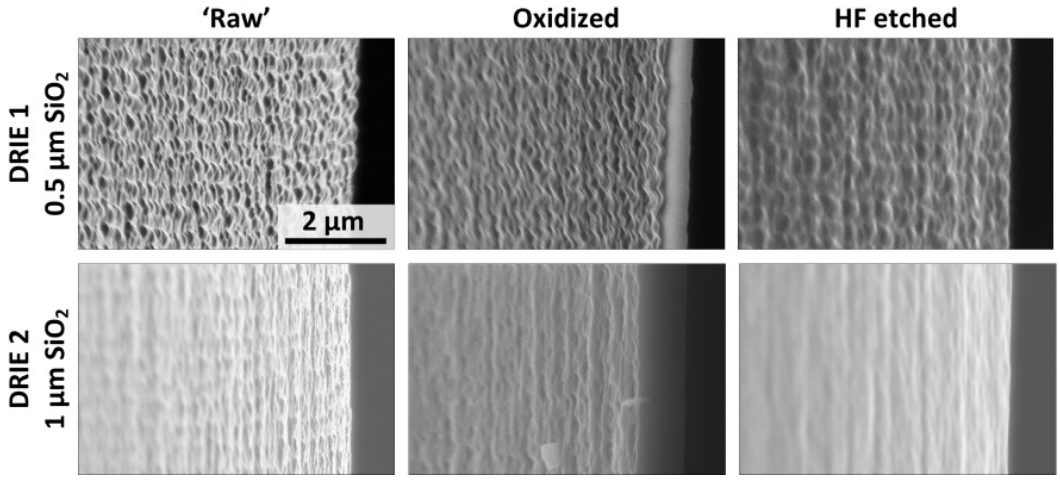

Figure 3.20. Surface smoothing as a DRIE post-process. DRIE 1 and DRIE 2 are slight variations of the optimized recipe given in Table 3.1.

3.7 Packaging

After DRIE and surface smoothing, CRL chips need to be separated from the rest of the wafer. This was either done using a saw with fast spinning diamond blades (Disco, DAD321) or a laser cutting machine (3D-Micromac AG, microSTRUCT vario). While the saw is considerably faster, the laser cutting machine can handle fragile wafers. When using the saw it is advantageous to cover the lens structures with dicing tape (blue film) in order to avoid debris inside the cavities. For the same reason it is advantageous to laser cut from the wafer back side.

Therefore, alignment marks need to be present on the wafer that at first need to be laser milled through the wafer from the wafer front side. Both dicing methods may be assisted by etching trenches (~200 µm wide) at the perimeters of chips together with DRIE of the lens cavities. In this case ARDE needs to be considered in order to avoid accidental etching through the wafer. A 150 µm thick Si membrane should remain in order to avoid breakage of the wafer inside the chamber. Wafer breakage typically happens during de-clamping of the wafer. Partial etch-through may be tolerated as long as the stability and integrity of the wafer are guaranteed (e.g. by anchors of substantial width, cf. Chapter 4.2) and an etch stop layer is present on the wafer backside to avoid etching of the chuck (e.g. 1 µm thick SiO_2).

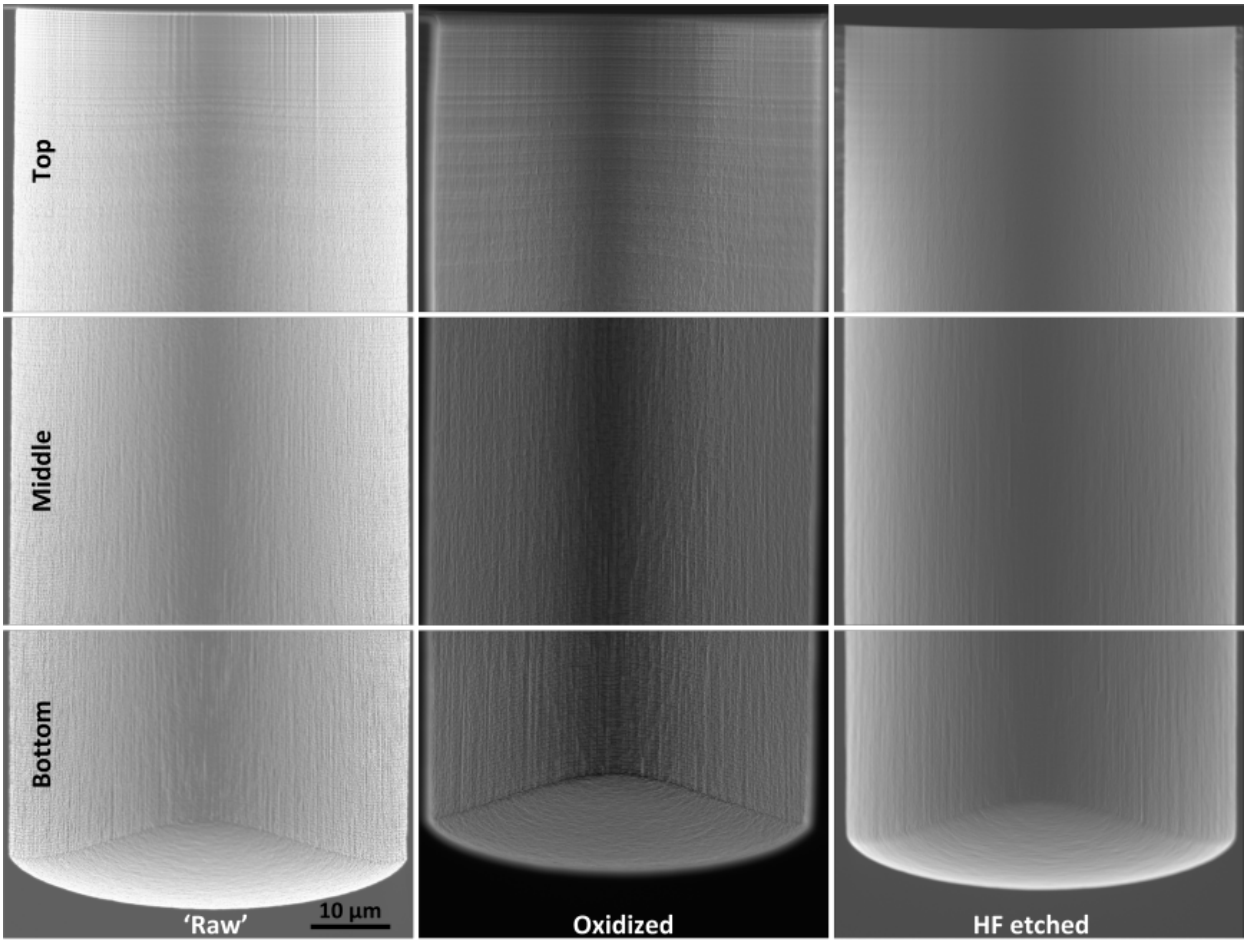

Figure 3.21. Surface smoothing after DRIE of 120 µm deep CRL cavities (XOPTIX4).

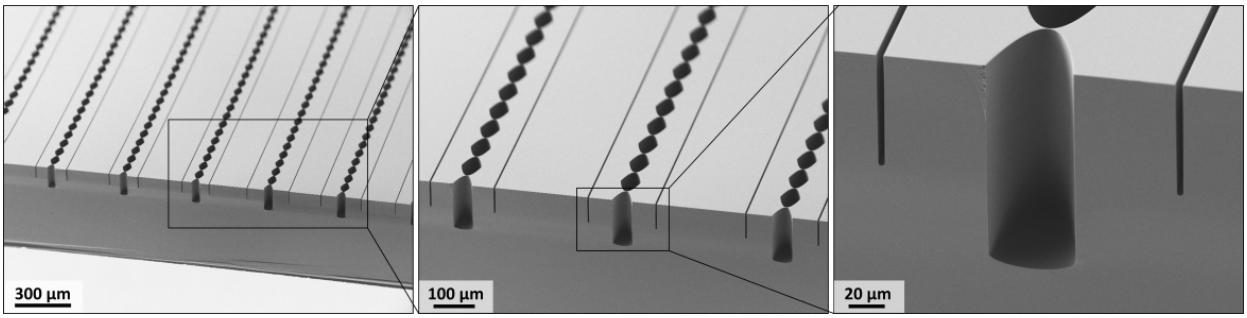

Figure 3.22. Final Si-CRLs ready to be used (XOPTIX4).

3.8 Summary

Deep reactive ion etching was presented as a powerful process for the manufacture of silicon CRLs. Structures need to be defined by lithography and may be transferred into SiO_2 or Al_2O_3 layers to withstand long Si etching. The Bosch process was introduced as a cyclic process in which the alternation of passivation and etching phases enable isotropic etching. Machine specifications, relevant parameters and their effects have been discussed. A sufficient passivation and a controlled local passivation removal are essential steps during the Bosch process. Characteristic effects such as ARDE have been discussed on the basis of experimental data. Thermal oxidation with subsequent etching of the grown oxide layer was introduced as an effective surface smoothing post-treatment to DRIE. Sawing and lacer dicing were introduced to obtain CRL chips.

4 Advanced Si-CRL manufacture

The parallelism, i.e. the verticality and straightness, of sidewalls of line-focusing x-ray lenses is crucial for their optical performance since any sidewall tapering or bowing causes deviations from the ideal lens shape and therefore optical aberrations (cf. Chapter 2.4). Traditionally, silicon CRLs were manufactured using the basic process flow illustrated in Figure 3.1 using processes and materials outlined in Chapter 3 [146,189,192,200,278,286,298].[18] DRIE using the Bosch process suffers from ARDE, which besides the etch rate strongly affects the shape of sidewall profiles (cf. Chapter 3.5). Targeted profile control must therefore focus on simple and homogenous features, e.g. trenches or holes of one width or diameter only. The etching and passivation phases must then be balanced for these specific features (cf. Chapter 3.5.3). However, etching performance also depends strongly on the specific dimensions and geometries of the features.

Figure 4.1. (a) Sidewall angle α of a wide trench with depth d is largely affected by lateral etching originating from isotropically etching radicals, ionic species having a finite ion angular distribution (IAD) and images forces (IFs) deflecting ionic species toward the sidewalls. (b) and (c) Dividing a wide trench into smaller subunits facilitates anisotropic etching and vertical sidewalls.

4.1 Sidewall profile control

DRIE is characterized by the cyclic isotropic passivation, local removal of the passivation, and (ion-enhanced) etching. In this process the ion angular distribution (IAD) and ion deflection by image forces (IFs) play a crucial role (cf. Figure 4.1(a) and Chapter 3.5.4). As the etch depth increases, ion shadowing occurs, which is more pronounced in features with higher aspect ratios. This effectively reduces the etch rate, but simultaneously narrows the IAD. Whereas sidewalls of wide features are constantly subject to at least half the IAD, narrow features collimate ions more efficiently [400]. Additionally, the image forces at opposing sidewalls of

[18] Slight variations may have occurred, namely using e-beam instead of UV lithography or using different masking materials for DRIE.

narrow features may balance each other, further favoring profile control [345]. Hence, if vertical sidewalls are required, it is imperative to focus optimizations on simple and homogenous features that are narrow. If relatively wide, free-standing or complexly shaped structures with high-aspect ratios are required and profile control is critical, it is advantageous to define patterns homogenously by equally wide trenches at the perimeter of the structures according to following design criteria:

Design Criteria

(1) The width of the trench allows a uniform definition of the perimeter.

(2) The final aspect ratio must not get exceedingly high.

(3) The final average etch rate must not be reduced excessively.

(4) Surface defects such as vertical striations or local passivation breakthroughs can be avoided by properly tuning of critical process parameters.

Figure 4.1 illustrates how a large opening may be divided into smaller ones. Certainly, remaining unwanted (or sacrificial) material inside the structures need to be removed subsequently to DRIE. Hence, processes were developed that allow the uniform etching of the perimeters of target structures, while open areas are temporarily filled with sacrificial structures of various shapes. These processes imply multiple process steps, including the removal of the sacrificial structures after shaping the main structures.

For example, expensive silicon-on-insulator (SOI) substrates combined with notching may be used, which occurs during DRIE once the buried oxide layer has been exposed (cf. Chapter 3.5.4). Sacrificial structures in the shape of, e.g., waffles with narrow segments are undercut and may be removed mechanically [402] or by plasma etching [401]. Using single crystalline wafers, the sidewalls of structures may be temporarily protected by thermal oxidation [400] or reinforced passivation using C_4F_8 [413], followed by anisotropic etching of the bottom protection and isotropic under-etching of sacrificial silicon. If mechanical removal is impermissible, wide structures may be isotropically etched subsequent to the etching of narrow structures, employing an additional lithography step and a separate masking layer [414,415]. If structures can be aligned along crystal planes, sacrificial ridges between elementary patterns can be structured by DRIE and removed by anisotropic wet etching, guaranteeing sidewall verticality [416].

Possibly, shape-defining trenches may be completely etched through a silicon wafer, releasing material that was completely surrounded by trenches [356,417,418]. This method was previously used to realize other devices with stringent requirements on sidewall quality upon DRIE such as integrated optical mirrors [418] and atom vapor micro-cells [356]. However, realizing the cylindrically parabolic shapes of CRLs represents a unique challenge, since e.g. anisotropic etching in aqueous KOH previously used as an effective surface straightening and polishing post-treatment to DRIE is not suitable. The surface verticality of silicon CRLs can merely be determined by the quality of DRIE. The surface smoothing step based on thermal oxidation with subsequent etching in hydrofluoric acid (HF) could reduce surface defects other than roughness only to a limited extent (cf. Chapter 3.6). In this thesis and for the first time, through wafer etching was applied to manufacture x-ray lenses. The process flow is the topic of Chapter 4.2 and final devices are presented in Chapter 6.1 and 6.2.

Alternatively, shape defining and DRIE facilitating sacrificial material inside target structures may be dimensioned such that it can be completely oxidized and thus selectively etched in HF. This method was previously used to control height profiles [419]. In this thesis and for the first time, it was explored for facilitation of controlling the etch profile. A design parameter study is presented in Chapter 4.3 and final devices are presented in Chapter 6.3 and Chapter 6.4.

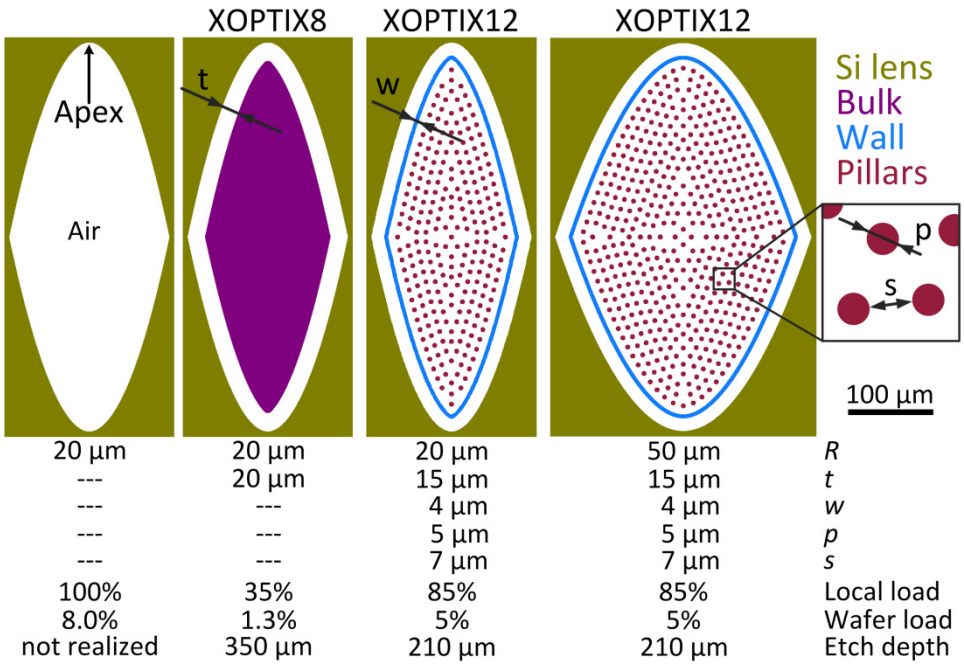

Figure 4.2. Lens pattern designs used in this study. Radius of curvature R, trench width t, wall thickness w, pillar diameter p, spacing s. The local loads refer to the shown areas inside the lens cavities. The wafer loads refer to the final masks. The etch depths are targeted values. The apertures and lengths of shown cavities differ from those in the actual mask designs for clarity.

4.2 Strategy A: Through wafer etching

4.2.1 Design

A trench is an elementary structure. Apart from its extremes, it etches uniformly, i.e. over its whole length it typically shows the same etch rate and sidewall profile. Given the stringent requirements on the sidewall profile, the bi-parabolic cavities necessary for CRLs must be considered as complex structures. Inspection of the basic lens pattern in Figure 4.2 reveals that etching conditions will vary between the apex and the aperture. Especially, at increased etch depths, the IAD, the IF and the molding of the plasma sheath will be non-uniform across the cavity, ultimately yielding non-uniform ion bombardment and etching. A variation of the etch profile within the same cavity has indeed been measured within this thesis (cf. Figure 3.22 and Chapter 5.4 (XOPTIX4)).

The non-uniformity encountered in the manufacture of XOPTIX4 is most probably the reason why Si-CRLs with heights beyond 50 µm were rarely reported and typically resulted in a non-uniform optical performances [146,281]. It may be encountered by defining the structures by trenches of uniform width. The width of the trench t becomes an important design parameter (cf.

Figure 4.2). It must be chosen according to above Design Criteria. In case of a parabola, t must be smaller than R to allow a uniform definition, and as will be seen in Chapter 6.1 and Chapter 6.3, it should be limited by $t \leq R/2$. As visible in Figure 4.2 the sacrificial portion may get sharp at the apex and therefore prevent a uniform etching. Using sacrificial structures, R is typically ≥ 20 µm during this thesis. Reasonable trench widths can thus be readily realized using standard UV lithography. However, if parabolas with radii smaller than 5 µm are required, projection exposure systems or e-beam lithography may be used instead.

Figure 4.3 shows the layout of the mask XOPTIX8, which has been used to manufacture 1D-focusing lenses (cf. Chapter 6.1). The basic features are bi-parabolic openings with R = 20 µm and $2R_0$ = 300 µm aligned in arrays with varying N and arranged on multiple chips. The target web thickness d is 10 µm. All structures in the design, including lenses and outlines of the chips, are defined by 20 µm wide trenches. Given a target etch depth of 350 µm, this results in final aspect-ratios of 17, which can readily be achieved by DRIE. The integrity of the wafer is guaranteed by multiple ~100 × 30 µm^2 large anchors. Individual chips vary by the degree of shape compensation (u = -2.3 µm to u = -3.5 µm, cf. Chapter 2.4).

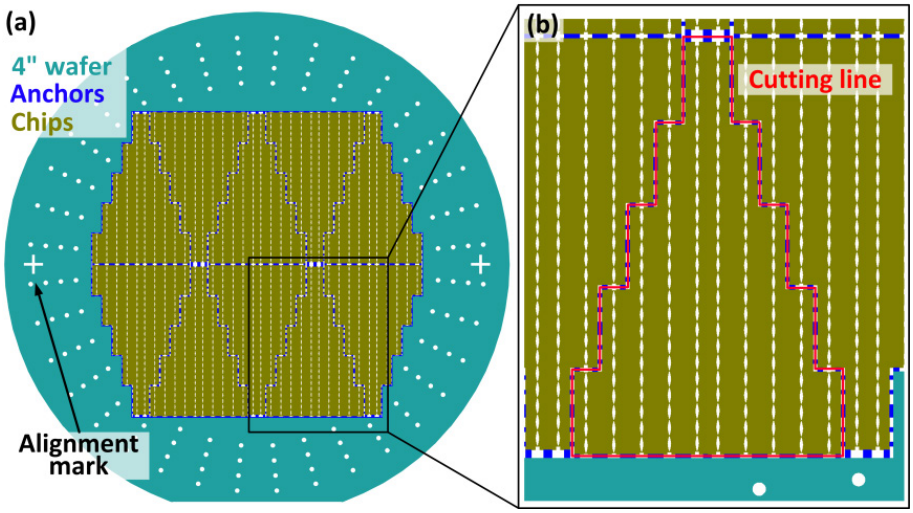

Figure 4.3. Wafer layout XOPTIX8. Sacrificial portions are not shown for clarity. All openings are defined by 20 µm wide trenches. (a) Full 4-inch wafer layout. (b) Zoom-in highlighting the outline of one lens chip. Alignment marks are exaggerated.

4.2.2 Process flow

Figure 4.4 illustrates the manufacture of Si-CRLs by wafer-through etching. The essential modifications to the standard Si-CRL process flow described in Chapter 3.1 concern the initial mask design and the necessity of a wafer-bonding step for stabilizing the fragile through-etched wafer. As starting materials double side polished, 350 µm thick (100) single-crystal silicon wafers with 100 mm diameters may be chosen. A hard mask able to withstand DRIE through the whole wafer thickness is required. 3 µm thick SiO_2 is sufficient and may be patterned using above procedures (cf. Chapter 3.3 and Chapter 3.4).

A total of ~800 cycles, i.e. ~60 min, of the optimized recipe given in Table 3.1 is sufficient to etch through a wafer of 350 µm standard thickness. Once the bottom SiO_2 layer has been

exposed vertical etching essentially stops. Slight over-etching guarantees that the target depth has been reached across the whole wafer and slight notching may occur (cf. Chapter 3.5.4). Sacrificial portions are supported by the thin SiO_2 backside layer only and during de-clamping from the chuck these membranes tend break. In such a case released parts remain inside the processing chamber upon wafer unloading, which necessitates opening of chamber and their manual removal.[19] Loss of wafer pieces was limited but unpredictable and strategies may be found to avoid it in future [420]. Since through etched wafers are fragile, a handling robot may not be used.

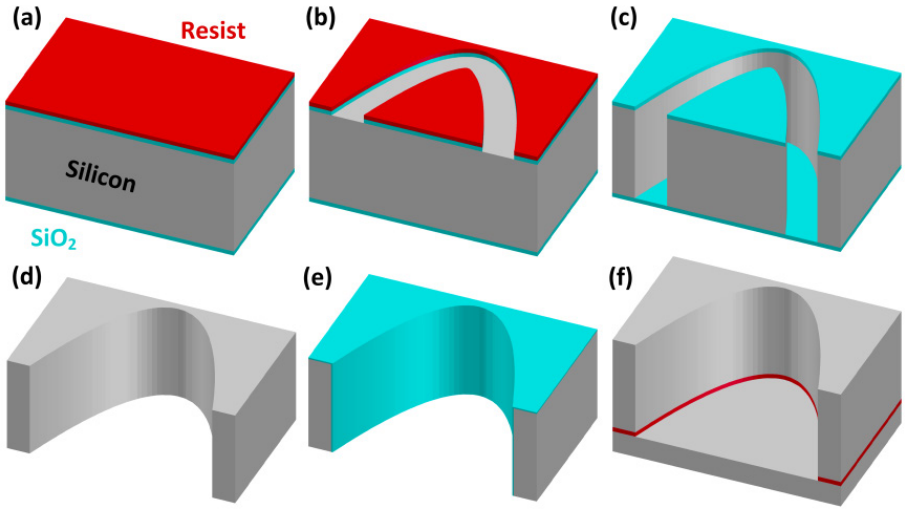

Figure 4.4. Process flow for advanced Si-CRL manufacture according to Strategy A.

During process optimization, 525 µm thick test wafers were etched to the target depth of 350 µm and cleaved along their optical axis for inspection (cf. Chapter 5.3). Ramping of parameters was used to optimize DRIE [421,422]. In particular, the cycle time was linearly increased during DRIE, while the passivation phase time was left constant. This effectively compensated for varying conditions due to increasing aspect-ratios of the etched trenches and its effect can be seen in Figure 4.5. No ramping resulted in positive tapered profiles, while too much ramping caused passivation breakthrough near the top of trenches.

Figure 4.6 shows the best DRIE result achieved during this thesis work and demonstrates the powerfulness of this approach for manufacturing high-quality CRLs. Unfortunately, this specific result never made it to final devices, because of process drifts discussed in Chapter 3.5.2. It highlights the sensibility of DRIE, emphasizes the timely limited process window and stresses the need for accurate optimizations and process stability.

[19] Chamber opening is unpleasant in terms of time and process stability. Since the platen is cooled to -19ºC for processing, it needs to reach room temperature to avoid condensation of water. Upon venting the chamber, vacuum needs to be reestablished.

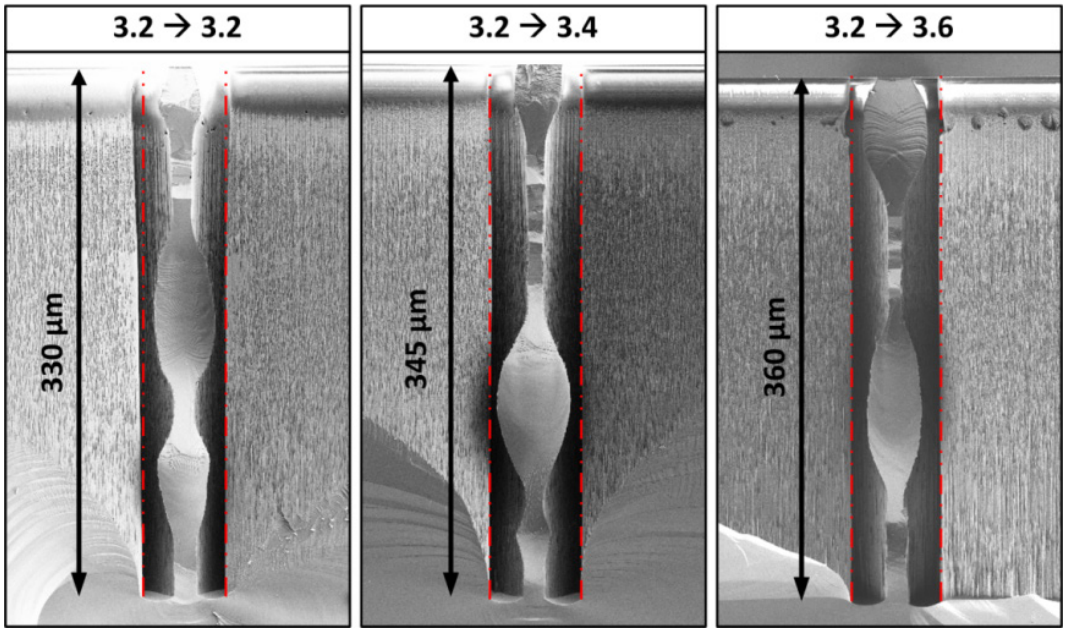

Figure 4.5. SEM images of cross sections of trenches after 750 cycles DRIE with different degrees of ramping of cycle times. The etch phase times are indicated in seconds (cf. Figure 5.4).

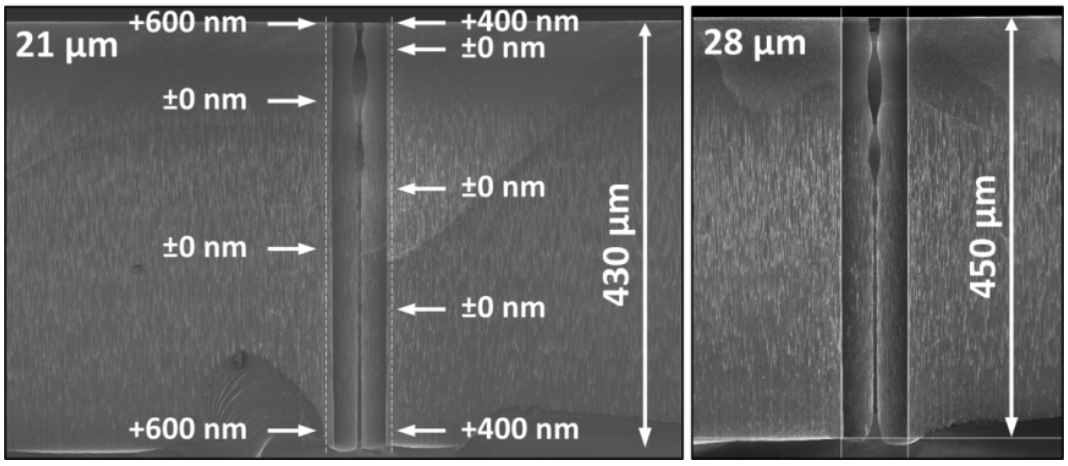

Figure 4.6. Extraordinarily straight profiles upon a 100 min DRIE recipe. The trench widths are 21 µm and 28 µm, respectively (cf. Figure 5.4).

4.2.3 Wafer bonding

After DRIE and an oxygen-plasma treatment to remove residual sidewall passivation, sacrificial portions were removed by etching the SiO_2 backside membrane and carefully applying shots from a nitrogen spray gun. Subsequently, surfaces were smoothed (cf. Chapter 3.6). Through-etched wafers were fragile at this stage, because of the ~15 µm wide bridges between bi-parabolic cavities, necessitating careful handling and prohibiting any processes that apply high mechanical stress on the wafers, such as spin drying. Upon wet treatments, wafers were dried overnight inside a fume hood.

Subsequent to surface smoothing, wafers were stabilized by adhesive bonding. This allowed safe handling of wafers, obtaining individual lens chips and ensured the stability of the chips

when mounted in a synchrotron beamline. As-received single side polished silicon wafers with a wafer bow <10 µm were selected using a stylus profilometer (Bruker, Dektak XTA) and spin coated with photo resist (AZ4562, 10 µm, soft bake temperature 100°C), which acted as an adhesive layer. Device and handle wafers were bonded under vacuum at a pressure of 2×10^{-3} mBar at 240°C by applying a piston force of 1000 N for 5 min (EV Group, EVG 520). Subsequently, photo resist inside the lens cavities was removed by plasma ashing. Individual lens chips were separated from the rest of the wafer using laser cutting (cf. Chapter 3.7).

4.3 Strategy B: Sacrificial oxidation and selective etching

Strategy A relies on through-wafer etching and results in fragile wafers. Alternatively, thin sacrificial structures may be used that can be completely oxidized in a reasonable amount of time and removed by selective etching in buffered hydrofluoric acid (bHF). In contrast to previous methods (cf. Chapter 4.1), the here proposed Strategy B necessitates only one lithography step and one plasma etching step. It does not depend on the chosen wafer thickness and structures may be etched to arbitrary depths. Single crystal wafers can be used and it does not rely on under-etching. Free-standing structures with high-aspect ratios can be realized, while profile control during DRIE is facilitated.

4.3.1 Design

Figure 4.2 illustrates how lens patterns may be defined by thin sacrificial structures. A narrow trench width *t* defines the perimeter of the bi-parabolic opening, a thin wall with thickness *w* confines the trench and dots with diameter *p* fill out the remaining space uniformly. Similar to ARDE affecting trenches of variable widths (cf. Chapter 3.5.4), the mean spacing *s* between pillars regulates the etch rate and hence needs to be matched to the trench width in order to reach a uniform etch depth of the entire structure. Notably, this design slightly reduces the local etch load, further facilitating process control.

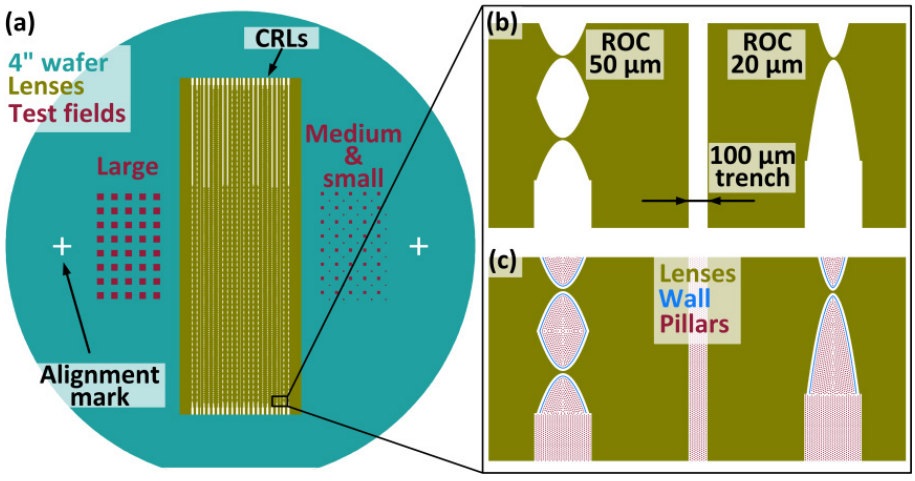

Figure 4.7. Wafer design XOPTIX12. (a) Full 4-inch wafer layout. The middle part with lens structures was used to obtain a nickel mold insert (cf. Chapter 6.3), while the test fields were used to explore design parameters. (b) Zoom-in highlighting the lens structures. (c) Inclusion of sacrificial structures. Alignment marks in (a) are exaggerated.

The trench width t needs to be chosen according to aforementioned Design Criteria, i.e., such that profile control is enabled and the target etch depth can be reached with reasonable etch rates. The thickness w of the guarding wall and the diameter p of the dots (or pillars) need to be chosen such that a) their integrity is guaranteed until the end of the etching and b) they can be completely thermally oxidized within a reasonable amount of time.

Figure 4.7 shows the layout of the mask XOPTIX12, which has been used to manufacture a silicon master, which in turn was used to obtain nickel mold inserts and ultimately injection molded polymeric 1D-focusing lenses (cf. Chapter 6.3). The layout also includes test fields that allow systematically studying design parameters of the sacrificial structures (cf. Chapter 4.3.3). The basic features for the CRLs are bi-parabolic openings with R = 20 µm or R = 50 µm and $2R_0$ = 300 µm. Multiple lenslets are arranged in arrays with varying N. The structures were defined by 15 µm wide trenches, w = 4 µm, p = 5 µm, s = 7 µm. Given a target etch depth of 210 µm this results in final aspect-ratios of 14, which can readily be achieved by DRIE. The degree of shape compensation was constantly u = -3 µm (cf. Chapter 2.4). Simple trenches of different widths are also present (cf. Figure 3.10). The total wafer etch load (i.e. exposed silicon) is ~5%.

4.3.2 Process flow

Figure 4.8 illustrates the manufacture of Si-CRLs using thin sacrificial structures. The essential modifications to the standard Si-CRL process flow described in Chapter 3.1 concern the initial mask design and the necessity of a high temperature treatment. The starting materials were single side polished, 525 µm thick (100) single-crystal silicon wafers with 100 mm diameters. SiO_2 typically with 1 µm thickness was a sufficient masking material and it was patterned using above procedures (cf. Chapter 3.3 and Chapter 3.4).

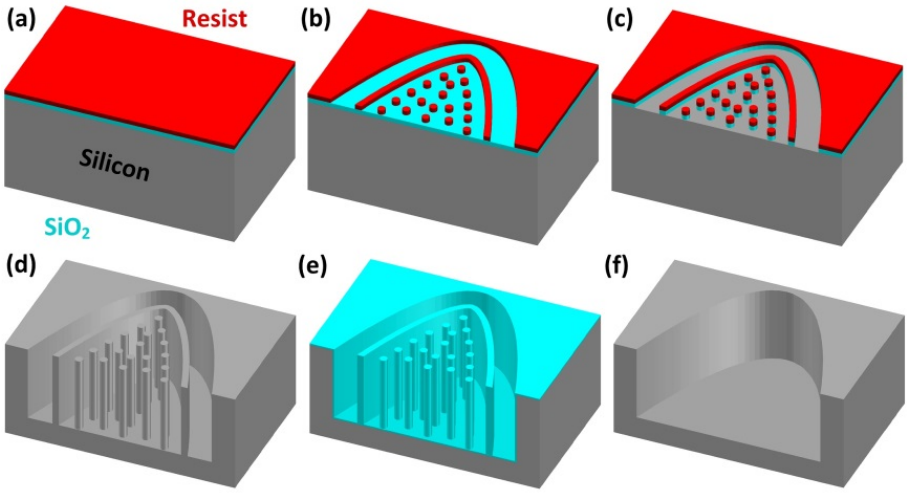

Figure 4.8. Process flow for advanced Si-CRL manufacture according to Strategy B.

Applying a BARC layer prior to lithography was found to be essential for resist adhesion in case of 3 µm diameter dots. A total of ~450 cycles, i.e. ~32 min, of the optimized recipe given in Table 3.1 were sufficient to etch to the target depth of 210 µm. Subsequent to DRIE and oxygen-plasma treatment, sacrificial structures usually collapsed in the course of their immersion into the solutions during the RCA clean prior to thermal treatments. However, this

structural collapse did not hinder their efficient removal. Multiple oxidation and bHF etch steps successively removed the pillars and walls, simultaneously smoothing sidewalls (cf. Chapter 3.6).

4.3.3 Parameter study

A parameter study was conducted in this thesis work and published [150]. To study the effect of sacrificial structures in detail, test patterns comprise square patterns with edge lengths of 1500 µm, 750 µm and 375 µm uniformly filled with dots only, hereafter referred to as large, medium and small fields, respectively (cf. Figure 4.9). The dots are arranged on square lattices with pitch lengths (or spacings) *s*, and *s* varies from 3 µm to 10 µm in increments of 1 µm. At the edges of the fields, a distance of 1 µm is added to the start of the dot lattice to compensate for locally changing etching conditions. The dot diameter *p* varies in increments of 0.5 µm from 3 µm to 5 µm such that complete thermal oxidation of resulting pillars is possible within a reasonable amount of time (<48 h in multiple steps). Two fields of 40 and 80 squares, respectively, are arranged in a grid as illustrated in Figure 4.9(c) with a constant pitch of 1.5 mm to reduce influences from detrimental effects such as micro loading (cf. Chapter 3.5.4). Additionally, the design contains square patterns with edge lengths of 1500 µm that were defined at their perimeters by trenches with varying widths (*t* = 5 µm, 10 µm, 15 µm, and 20 µm), guarding walls with thicknesses *w* (*w* = 3 µm and 4 µm), and *p*-*s*-combinations deliberately chosen from the squares with dots only.

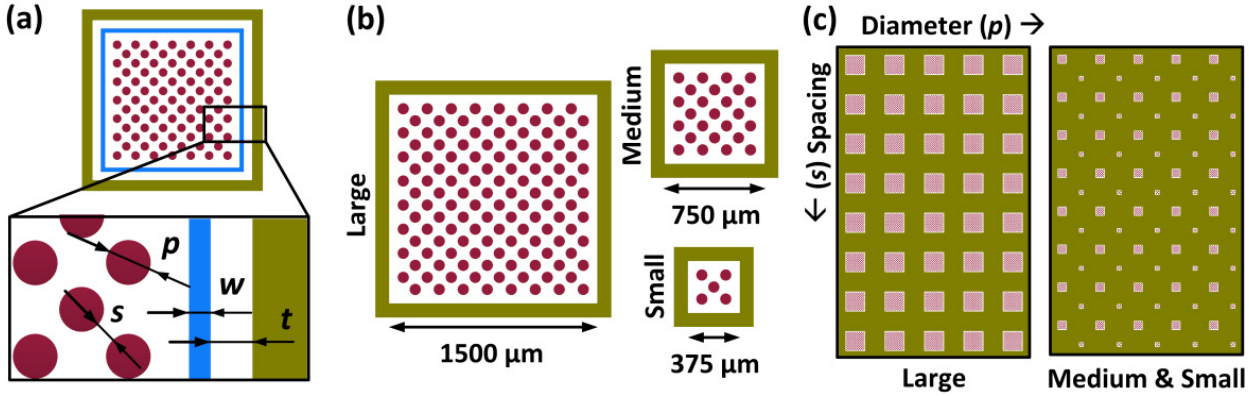

Figure 4.9 (a) Micro-patterns under investigation in this study. The perimeter of target structures is defined by a trench of width *t*. The trench is confined by a guarding wall with thickness *w* and the remaining space within the structure is uniformly filled with dots (or pillars) with diameter *p* and average spacing *s*. Fields with varying *p* and *s* were designed in three different sizes (b) and arranged in grid patterns on the wafer (c). See also Figure 4.7.

In the experiments being presented, 450 cycles DRIE have been used (cf. Table 3.1 and Figure 3.10). Subsequently, a total of 5.6 µm SiO_2 was grown in five steps (1100 °C, 1 × 16 h + 4 × 3 h), each step followed by SiO_2 removal in bHF. A total of 2.6 µm silicon was consumed, completely removing the sacrificial structures and effectively smoothing the sidewalls. The depth of the square fields was measured using a stylus profilometer (Bruker, Dektak 8).

Figure 4.10(a) and (b) show etched large square fields (*p* = 5 µm and *s* = 7 µm) before and after removal of the sacrificial structures, respectively. The sacrificial structures partially collapsed

during the wafer cleaning and SiO_2 etching after DRIE, but were completely removed from the structures and wafer surface. The etch depth is 240 µm at the center of the field. At the cleared sidewall, regular vertical striations are visible, originating from pillars that locally influenced the etching conditions. The bottom of the field is shaped by corrugations from pillars whose bases were not completely oxidized. Pillars closest to the sidewalls leave larger residues, suggesting locally slight increase of the wall-pillar spacing in the future. When a trench and a guarding wall were used (w = 4 µm and t = 15 µm), sidewall defects were largely reduced (cf. Figure 4.10(d)).

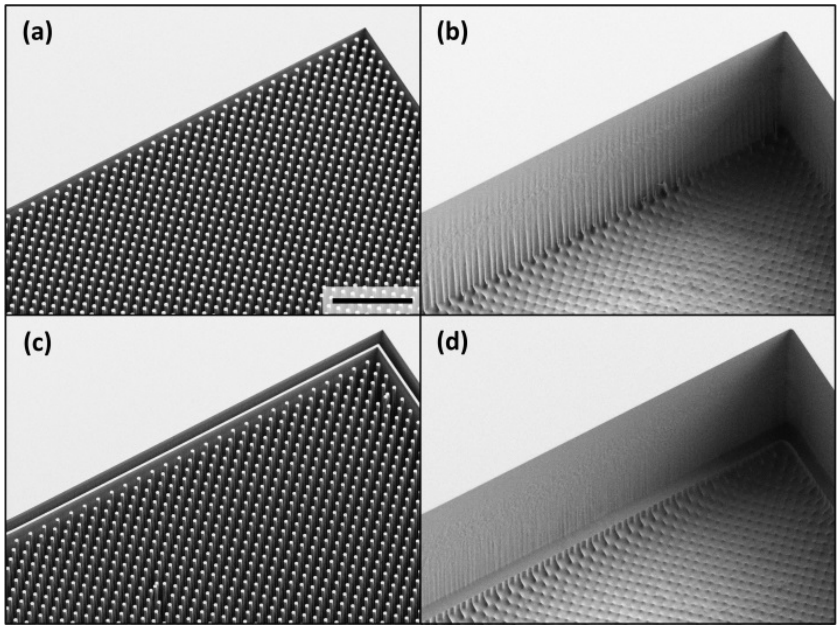

Figure 4.10. (a)-(d) Scanning electron micrographs of corners of 1.5 × 1.5 mm^2 deep reactive ion etched test fields before (a) and (c) and after (b) and (d) removal of sacrificial structures. Vertical marks on the sidewalls are apparent in (b), while being absent in (d) where a guarding wall was used. The scale bar is 100 µm and the view tilt angle is 30°.

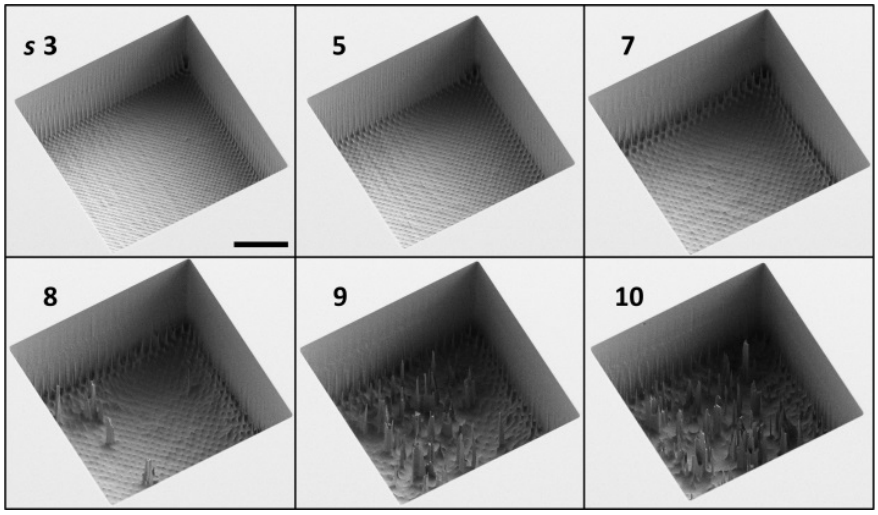

Figure 4.11. Effect of varying the pillar spacing. Scanning electron micrographs of small fields after deep reactive ion etching and removal of sacrificial structures. The diameter of the pillars was 4 µm and the pillar spacing s of each field is indicated in micron. The scale bar is 100 µm and the view tilt angle is 30°.

The effect of *s* on their integrity was investigated (c.f. Figure 4.11). Larger *s* resulted in faster vertical etching, but more pronounced lateral etching, and at a certain point caused the collapse of pillars during DRIE. The collapse of small-diameter pillars was more likely and once it happened, uncontrolled etching occurred, leaving large residues inside the structures. At the onset of structural collapse the aspect ratio of pillars was 67 (p = 4 µm and s = 7 µm). Notably, the collapse of pillars was more likely in the small fields indicating a more effective etching of areas with less exposed silicon, which is consistent with the micro loading effect (cf. Chapter 3.5.4).

Figure 4.12 and Figure 4.13 illustrate how the etch depth (and hence etch rate) of areas filled with pillars depends on the pillar spacing and diameters. This dependence is similar to ARDE encountered in the case of trenches or holes with varying widths or diameters, respectively. Evidence of micro loading is also apparent when comparing etch depths of differently sized fields with identical dimensions of sacrificial pillars (cf. Figure 4.12, p = 5 µm). Generally, the etch depths of large fields are up to 3% smaller than those from smaller fields.

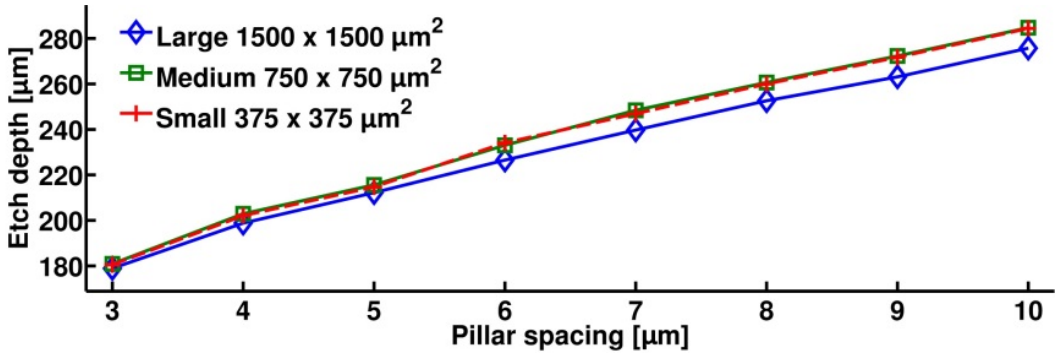

Figure 4.12. Dependence of the etch depths on the spacing *s* between pillars. The pillar diameter *p* is constantly at 5 µm.

The interdependency of the *s* and *p* affecting the etch depth of the large fields was investigated. In Figure 4.13 the etch depth is color encoded in an interpolated surface plot. A local etch load of the corresponding field was assigned to each *p*-*s*-combination and drawn on the abscissa. Similarly, a silicon area per masking dot can be assigned and its square-root is drawn on the ordinate. Isolines corresponding to the etch depths of trenches with certain widths are included. This diagram facilitates finding the optimum *t*-*p*-*s*-combination for obtaining a certain etch depth, while maximizing etch rate and minimizing *p*, which reduces the amount of necessary thermal oxidation for sacrificial structure removal. It also sheds light onto how a certain trench may be associated with a *p*-*s*-combination and a local etch load, which is worth a separate, more detailed analysis.

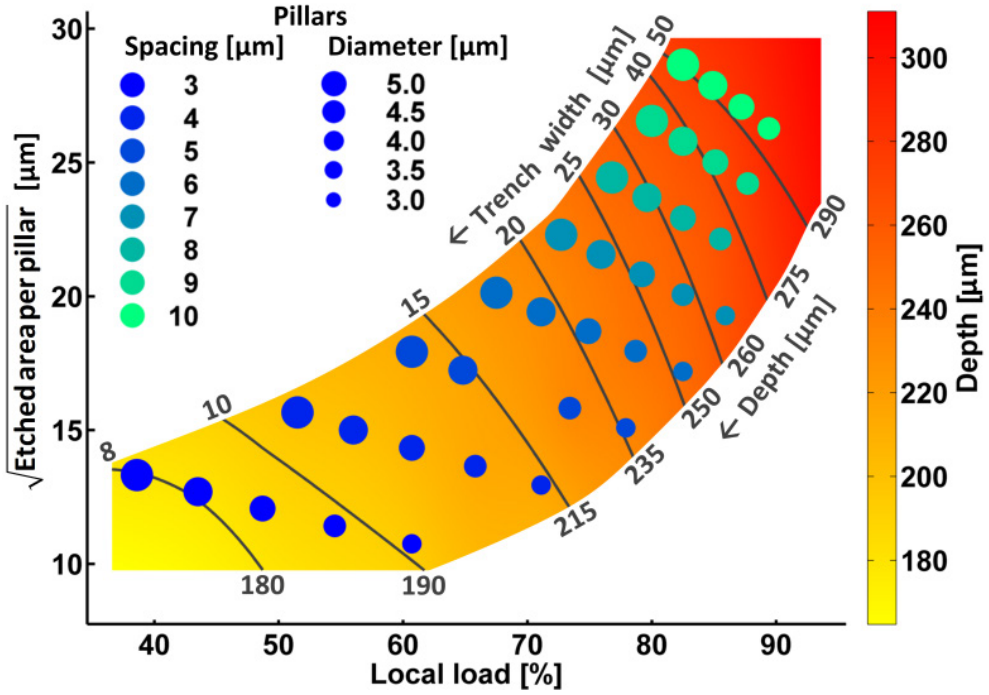

Figure 4.13. Dependence of the etch depth of the large fields on the diameter p of the pillars and the spacing s between the pillars. Additionally, the etch depths of trenches with different widths are indicated by isolines. The measuring point with p = 4 µm and s = 5 µm is missing, because of an error in the mask design. The measuring points with p = 3 µm and s = 8-10 µm are missing, because the pillars collapsed prior to the completion of the etching process.

Figure 4.14 shows fields with varying t-w-p-s-combinations. Clearly, the etch depths at the sidewalls and the insides of structures could be readily controlled by the proper dimensioning of sacrificial structures. The interior could be etched deeper than the perimeter (e.g. t = 5 µm, w = 4 µm, p = 5 µm, and s = 9 µm) and vice versa the perimeter could be etched deeper than the interior (e.g. t = 15 µm, w = 4 µm, p = 5 µm, and s = 4 µm). Structural defects as e.g. in the field (t = 10 µm, w = 3 µm, p = 4 µm, and s = 7 µm) rarely occurred and in this particular case the residue in the middle of the field was most likely caused during the lithography. Vertical striations are more pronounced on the sidewalls of fields defined by wider trenches (t = 15 and 20 µm, corresponding to d = 215 and 235 µm, respectively), than in the case of narrower trenches (t = 5 and 10 µm, corresponding to d = 150 and 190 µm, respectively). This variation may be attributed to partial breakthrough of the guarding wall, as is evident by a comparison of sidewalls of fields that only differ by the wall thickness. Wall breakthrough, which is more likely for a thin wall (w = 3 µm) than for a thick wall (w = 4 µm), causes a partial coalescence of a trench with the pillar-filled area, and hence results in a local change of etching conditions. Arbitrarily shaped multilevel structures are feasible, as previously demonstrated for structures aligned along crystal planes [416].

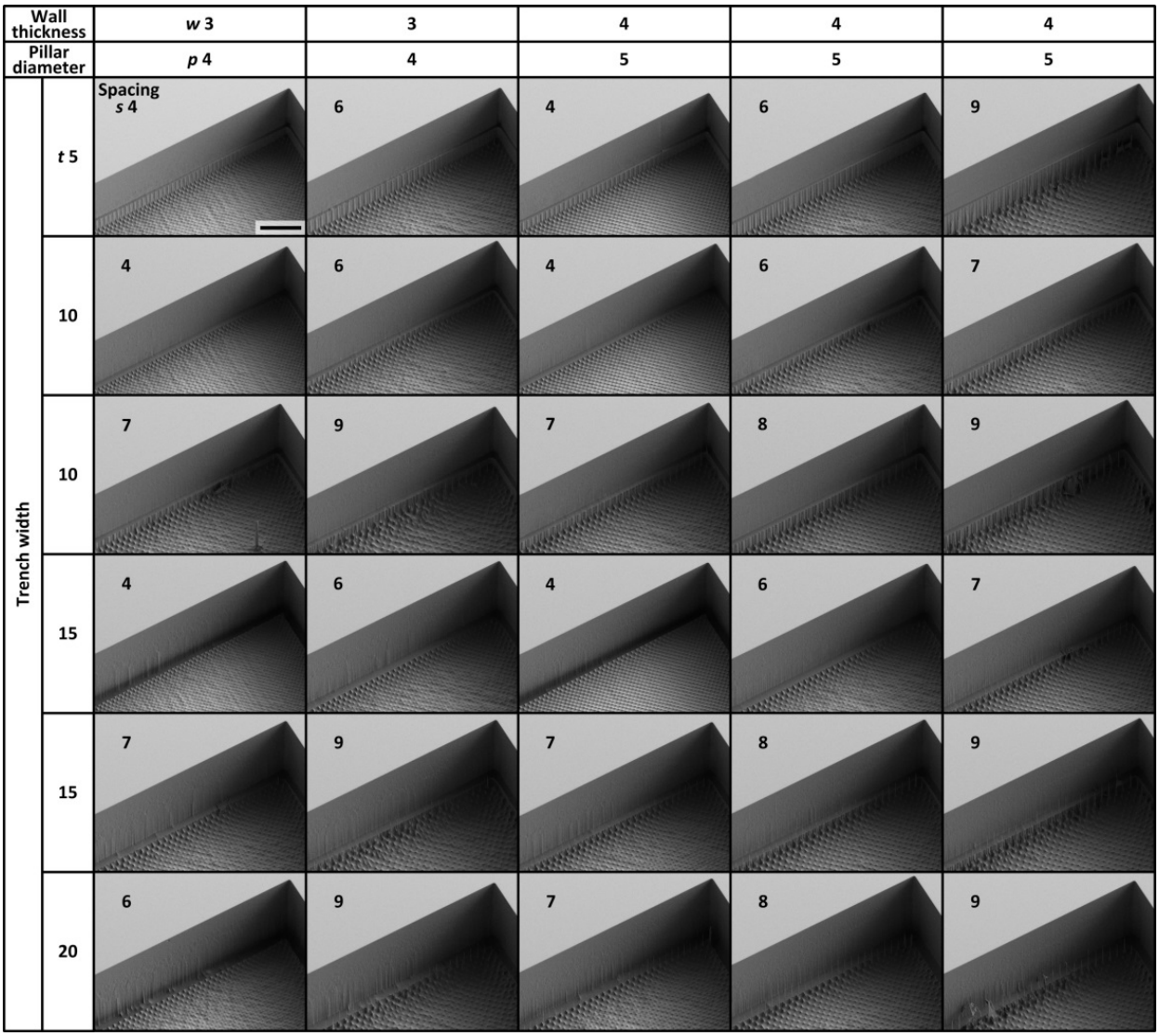

Figure 4.14. SEM images of corners of large fields with varying *t*-*w*-*p*-*s* combinations after deep reactive ion etching and removal of sacrificial structures. The scale bar is 100 µm and the view tilt angle is 30°. The unit of all values is 1 µm.

4.4 Summary

It was argued that defining primary structures uniformly by narrow trenches assists accurate profile control during DRIE. Sacrificial structures need to be removed in process steps subsequent to DRIE. Two novel strategies suitable for the manufacture of Si-CRLs were presented. Strategy A uses through-wafer etching to release sacrificial material. Since through-etched wafers are fragile, they must be stabilized by adhesive bonding in order to guarantee a safe handling of wafers. General design criteria were found and an example for a wafer design was presented. Strategy B utilizes thin walls and pillars, which can be removed by complete thermal oxidation and selective etching in hydrofluoric acid. A guarding wall proved to be necessary for achieving smooth sidewalls. The effects of critical dimensional parameters such as wall thicknesses, pillar diameters, and pillar spacing on the etching were systematically studied. The etch depth of sacrificial pillars can be controlled and adapted to the etch depth of shape-

defining trenches by adjusting the spacing between pillars. A maximal aspect ratio of ~60 of the final pillars was found to guarantee the integrity of sacrificial structures. Narrower trenches yielded smoother sidewalls, but also lower etch rates. Structural units of sizes between 375 × 375 μm^2 and 1500 × 1500 μm^2 did only show minor differences in etch depths. Sacrificial structures were completely removed, leaving no residues if their integrity was maintained during DRIE.

5 Metrology

This chapter describes the methods used throughout this thesis to analyze the shapes of lenses during and subsequent to their manufacture. During the manufacture it enables process control and optimizations. Subsequent to the manufacture it allows to predict their optical performance and compare expectations with measurements for a better understanding of the lenses and an improved manufacture. The combined use of scanning electron microscopy, optical profilometry and atomic force microscopy guided the microfabrication throughout this thesis work. Replica molding is established as an essential step to access the apexes of lenslets. Techniques to quantitatively characterize the optical performances of lenses are discussed and the beamlines are presented at which experiments have been performed.

5.1 Characterization tasks

The manufacture of high-quality x-ray optical components requires adequate dimensional characterization techniques independent of measuring their optical performance. To achieve an x-ray line beam with a minimum waist, the shapes of lens cavities must be close to ideal parabolic cylinders, including nearly vertical sidewalls with a minimum of texture and roughness (cf. Chapter 2.4). Any deviation from the ideal shape causes spherical aberration and scattering, resulting in a blur of the focus. The overall topography of the lenses needs to be measured with a precision in the nanometer range to model and understand their performance when applied in a synchrotron experiment. Additionally, the characterization method needs to be fast and reliable, to allow a continuous optimization of the manufacturing process.

The structures under investigation in this thesis are basically cavities etched into a single crystal silicon wafer by DRIE. A single cavity is defined by a pair of adjacent parabolas and has a lateral dimension of 50 µm – 1 mm and is etched to depths beyond 100 µm (cf. Figure 3.22). Furthermore, the radius of curvature of the shape defining parabolas typically ranges from 5 µm – 50 µm. The aspect ratios are generally larger than 1 and locally may approach 20. The following properties of these lenses have to be optimized to obtain a minimum beam waist and should therefore be carefully measured:

1. the straightness of etched sidewalls,
2. the deviation of the actual shape from the desired parabolic shape along the depth,
3. the radius of curvature of the parabolic shape along the depth,
4. the size of striations and other surface defects, and
5. the roughness of the etched surface.

In previous reports on the manufacture of silicon x-ray lenses, characterization has been limited to measuring the shapes at the very top surface in combination with inspecting the straightness of cross sections of etched trenches by SEM [286]. Sidewall roughness, although it is not

regarded as being crucial for the lens performance, was so far only assessed qualitatively by SEM [146]. Polymeric lenses made by DXRL (cf. Chapter 2.3.4) have been characterized by a technique that involves serially sectioning of a sample and acquiring photographs of each section, to measure the radius of curvature of the parabolic shape along the depth [423]. White light interferometry was used to characterize spherical parabolic x-ray lenses with radii of curvatures of ~200 µm, but the limitation regarding the maximum detectable slope of the structures has been recognized [224,424]. Previously, computed tomography was used, which allowed to visualize voids in embossed beryllium lenses [241,242,425]. The shape of single x-ray lenses may be reconstructed from measured x-ray wavefront distortions and Ronchi tests may be performed for a qualitative characterization of lens aberrations [426–429].

In this thesis different techniques have been used for process control and for characterizing the shape of final devices. Figure 5.1 gives an overview of the techniques that have been applied and the specific information that could be gained. First, the top parabolic shapes have been analyzed by detecting their edges in images obtained by SEM or optical microscopy. Second, the sidewalls have been inspected using optical profilometry. Specifically, the 3D shape and straightness of sidewalls have been analyzed upon cleaving lenses in *Z*-direction. Optical profilometry can also be used to determine the straightness of the apex region; measuring the 3D shape, however, is limited by the maximal detectable slope of the technique. Third, the 3D shapes of the apexes have been measured using atomic force microscopy in combination with replica molding for which samples have to be cleaved in *X*-direction. In the following sections each technique is discussed in detail.

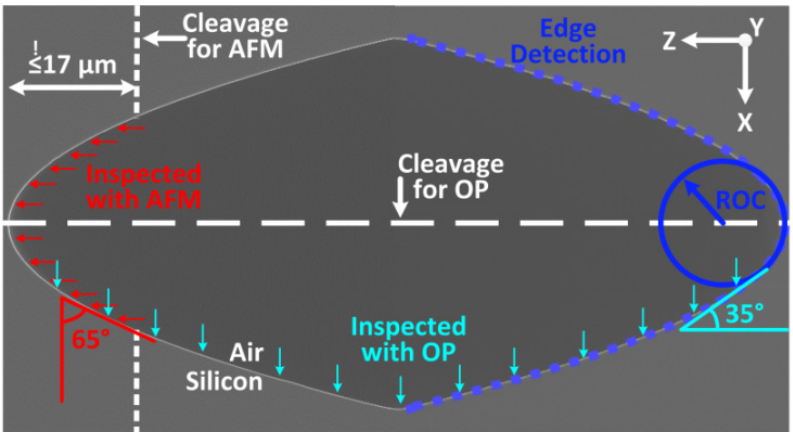

Figure 5.1. Top view SEM image of a single lenslet (XOPTIX4) highlighting the used characterization techniques. The cleavages necessary for characterizing the sidewalls by optical profilometry (OP) and atomic force microscopy (AFM), as well as respective maximum detected slopes are indicated. The dotted blue line is the result of an edge detection routine implemented in MATLAB.

The general demands in dimensional micro- and nanometrology have been pointed out recently [430,431]. Optical microscopes, scanning electron microscopes (SEM) and atomic force microscopes (AFM) are essential characterization tools in a microfabrication facility [432,433]. However, when characterizing 3D microstructures, these instruments are often limited in terms of range, resolution and throughput. Unless equipped with a software package for 3D reconstruction [434–437], electron microscopy is inherently 2D, while optical profilers are

limited by the maximum detectable slope and have relatively poor lateral resolution [438]. In contrast, AFM is an inherently 3D technique with nanometer resolution. However, ranges of typical AFM instruments are limited, scan rates are slow compared to SEM and the dimensions of AFM probes hinder complex structures to be measured. Very demanding dimensional characterization tasks are tackled by custom-built instruments available at national metrology institutes [439–446].

5.2 Top 2D analysis

The characterization of the surface shape of the bi-parabola openings allows checking the quality of the lithography mask, detecting shape widening or shrinking in the course of the lithography, hard mask preparation, or DRIE, and controlling silicon consumption upon surface smoothing steps. To this end, top view images must be obtained by using an optical microscope or a scanning electron microscope. Preferably, samples should be well aligned with respect to the camera or scanning direction. This allows the shapes to be extracted without complex image post-processing. To detect systematic errors originating from misalignment, it is beneficial to capture images of full bi-parabolic openings and analyze both parabolas. Samples need to be in focus and aligned strictly normal to the imaging direction.

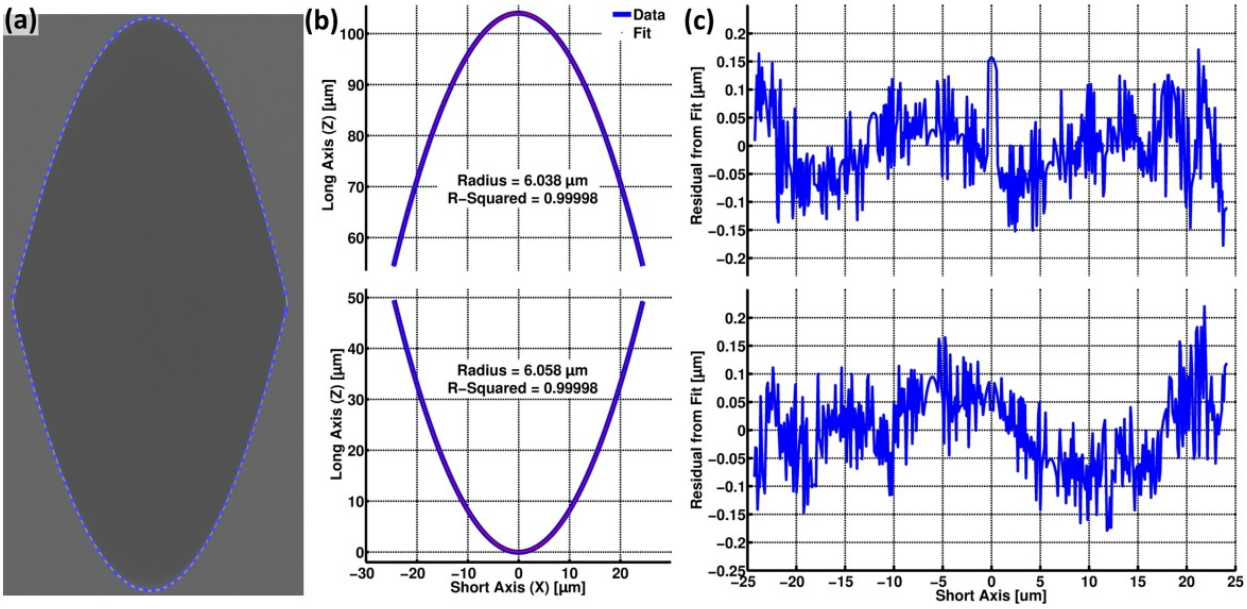

Figure 5.2. Top surface analysis via edge detection. (a) SEM image of one lenslet with overlaid detected edge. (b) Parabolic fits to the detected data. (c) Deviation of the fits from the data.

The images may be cropped using ImageJ,[20] so that only one single feature is visible. The cropped images are further processed using MATLAB. A routine was programmed, which loads an image, detects the edge of the feature automatically using the Canny edge detection algorithm [447], fits parabolas to the edge, exports the model fit including the radii of curvature and the R^2-values (coefficients of determination), and illustrates the deviation of the actual shape from the fit. The extracted data is fit to $z(x) = \pm x^2/2R$ with the fitting parameter R.

[20] http://imagej.nih.gov/ij/index.html (Dec, 2015).

The fit range in *X*-direction may be specified and images may be analyzed in batches for convenience. Analyzing images obtained by SEM or optical microscopy gives equal results. Given the size of lenslets, the spatial resolution of an optical microscope may be better than that of an SEM. However, SEM is more flexible with respect to magnifications, etc.

As an example, Figure 5.2 shows a SEM image of the top surface of a lens cavity. The detected edge is indicated, demonstrating the high quality of the algorithm. Generally, a low image contrast was found to give best results. The parabolic fits with an *X*-fit-range of 49 µm gave R = 6.04 ± 0.05 µm for the upper and R = 6.06 ± 0.05 µm for the lower parabola, with mean deviations of 53 nm and 58 nm, respectively. The differences ΔZ between the fits and the data are plotted in Figure 5.2(c). The *X*-fit-range has a major effect on the analysis, since actual profiles are not strictly parabolic. Figure 5.3 shows the results of its influence. The top shapes of multiple lenslets with different degrees of compensation were analyzed (XOPTIX4, cf. Chapter 3.2 and Figure 3.22). Generally, the better the fit results match using different *X*-fit-ranges, the more parabolic are the profiles. In this particular case, lenses with a compensation of 1.25 µm are optimal. The accuracy of the analysis is limited by the pixel size, the calibration, image distortions, sample alignment and the edge detection algorithm.

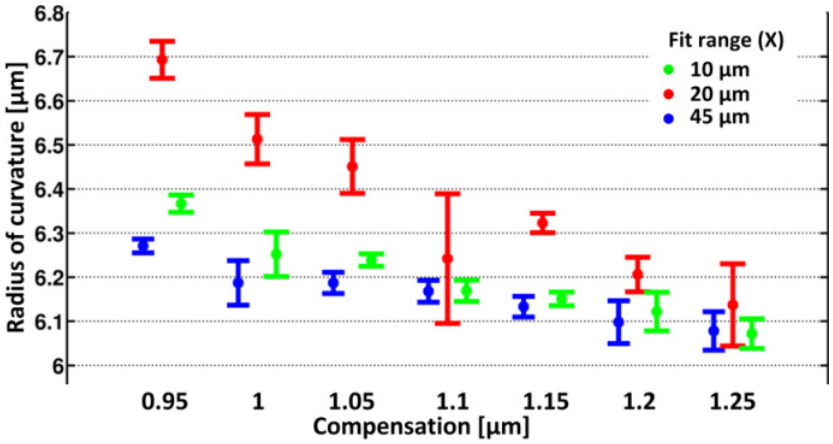

Figure 5.3. Results of fitting the edge-detected 2D parabolic shapes. The fitting range was varied and lenses with different degrees of compensation for shape widening were analyzed. Each data point is the average of 4 measurements.

5.3 Cross sections

Inspecting cross sections obtained by cleaving or dicing samples is commonly used to obtain essential information about the quality of structures with high aspect ratios. Various features of DRIE, including mask undercut, passivation break-through, etch depth, and profile straightness can readily be characterized this way (cf. Chapter 3.5.4). Cross sections are typically analyzed by SEM. SEM has the advantage of a high depth of focus, which allows features at different heights to be visualized simultaneously. Alternatively, optical microscopy allows a much faster inspection of e.g. sidewall profiles since it does not rely on high vacuum. Cross sections are also used to obtain 3D sidewall information by OP and AFM (cf. Chapter 5.4 and Chapter 5.5).

Throughout this thesis, cross sections have been obtained by manual cleaving. It is strongly facilitated by the crystallinity of wafers. A blank (100) wafer easily cleaves parallel and normal

to its major flat by initiating a crack at the wafer edge with a diamond scribe. Therefore it is advantageous to align structures accordingly. If the wafer is structured with deep cavities, the propagation of the initiated crack may be distorted by these cavities, resulting in non-straight cross sections. Wafers containing CRLs preferentially cleave along their optical axis (cf. Figure 4.3 and Figure 4.7). Cleaving CRLs normal to their optical axis can be facilitated by using an automatic wafer scriber and gently cleaving the wafer over an edge. Figure 5.4 shows a cross-section of a CRL after DRIE (XOPTIX8, cf. Chapter 4.2). The region at the apex was inspected for verticality and sidewall texture (Figure 5.4 (b) and (c)). Faint vertical striations are visible; most probably they originated from corrugations at the edges of the SiO_2 used as the masking material or passivation built-up (cf. Chapter 3.5.4). No mask undercut was observed and the surface scallops inherent to the Bosch process were essentially smeared over in the course of the ~60 min long etching process. The etch profiles appear straight and vertical and a more detailed analysis will be given in Chapter 5.4 and Chapter 6.1).

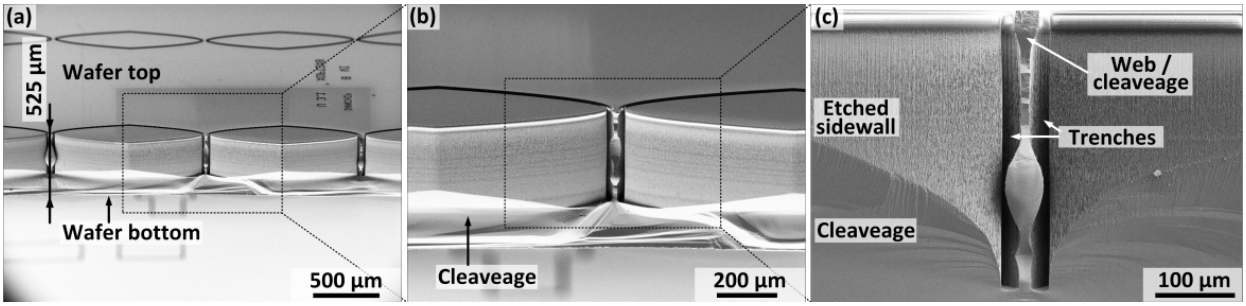

Figure 5.4. Scanning electron micrographs of cross-sections of lens structures realized on a 525 µm thick silicon wafer after DRIE to the target depth of 350 µm. The sacrificial material inside the lens cavities is visible. (a) Extended view of a section of an x-ray lens. (b) The structures have been cleaved along the optical axis of the lenses through the lens apexes. (c) Zoom-in of a frontal view of the cross-section at the apex of a lens illustrating the straightness of the etching. Note that the web material cleaved non-uniformly. The tilt angle to the wafer surface is 30° in (a) and (b).

5.4 Optical profilometry

Optical profilometry allows the roughness of surfaces and height profiles to be measured. Commercially available optical instruments may differ with respect to the specific technique for obtaining 3D data [438]. The mode of the instrument used throughout this thesis is imaging confocal microscopy [448]. Confocal microscopy illuminates the sample through the same objective as it images, i.e. it uses coaxial illumination. It relies on light being reflected from the sample surface and captured by the objective. As a consequence, the maximum detectable slope α_{max} of a surface to be measured is limited. Assuming a flat and optically smooth surface, it depends on the numerical aperture of the objective via $\alpha_{max} = \arcsin(\mathrm{NA})$. For an objective with NA = 0.90, α_{max} is 64°.[21] This theoretical value may improve in case of optically rough surfaces. It is further affected by the limited sensitivity of the CCD, the use of a signal threshold to avoid wrong data, and adjusting the light intensity to avoid saturation of the CCD over the whole scan range. An alternative technique called focus variation does not rely on coaxial

[21] As specified by our vendor the maximum detectable slope is 51°. Objectives with NA = 0.95 are available. However, respective working distances are only 200 µm, compared to 1 mm for NA = 0.90 objectives.

illumination and promises higher slopes to be measured [449]. Controlled tilting of the sample may be used to increase the maximum detectable slope [450].

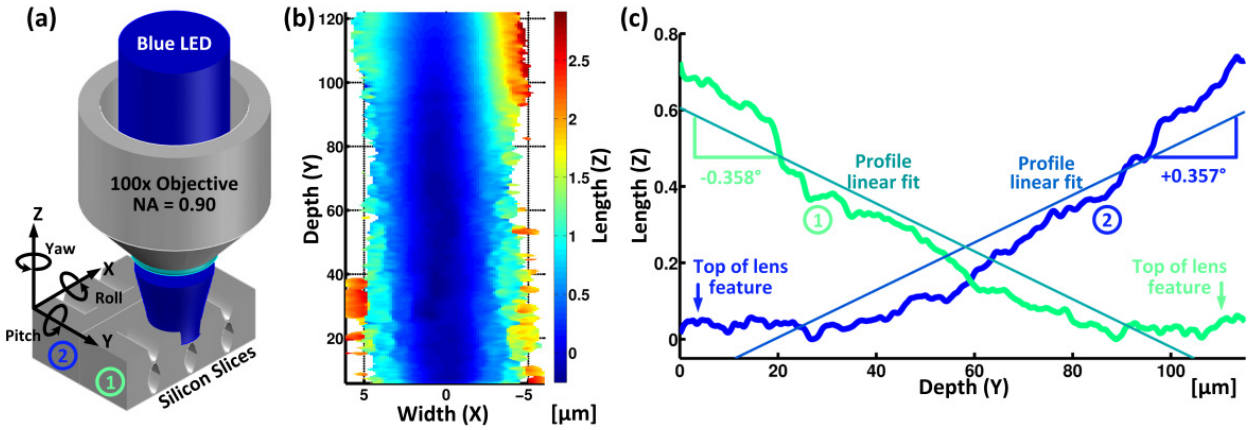

Figure 5.5. Optical profilometry for measuring sidewall slopes. (a) Conceptual drawing showing two slices of wafer cross sections aligned 'back-to-back' under the objective of an optical profiler. (b) Sidewall topography at the apex of a lens feature. The limitation of optical profilers regarding the maximum detectable sidewall slopes is visible. Above $X = \pm 4$ µm the number of void pixels increase and the surface appears increasingly corrugated. (c) Sidewall profiles at the very apex of the features compensated for sample rotation around the X-axes. Profiles measured on the two opposing features are symmetric to each other.

The limits of our instrument needed to be tested. Firstly, the cavities shown in Figure 3.22 have been measured. Therefore samples have been cleaved perpendicular to the optical axis (cf. Figure 5.1, cleavage for AFM). A PLu neox from Sensofar is used in confocal mode with light from a blue LED (460 nm) and equipped with a 100x magnification objective with NA = 0.90, a field of view (FOV) of 175 µm x 132 µm, a lateral resolution of 165 nm and a vertical resolution of 2 nm (as specified by the vendor). Special care must be paid to a proper alignment of the sample and data analysis. Rotation about the X-axis may controlled by mounting two wafer cross sections back-to-back in the microscope as shown in Figure 5.5(a). Given that the backsides of the wafer slices are flat, measured profiles of both samples must be symmetric relative to each other. Thus, the characterization procedure is as follows:

1. profiling of a cross section on one slice,
2. translating the sample stage in Y-direction only,
3. subsequent profiling of a cross section of the opposing slice,
4. analyzing the raw data and extracting the slopes ϕ_1 and ϕ_2 of both datasets, and
5. rotation of the raw data around the X-axis by half of the difference angle between both measured slopes $(\phi_1 + \phi_2)/2$.

After this compensation for misalignment, both profiles are symmetric and the sidewall slope of the attached sidewall is known (cf. Figure 5.5(b) and Figure 5.5(c)). The raw data from the instrument (plu-files) was converted into ASCII files using Gwyddion[22] and analyzed in a program written in MATLAB.

[22] http://gwyddion.net/ (Dec 2015).

The maximum detectable slope is ~35°. Above this slope the data has void or invalid pixels (cf. Figure 5.5(b)). The height is limited to ~3 µm, which is not enough to reliably determine the parabolic shape and the respective radius of curvature. Nevertheless, it is a reliable procedure to measure the sidewall angles of the apexes. The relatively small maximum slope is most probably due to the parabolic shape of our structures. In fact, higher slopes can be detected if the intensity of the illumination is increased. However, as the intensity is increased and light reflected from steeper regions is indeed detected, the detector is over-saturated at the very apex of the structure rendering the dataset invalid. Thus in principle, the maximum detectable slope may be higher, however not at the same time as features with considerably lower slopes coexist. Unfortunately, specifying an illumination gradient does not improve the analysis.

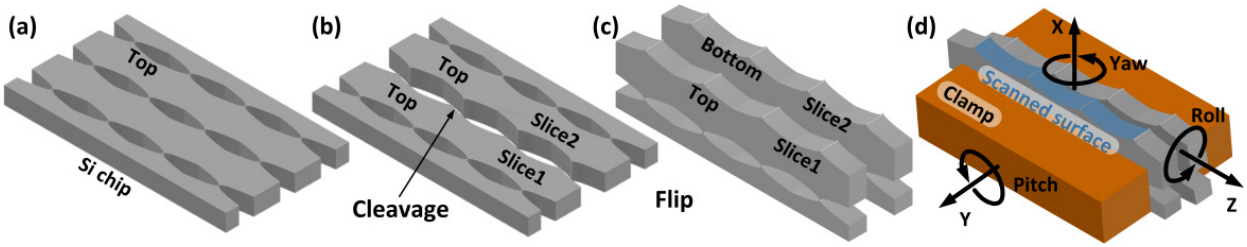

Figure 5.6. Procedure to analyze CRL sidewall cleaved along the optical axis. (a) CRLs. (b) Cleavage of CRLs. (c) Position of halves back-to-back. (d) Clamping of samples and axis assignments.

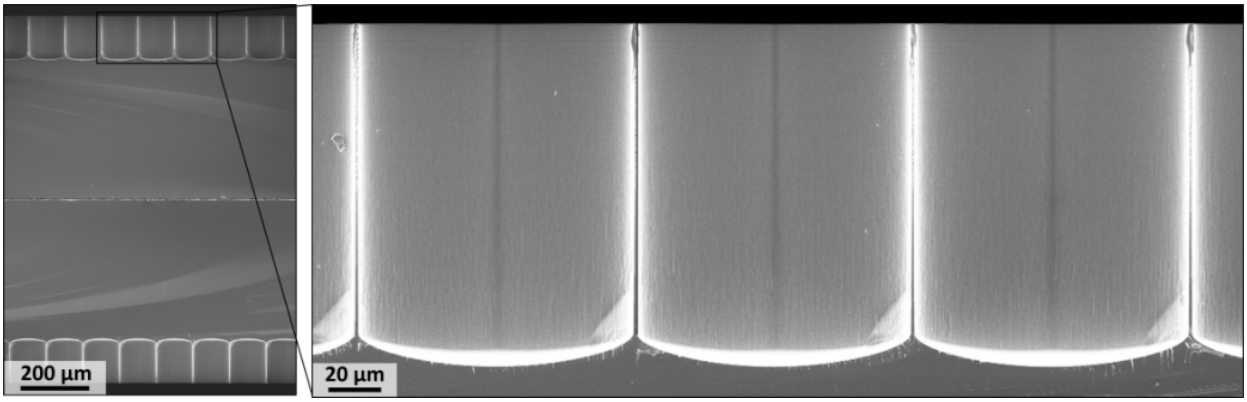

Figure 5.7. Scanning electron micrographs of cross-sections of CRLs on a 525 µm thick silicon wafer cleaved along their optical axis and positioned back to back.

Secondly, the same procedure was used to characterize the sidewalls of CRLs cleaved along their optical axis (cf. Figure 5.1, cleavage for OP; Figure 5.6 and Figure 5.7). Multiple profilometric measurements may be stitched together as shown in Figure 5.8, where 9 scans with 20% area overlap result in a total FOV = 0.13 × 1 mm. The total measurement time was ~10 min. It allows inhomogeneities between lenslets to be detected and the sample to be aligned around the *Y*-axis. Figure 5.8 shows the surface profile of a single lenslet. Most notably the surface is generally negatively tapered, whereas we have seen above that the apex is positively tapered (cf. Figure 5.5). This is evidence for varying etching conditions within one and the same feature and it emphasizes the need for DRIE facilitated by sacrificial structures (cf. Chapter 4).

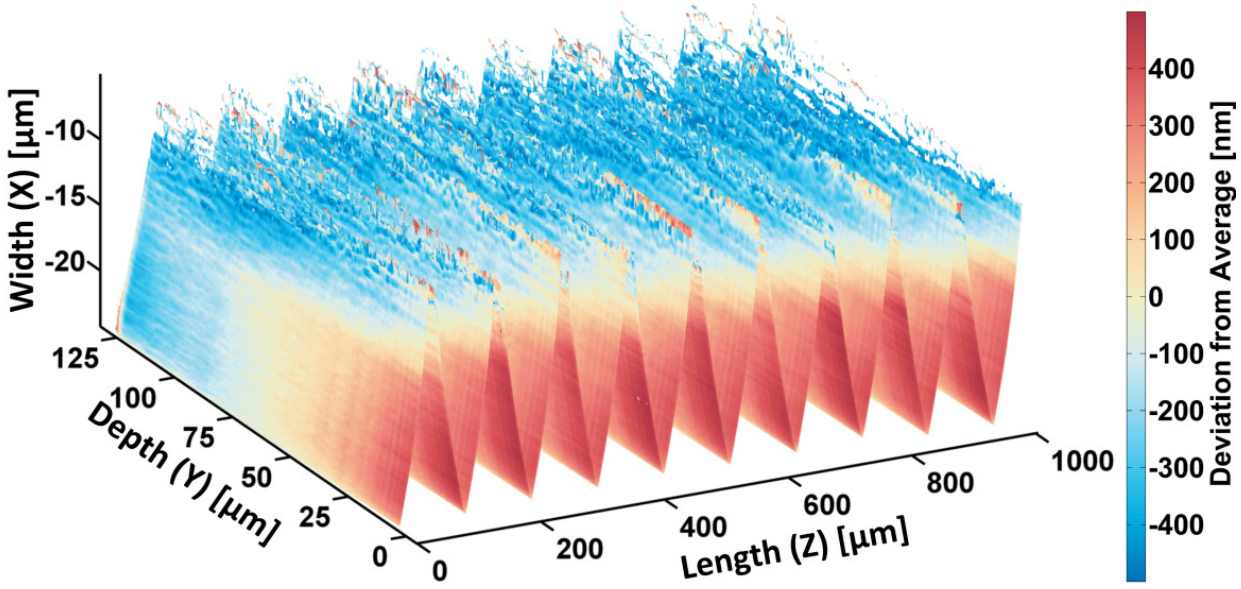

Figure 5.8. Surface map obtained by OP of the sidewall of a single lenslet cleaved along its optical axis as indicated in Figure 5.1. A 100x magnification objective with NA = 0.9 was used in confocal mode. The pixel size is 166 nm x 166 nm and the step size of the piezo scanner is 200 nm. 9 scans were stitched together with an overlap of 20%. The color code corresponds to the deviation of a single profile (elongating in Z-direction) from the top profile at Y =0 µm.

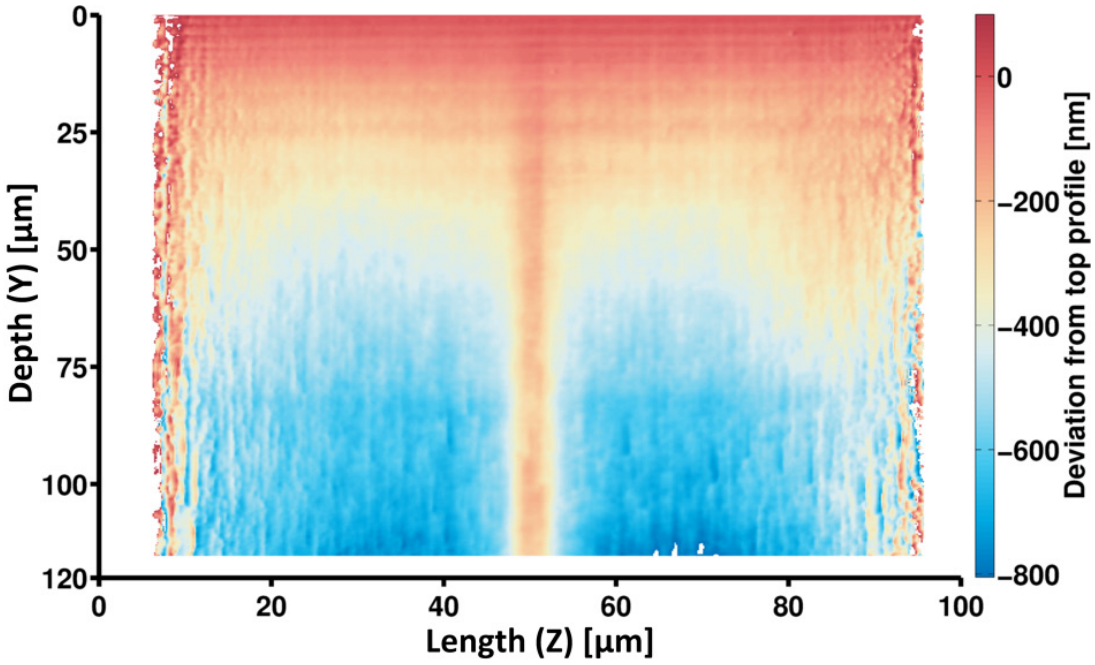

Figure 5.9. Surface map obtained by OP of the sidewall of a single lenslet cleaved along its optical axis as indicated in Figure 5.1. A 100x magnification objective with NA = 0.9 was used in confocal mode. The pixel size is 166 nm x 166 nm and the step size of the piezo scanner is 200 nm. The color code corresponds to the deviation of a single profile (elongating in Z-direction) from the top profile at Y =0 µm. In general, this region of the lens has a negative slope, in particular the lens profile widens along the depth. The seemingly straight section at the widest point of the lens at Z = 52 µm is maybe a measurement artefact, but is not of further importance for the characterization of the lenses. At the outer regions, i.e. at Z < 10 µm and Z > 95 µm, where the sidewalls approach the maximum detectable slope, the obtained profiles get corrugated.

5.5 Atomic force microscopy & replica molding

AFM allows 3D imaging with nanometric resolution and is well suited for measuring surface roughness. Nowadays, AFMs are commercially available with scan fields of e.g. 100 × 100 µm^2 and height ranges exceeding 10 µm, making them promising tools for tasks beyond nano-scale measurements such as more traditional profiling. AFM relies on probes being in close contact with the specimen. Cavities, undercuts, bottoms of trenches or holes, and sloped or vertical sidewalls, and structures with high-aspect ratios pose special challenges to AFM. Some variations to traditional AFM exist: Custom-made probes enabled the characterization of sidewalls of high-aspect ratio micro-structures [451,452]. Oscillation and servo control of flared probes in both the lateral and vertical direction allowed true 3D metrology of nanostructures [453,454]. Tilting the sample stage [455,456] or rotating the scanner head [457] allowed probes to scan sidewalls effectively. Clearly, the finite widths of commercially available AFM cantilevers and the limited lengths of their tips compromise the scanning of deep and shallow cavities (cf. Figure 5.10(a)). Protrusions, on the other hand, do not pose such difficulties. By polymer casting an inverted replica of a given specimen, indentations are turned into protrusions. Thus, replication molding for the sake of characterizing the master is an effective strategy whenever a challenging specimen is at hand [458–460].

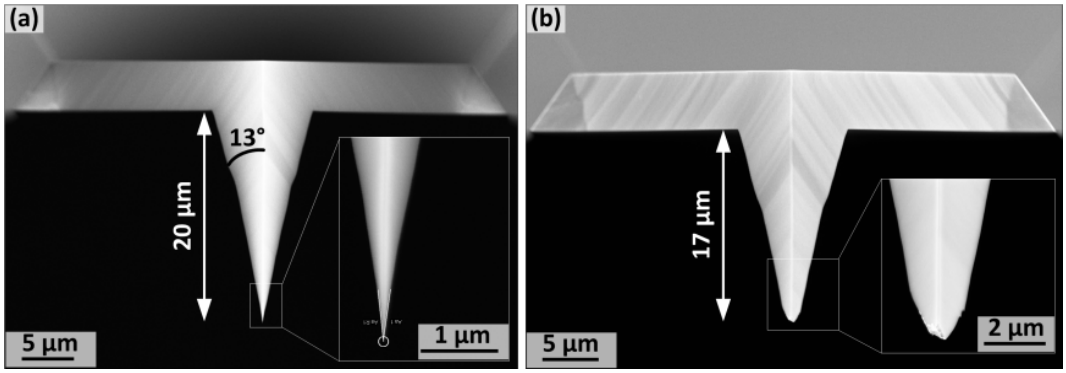

Figure 5.10. SEMs of AFM tips fresh out of the box. (a) Sharp flawless tip. (b) Defect tip.

The small radii of curvature of lens cavities make their characterization difficult. SEM and optical microscopy allows 2D information of the sidewalls and the top shapes to be obtained (cf. Chapter 5.2 and Chapter 5.3), while optical profilometry allows the steepness of sidewalls to be measured (cf. Chapter 5.4). The apexes of lenslets of CRLs are very critical parts. X-ray transmission is highest through these on-axis regions (cf. Figure 2.7). An efficient focusing necessitates these regions to be parabolic and uniform along their height (cf. Chapter 2.4). A reliable technique to characterize the 3D shape of apexes must therefore be found. In this thesis work a procedure based on replica molding and large-range atomic force microscopy was developed and published [148].

5.5.1 Sample preparation

To obtain inverted replicas of cross sections of etched cavities, finished processed wafers were manually cleaved perpendicular to the axis of the lens arrays into slices of ~1 cm widths (XOPTIX4, c.f. Figure 3.22 and Figure 5.11). These slices were stacked and fixed with a

purpose-made clamp (cf. Figure 5.12(a)). To facilitate release of the polymer cast, the surface of this unit of stacked and clamped slices was functionalized with a self-assembled monolayer of perfluorodecyltrichlorosilane (FDTS) using molecular vapor deposition (MVD).[23]

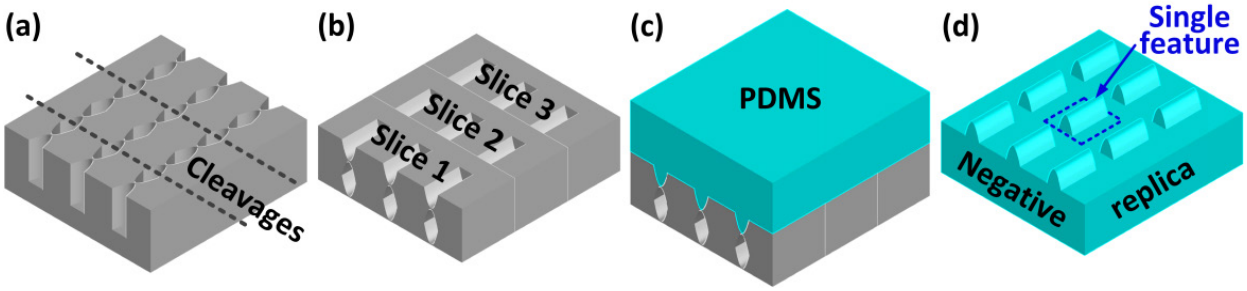

Figure 5.11. Negative replica molding of cross sections. (a) Wafers were cleaved into slices of ~1 cm width. (b) Stacking of the slices and tight clamping to obtain a mold. (c) Casting the cross sections with PDMS. (d) Release of the thermally cured PDMS.

Polydimethylsiloxane (PDMS) was used as a cast material. PDMS is known for its unique flow properties in its uncured state and its low elastic modulus in its cured state, and is widely used in soft-lithography of e.g. microfluidic circuits [461,462]. We combined ~50 grams of monomer and hardener from our PDMS kit (Sylgard 184, Dow Corning) in a weight ratio of 10:1 and manually mixed it with a spatula for 10 min. The mass was degassed in a desiccator evacuated to 2×10^{-3} mbar until air bubbles were removed [463]. The outgassed mixture was poured into the prepared mold, and again degassed at 2×10^{-3} mbar. After 30 min of degassing, we removed the casted mold from the desiccator and cured the PDMS in an oven at 60°C and atmospheric pressure for 6 hours. The cured and cooled PDMS (room temperature) was released from the mold, ready to be characterized (cf. Figure 5.12(b)). Figure 5.13 shows the cross section of a Si lens cavity and its inverted replica in PDMS.

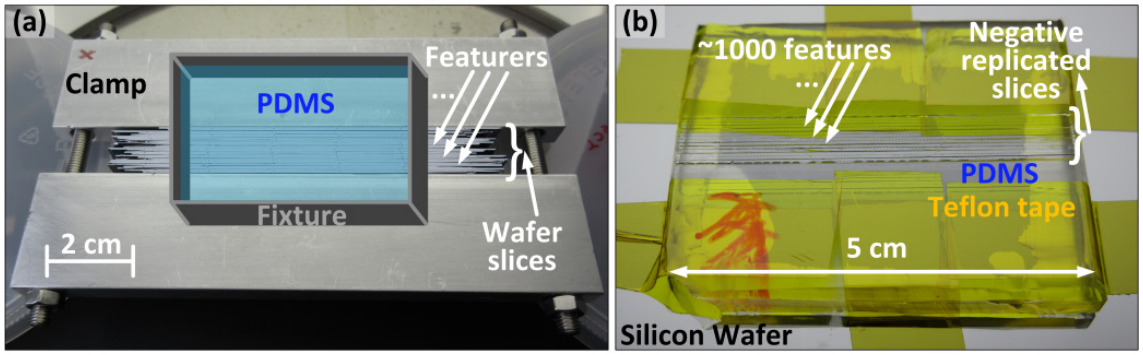

Figure 5.12. Photographs of a mold and a cast of wafer cross sections. (a) Mold comprised of stacked and clamped slices of finished processed x-ray lens wafers. A schematics of a fixture needed to cast PDMS is inserted. (b) A cured PDMS cast, which is fixed to a silicon wafer with Teflon tape and which is ready to be measured with an AFM.

To confirm the AFM linearity and calibration, reference structures comprising silicon V-grooves were fabricated by anisotropic etching of (100)-oriented silicon wafers using aqueous potassium

[23] Applying this FDTS is essential for a successful release. Its abstinence results in failure.

hydroxide (KOH). A silicon nitride layer deposited on a silicon wafer by LPCVD was patterned by standard UV-lithography and reactive ion etching (cf. Chapter 3.3. and Chapter 3.4). The patterned wafers were etched in aqueous KOH at 80°C until the {111} crystal planes had met and essentially stopped further etching. The silicon nitride mask was subsequently removed in phosphoric acid at 180°C, resulting in V-grooves of 160 µm lengths, 15 µm widths and 11 µm depths. Inverted PDMS replicas of fabricated silicon V-grooves were obtained in the same way as DRIE cross sections, although mold preparation was limited to placing patterned wafers in a dish formed of aluminum foil.

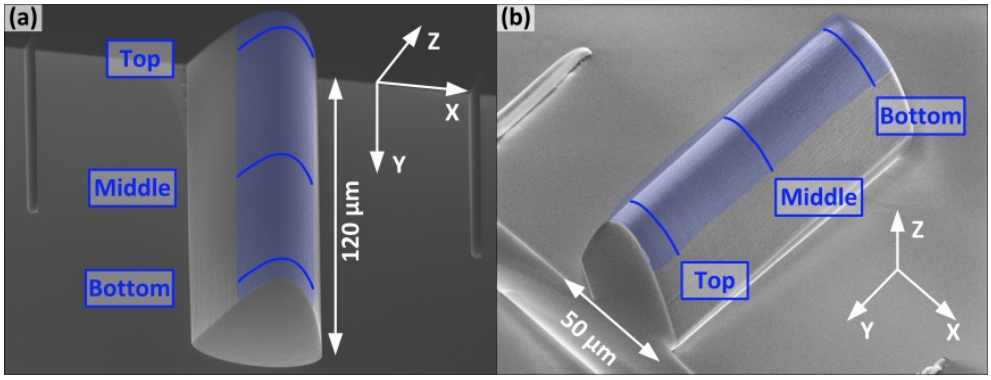

Figure 5.13. Scanning electron micrographs. The view tilt angles are all 30°. (a) A cross section of a silicon cavity equivalent to one half of an x-ray lens element. (b) An inverted replica in PDMS. The area of interest and single profiles scanned with AFM are highlighted.

5.5.2 Characterization procedure

Cross-sections of fabricated silicon x-ray lenses and inverted replicas were inspected with atomic force microscopy (AFM). We used a closed-loop AFM (NX20, Park Systems) where the scanning tip is mounted on a separate *Z*-flexure stage and thus decoupled from the horizontal scanners to avoid any image bow from crosstalk. It has *X*- and *Y*-scan-ranges of 100 µm, and a *Z*-range of 15 µm. All AFM measurements were carried out in intermittent contact mode. The linear scaling of the *Z*-axis is based on a silicon V-groove, i.e. the angle between the {111} crystal planes. The influence of small nonlinearities was corrected by applying correction parameters calculated from images of high quality step heights and gratings.

Figure 5.14 shows a conceptual drawing of the AFM probe scanning an inverted replicated lens feature. Since the radius of curvature of the features needs to be determined, *X* is taken as the fast scan direction and *Y* as the slow scan direction. 10-100 individual profiles separated equally along the full *Y*-range of 100 µm were sufficient to obtain relevant 3D information. Each profile could be fit to a parabola from which the average radius of curvature could be extracted and plotted over *Y*. To avoid tip-sample convolution, AFM probes with sharp and long tips were chosen (ATEC-NC, Nanosensors^{TM}) and fast scanning axis was set perpendicular to the probe's cantilever axis. At the beginning of every measurement, the tip was centered at the very apex of a feature. The scan range in *X* was increased and the *Z* scanner position readjusted, until the measurement volume was maximized. A typical scan rate was 0.1 Hz (fast scan direction).

The quality of AFM measurements heavily relies on the scan settings (skills of the operator) and the probes. Figure 5.10(a) shows a sharp AFM tip and Figure 5.10(b) shows a defect tip; both

probes were fresh out of the box. No reliable statistics was made, but >20% of delivered tips of this specific type (ATEC) may be defective. Therefore cautions must be paid during measurements and in case of doubt measurements need to be repeated with different tips.

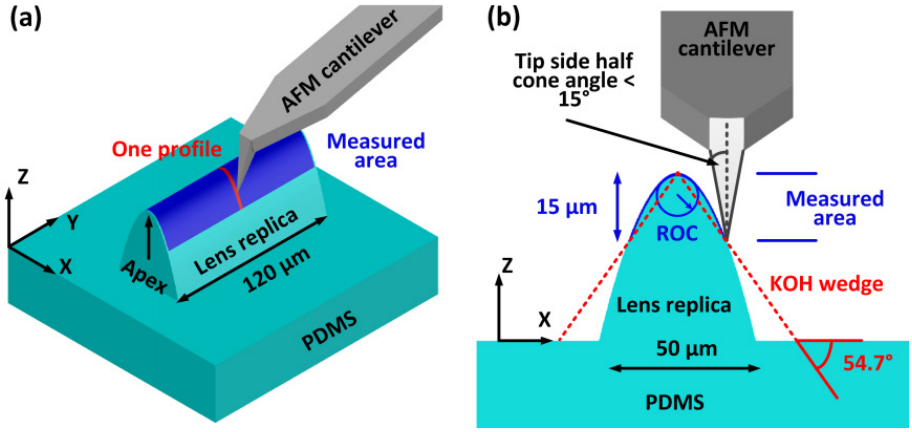

Figure 5.14. Concept of AFM profiling. (a) 3D view of one of the casted lens cross sections and axis assignment. (b) Front view of one of the casted lens cross sections with approached AFM tip. The AFM tip and the PDMS feature are to the same scale. The geometry of an inverted KOH etched silicon V-groove is superposed and indicated by the dotted red lines.

AFM was also used to measure the surface texture of the features. In this case, the field of view was restricted to 10 µm (*X*) × 10 µm (*Y*) and the tip was placed at the very apex of the structures. Since the texture is strongly characterized by scallops elongated along the *Y*-axis as a consequence of the Bosch process used during silicon etching, the *Y*-axis was chosen as the fast scanning axis and 256 profiles were taken in the *X*-direction. A typical scan rate for these measurements was 0.5 Hz (fast scan direction).

The raw data was analyzed in a MATLAB program which included the application of the calibration factors, data levelling, i.e. data rotation around the *X*-, *Y*- and *Z*-axes by specified angles, curve fitting and plotting. Despite careful alignment of the samples in the microscopes, data rotation is necessary to obtain nice and symmetric surface plots, but is limited to angles smaller than 1°, which leaves the individual profiles as the basis for curve fitting unaffected.

5.5.3 Results

Silicon V-groove and inverted replica

A V-groove etched into a (100)-oriented silicon wafer is a good representation of the apex of a lens feature (Figure 5.14(b) and Figure 5.15). Its shape is known a priori, since it is defined by {111} crystal planes, which are flat and nominally have a relative angle of 70.6°. The silicon groove and its inverted replica in PDMS were scanned with the AFM taking 20 profiles along 100 µm and calculating their average. Figure 5.15(b) includes the height difference between the averaged profiles of the replica and its master, which does not exceed ±200 nm over the full scan volume. Since the height difference is symmetric about the *Z*-axis it may be partially caused by slight relative misalignment of the grooves in the microscope. Also, the sidewalls of both the silicon master and the PDMS replica were flat to within 50 nm, thereby confirming the linearity of the scanners. Individual profiles taken over the full horizontal range of 100 µm show

consistency for both the silicon master and the PDMS inverted replica: The relative angles of sidewall profiles of the master and the inverted replica were measured to 70.6 ± 0.15° and 70.8 ± 0.15°, respectively.

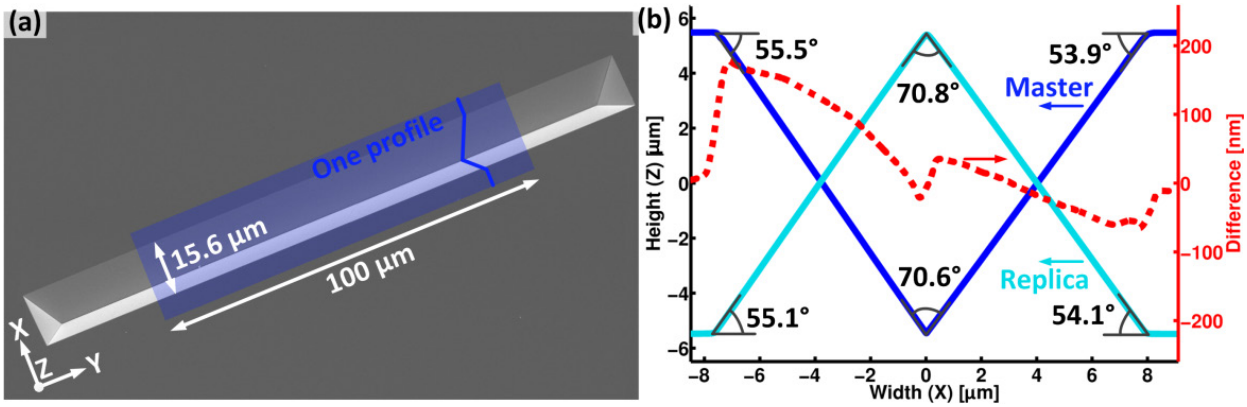

Figure 5.15:. Confirming the AFM linearity. (a) Scanning electron micrograph of a KOH etched silicon V-groove defined by the {111} crystal planes. The AFM imaged region is highlighted and the view tilt angle is 20°. (b) AFM scans of a silicon groove (master) and a PDMS inverted replica of the same feature. Averages of 20 profiles along the *X*-direction every 5 µm in the *Y*-direction for the silicon master and PDMS replica, respectively, are shown. The dotted red curve is the corresponding height difference, referring to the scale to the right.

X-ray lenses and inverted replicas

The 3D shapes of the silicon cavity and its PDMS inverted replica from Figure 5.13 were measured. As an example, a surface plot obtained from scanning a PDMS feature is shown in Figure 5.16(a). The surface plot is symmetric about the *Y*-axis, which is an indication of the high quality of the scan. The color code of the surface plot corresponds to the deviation of a single profile (elongating in *X*-direction) from the profile at the very top of the lens. The deviation spans -600 nm to +600 nm, which corresponds to sidewall slopes of ±0.4°.

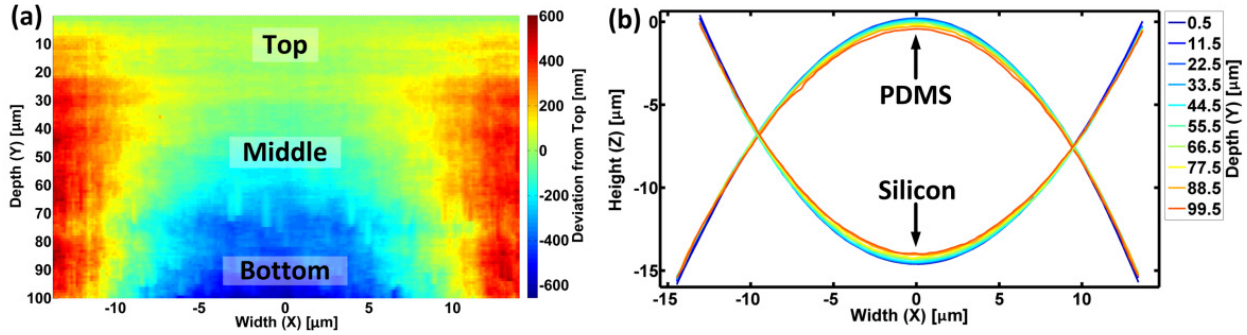

Figure 5.16. AFM data from scans of PDMS and silicon features. (a) Surface plot of data obtained of one PDMS feature by scanning 100 profiles along its *X*-direction, 100 µm in its *Y*-direction. The color code represents the difference from the topmost profile. (b) Some individual profiles measured on the silicon master and the PDMS replica, respectively.

The very apex of the PDMS feature ($X = 0$ µm) has a positive taper, whereas at $X \approx \pm 7$ µm the surface slope becomes negative. This characteristic is a consequence of the well-known

phenomenon of aspect ratio dependent etching (cf. Chapter 5.4). Striations can be identified at the bottom of the feature and a more detailed scan will be discussed later.

Figure 5.17(b) shows some individual height profiles of the PDMS feature, where profiles obtained from scanning a silicon feature are also included for qualitative comparison. Every single profile is subject to a fit to $z(x) = \pm x^2/2R$, where the fitting parameter is R. This allows plotting of R over the feature depth. R linearly increases from ~6 µm at the feature's top to ~6.6 µm at its bottom (cf. Figure 5.17). This variation was observed on two independent PDMS replicas and on the silicon master.

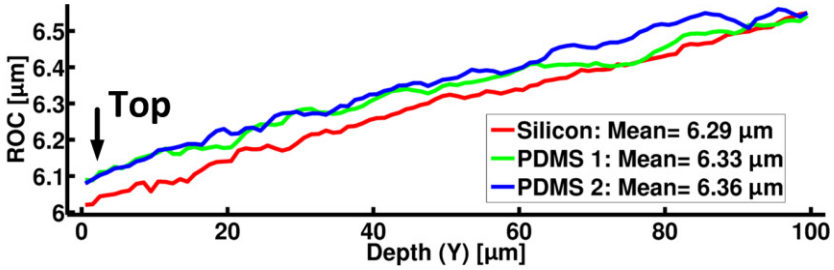

Figure 5.17. Fitting of the individual scanned profiles yields the variation of the radii of curvature over the depth of the lens features. Results for one silicon feature and two independent PDMS replicas are shown.

Reliability and reproducibility

Multiple measurements on one silicon sample (master) and two independently manufactured PDMS samples (inverted replicas) were performed to verify the reliability and reproducibility of the characterization procedure and to determine its accuracy. Both PDMS samples comprise a multitude of inverted replicas of individual lens cross sections (cf. Figure 5.18(a)). Each sample was scanned with a new AFM tip. Features on the PDMS sample were divided into sets, indicating that they have the same slice of silicon sample as the master. Every data set includes data obtained from different features and a minimum of 5 individual data points contribute to each data set. Each of these points corresponds to one cycle of approaching the tip, scanning, and lifting the tip. Each scan was performed with settings similar to those presented in Figure 5.16. The *Y*-range was always 100 µm, the *X*-range varied from 25-28 µm and at least 20 profiles were taken evenly spaced along the *Y*-direction.

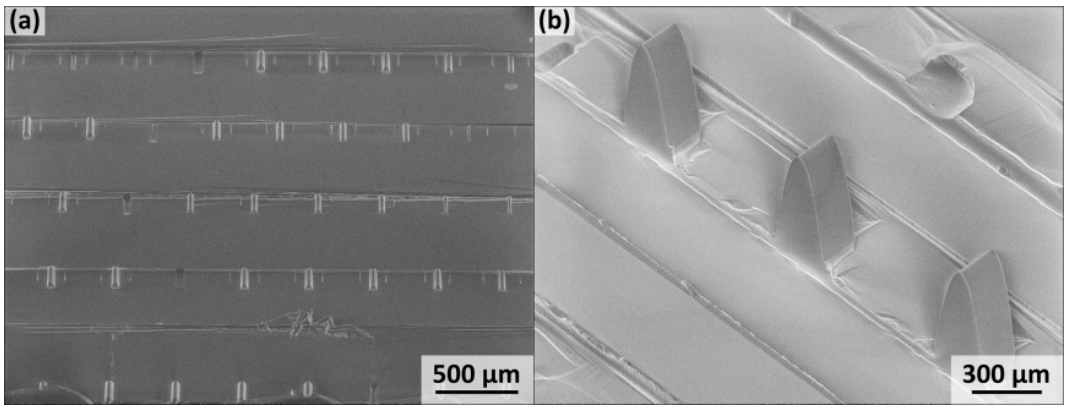

Figure 5.18. Overview of inverted features on PDMS samples. (a) XOPTIX4. (b) XOPTIX12.

In total 41 individual AFM measurements on 30 different cross sections or inverted replicas contribute to the statistics (cf. Figure 5.19). We particularly compare the mean R of the scan profiles, R of the topmost profile, and the range of R within one feature. Generally, the obtained values and the respective standard deviations from the silicon master and its inverted replicas agree well with each other. Based on measurements of the PDMS features $R = (6.32 \pm 0.06)$ µm. The topmost R is (6.05 ± 0.05) µm. All measurements show a linear increase of R from the top to the bottom of the features. The range of R is (0.52 ± 0.03) µm.

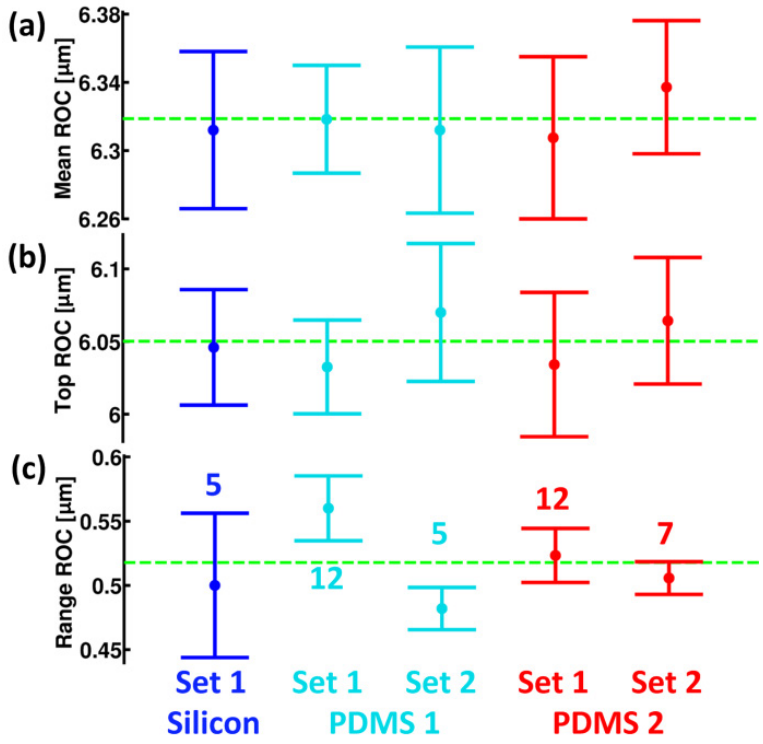

Figure 5.19. Statistics on evaluated AFM scans of one silicon and two PDMS samples. The numbers of individual data points contributing to each data set are noted. (a) Mean R over depth. (b) R of the profiles at the very top of the features. (c) The range between the smallest and largest R. The dashed green line corresponds to the mean of the data obtained from the PDMS samples only. The error bars indicate the standard errors on the mean.

Roughness measurements

Detailed AFM scans were performed at deeper parts of the lens features, since surface texture is more pronounced there (cf. Figure 5.16). Figure 5.20 shows typical AFM scans of a PDMS lens replica prior and after surface smoothing of respective Si cavities. The parabolic background in X and the linear background in Y were removed. Scallops and vertical striations are visible. Figure 5.21 shows the averages of 1D power spectral density functions (PSD) of individual AFM profiles scanned along the Y-axis, i.e. along the scallops. The distinct peaks at 2.3×10^{-3} nm^{-1} correspond to the periodicity of the scallops, which is ~430 nm. Integrating the PSD from 1×10^{-4} nm^{-1} to 1×10^{-1} nm^{-1} and taking the square root yields the RMS surface roughness. Before surface smoothing, the RMS roughness is 79 nm and 53 nm, measured on the master and the replica, respectively. After surface smoothing, the respective RMS values are 35 nm and 41 nm.

Although the accuracy for roughness measurements slightly decreases due to the replication procedure, trends of the surface quality can be clearly identified.

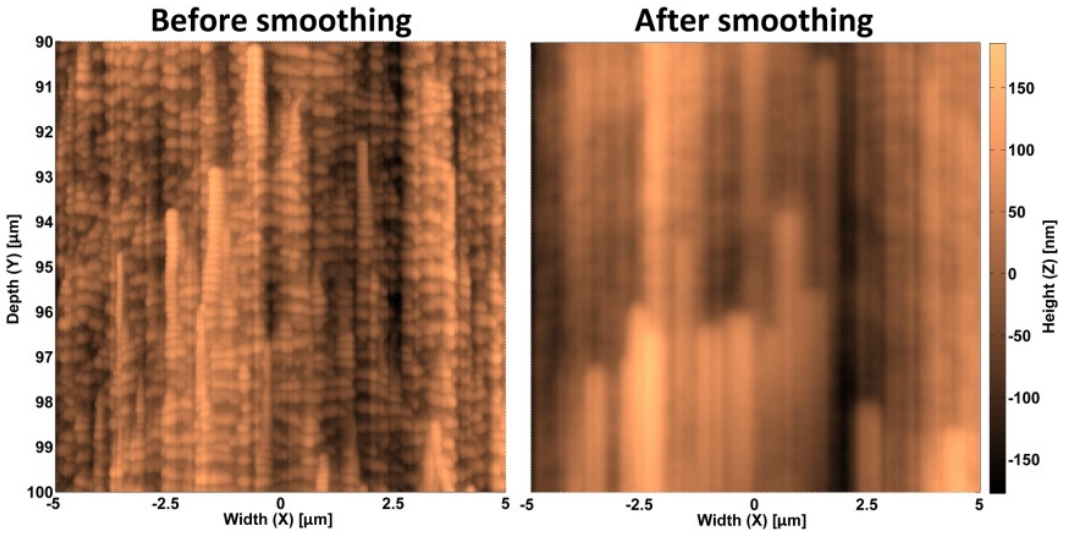

Figure 5.20. Detailed AFM scans at the very bottom of the apex of the PDMS replica of Si cavities before and after surface smoothing. The parabolic background was subtracted.

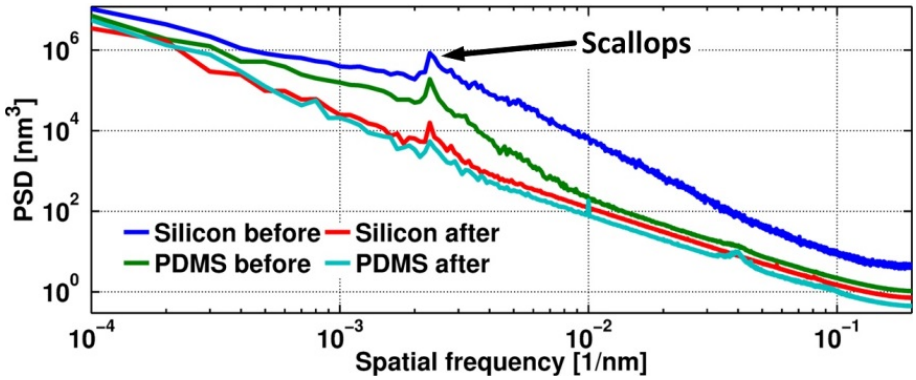

Figure 5.21. Averaged 1D power spectral density functions of individual scans for silicon lenses before and after surface smoothing, and the respective replicas in PDMS.

5.5.4 Discussion

The procedure presented here allows characterization of silicon x-ray lenses to an unprecedented accuracy. Casting in PDMS preserves the complex three-dimensional shapes of microstructures to a very high degree. In addition to measurements in the nanometer range, the use of a large-*Z*-range AFM allows one to measure absolute values of the radius of curvature with 1% accuracy. The uniformity of the features along the etch depth and nanometer sized surface defects can be readily determined. Statistical analysis of a large set of measurement data combined with the use of a KOH etched V-groove in (100)-oriented silicon as a reference structure proved the method to be reproducible and reliable. Shrinkage of the PDMS during thermal curing may explain the difference of 0.2° in the measured critical angles of the master and the replica [464]. Based on these measurements, atomic force microscopy combined with replica molding is well suited to measure the apexes of the lenslets. Such characterization tasks would benefit from a next generation of AFMs with an extended measurable volume, i.e. larger scan ranges.

The proposed replication procedure has several advantages. First, it circumvents the limitations of commercially available AFM tips when measuring shallow and deep cavities. Second, the full height range of the AFM can be utilized. Third, multiple features may be integrated into a single sample. Characterization tasks are then accelerated considerably since sample alignment needs to be performed only once. Forth, AFM tip wear is reduced when scanning a PDMS replica rather than its silicon master. If the silicon cross sections were scanned, tips break more easily compared to scanning PDMS samples. Sharp edges of the silicon features caused by the cleaving process favored tip fracture, yet such sharp edges do not exist in case of PDMS replicas. Worth mentioning, more common tactile profilers are not suitable tools, because their probes cannot penetrate the silicon cavities and deform the PDMS inverted replicas due to the stylus tracking force. Hence, AFM operated in intermittent contact mode was the preferred characterization tool to analyze the roughness, parabolic shape at the apex, and its uniformity.

5.6 Optical performance

X-ray lenses are primarily used to create small probe beams and for imaging. A lens can be characterized by its focal length, the optical efficiency, i.e. its transmission together with the lateral dimensions of the focus, the longitudinal size, i.e. the depth of focus DOF, and the achievable resolution given an imaging setup.

5.6.1 Knife edge scans

A variety of techniques have been developed to measure the spot sizes of focused x-ray beams [465]. A common method for characterizing hard x-ray beams from synchrotron sources is the performance of knife-edge scans. Therefore a sample with a sharp edge (hereafter referred to as knife) is moved through the beam perpendicular to the optical axis (either horizontally or vertically), while recording the transmitted intensity or the knife's fluorescence (cf. Figure 5.22). An absorbing sample must be optically thick to guarantee sufficient contrast between the attenuated and the direct beam (cf. Table 2.2), while a fluorescing sample must show sufficient fluorescence upon the incident x-ray energy. The response of an absorbing knife is convolved with the knife's shape and its thickness along the optical axis and a respective deconvolution may be necessary to obtain reliable results [466].

In this thesis 1D focusing lenses were characterized. In order to measure line foci, the knife needs to be carefully aligned with respect to the beam, especially with respect to rotations around to *Z*- and *Y*-axis (cf. Figure 5.22). Typical focal lengths were 0.2 – 1 m and the minimal DOF was 2 mm. Therefore a maximal 2 mm thick sample is required to measure the beam with sufficient longitudinal precision. Figure 5.23 shows a 1 × 1 mm^2 cleaved sample from a polished fused silica wafer. It provides sufficient absorption contrast for E = 17 keV x-rays, since the attenuation length μ^{-1} of SiO_2 is ~1 mm. However, it is not suitable for using it with E = 56 keV x-rays ($\mu^{-1} \approx 14$ mm). Sputter coating it with 50 nm copper and using it in fluorescence mode is therefore more appropriate (Cu $K\alpha_1$ ~8.05 keV).[24] Diffusion of Cu into silica needs to be considered and a thin titanium layer forming titanium oxide may be a viable alternative (Ti $K\alpha_1$ ~4.51 keV) [467,468]. Saturation of the fluorescence may also play a crucial role [469]. The

[24] X-Ray Data booklet http://xdb.lbl.gov/ (Dec 2015).

fluorescing signal from a thin layer directly yields beam profiles without the need for differentiation or data fits and full width at half maxima are readily obtained.

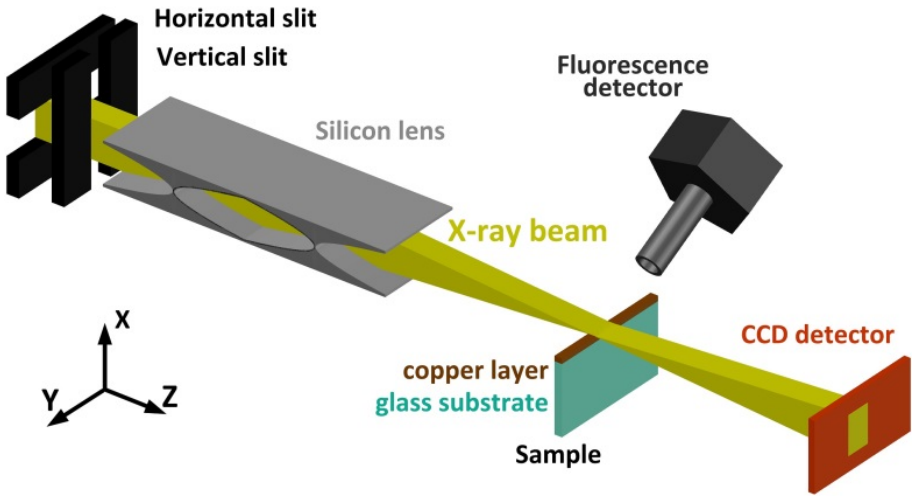

Figure 5.22. Conceptual drawing of the experimental setup for characterizing the performance of the lenses.

Knife scans are particularly useful in actual experiments, since subsequent to characterizing the beam, the knife at the lenses' focal positon may be simply replaced by a specimen of interest. It is a direct method without the need for sophisticated reconstruction algorithms and it allows relatively long line beams to be measured. If an absorbing sample in combination with a spatially resolved CCD camera is used, the uniformity of the line focus can readily be analyzed given the data from one scan only (cf. Chapter 6.4). In contrast, operating in fluorescence mode necessitates multiple scans for obtaining the same information (cf. Chapter 6.1). The method is limited by the flatness and sharpness of the knife, potential defects (cf. Figure 5.23), misalignments with respect to the beam, as well as the step sizes and accuracies of the scanning stages. Minimal spot sizes of 200 nm were expected during this thesis and spot sizes down to 250 nm could be reliably measured using knife scans. Fortunately, the experimental beam size is always larger than the intrinsic beam size. For characterizing beams smaller than 200 nm other methods must be used in the future.

Alternative to fluorescence or absorption, total external reflection at grazing incidence may be used, which occurs from the edge of the knife while it is scanned through the focus. Since this method does not rely on absorption, a thin knife may be used and no deconvolution is necessary. Using a CCD camera it was observed during this thesis that both signals may be recorded simultaneously, allowing mutual verification. Another very sensitive variation of the knife-edge method is measuring the diffracted beam, while scanning a thin micro-bridge structure with flat surface through the focus [61,470,471]. Suzuki et al. called this scanning in 'dark-field geometry' and proposed to block the direct beam with an aperture, while only recording the scattered portion [470].

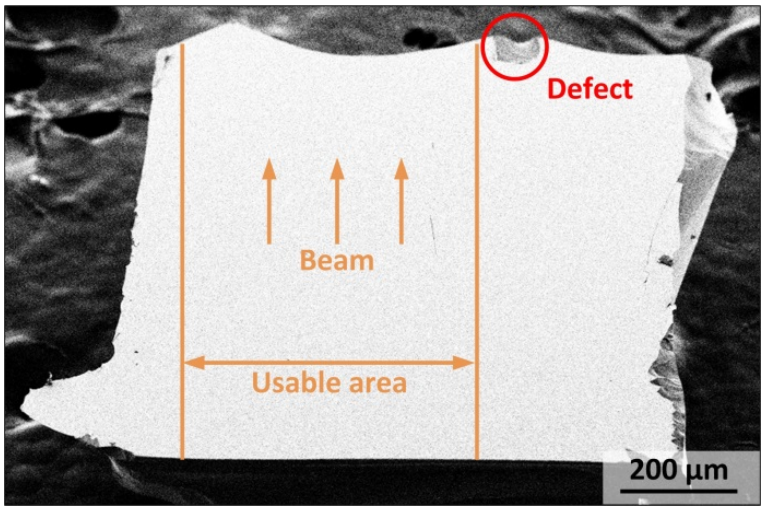

Figure 5.23. SEM image 1 × 1 mm^2 fused silica sample sputter coated with 50 nm copper.

5.6.2 Direct imaging

In the course of this thesis beams were also characterized by direct imaging. The x-ray beam transmitted through lenses may be visualized using luminescence from a YAG crystal (scintillator), which is then imaged onto a CCD by microscope optics. It can be used for initial lens alignment, determining focal positions by scanning the scintillator through the focus along the optical axis, and to record far-field images for detecting lens non-uniformities. At one of the beamlines where experiments have been performed a CRL composed of rotational parabolic beryllium lenslets was available, which was optionally used to magnify the focused x-ray beam and resolving fine details (cf. Chapter 6.3).

5.6.3 New developments

A very powerful method to characterize focused x-ray beams is ptychography. It was originally developed for lens-less coherent diffraction imaging [472–481]. Therefore, an arbitrary quasi-2D object with sufficient details (e.g. a Siemens star) is positioned in some plane perpendicular to the optical axis, either in or near the focus, and raster-scanned with considerable overlapping illuminations, while recording far-field diffraction patters. Using iterative algorithms, the phase of the diffraction patterns may be retrieved, which allows the complex illumination and object functions to be recovered. The full caustic of the x-ray beam between optic and the detector may be reconstructed and its focal sizes extracted [115,144,475,482–487]. A variation of this method, which requires a priori knowledge of the object has been reported [469,488]. These methods are particularly attractive to characterize probe beams with spots below 1 × 1 µm^2 and to determine aberrations due to the lenses or upstream components of the beamline. In particular for spots below 100 nm ptychography is regarded as the most reliable characterization method. Whether it is also suitable to characterize 0.1 × 500 µm^2 line beams remains unknown at the end of this thesis. It is anticipated that the complexity of the measurement scales with the size of the beam to be characterized. Worth mentioning, measuring ablation imprints is another common method and was recently used for characterizing focused soft x-ray beams from a free-electron laser [489–491].

5.6.4 Imaging resolution

During this thesis an x-ray imaging objective was tested. For characterizing spatial resolutions in full-field microscopes it is practical to image well known test patterns and to determine the dimensions of the smallest resolved features. A Siemens star pattern[25] is commonly used, which typically contains features down to 50 nm [269]. Alternatively, a sharp absorbing edge may be imaged and the width of the transition region determined [182]. Imaging meshes allows spherical aberration to be detected [224]. A more thorough and quantitative approach is to calculate the modulation transfer function (MTF) from experimental data obtained by e.g. imaging a grating and extracting the cutoff frequency [492].

5.6.5 Beamlines

The optical performances of lenses produced within this thesis have been assessed at two beamlines both located at the European Synchrotron Radiation Facility (ESRF). Next to the Advanced Photon Source (APS) at the Argonne National Laboratory in the USA, PETRA III at DESY in Germany and SPring-8 at RIKEN in Japan, it is currently one of the most powerful third-generation x-ray sources worldwide. Its storage ring has a circumference of 844 m and it stores 6 GeV electrons with a maximum beam current 200 mA. It hosts 40 beam lines, some of which are dedicated to imaging with hard x-rays up to 140 keV.

ID11

ID11 is a materials science beamline, which is dedicated to perform simultaneous hierarchical characterizations, both in direct and reciprocal space, from the micro- to the nanometer scale using techniques such as three dimensional x-ray diffraction or diffraction contrast tomography [493]. It has 3 experimental stations, of which the third starts 93 m away from the x-ray source, thus allowing very high optical defocusing ratios. X-rays are generated by an in-vacuum undulator and the source size is specified as 57 × 10 μm^2 (H × V, FWHM) with a source divergence of 88 × 5 μrad^2 (H × V, FWHM).[26] A monochromatic beam may be selected by a horizontal bent Laue-Laue Si(111) monochromator with an energy band width of $\Delta E/E \sim 10^{-3}$. At a distance of 91.5 m away from the synchrotron source, the beam is typically spatially limited by horizontal and vertical slits. For our experiments presented in Chapter 6.1 the silicon lens was mounted 0.5 m downstream the slits on a stage with five degrees of freedom and oriented for vertical focusing. For spot size measurements, a sample positioned on a piezo stage (Physik Instrumente, P-561) was scanned vertically (along X) through the focused x-ray beam (cf. Figure 5.22). The sample was a 1 x 1 mm^2 piece of a 500 µm thick fused silica wafer sputter coated with a 50 nm copper layer (cf. Figure 5.23). An energy dispersive x-ray detector (SGX Sensortech, SiriusSD) was used to detect fluorescence from the copper. A camera equipped with a cerium-doped YAG scintillating crystal coupled to a CCD detector (Basler, acA1300-30gm) was positioned 1.6 m downstream from the sample and used to record images of the x-ray source.

[25] Commercially available: http://www.ntt-at.com/product/x-ray_chart/ (Dec 2015).
[26] Cf. http://www.esrf.eu/UsersAndScience/Experiments/StructMaterials/ID11/ID11Source (Dec 2015).

ID06

ID06 is officially a beamline dedicated for instrumentation and machine tests. It has two experimental hutches, whereas the second hosts a large volume press. The first hutch is currently refurbished and will host a diffraction based transmission x-ray microscope, d-TXM, for non-destructive structural characterization of polycrystalline materials.[27] The x-ray beam is provided by an undulator source, which is specified by 415 × 10.3 μm^2 (H × V, FWHM) with a source divergence of 10.3 × 2.9 μrad^2 (H × V, FWHM). A monochromatic beam may be selected by Si(111) double crystal monochromator with an energy band width of $\Delta E/E \sim 1.4 \times 10^{-4}$. At a distance of 55 m away from the source, the beam was typically spatially limited by horizontal and vertical slits. Condenser lenses were typically mounted ~0.5 m downstream the slits for vertical focusing (cf. Chapter 6.3 and Chapter 6.4). For characterizing the focused beam, a scintillator screen coupled to a FReLoN CCD camera by microscope optics with an effective spatial resolution of 1.4 µm was used (near-field detector) [494,495]. Alternatively, a 10 µm thick LAG:Eu scintillator fitted by a 10x microscope objective to a Sensicam QE (PCO) equipped with a CCD with 6.45 × 6.45 μm^2 pixel size may be used. Knife-edge scans in absorption mode were performed using a thin glass sample. For imaging the focused x-ray beam 71 beryllium lenslets with R = 50 µm were available. Magnified x-ray images were recorded 5 m downstream using a scintillator screen coupled to another FReLoN CCD camera (far-field detector). Optionally, the monochromatized beam may be pre-focused using a transfocator equipped with beryllium lenslets.

5.7 Summary

Optical microscopy and atomic force microscopy with the support of replica molding have been identified as essential methods to characterize the 3D shapes of microfabricated silicon CRLs with sufficient accuracy. Respective procedures for sample preparation and data analysis have been presented. Only the top dimensional shape can be characterized in a non-destructive way. For obtaining essential over-depth information samples need to be cleaved. Replica molding in PDMS is very reliable and allows radii of curvature to be measured with an accuracy of 1%. It has been found that variable etching conditions indeed are present within one and the same cavity, which stresses the demand for advanced DRIE facilitated by sacrificial structures. ID11 and ID06 are two high-energy beamlines at the European Synchrotron Radiation Facility, which are dedicated to 3D micro-structural analysis of thick samples. Both may benefit from improved x-ray optics. The spot sizes expected in this thesis can readily be characterized using absorption and fluorescence knife-edge scanning. However, future versions of the developed lenses may require more sophisticated means such as ptychography.

[27] Cf. https://erc.europa.eu/diffraction-based-transmission-x-ray-microscopy (Dec 2015).

6 Results and discussion

The manufactures of four different x-ray lens systems are presented. This includes a thorough characterization of their 3D shapes according to the procedures outlined in Chapter 5. The optical performances of all systems were tested using hard synchrotron radiation ($E \geq 17$ keV) and the results are presented. To facilitate sidewall profile control, while increasing the lens heights (i.e. the etch depths), sacrificial structures have been used according to Strategy A and Strategy B introduced in Chapter 4. The first lens system utilizing Strategy A comprises silicon lenslets with radii of curvature $R = 20$ µm and heights of 350 µm. A 310 µm wide line-focus with a waist of 980 nm was demonstrated with 56 keV x-rays. The second lens system utilizing Strategy A comprises two silicon 1D-focusing lenses, which have been interdigitated to mimic rotationally parabolic lenslets. It was used to demonstrate x-ray bright-field imaging of a test sample with a spatial resolution of ~280 nm at 17 keV. The third lens system utilized Strategy B to obtain silicon masters, which were inverted by electroplating to obtain nickel inserts for a polymer injection molding machine. Lens chips made of polyethylene were produced with a rate of 10 chips per hour. A 55 µm long line focus with a minimal waist of 770 nm (FWHM) and a total lens transmittance of 32% was measured at 17 keV. The fourth lens system utilizing Strategy B comprises silicon kinoform lenslets with structure heights of 200 µm. A 180 µm long line beam with a waist of 430 nm (FWHM) was measured at 17 keV. Generally, x-ray lenses with close to vertical and straight sidewalls were achieved. Defects identified by characterizing the lens shapes are in agreement with their optical performance, facilitating future improvements in the manufacture.

6.1 Strategy A: Deep 1D Si lenses

Line-focusing silicon compound refractive lenses (Si-CRLs) with structure heights exceeding 300 µm were fabricated according to the manufacturing strategy outlined in Chapter 4.2. Respective results were published [149].

Briefly, profile uniformity over the full height was ensured by defining the perimeter of the structures by trenches of constant width. The remaining sacrificial material inside the lens cavities was removed by etching through the silicon wafer. Since the wafers become fragile after through-etching, they were then adhesively bonded to a carrier wafer. Individual chips were separated using laser micro machining and the three dimensional shape of fabricated lenses was thoroughly characterized by a variety of means (cf. Chapter 5). Optical testing using synchrotron radiation with a photon energy of 56 keV yielded a 300 µm wide beam with a waist of 980 nm at a focal length of 1.3 m. Optical aberrations are discussed in the context of the shape analysis, where a slight bowing of the lens sidewalls and an insufficiently uniform apex region are identified as resolution-limiting factors. Despite these, the proposed fabrication route proved a

viable approach for producing x-ray lenses with large structure heights and provides the means to improve the resolution and capabilities of modern x-ray techniques such as x-ray microscopy and three-dimensional x-ray diffraction.

6.1.1 Microfabrication

The wafer design and the process flow were discussed in Chapter 4.2. The wafer comprises 1000 bi-parabolic cavities with nominal dimensions: radius of curvature R = 20 µm, geometrical aperture $2R_0$ = 300 µm, cavity length T = 1.1 mm and web thickness T_0 = 10 µm (Figure 2.5). All structures on the wafer were defined by 20 µm wide trenches and through-wafer etching released the sacrificial portions (SPs). Figure 6.1 shows a through-etched 350 µm thick silicon wafer, which demonstrates the reliability of the SP removal. Typically, ~95 % of SPs release during HF-etching the backside SiO_2 after DRIE. The remaining ~5% SPs may be removed by gently applying shots from a nitrogen spray gun. Since the SPs are rather large they even may be pushed slightly by hand using a sharp pair of tweezers. It is required that wafers have actually been etched through completely. This can be guaranteed by a slight over-etching, which results in some notching and therefore in a small reduction of the usable lens height relative to the wafer thickness by ~10 µm.

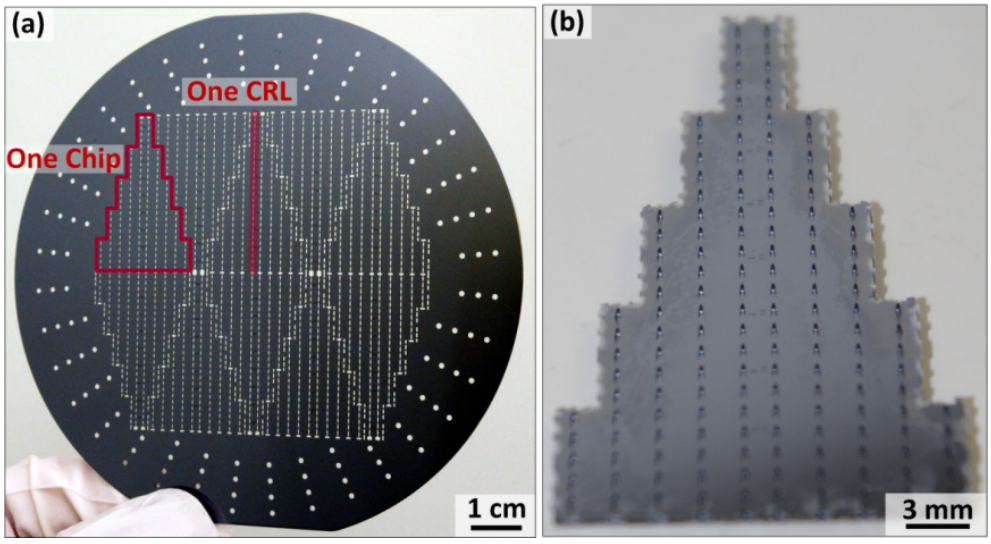

Figure 6.1. Photograph of a through-etched 100 mm silicon wafer. The outline of a lens chip and a compound refractive lens (CRL) are highlighted in red. In total, 10 chips and 1000 single bi-concave lens elements are included in the design.

Most notably, wafers are fragile upon stress and shock. Nevertheless, in case of carful manual handling they are sufficiently robust. Immersion into fluids and moving wafers between wafer carriers or boats is unproblematic. This is even more impressive, given that the webs between cavities are merely 10 µm thick. Obviously, these webs are most prone to break. However, this does usually not occur during handling. Breakage of webs was even not observed upon the wafer-bonding step prior to chip-dicing. However, it regularly occurred during wafer de-clamping after DRIE inside the machine. In such a case, 1-2 full CRLs were broken along their optical axis. Nevertheless, the integrity of the whole wafer remains, wafers may be successfully unloaded using the automatic handler and final chips are still functional, merely containing one

or two defect CRLs. Inevitably, final chips need to be inspected for such breakage and defect CRLs need to be noted or marked. Typically, ~80% of the chips were flawless.

As an experiment, device wafers were bonded to carrier wafers by Crystalbond[28] prior to DRIE. Although this strategy successfully prevented breakage of webs, it negatively affected the etching. Using a carrier wafer decreases heat conduction and hence control of the etching. Crystalbond starts to flow at elevated temperatures (~150°C) that occur during DRIE, which becomes problematic once wafers have been etched through. Molten Crystalbond causes rupture of the back-side SiO_2 membrane, releases SPs during DRIE and gets exposed to the plasma, thereby locally affecting plasma conditions. Performing the crystal-bonding procedure under vacuum for avoiding the inclusion of air bubbles in the bonding layer was not successful either. Because of the fragility of crystal-bonded wafers, they need to be separated in hot water, which also effectively removes residues of the Crystalbond.

Alternatively, wafers may be bonded using photoresist similar to the wafer-bonding step subsequent to surface smoothing. This efficiently suppressed any problems during DRIE. However, the bonding is so strong that the carrier wafer cannot be released subsequent to DRIE, which is problematic with respect to releasing the SPs and the surface smoothing step.

Finding an efficient way to temporarily bond wafers for DRIE would make the process more robust, more reproducible and would additionally avoid residues in the plasma chamber. Alternatively, rupture of webs during wafer de-clamping may be caused by a residual charging of the wafer and a related stiction of the wafer to the chuck after processing. This may be avoided in future by a proper discharging and this option remains to be investigated. Nevertheless, allowing for defects here and there, as well as sporadic manual cleaning of the wafer chuck allows obtaining Si-CRLs with substantially increased lens heights.

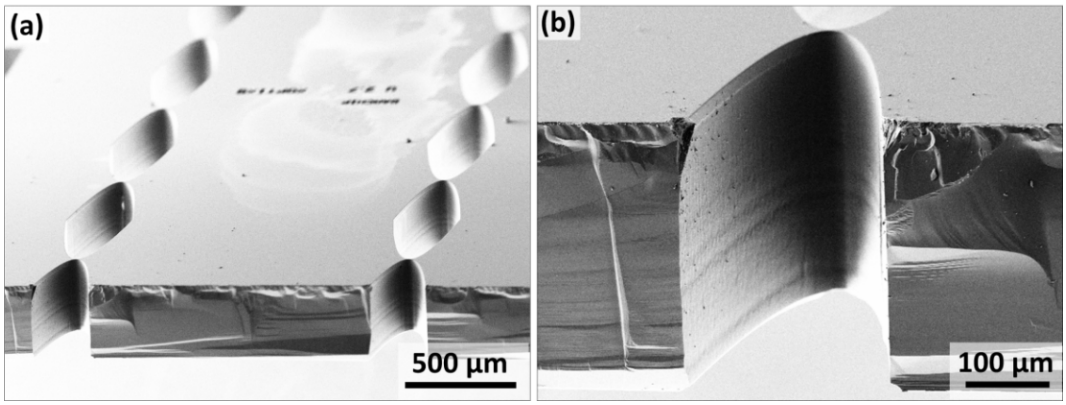

Figure 6.2. SEM images of through-etched silicon cavities. (a) Cross-section of arrays of x-ray lenses. (b) Close-up of the apex of a single through-etched cavity. The view angles are 30°.

Figure 6.2(a) shows a SEM image of through-etched lens structures. Magnifying the cavity cross-section shows faint horizontal defects which may be attributed to break-through of the sidewall passivation during etching (cf. Figure 6.2(b) and Chapter 3.5.4). Figure 6.3 shows structures after surface smoothing and adhesive bonding for lens stabilization.

[28] E.g. Crystalbond™ 555 & 555-HMP from TedPella/PELCO
https://www.tedpella.com/Material-Sciences_html/Sample_Mounting_Adhesives.htm#_821_1 (Dec 2015).

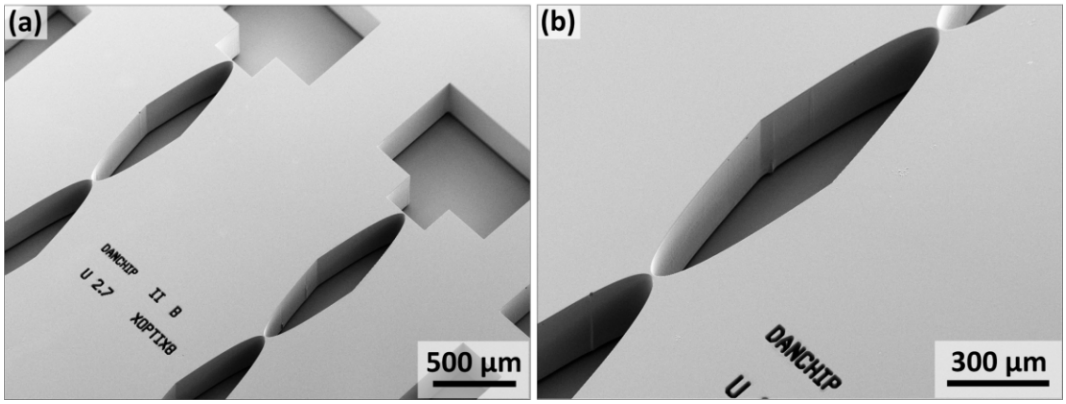

Figure 6.3. (a) Top view of an end section of a silicon lens chip that has been bonded to a carrier wafer for safe handling. (b) Close-up of a single element. The view angles are 30°.

6.1.2 Shape characterization

Top shape

The top parabolic shapes of the final lens structures were characterized by SEM according to the procedure presented in Chapter 5.2. The wafer design included CRLs with different degrees of compensation u for shape widening during processing (cf. Chapter 2.4 and Chapter 4.2.1). As an example, a SEM image of the top surface of a lens cavity with u = 2.7 µm was analyzed. The edges of the bi-parabolic cavity were detected by a routine written in Matlab using the Canny algorithm [447]. The extracted data were subject to a fit to $z(x) = \pm x^2/2R$, where the fitting parameter is the radius R. The parabolic fits gave R = (19.86 ± 0.04) µm for the one and R = (19.75 ± 0.22) µm for the other parabola, with RMS deviations of 1.1 µm and 1.6 µm, respectively. The differences Δz between the fits and the data are plotted in Figure 6.4. Figure 6.5 shows the results of a statistical analysis, which also includes varying fit ranges. Clearly, u = 2.7 µm is a good compromise and u = 3.1 µm would be the optimal choice.

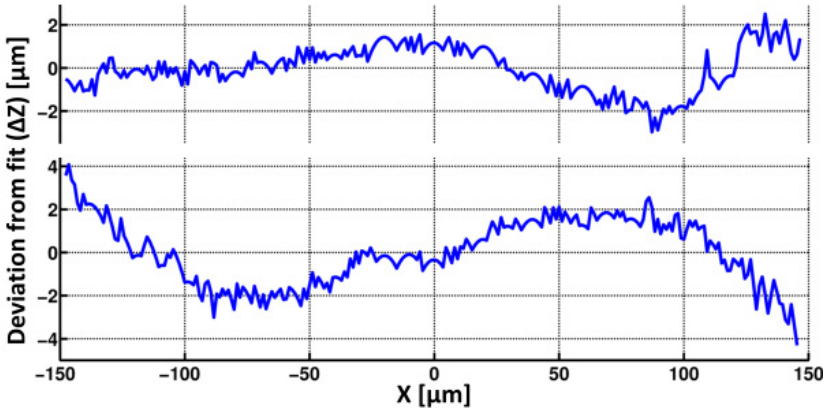

Figure 6.4. Top shape analysis of XOPTIX8. Deviation of the detected edges from the fit curves of the one and the other parabola of a single etched cavity. For axis assignment cf. Figure 5.2.

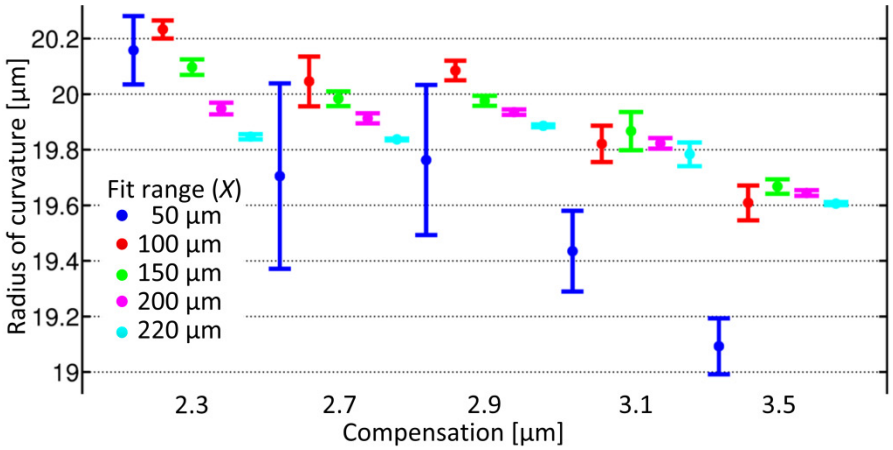

Figure 6.5. Results of fitting the edge-detected 2D parabolic shapes. The fitting range was varied and lenses with different degrees of compensation for shape widening were analyzed. Each data point is the result of 3 measurements.

Etch uniformity

The lenses were cleaved along the optical axis and the 3D shape of the lens cavity sidewall was measured by optical confocal profilometry (cf. Chapter 5.4). Figure 6.6 shows a surface plot of the sidewalls of three closely spaced lens cavities, which allowed data leveling about the *Y*-axis. A 20x objective (NA0.45) was used, 1 × 9 fields of view (FOVs) were stitched together with 25% overlapping area and the pixel size was 820 nm. To map one lens sidewall a 50x (NA0.45) objective was used and 8 × 2 FOVs were stitched together with 25% overlap and a pixel size of 330 nm. Figure 6.7(a) shows a SEM image of the profiled area and Figure 6.7(b) shows the respective surface plot. The cavity was originally defined by a trench of uniform width, resulting in sidewall profiles along *Y* that are expectedly uniform across *Z*. The color code of the surface plot corresponds to the deviation of a single profile (elongating in *Z*-direction) from the average profile. The deviation spans -900 nm to +900 nm, and the normalized mean deviation is 210 nm. Generally, the measured sidewall is vertical, but shows a bow of ~0.8 µm along the *Y*-direction. Three horizontal indentations with maximum amplitude of ~1.2 µm relative to the top profile are present; they can also be identified in the SEM image. Faint striations along the *Y*-direction are visible, but their amplitude was largely reduced by the surface smoothing step.

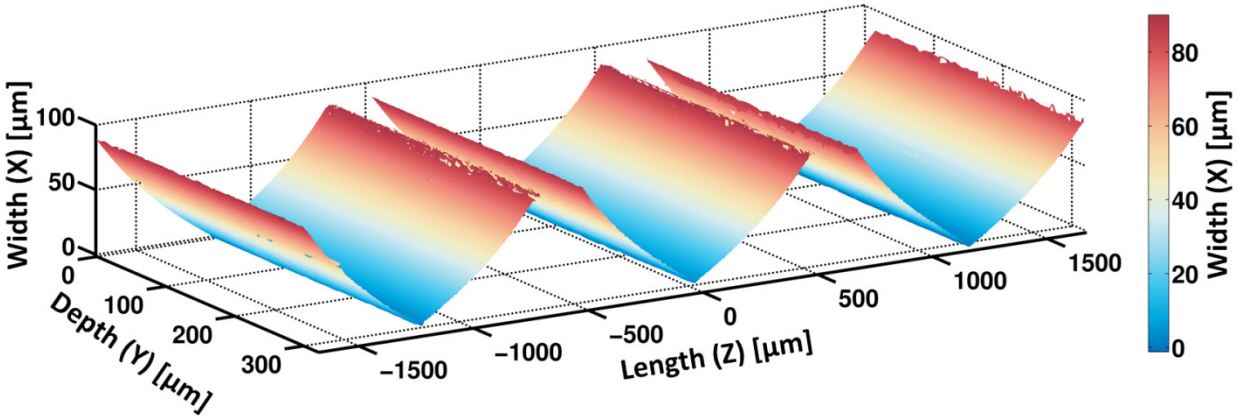

Figure 6.6. Confocal optical profilometer surface plot of the sidewalls of a CRL.

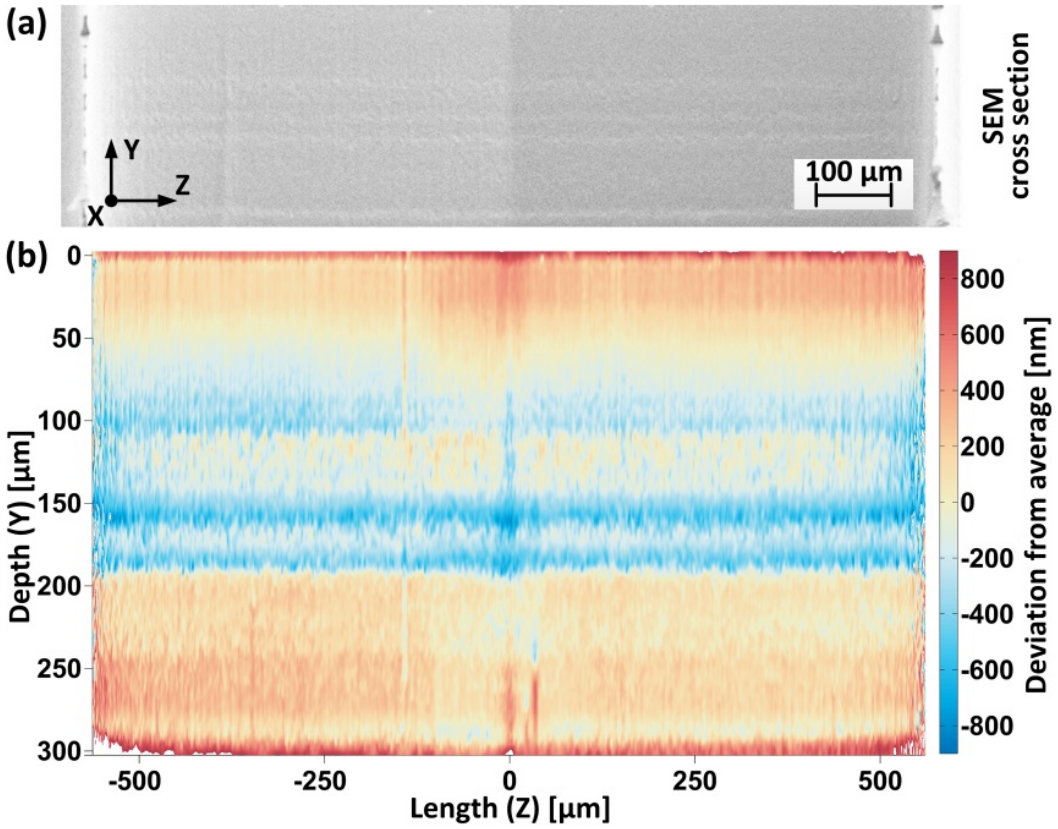

Figure 6.7. Straightness and uniformity characterization of a through-etched and surface smoothed silicon cavity sidewall. (a) SEM picture of the lens sidewall that has been profiled. (c) Confocal optical profilometer surface plot of the lens sidewall. The color code corresponds to the deviation of a single profile (elongating in *Z*-direction) from the average profile.

Apex uniformity

The 3D shape of the cavity apex was characterized by molding in PDMS and the obtained inverse replica was inspected by atomic force microscopy (AFM, cf. Chapter 5.5). Cross-sections of the apexes of the silicon cavities were cast with PDMS to obtain negative replica that were protruding from the surface and could be approached with an AFM probe. Figure 6.8(a) shows a SEM image of an inverted PDMS replica of a lens element. Figure 6.8(b) shows a surface plot obtained by AFM of the top 50 µm of the apex. The data were fit to a function of a parabolic cylinder and the color code corresponds to the deviation from the fitted surface. The radius of curvature is (19.85 ± 0.01) µm, the r-squared value is 0.998 and the normalized mean deviation is 100 nm. Individual profiles were fit to a parabola and R was plotted along the depth of the feature (cf. Figure 6.9). Since the field of view of the AFM is limited, scans were stitched together. R varies between extreme values of 20.2 µm and 17.5 µm, with a mean R = (18.5 ± 0.9) µm and a relative standard deviation of 4.8%.

Figure 6.10(a) shows individual AFM scans at different depths of the structure and Figure 6.10(b) the respective deviations from parabolic fits to the profiles. The top profile was fit to a parabola with high goodness and shows a mean deviation of ~30 nm. Generally, the mean deviation from a parabola increases toward the lens depth to ~200 nm and maximum deviations reach 700 nm. The profiles clearly flatten in the region x = -3 µm to x = +10 µm, especially at

depths of 100 µm to 250 µm. This means that this region will essentially not contribute to x-ray focusing, but rather blur the focus and increase the background intensity. The gradual decrease of the shape fidelity can be associated with the definition of the parabolic shape with the 20 µm wide trench. As can be seen in Figure 4.2 the apex was less well defined compared to the remaining parabolic shape. Furthermore, the sacrificial material inside the lens cavity shows a sharp tip at the lens apex, which may have caused a non-uniform deflection of ionic species during DRIE.

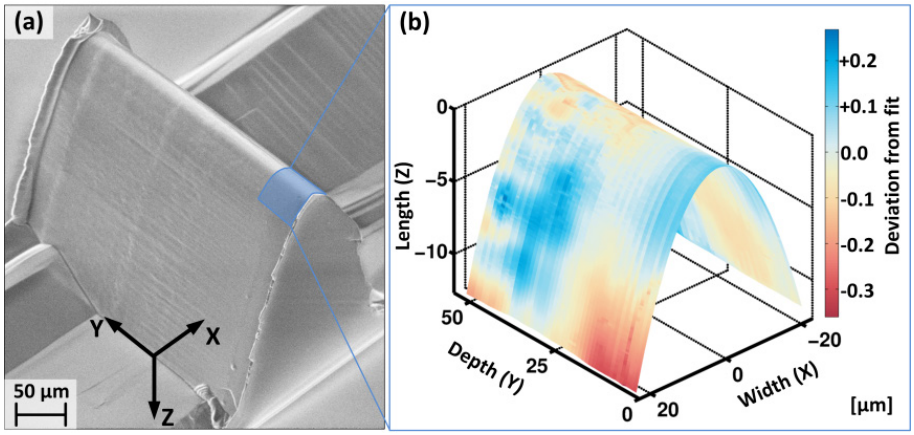

Figure 6.8. Uniformity characterization of the cavity apex. (a) Scanning electron micrograph of an inverse replica of a cross-section of a single lens element in PDMS. (b) Apex topography obtained by measuring the highlighted area in (a) with a large Z-range AFM.

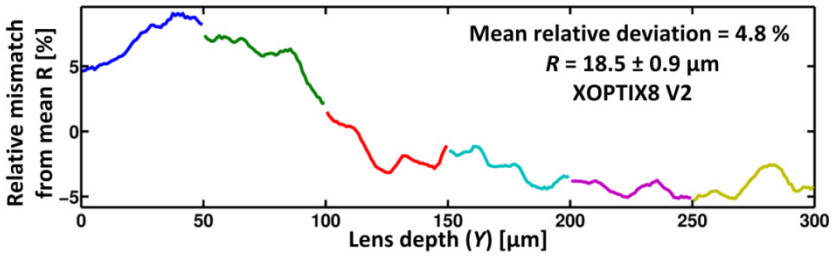

Figure 6.9. Variation of the radius of curvature along the etch depth obtained by fitting individual AFM profiles to parabolas. Different colors correspond to data originating from different AFM scans.

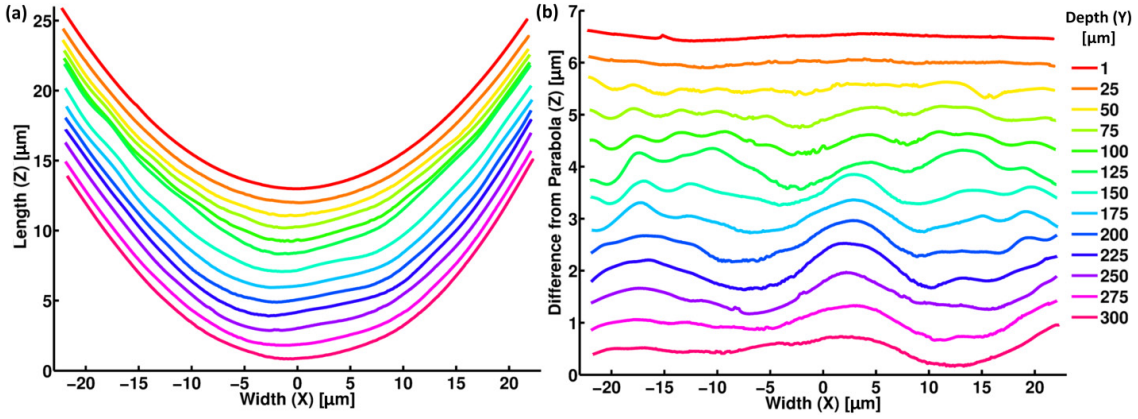

Figure 6.10. (a) Individual apex profiles along the depth of the structure. (b) Deviations of the profiles from their parabolic fit. Profiles are offset relative to each other for clarity. The labelling of the abscissa is equal in (a) and (b).

6.1.3 Packaging

The quality of the lenses presented here was regarded sufficiently good to pursue with their installation at a beamline and tests of their optical performance. To this end lens-wafers adhesively bonded to handle wafers were laser cut (cf. Chapter 3.7). The individual lenslets combined to CRLs with various N are arranged on chips and these chips are positioned on the wafer such that dicing is considerably facilitated. Depending on the actual laser dicing, 'single-' or 'double-' chips may be obtained comprising maximally 25 or 50 lenslets, respectively. Figure 6.11 illustrates the dicing procedure. After dicing, remaining debris is removed by immersion in an ultrasonic bath and subsequent blow drying using compressed air.

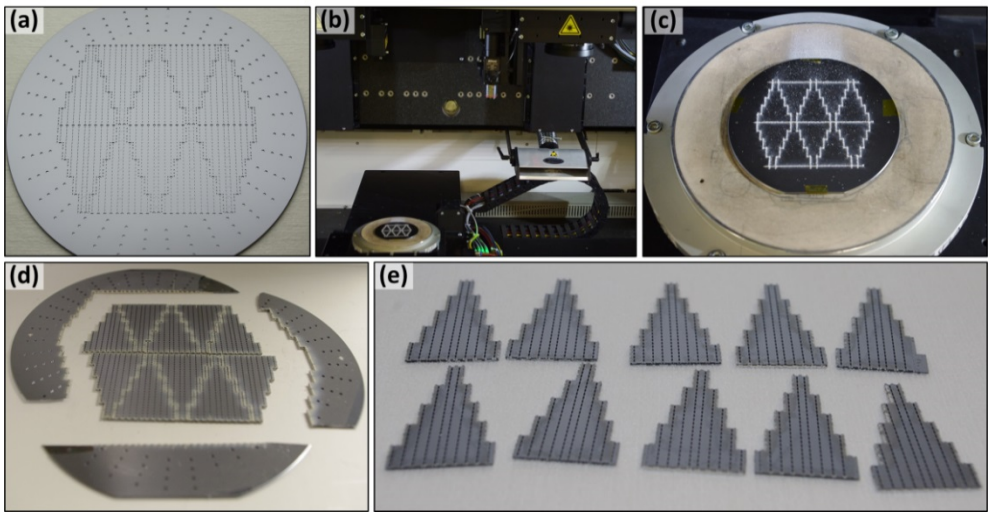

Figure 6.11. Laser dicing of lens chips XOPTIX8. (a) Lens-wafer adhesively bonded to a carrier wafer. (b) Wafer inside the laser micromachining tool. (c) Wafer subsequent to lasing lying on the vacuum chuck and mounted upside down on top of a support wafer using Teflon tape. (d) Released lens chips. (c) Final chips after ultrasonic bath and blow-drying.

6.1.4 Optical performance

The focused x-ray beam was characterized at the experimental hutch 3 of the beamline ID11 at the ESRF. The experiments were carried out on May 25th – 26th 2015 during the 4-bunch filling mode with an electron beam current of 27 mA to 43 mA. The x-ray energy was set to E = 56 keV, giving a focal length of f = 1.3 m for a silicon lens ($\delta = 1.54 \times 10^{-7}$) with R = 20 µm and N = 50 single bi-concave lens elements. A chip with u = 2.7 µm was selected as a good candidate to show minimal aberrations. The slit openings were set to 350 µm (X) and 310 µm (Y). In order to obtain the best possible focal size, the lenses were tilted by ϕ = 0.12 degrees from their optimal alignment parallel to the beam axis (rotation around the Y-axis, cf. Chapter 2.4). This tilt appears to have suppressed optical aberrations most likely originating from the partially non-parabolic shape at the apex region (cf. Figure 6.10) at the cost of a reduced effective aperture, resulting in ~30% less transmittance.

Figure 6.12(a) shows the data from a fluorescence scan that was performed at the focal position yielding a waist of 980 nm (FWHM). The signal-to-noise ratio (S/N) at two standard deviations (2σ) from the peak is 5, S/N=19 at 4σ and S/N=70 at 10σ (cf. Figure 6.12(b)). Figure 6.13(a)

shows the x-ray beam a distance of 1.6 m downstream the focal position. The relative standard deviation of the photon intensity in *Y*-direction is ~5.2% with local extrema of ±14%. The x-ray transmittance through the 300 µm wide aperture is 32%, resulting in a gain in photon flux density of 97 relative to the unfocused x-ray beam. A waist of 310 nm (FWHM), a transmittance of 39% and a gain of 380 were expected for ideal lenses (cf. Chapter 2.2).

To characterize the uniformity of the lens, the vertical slit was narrowed down to 50 µm (*Y*). The so defined beam was scanned along the height of the lens in increments of 50 µm (denoted as Section 1-6 in Figure 6.13(b)) and at each position a fluorescence scan was performed. These measurements were repeated at different distances in *Z*-direction around the focal position (cf. Figure 6.13(b)). The beams for each section were approximately Gaussian and the spot sizes w were fit to $w(z) = w_0\sqrt{1+\left((z-\Delta z)/z_R\right)^2}$, where w_0 is the minimum spot size at the beam waist, z_R is the Rayleigh range and Δz is the offset of the beam waist from the average focal position at z = 0.

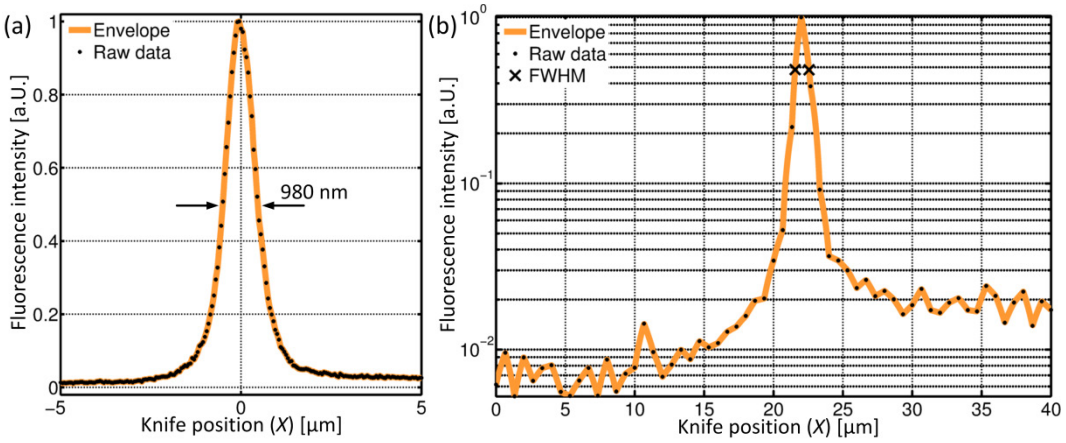

Figure 6.12. Optical performance of the silicon x-ray lenses. (a) Measured x-ray fluorescence signal from the copper sample scanned through the focal plane of a 310 µm long line beam. (b) Logarithmic plot over a wider range. The increased fluorescence on the right-hand side originates from the bulk of the knife (fused silica, cf. Chapter 5.6.1).

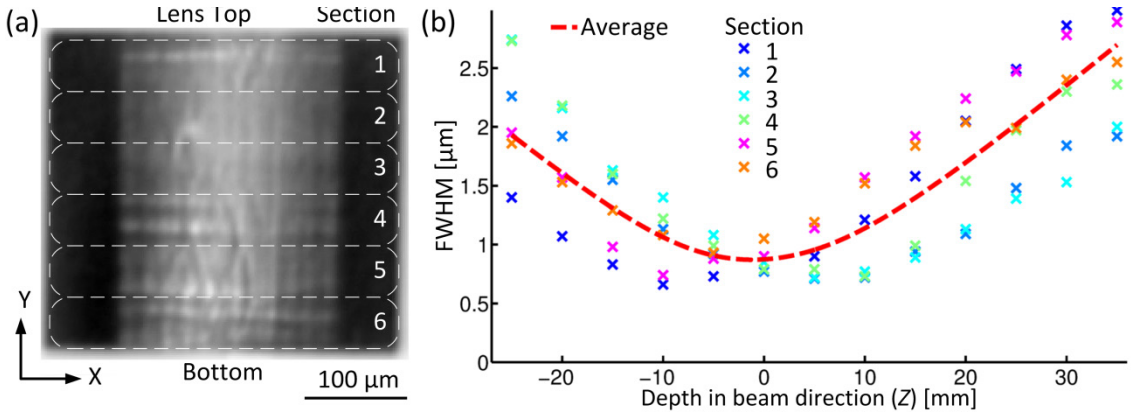

Figure 6.13. Beam profiling. (a) CCD image of the transmitted beam 1.6 m downstream the focal plane. Sections 1-6 are subject to separate analyses. (b) Depth of focus scans performed for different sections of the lens. Each data point corresponds to a separate fluorescence scan. The average of the Gaussian beams from different lens sections is indicated by a dashed red line.

For each section Table 6.1 lists the minimum spot sizes measured, the respective offsets Δ*z* and the results from data fits. A waist of 661 nm (FWHM) was measured at the uppermost 50 microns (cf. Figure 6.14(a)). Generally, the beam quality deteriorates toward the bottom of the lens (cf. Figure 6.14(b)). Different beam offsets corresponding to varying focal lengths were measured at each section of the lens; the variation in focal length spanned ±10 mm. The center of the lens (Sections 2-4) showed shorter focal lengths than the lens top and bottom (Sections 1, 5 and 6). The average measured beam waist at z = 0 equals 856 nm. If the focal positions coincided in one plane, the average beam waist would have been ~750 nm. The measured spot sizes are consistent with Gaussian beams. Inspection of the average beam profile yields a depth of focus of approximately 5 mm.

Table 6.1. Results from the characterization of the x-ray beam.

	Measured		Fitted			
Section	w_0[a] [nm]	Δz [mm]	w_0[a] [nm]	Δz [mm]	z_R [mm]	R^2
1	661	-10	591	-6.8	8.2	0.99
2	712	5	657	5.9	9.8	0.98
3	722	5	675	8.3	9.4	0.97
4	733	10	664	4.5	8.0	0.96
5	743	-10	857	-5.0	11.2	0.96
6	933	-5	1080	-3.8	16.9	0.94
Average	856	0	841	0.7	11.7	0.98

[a] FWHM

Inspection of the data from individual knife scans gives information about optical aberrations. Figure 6.14(c) shows the fluorescence signal from the bottom 50 µm beam-section 35 mm downstream the average focal position. A double peak is clearly visible, and it may be attributed to

1. the fact that the parabolic lens shape is not the ideal lens shape (cf. Chapter 2.2.2),
2. an overcorrected lens (cf. Chapter 2.4),
3. the slight intentional misalignment (cf. Chapter 2.4),
4. sidewall defects such as vertical striations (cf. Chapter 3.5.4), or most likely
5. a combination thereof.

Figure 6.15 shows the same data set from Figure 6.13 in intensity surface plots. The fluorescence data was normalized to the electron beam current in order to obtain the relative intensity distributions. The 13 × 201 ($Z \times X$) data points from each section were interpolated for clarity. Every section yields roughly the same total fluorescence signal, although it is slightly higher in the middle sections, which is consistent with a slight bowing of the sidewalls. Optical uniformity seems to be best in Section 2 and worsens towards the bottom. This suggests that vertical striations that were more pronounced at the lens bottom have a significant impact. Figure 6.16 shows the intensity surface plot of the sum of all sections.

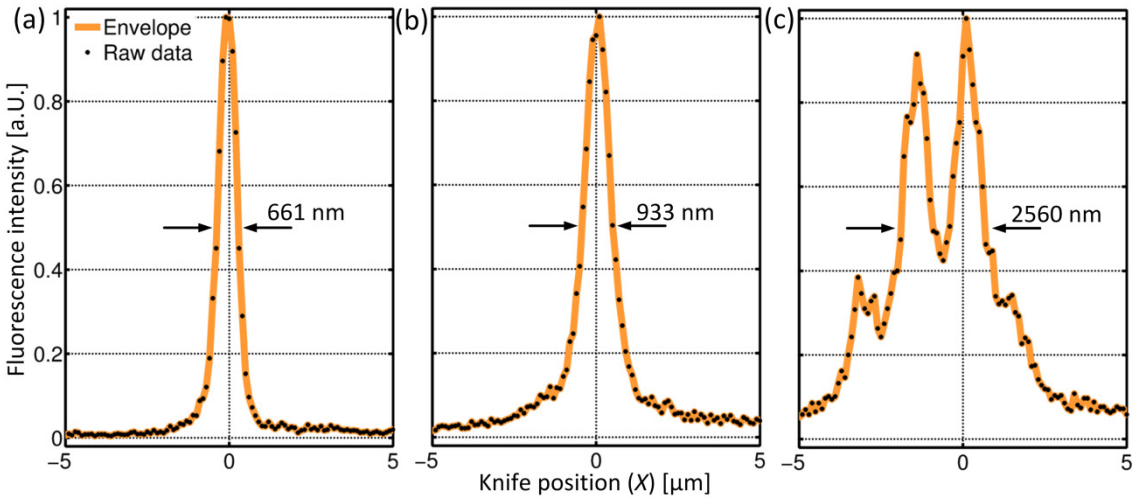

Figure 6.14. Measured x-ray fluorescence signal from the copper sample scanned through 50 µm wide sections of the focused beam at various positions. (a) Section 1, Δz = -10 mm. (b) Section 6, Δz = -5 mm. (c) Section 6, Δz = +35 mm.

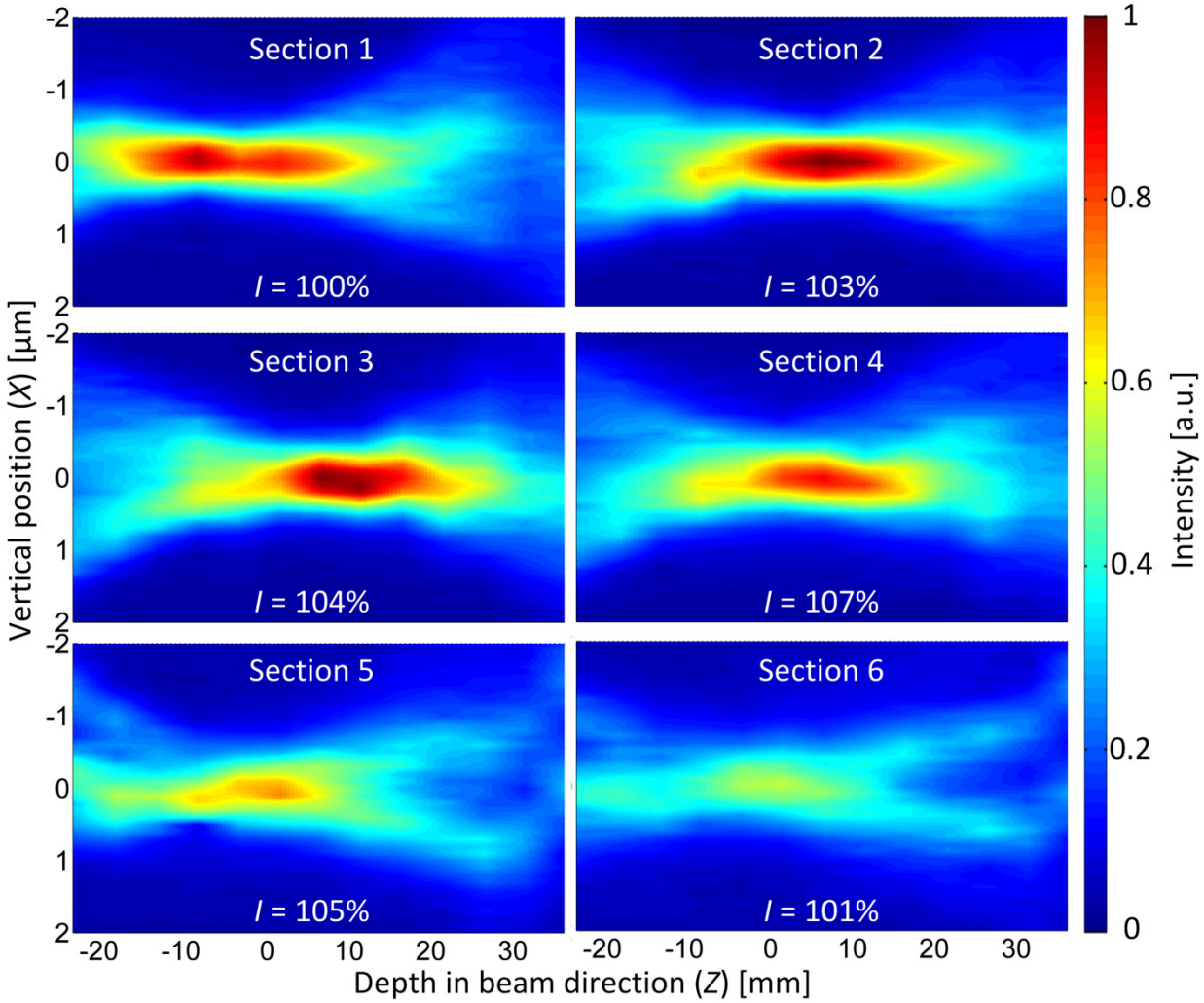

Figure 6.15. Interpolated intensity surface plots of 50 µm deep lens sections (cf. Figure 6.13). The total intensities (*I*) are indicated and normalized to Section 1.

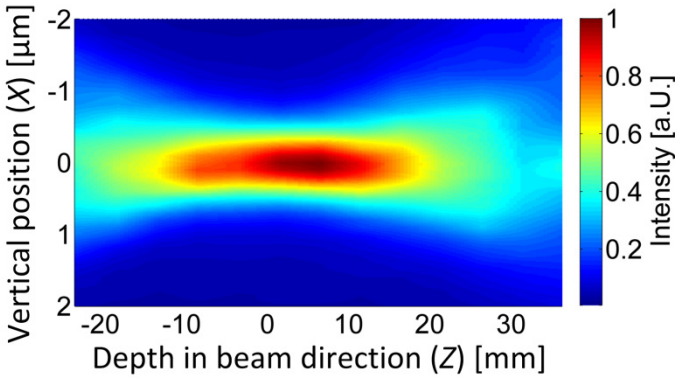

Figure 6.16. Interpolated intensity surface plots of the sum of all 50 µm deep lens sections (cf. Figure 6.13 and Figure 6.15).

6.1.5 Discussion

Our attempt to increase the line beam width and hence the silicon lens height resulted in a minimum waist of 661 nm (FWHM), which was obtained from the top 50 µm section (c.f. Figure 6.12 and Table 6.1), whereas 310 nm (FWHM) was theoretically possible (based on source demagnification and the diffraction limit determined by x-ray absorption, cf. Chapter 2.2.5). The discrepancy between theory and experiment is likely to be a combination of issues related to the optics test (an underestimated source size, vibrations, the fluorescing sample) and issues related to the lens geometry. With respect to the latter, the inspection of the shape at the lens top surface showed a minor deviation from the ideal bi-parabolic shape (c.f. Figure 6.4), which may account for the broadened spot size for the uppermost 50 µm. The fact that the lenses were slightly tilted from optimal alignment also resulted in an effective deviation from the ideal parabolic lens shape.

The characterization of the lens sidewall in 3D by optical profilometry showed a bowing of ~0.8 µm, which corresponds to an increase of R by ~0.3 µm or 1.5% at the lens center (c.f. Figure 6.7). This minor non-uniformity can account for the observed variation of the focal length between the lens top, center and bottom sections (cf. Figure 6.13). In terms of sidewall angle α, the first 150 µm depth is negatively tapered (α = 89.7°), while the second 150 µm is positively tapered (α = 90.3°). However, given the observed focal depth of ~5 mm, the variation of R must not increase 0.4% or 0.1 µm, corresponding to $\alpha \cong 90° \pm 0.1°$. The lens apex showed a relatively large deviation from the ideal parabolic cylinder (cf. Figure 6.8, Figure 6.9 and Figure 6.10), which additionally caused blurring of the focus. The effective R varied by 4.8% along the lens depth, which locally varies the focal length at the apex region.

Despite the deviation of the actual lens shape from the ideal and the non-optimal optical performance, the demonstrated 310 µm long line beam with a waist of 980 nm (FWHM) is the longest reported line beam with a sub-micron waist created by a silicon x-ray lens made by DRIE at the date of submission of this thesis. The developed lenses will serve as efficient condenser optics for microstructural analysis.

Notably, a previous version of the same type of lenses has been tested ~8 month earlier. The main difference was that during the manufacture alumina instead of the silicon oxide was used as the hard mask material for DRIE. As a consequence, the lens sidewalls were distinguished by

vertical striations with amplitudes of 1 µm, which considerably affected the optical performance.[29] CRLs with N = 25 of this previous version have been tested on 21st – 23rd September 2014 at ID11 using 40 keV x-rays and briefly at ID6 using 17 keV x-rays. The experimental setups were very much like those discussed in Chapter 5.6.5 and knife edge scans have been performed to measure the spot size and its uniformity along the depth. Results can be summarized as follows: The focal lengths were 1.33 m and 0.24 m, for 40 keV and 17 keV, respectively. In both cases the minimum average waist was ~2 µm over the full height (350 µm) of the lens. The waist significantly degraded from the top to the bottom of the lenses. While a minimum waist of ~800 nm was measured for the top 50 µm section it steadily increased to ~2.3 µm for the bottom 50 µm section. The differences in focal length between the top and bottom sections were 30 mm and 44 mm for 40 keV and 17 keV, respectively. Hence, the optical performance of the lenses was considerably improved in this second version of XOPTIX8 by avoiding large vertical striations and assuring smooth and straight sidewalls.

6.2 Strategy A: Interdigitated Si objective

Two dimensional focusing silicon compound refractive lenses (Si-CRLs) with physical apertures exceeding 300 µm and radii of curvature of 20 µm were fabricated according to the manufacturing strategy outlined in Chapter 4.2 and demonstrated in Chapter 6.1 for the fabrication of 1D focusing lenses. Respective results were published [152].

Instead of bonding lenses to carrier wafers for their mechanical stabilization, slices comprising N = 20 1D-focusing lenslets were interdigitated, aligned on a common optical axis perpendicular to each other and fixed by glue onto a solid metal block. Interdigitating individual horizontal and vertical lenslets, mimics rotational parabolic lenses and avoids astigmatism. Pre-alignment of lenses facilitates their use in a beamline. A proof-of-concept interdigitated system was used as an objective in a bright-field microscope using 17 keV x-rays. A spatial resolution marginally better 300 nm was obtained using a magnification ratio of 11. It is anticipated that further advancements of the manufacture of Si lenses and a higher compactness of the interdigitated system will allow competing with existing x-ray lenses in terms of achievable spatial resolutions and most probably cost. Especially at working x-ray energies >30 keV, these systems may give a boost in studying the internal structure of bulk samples using techniques such as bright-field and dark-field imaging.

6.2.1 Two-dimensional x-ray focusing lenses

Strategy A utilizing wafer through-etching for the removal of sacrificial structure was also used for the manufacture of two-dimensional focusing CRLs, which are advantageous when used as objectives in bright-field or dark-field x-ray microscopes [152]. Previously, two sets of silicon CRLs were positioned subsequent to each other in a crossed geometry to create pencil probe beams, which find widespread use in scanning x-ray microscopy (cf. Chapter 2.3.4, [145]). Traditionally, CRL chips are separate from each other and mounted on individual stages which allow alignment for horizontal and vertical focusing. Two CRLs need to be carefully positioned

[29] These lenses were manufactured parallel to those presented in Chapter 6.2, which also suffered from large vertical striations.

relative to each other along the optical axis such that their foci meet at a common focal plane. Their individual focal lengths need to differ in order to compensate their different on-axis positions. This geometry has the advantage that different image magnifications may be obtained horizontally and vertically such that the eccentricity of the source image can be controlled, which allows round spot shapes to be obtained from usually asymmetric x-ray sources. However, if such geometry is used on the objective side for sample imaging, this astigmatism results in unwanted distortions. Rotationally parabolic lenses may be better mimicked by alternately crossing (or interdigitating) individual horizontal and vertical focusing lenslets as was previously demonstrated by CRLs manufactured by deep x-ray lithography (DXRL, cf. Chapter 2.3.3, [245]). It is anticipated that this interdigitated geometry greatly reduces astigmatism with the additional benefits that only one set of stages is required and lens alignment in the beamline is greatly facilitated.

The realization of interdigitated silicon lenses requires the manufacture of a pair of linear focusing CRLs and their subsequent assembly. The advantages of silicon objectives may be summarized as follows (cf. Chapter 2.3):

1. extreme radii of curvature may be realized, which allows to maximize the refractive power per unit length,
2. extreme focal lengths may be realized, which increases the numerical aperture and thus the achievable spatial resolution
3. the web thickness can be controlled and <10 μm is feasible, which increases x-ray transmission,
4. the thickness of lenslets may be adapted to the effective aperture of the CRL,
5. lithographic techniques allow highest precession in the manufacture,
6. multiple lenslets may be obtained from a single silicon wafer, thereby reducing cost,
7. Individual 1D lenslets are well aligned with respect to each other, avoiding subsequent high precision assemblies,
8. more complex geometries such as adiabatic arrangements or kinoforms are feasible,
9. high radiation stability, and
10. decent refractive power of Si, particularly relevant for x-ray energies >30 keV.

Most crucially, an optical regime may be found, where silicon CRLs outperform today's commercially available rotationally parabolic beryllium CRLs manufactured by embossing. The reasons are of technological nature, although not of principle nature. The maximal achievable numerical apertures of embossed Be lenses are limited by their minimal reliably realizable radii of curvature (R > 50 μm) and the minimal thickness of lenses (T > 1.5 mm, i.e. the thickness of the dies used for embossing). Beryllium is generally a superior lens material with respect to lens transmission, which favors higher effective apertures (cf. Chapter 2.2.4). However, the technological constraints limit practical achievable focal lengths, i.e. the numerical aperture determining the resolution. Because Si lenses can generally be more compact in space, smaller focal lengths (and working distances) can be achieved and above a certain energy E = 30 keV Si-CRLs with R = 5 μm are superior to Be CRLs [152]. Hence, the main advantage of Si technology is compactness. Additionally, once the manufacturing process has been established Si lenses would be considerably cheaper than equivalent Be lenses. Its disadvantages can be summarized as follows:

1. a pair of 1D CRLs need to be assembled with high precision relative to each other,
2. the focal power per unit length is less than half of that of a rotational CRL,
3. the construction of flexible lens systems similar to transfocators is more complex, and
4. reduced flexibility than with CRLs made by DXRL, where multiple CRLs are present on one substrate.

6.2.2 Design

As a proof-of-concept a Si-based interdigitated objective has been developed. Figure 6.17 shows the layout of the lithography mask XOPTIX9, which has been used to manufacture multiple slices of 1D-focusing CRLs. The basic features are bi-parabolic lenslets with R = 20 µm, $2R_0$ = 300 µm and T = 1.2 mm. The target web thickness d is 15 µm and the degree of shape compensation is constantly u = -2.9 µm (cf. Chapter 2.4). As in XOPTIX8, all features are defined by 20 µm wide trenches, which upon wafer-through etching guarantees close to vertical sidewalls and a release of sacrificial portions (cf. Chapter 4.2). Lenslets were arranged in arrays on slices of 5 mm width. Each slice comprises N = 20 lenslets with a lenslet-to-lenslet distance of 3 mm securing the possibility of interdigitation using a second slice. One slice is 60 mm long and a total of 13 slices are arranged on the wafer. Given a target etch depth of 350 µm this results in final aspect-ratios of 17, which can readily be achieved by DRIE (cf. Chapter 6.1). The integrity of the wafer is guaranteed by multiple ~300 × 30 µm^2 large anchors on each end of the slices.

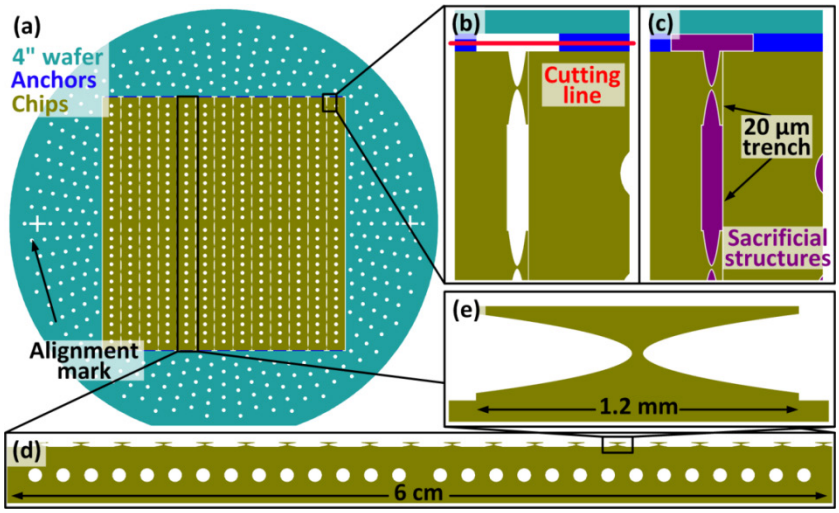

Figure 6.17. Wafer layout XOPTIX9. Sacrificial portions are not shown for clarity. All openings are defined by 20 µm wide trenches. (a) Full 4-inch wafer layout. Alignment marks are exaggerated. (b) Zoom-in at lenslets. The line for laser cutting is indicated. (c) Zoom-in at lenslets including sacrificial portions. (d) Layout of one slice comprising 20 identical lenslets spaced with a pitch of 3 mm. (e) Zoom-in of one lenslet.

6.2.3 Fabrication

The fabrication is essentially equal to that presented in Chapter 4.2 and Chapter 6.1. Double side polished wafers 350 µm thick were used. Once the wafer has been etched through using DRIE and sacrificial material has been released by etching the backside dielectric membrane,

individual slices remain connected to the rest of the wafer by the two anchors on each side of the slices only (cf. Figure 6.18). Worth mentioning, less failure-proneness during the manufacture was observed than for the 1D CRL chips presented earlier (cf. Chapter 6.1). Notably, wafer de-clamping was less critical, which may be attributed to the higher flexibility of the silicon slices than the more rigid 1D chips. Accidental breakage of wafers never occurred.

Figure 6.19 shows SEM image of lens structures prior and after surface smoothing. For these lenses alumina 50 nm thick deposited by ALD was used as the masking material for DRIE, which negatively affected the sidewall quality. Although sidewalls were generally straight due to defining the structures by trenches of uniform width, erosion of the alumina caused micro masking and large vertical striations with amplitudes of ~2 µm towards the bottom of the etchings. This can be considered as severe surface roughness and will deteriorate the optical performance significantly (cf. Chapter 2.4 and Chapter 6.1). Surface smoothing by thermal oxidation with subsequent removal of the grown oxide layer allowed the amplitude of striations to be reduced to some extent.

Worth mentioning is the stability of the lenslets, despite one halve of each lenslet is merely connected to the rest of the slice by the ~15 µm thick webs. In fact, failure due to breakage at the webs was no issue during processing or the final assembly. Nevertheless, caution must be paid since these lenslet are indeed fragile.

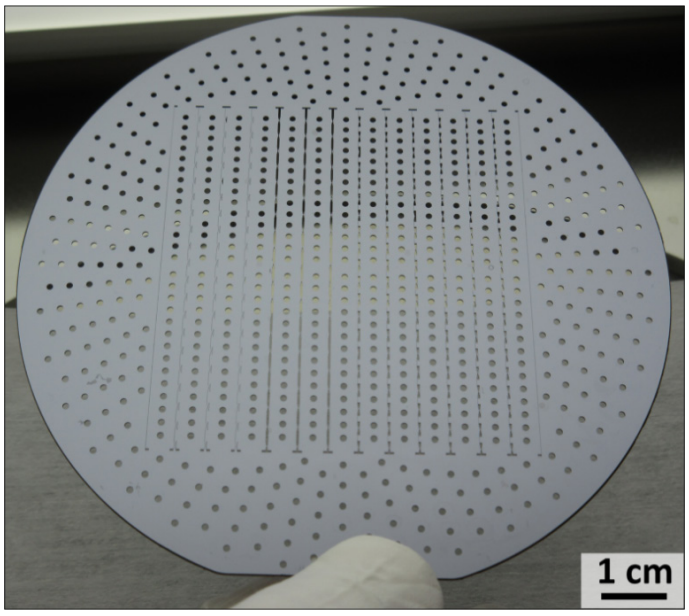

Figure 6.18. Photograph of a through-etched silicon wafer with design XOPTIX9.

The 3D shapes of lenses of type XOPTIX9 are hard to be characterized directly using aforementioned procedures because of their fragility (cf. Chapter 5). Characterizing the shapes of more rigid XOPTIX8 lenslets is considerably easier, since they may be cleaved in a controlled way (cf. Chapter 6.1). XOPTIX8 and XOPTIX9 merely differ in the arrangement of lenslets, so there are no differences in terms of processing and their shape. Hence, shapes of XOPTIX9 may be assumed by measuring samples of parallel processed wafers of design XOPTIX8, which was done here.

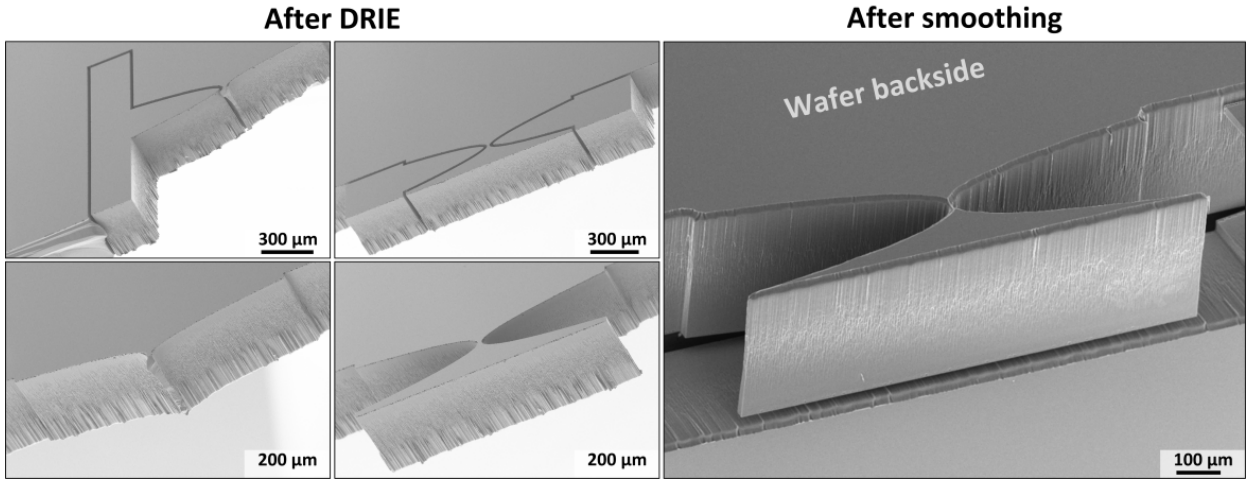

Figure 6.19. SEM images of XOPTIX9 lens structures before and after surface smoothing.

The 3D shape of the cavity apex of a parallel processed wafer of type XOPTIX8 was characterized by molding in PDMS and the obtained inverse replica was inspected by AFM (cf. Chapter 5.5). Cross-sections of the apexes of the silicon cavities were cast with PDMS to obtain negative replica that were protruding from the surface and could be approached with an AFM probe [148]. Figure 6.20(a) shows a contour plot obtained by AFM of the central 100 µm of the apex. It is highly non-uniform in comparison to that fabricated using a silicon dioxide hard mask for DRIE (cf. Chapter 6.1.2). Fitting parabolas to individual profiles elongating in X yields a radius of curvature $R = 20.52 \pm 0.53$ µm. Subtracting a parabolic cylinder from the data reveals large vertical striations (cf. Figure 6.20(b)).

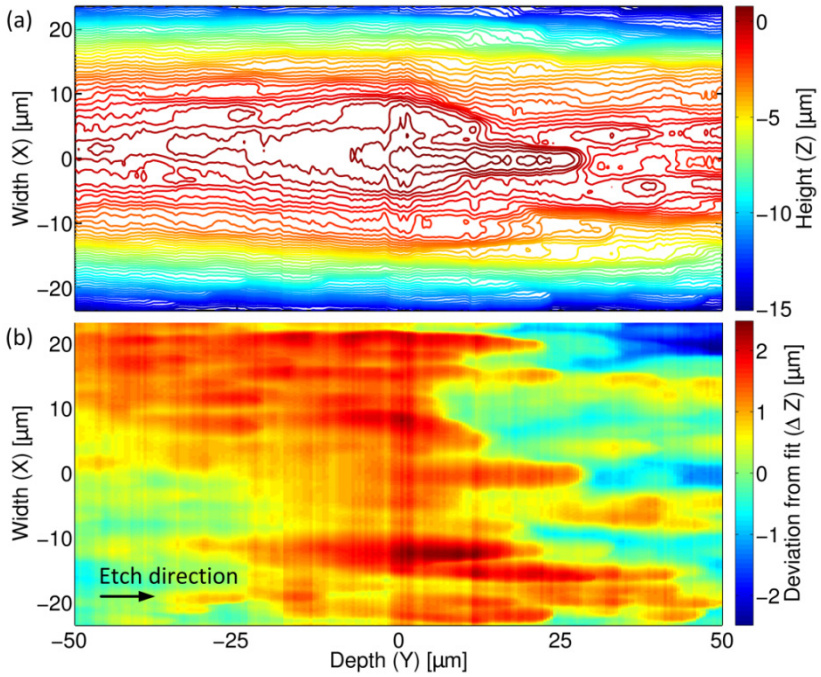

Figure 6.20. AFM scan of an inverted PDMS replica of a lenslet of XOPTIX8 (Version1) that has been deep etched using an alumina hard mask. (a) Contour plot at the center of the apex of the lenslet. (b) The fit of a parabolic cylinder has been subtracted to visualize the shape deviations. Large vertical striations are apparent.

The quality of the lenses was considered sufficiently good to justify optical tests. Individual slices were laser-cut from the rest of the wafer and carefully assembled on a steel block using a micromanipulator and an optical microscope (cf. Figure 6.21). The steel block was custom-made with high demands on perpendicularity, which was verified using a precision angle. One side of each Si slice was covered with Torr Seal, which is a two-component glue with relatively long curing time and allowed parts to be manipulated once they were attached. One slice was attached and roughly aligned to the edge of the block. The block was flipped 90° and the other slice was attached, while assuring interdigitation of the lenslets. By using a microscope and a micromanipulator, the slices were properly aligned. Perpendicularity is guaranteed by the steel block. The other rotations were controlled by minimizing the difference of the gap between the lenslets and the edge of the other slice. The alignment was measured to be better than 0.01° and thus sufficient for distortion-free imaging. The whole assembly took around 1 hour and is thus not an argument against their potential low cost. The final lens had 20 lenslets each in horizontal and vertical direction, respectively.

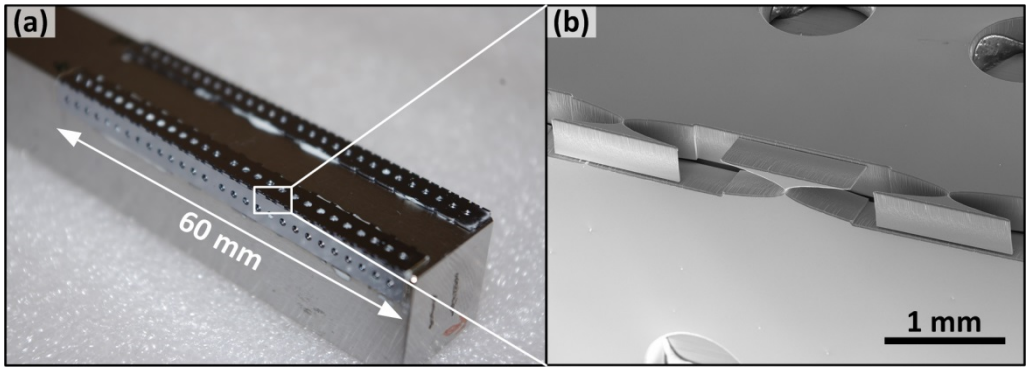

Figure 6.21. Prototype interdigitated silicon CRLs. (a) Photograph of Si slices glued perpendicularly to each other on the edges of a steel block. (b) SEM image of interdigitated lenslets.

6.2.4 Optical performance

The 2D lens was tested in a full-field XRM using incoherent x-rays of energy 17 keV. The experiments were carried out on 18th – 20th September 2014 at beamline ID06 at the ESRF (cf. Chapter 5.6.5). The microscope was positioned 60 m from the source and 2 m from a rotating decoherer of amorphous carbon. The illuminating beam was limited by slits. The sample-objective distance was ~380 mm, while the objective detector distance was ~3540 mm, resulting in a magnification ratio $M \approx 11$. The imaging configuration was intentionally diffraction-limited by the objective and oversampled by the CCD detector to reduce the contribution of the detector optics to the optical performance and resolution. After all optics the final pixel size of obtained images was ~59 nm.

A direct and straightforward measure of the resolution and aberration of the microscope can be made by inspecting the image of an absorbing Siemens star with radial features ranging from 5 µm to 50 nm (XRESO-50HC resolution chart, NTT-AT). Figure 6.22 shows a rapid degradation of contrast between 500-200 nm, which is consistent with the theoretically expected resolution of ~300 nm (cf. Chapter 2.2.5). Also visible are horizontal striations and inhomogeneous image contrast over the field of view. Both artifacts can be attributed to the observed striations on the

lens sidewalls. While this does not reduce the ultimate resolution of the lens, it is undesirable and ultimately avoidable by optimizing the etching parameters to improve lenslet profile accuracy and uniformity. Further details on astigmatism and the achieved resolution measured by analyzing a grid pattern may be found in [152].

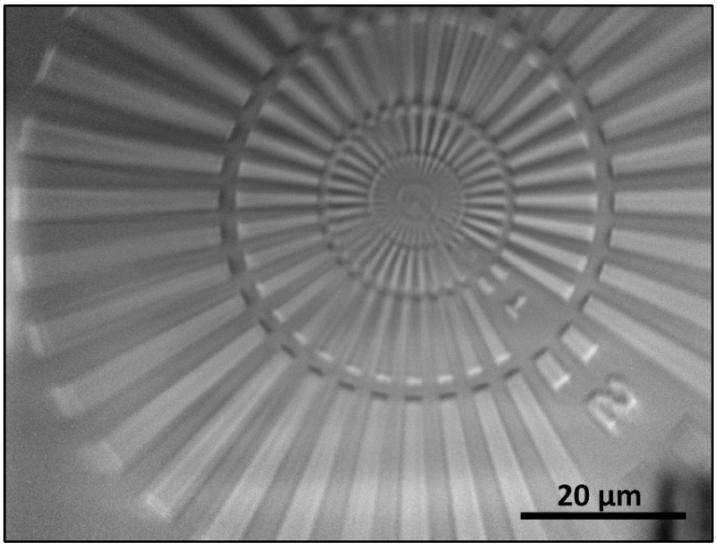

Figure 6.22. Image of resolution chart at M = 11. The image has been post-processed by flat-field correction.

6.3 Strategy B: Polymeric 1D lenses

A novel and economical approach for fabricating compound refractive lenses for the purpose of focusing hard x-rays is described. A silicon master was manufactured by UV-lithography and deep reactive ion etching (DRIE). According to Strategy B sacrificial structures were utilized, which enabled accurate control of the etching profile and were removed after DRIE (cf. Chapter 4.3). By electroplating, an inverse nickel sample was obtained, which was used as a mold insert in a commercial polymer injection molding machine. A prototype lens made of polyethylene with a focal length of 350 mm was tested using synchrotron radiation at photon energies of 17 keV. A 55 µm long line focus with a minimal waist of 770 nm (FWHM) and a total lens transmittance of 32% were measured. Due to its suitability for cheap mass production, this highly efficient optics may find widespread use in hard x-ray instruments. Respective results were published [151].

6.3.1 Polymeric x-ray lenses

Polymers composed primarily of hydrogen, oxygen and carbon show high transmittance similar to diamond and are therefore attractive lens materials (cf. Chapter 2.2.4). Polymers have previously been used for x-ray lenses (cf. Chapter 2.3, [222,223,234]). While lenses made of PMMA and epoxy-based SU-8 are routinely used in synchrotron beamlines [244,247,264], their common manufacture by rarely available x-ray lithography is expensive. As an economic alternative, polymeric multi-prism lenses were molded from anisotropically etched silicon masters [301,318] or structured by laser ablation [319]. However, these optics face technological challenges when sub-micron focusing is required [323]. A photopolymer was used to obtain

rotationally symmetric lenses [337], but individual lenslets were produced serially, resulting in long production times and similar issues as with embossing beryllium.

Here, a novel route for x-ray lens manufacture is proposed that harnesses the high transmittance of low-Z thermoplastics and is suitable for cheap mass production, while capitalizing on the technological advantages of structuring silicon without sacrificing achievable resolution. CRLs made of polyethylene (PE) were injection molded from a nickel mold insert produced by electroforming from an etched silicon master. Compared to silicon, PE has a fourfold greater D_{eff} at 15 keV (cf. Figure 2.8), enabling one to halve the achievable spot size with a tenfold increase in photon flux density (i.e. gain) considering a line-focusing lens.

6.3.2 Silicon master

The silicon master was fabricated according to Strategy B presented in Chapter 4.3. The wafer design XOPTIX12 is shown in Figure 4.7. The lens patterns including sacrificial features are illustrated in Figure 4.2. The CRLs were characterized by R = 50 µm or R = 20 µm, d = 20 µm or d = 5 µm, $2R_0$ = 300 µm, and N varying between 41 and 147. The target etch depth was 200 µm. The shape defining trench width was 15 µm, the wall thickness 4 µm and the diameter of the pillars 5 µm, while the mean spacing between pillars was 7 µm. The manufacture of the silicon master included standard UV-lithography and pattern transfer by reactive ion etching into a thermally grown 700 nm thick silicon oxide layer, which served as a hard mask for DRIE of the silicon using the optimized Bosch process (cf. Chapter 3, Chapter 4.3 and Table 3.1).

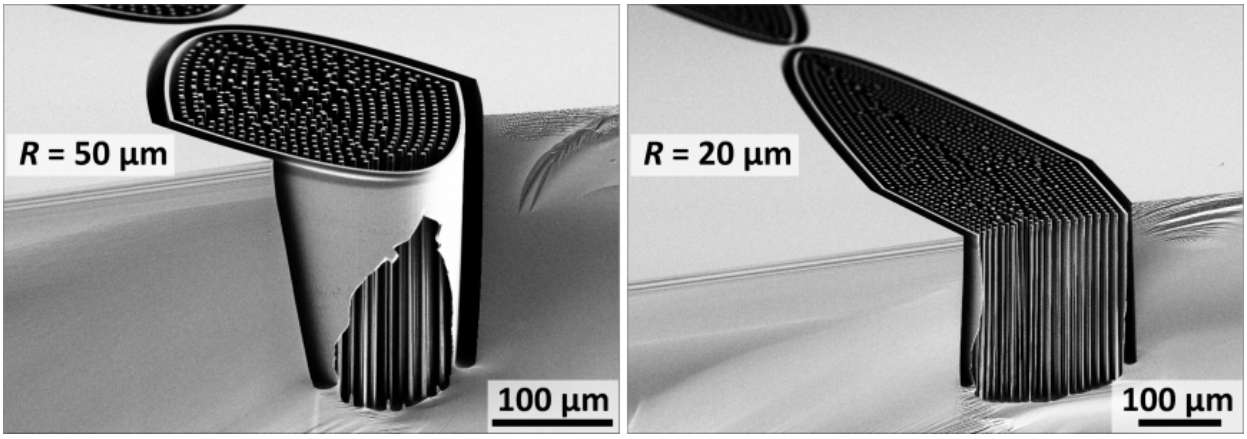

Figure 6.23. SEM images of cross sections of the silicon cavities after DRIE. View angles are 30°.

DRIE was a critical process step in ensuring the near-90° sidewalls required to guarantee both lens uniformity and the successful release of the polymeric part from the mold. To this end, we utilized sacrificial structures, which facilitated accurate profile control. Figure 6.23 illustrates these structures, where trenches define the perimeter of silicon cavities, thin walls confine the trenches and the remaining space inside the cavities is uniformly filled with pillars. This design reduced the etch load and allowed a local control of the etch depth by adapting the mean spacing between pillars to the width of the trench. The thickness of the wall and the diameter of the pillars allowed their complete thermal oxidation after DRIE and their selective removal by etching in hydrofluoric acid (cf. Figure 6.24).

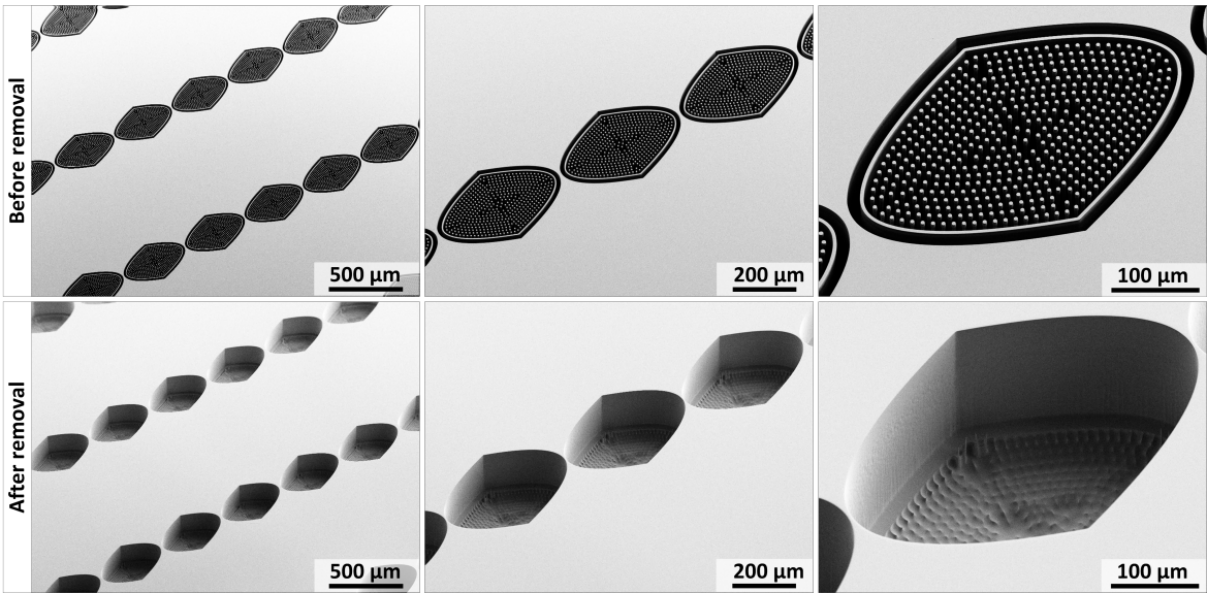

Figure 6.24. SEM images of the silicon master before and after removal of sacrificial structures.

Optical profilometry confirmed that the etched sidewalls were slightly positively tapered by 0.5°, which favored a successful release of the injection molded polymeric part. The parabolic shape at the apexes of the silicon cavities were characterized based on atomic force microscopy (cf. Chapter 5.5). Due to the slightly tapered sidewall, R varied by ±2% along the 200 µm deep structure. In comparison to lenses of type XOPTIX8 and manufactured using strategy A, the uniformity of R over the depth was considerably improved (cf. Figure 6.9). We accepted this minor deviation from an ideal cylindrically parabolic shape for the first demonstration of the injection molded polymeric lenses.

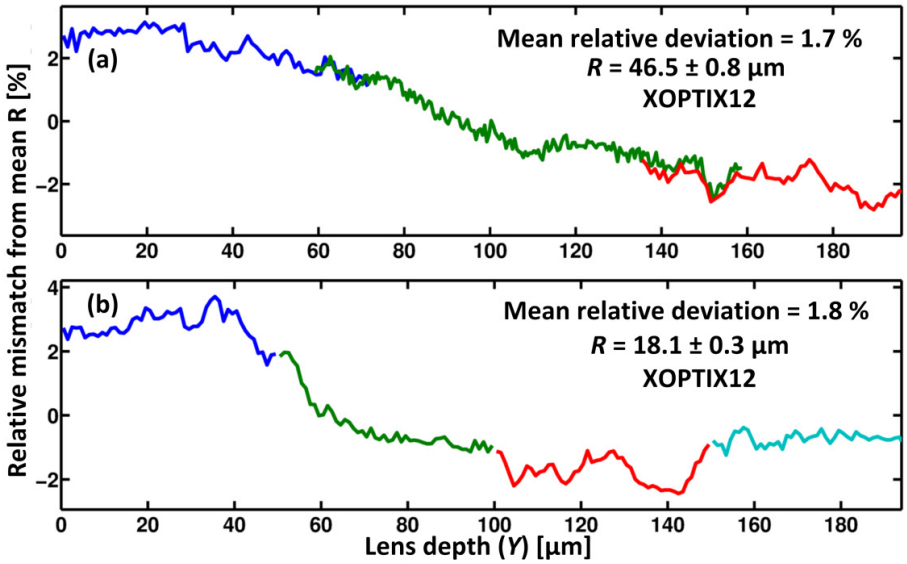

Figure 6.25. Variation of the radius of curvature along the etch depth obtained by fitting individual AFM profiles to parabolas. Different colors correspond to data originating from different AFM scans. (a) Lenses with nominal R = 50 µm. (b) Lenses with nominal R = 20 µm. Cf. Figure 6.8 for axis assignments.

6.3.3 Mold insert manufacture

The mold insert was obtained following the process flow illustrated in Figure 6.26. First, the silicon master was uniformly covered with a 70 nm thick layer of amorphous silicon by low pressure chemical vapor deposition (LPCVD), sputter coated with a 50 nm thick seed layer of a nickel-vanadium alloy (Kurt Lesker), and then conformably electroplated with nickel (microform.200, Technotrans). Special attention must be paid during wetting of the Si wafer with the provided solution prior to its immersion into the plating bath. It must be ensured that all cavities have been wetted to avoid any voids during plating. The total charge transferred onto the wafer was 30 Ah with a maximal current of 3.5 A over a time period of 9.5 hours.

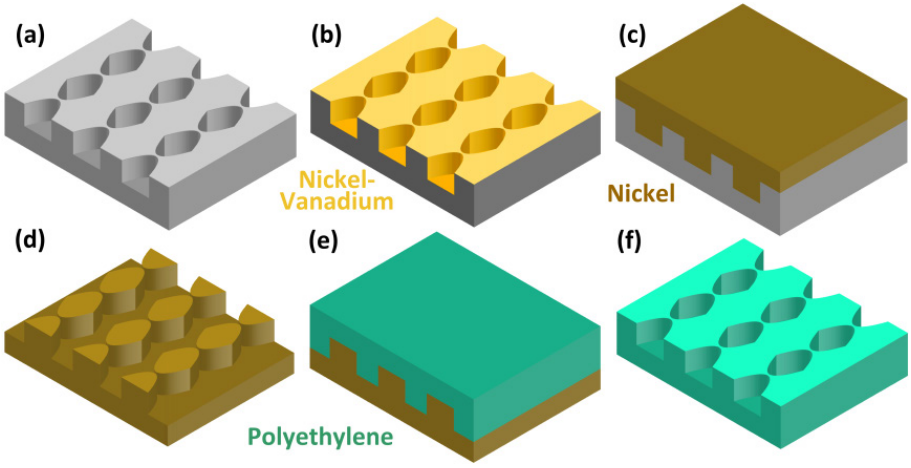

Figure 6.26. Process flow for injection molded x-ray lenses. (a) The silicon master is fabricated using Strategy B. (b) Sputter coating with a NiV-seed layer. (c) Nickel electroplating. (d) Silicon removal. (e) Polymer injection (e.g. polyethylene). (f) Demolding of the polymeric part.

By dissolving the silicon in aqueous potassium hydroxide (KOH), a 550 µm thick nickel wafer was obtained, which included the inverse lens structures (cf. Figure 6.27 and Figure 6.28). The nickel surface was functionalized with a self-assembled monolayer of a fluorocarbon-containing thin film (FDTS) using molecular vapor deposition (MVD).

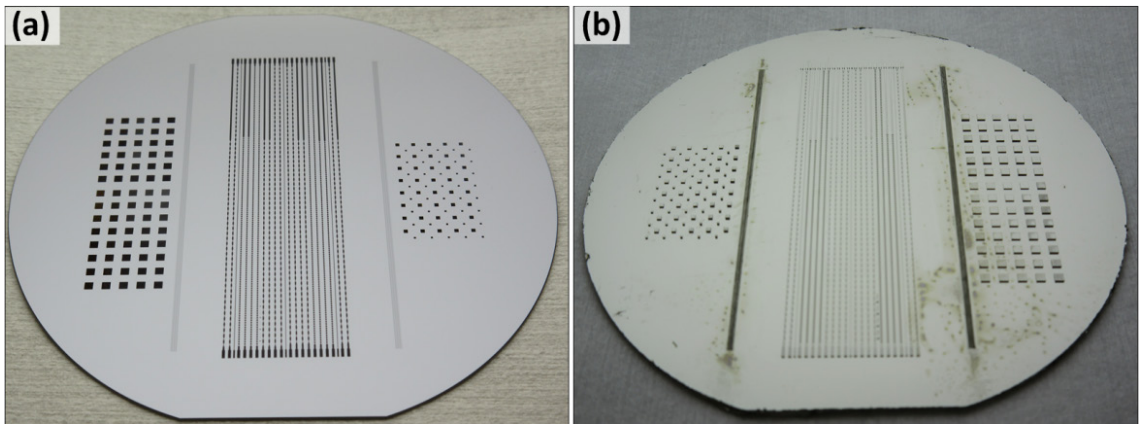

Figure 6.27. Photographs of wafers with design XOPTIX12. (a) Silicon master. (b) Electroplated nickel.

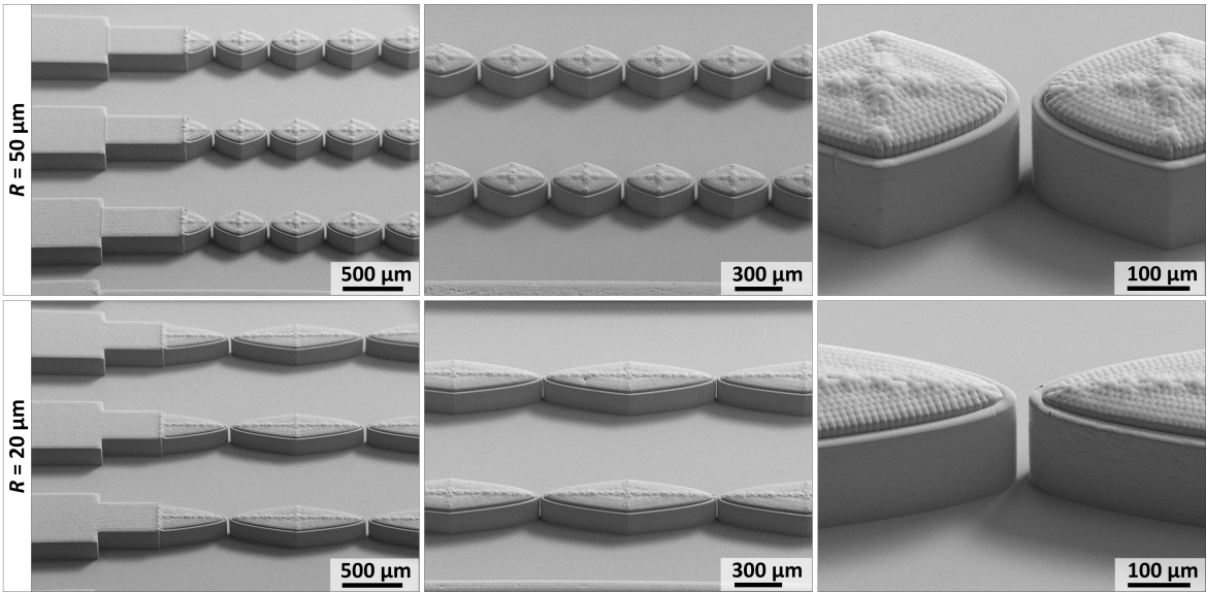

Figure 6.28. Scanning electron micrographs of the nickel mold insert.

6.3.4 Polymer injection molding

A shim was cut from the wafer by laser micro machining and inserted into the tool of an ENGEL Victory Tech injection molding machine (cf. Figure 6.29(a)). Linear low-density polyethylene (LLDPE, Flexirene® MT40A, Versalis) was used as the thermoplastic, due to its high melt flow rate, flexibility and high shrinkage upon solidification, which in combination guaranteed uniform mold filling and eased the release of the polymeric part. Its chemical formula is $(C_2H_4)_n$ and its density as specified by our supplier is 0.925 g/cm^3 (μ = 0.523 cm^{-1}, refractive index decrement $\delta = 7.584 \times 10^{-7}$ for E = 17 keV). Different thermoplastics have been tried, namely cyclic olefin copolymers (COC, 5013L-10 and 8007S-04, TOPAS) and polypropylene (PP, HD120MO, BOREALIS). Unfortunately, these other polymers were more rigid than LLDPE and did not show good results with respect to the demolding behavior and lens shape. However, optimizing the nickel shim, the tool and the demolding mechanism may allow a wide variety of different thermoplastics to be used.

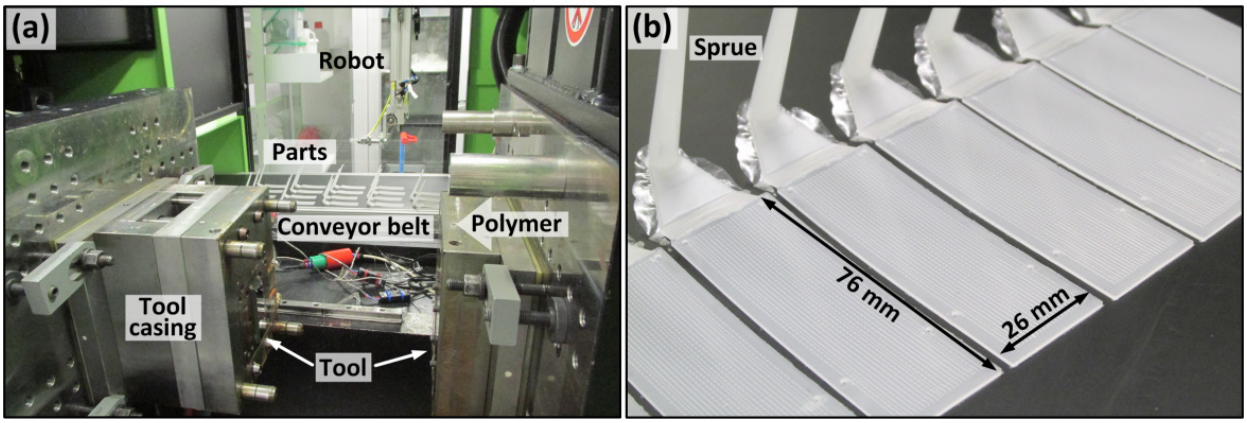

Figure 6.29. Photographs of (a) the injection molding machine and (b) polymeric lens parts.

Polymeric chips with dimensions of 1 × 26 × 76 mm^3 comprising 20 CRLs with up to N = 143 lenslets each and additional trenches for alignment were injection molded. A variotherm process with a cycle time of ~5 min was optimized. The nozzle temperature was 200°C, the injection speed 50 cm^3/s, the injection and holding pressures 600 bar, and the holding time 10 s. The mold temperature was 100°C during polymer injection (i.e. above the glass transition temperature of LLDPE) and was cooled below 25°C for releasing the polymeric part (cf. Figure 6.29(b)).

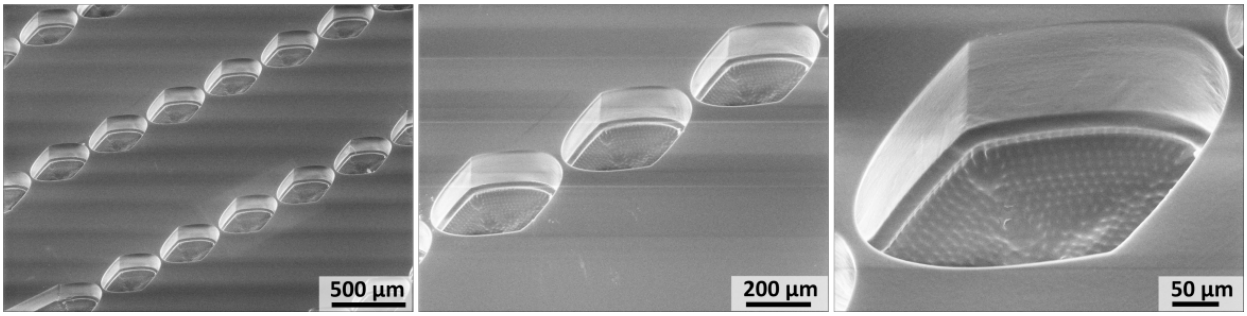

Figure 6.30. SEM images of injection molded polymeric lenses.

Figure 6.30 shows the final injection molded x-ray lenses. The lens sidewalls do not reveal any notable differences to the silicon master. The lens top surface was inspected by optical microscopy and the geometrical shape was analyzed by fitting parabolas to the lens edges, resulting in R = 52.5 ± 0.5 µm and a mean deviation from a perfect parabola of ~700 nm (Figure 6.31, cf. Chapter 5.2). The deviation from the nominal shape is due to polymer shrinking, which needs to be compensated for in future. Buckling of the parabola apex is visible, which is more pronounced on one of the parabolas and indicates local mechanical stress.

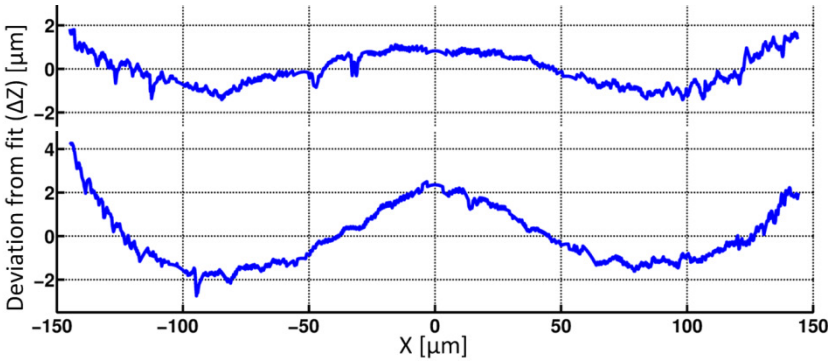

Figure 6.31. Differences between the detected edges and the fit curves of both parabolas of one lenslet. For axis assignment cf. Figure 5.2.

The most critical step during injection molding was the release of the polymeric part from the mold, which, if non-optimal, mostly affected the bridges between individual lens cavities. Figure 6.32 show these regions of lens structures with bridge thicknesses d = 20 µm and d = 5 µm. While the 20 µm thick bridges are mostly intact, deformations and partial rupture of the 5 µm thick bridge are clearly visible. This indicates that the latter bridge caused sticking of the polymeric part on the nickel mold and the part was released under mechanical stress. Since we included both structures on the same mold next to each other, mechanical strain on one feature

also affected the other. Hence, a future iteration needs to guarantee a release free of mechanical stress and a mold without any structures that may cause mechanical adhesion.

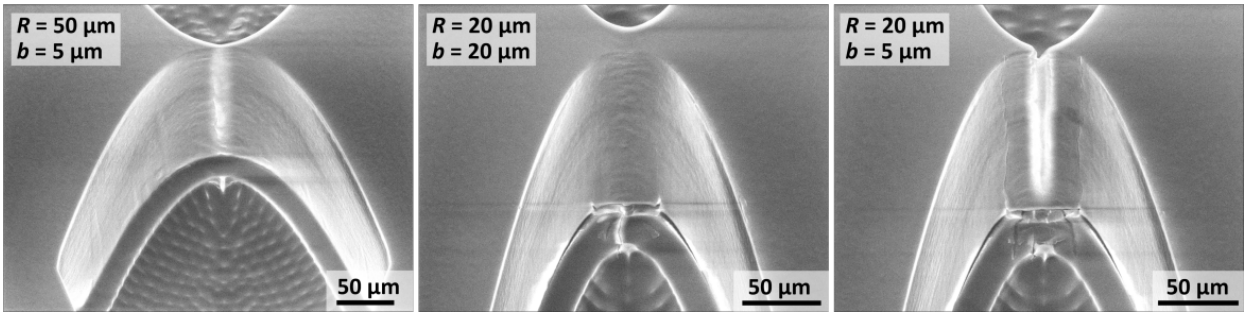

Figure 6.32. SEM images of the bridges between polymeric lens cavities.

Figure 6.33 shows the cavities at different positions relative to the injection nozzle. No differences of the sidewalls are apparent, however, the bridges are more deformed further away from the nozzle (lenslet 100). In fact, the demolding mechanism pulls on the sprue at the nozzle. Hence, demolding is most effective in this region.

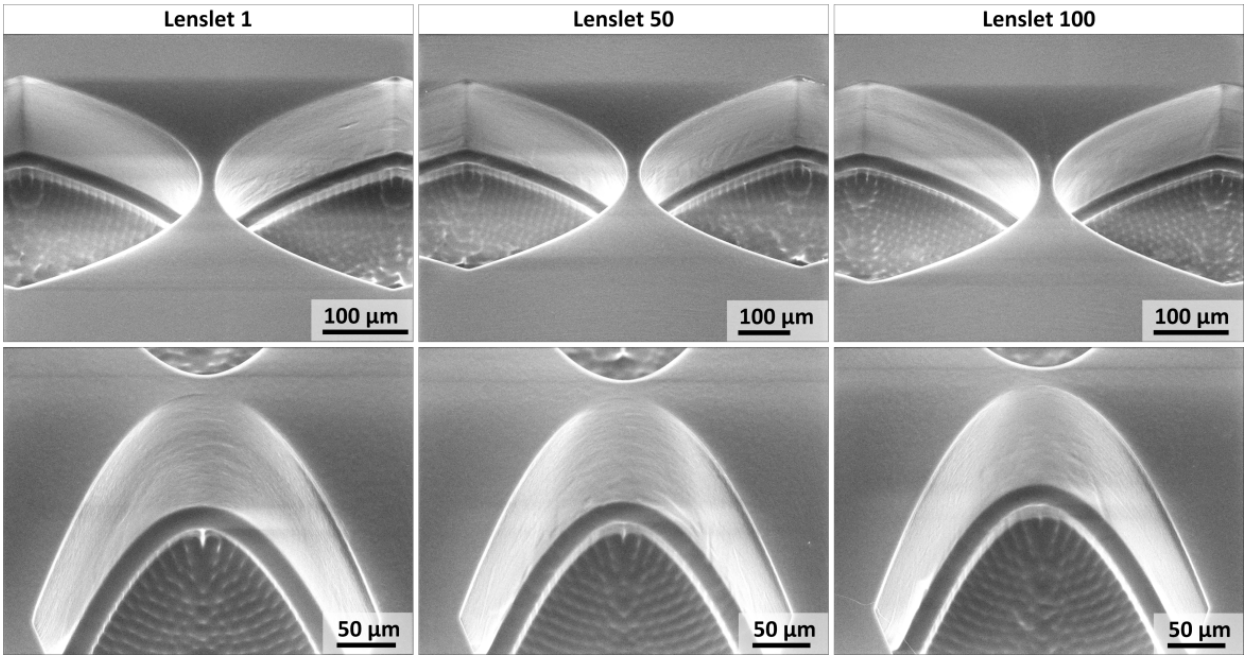

Figure 6.33. SEM images of the bridges between polymeric lens cavities. R = 50 µm, d = 20 µm.

6.3.5 Optical performance

The x-ray optical performance of a LLDPE CRL with R = 50 µm and N = 101 was tested by directly imaging the focused beam using a bright field x-ray microscope (cf. Chapter 5.6.5). The experiments were carried out on 6th May 2015 at the beamline ID06 at the ESRF. The optical setup is illustrated in Figure 6.34. The polymeric lens was mounted for vertical focusing 51 m downstream the undulator source and the x-ray energy was set to E = 17 keV by a Si(111) double monochromator ($\Delta E/E = 1.4 \times 10^{-4}$). A second CRL composed of 71 beryllium lenslets with R = 50 µm and a focal length p = 0.325 m was used as an x-ray objective to image the

focused beam at a distance q = 4.71 m, giving a magnification $M_{\text{x-ray}} = q/p$ = 14.5. A high-resolution detector comprising a scintillator screen coupled by microscope optics with magnification M_{Vis} = 10 to a FreLoN CCD camera with pixelsize Res_{CCD} = 14 µm was used. This yielded a theoretical spatial resolution of $Res_{\text{CCD}}/M_{\text{Vis}}/ M_{\text{x-ray}}$ = 97 nm.

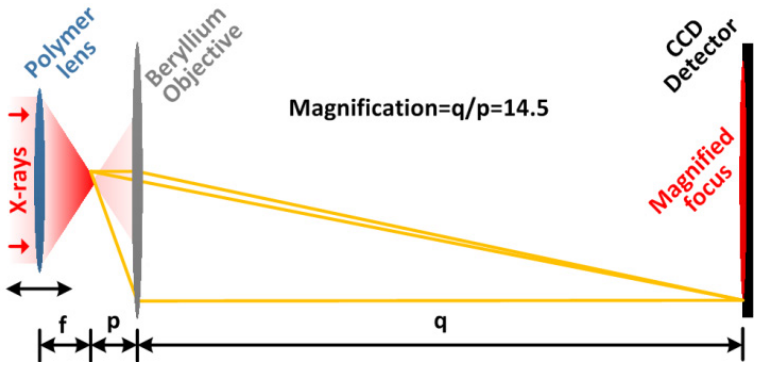

Figure 6.34. Setup for testing the optical performance of polymeric lenses.

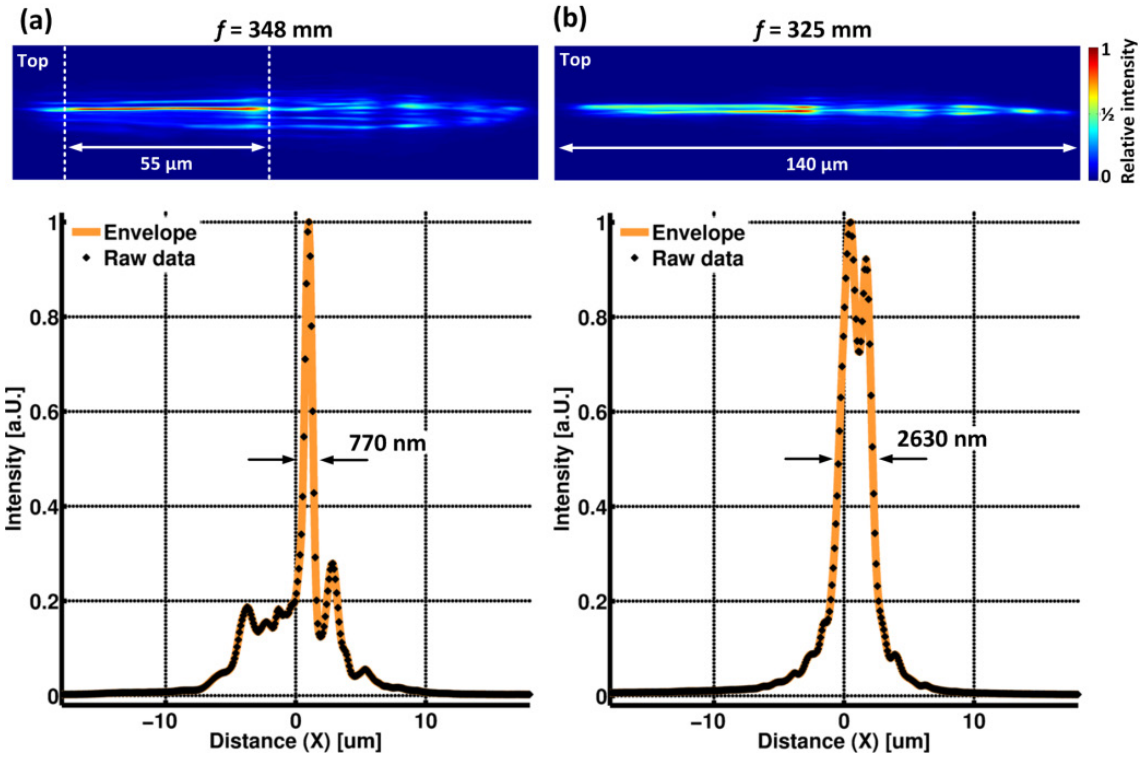

Figure 6.35. Image of the focal line and summed intensity at (a) f = 348 mm and (b) f = 325 mm. In (a) only the 55 µm long marked section contributes to the intensity profile.

Beam profiles were recorded while the position of the objective was fixed and the polymeric lens moved along the optical axis.[30] A 55 µm-long line focus with a waist of 770 nm (FWHM) was observed at f = 348 mm, which shows the high potential of injection molded polymeric lenses (cf. Figure 6.35(a)). However, the beam profile was highly irregular, whereas the

[30] See https://www.osapublishing.org/ome/viewmedia.cfm?uri=ome-5-12-2804&seq=v001 for a sequence of magnified images of the focused x-ray beam (Dec 2015).

uppermost part of the lens generally outperformed the lowermost. The complete, 140 µm-long line was 2.7 µm wide (FWHM) at f = 325 mm (cf. Figure 6.35(b)). The total transmittance of the lens was 32%, which corresponds to a gain in photon flux density of 125, assuming the measured 770 nm small focus and neglecting the large tails around the peak. For an ideal lens a transmittance of ~50%, a spot size of 170 nm and a gain of 600 were expected (cf. Chapter 2.2).

6.3.6 Discussion

This first optical test demonstrated the potential of injection molded x-ray lenses and future improvements can be readily realized. The observed irregularities in the beam profile likely originated from mechanical deformations of the lenses that occurred during the release of the polymeric part in the injection molding process. We anticipate that avoiding mechanical stress during demolding would substantially improve the optical performance of the lenses. The mold insert could be redesigned, such that friction is largely reduced, or additional ejector pins could be integrated into the tool to result in a more gentle release. The deposition of a thin layer of SiO_2 or Al_2O_3 by atomic layer deposition onto the nickel sample prior to MVD may increase the surface coverage and promote the adhesion of the anti-stiction coating applied [496]. Using thermoplastics with higher shrinking coefficients may further reduce mechanical adhesion.

The discrepancy in photon transmittance was partially due to a slight warpage of the polymeric chip, which reduced the effective depth of the lens from 200 µm to 140 µm. Furthermore, our polymer maybe contained residues of high-Z atomic species, which caused additional x-ray absorption.

The height of the lenses can be increased by optimizing DRIE during fabrication of the silicon master, which may include a redesign of sacrificial structures to guarantee deeper vertical etching. The encountered variation of the radius of curvature along the height of the lenses $\Delta R = \pm 2\%$ directly relates to a variation in focal length via $\Delta f = \Delta R / 2N\delta = \pm 2\%$. This variation must be reduced in the future, since it is significantly larger than the depth of focus (~1 mm, cf. Chapter 2.4). A more accurate control of the sidewall profile can readily be achieved by means of a more extensive optimization of the etching process of the silicon master [150]. Although, in terms of economy, this will consume additional resources, it will be insignificant, not least because we expect that more than 1000 polymeric parts may be obtained from a single master [497]. As an alternative to DRIE of silicon, x-ray lithography may be used to produce the mold insert (cf. Chapter 2.3.3, [248]).

In the x-ray community it is well known that degradation of polymer in the x-ray beam may be a show stopper for these types of lenses. It is known that the primary damages caused by radiation interaction with polymers are chain scission and cross linking. The first interaction softens the polymer, while the latter makes the polymer brittle. In fact chain scission is used in DXRL to make PMMA soluble. However, the illumination doses used in DXRL are relatively high and probably not representative for a highly monochromatic hard x-ray beam. Direct etching of polymers using x-rays is also known [326]. However, this also necessitates high photon fluxes and typically low energy x-rays. Generally, too little experimental data on the response of polymeric materials to the exposure of x-rays with energies higher 10 keV is available yet in literature. In the context of x-ray lenses, the lens shape and the chemical composition may be

affected, which both alters the optical qualities. These potential effects need to be addressed in the future. Over the course of the ~10 h long experiments performed here, no evidence for the degradation of the polymer in the x-ray beam was observed.

Comparable lenses made of SU-8 by x-ray lithography routinely produce focused x-ray beams with sub-micron spot sizes (FWHM) which are stable over extended time periods [245]. SU-8 polymer contains aromatic rings, which are known to be more radiation resistant. However, SU-8 also contains photo-initiators with strongly absorbing high-*Z* elements, in particular antimony, which besides x-ray transmission may also negatively affect the polymer. Restricting the use of polymeric lenses to shaping weak x-ray beams such as strongly monochromatized synchrotron radiation as in our study or those generated by x-ray tubes in small laboratory instruments would relax the requirement on radiation stability. However, long-term tests remain necessary to verify the radiation stability of lenses made of PE. Additionally, the precise composition of the polymer needs to be analyzed for residual elements other than oxygen and carbon, which e.g. were necessary during catalysis in the production of the polymer.

LLDPE was primarily chosen because it has excellent rheological properties. From the lens manufacture by injection molding point of view a plethora of thermoplastics exists: the list of materials may at first be reduced to those composed of low-*Z* elements. A suitable polymer should be easy to mold, easy to demold and stable in the x-ray beam. LLDPE was suitable for our proof of concept experiments to demonstrate that our approach is viable, but eventually it may not be the ultimate polymer to be used as an x-ray lens material due to (yet unknown) potential degradation in the beam. Polystyrene (PS) with pendant aromatic groups may be a viable alternative thermoplastic with respect to radiation resistance. Notably, however, PS is harder to process due to its generally low shrinkage and high rigidity.

6.4 Strategy B: Kinoform 1D Si lenses

While planar technology offers great design freedom and precision, silicon lenses are subject to x-ray absorption, which ultimately limits their effective optical apertures and thus their optical performance (cf. Chapter 2.2). To overcome this constraint, passive parts of lens material that merely cause absorption and a 2π wave front phase shift may be removed from the light path to obtain so-called kinoform lenses (c.f. Figure 6.36 and Chapter 2.2.7). This kinoform design allows lenses with higher transmittance and higher numerical apertures, hence more efficient optics yielding smaller, more focused beam waists.

Traditionally, lens patterns were etched directly (i.e. without utilizing sacrificial structures), and hence suffered from the aforementioned difficulties during DRIE (cf. Chapter 4.1). Consequently, silicon x-ray lens heights rarely exceeded 50 µm, and kinoform lenses were additionally prone to failures due to their sharp corners and thin triangular elements. Here, Strategy B was applied to increase the heights of kinoform lenses (cf. Chapter 4.3). The lenses were tested in terms of their focusing ability and refracting qualities using synchrotron radiation. Respective results were published [150].

6.4.1 Design

Kinoform lenses were designed for an x-ray energy E = 17 keV corresponding to a 2π path length λ/δ = 43.7 µm (c.f. Figure 6.36(a), wavelength λ = 0.73 Å, $\delta = 1.67 \times 10^{-6}$ for silicon). CRLs composed of N = 40 to N = 80 lenslets were arranged on six chips on a 4-inch wafer (cf. Figure 6.37).

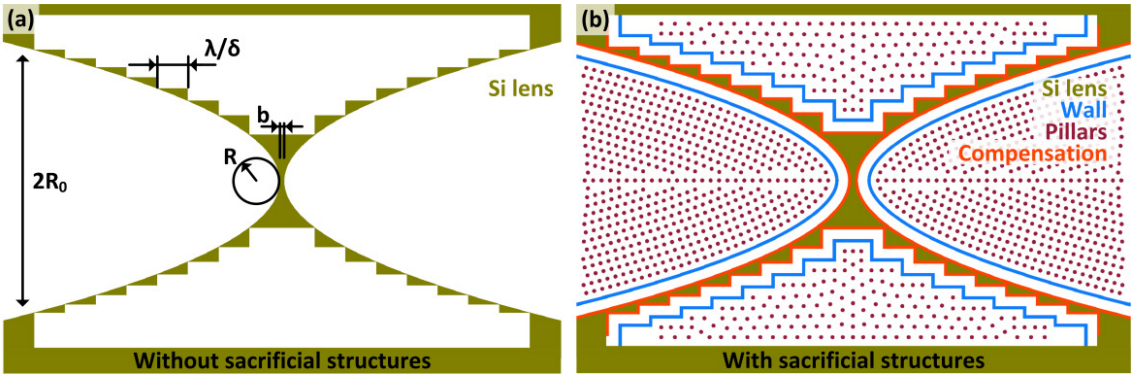

Figure 6.36. Single kinoform lenslet (a) with and (b) without sacrificial structures.

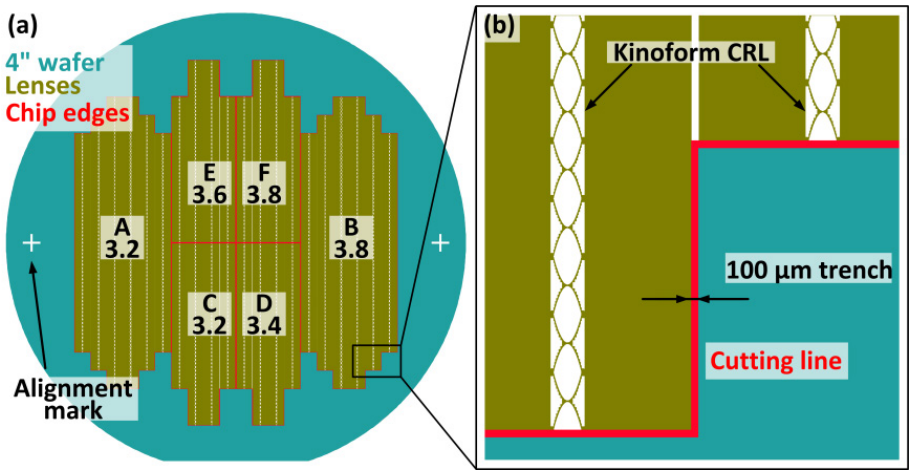

Figure 6.37. Wafer design XOPTIX13. (a) Full 4-inch wafer layout. Six chips differ by the degree of shape compensation. Alignment marks are exaggerated. (b) Zoom-in highlighting parts of CRLs and the laser cutting line.

The radius of curvature R_n and the aperture $2R_{0,n}$ of the nth lenslet were adapted to the contraction of the x-ray beam inside the lens, i.e., lenslets were arranged in an adiabatic fashion (cf. Chapter 2.2.8). The lenslet at the entrance of the CRL with N = 60 was specified by R_1 = 50 µm and $2R_{0,1}$ = 400 µm, while the lenslet at the exit of the CRL was specified by R_{60} = 41 µm and $2R_{0,60}$ = 360 µm. The total length of that CRL was 49 mm. The bridge thickness b was constantly 6 µm. Lens patterns including sacrificial structures were drawn using a code written in MATLAB, including a mesh generator for the uniform placement of dots [498] (cf. Figure 6.36(b)) The design parameters were t = 15 µm, w = 4 µm, p = 5 µm, and s = 7 µm (cf. Figure 4.2). Consumption of silicon, which occurred in the course of thermal oxidation and subsequent selective SiO_2 etching for sacrificial structure removal, was compensated for in the design by adding a uniform layer around the lens patterns. Individual chips on the wafer varied by the

degree compensation for shape widening (u = -3.2 µm to u = -3.8 µm, cf. Chapter 2.4). The total etch load of this wafer was ~7%.

6.4.2 Microfabrication

The kinoform lenses were fabricated according to Strategy B presented in Chapter 4.3. Subsequent to DRIE, surface smoothing and sacrificial structure removal, individual chips were diced using laser micromachining and ready to be used for x-ray focusing (cf. Chapter 3.7). Figure 6.38 shows cross sections of lenses after DRIE, where cleavages were obtained at different positions across the features illustrating the integrity of sacrificial structures and realization of uniform etch depths. The pillars have an aspect ratio of ~50, are intact, but show a slight bowing indicating lateral etching. The guarding wall is intact, but partial breakthrough is visible. The corners of the steps are sharp at the top ~100 µm, but slightly positively tapered toward the bottom.

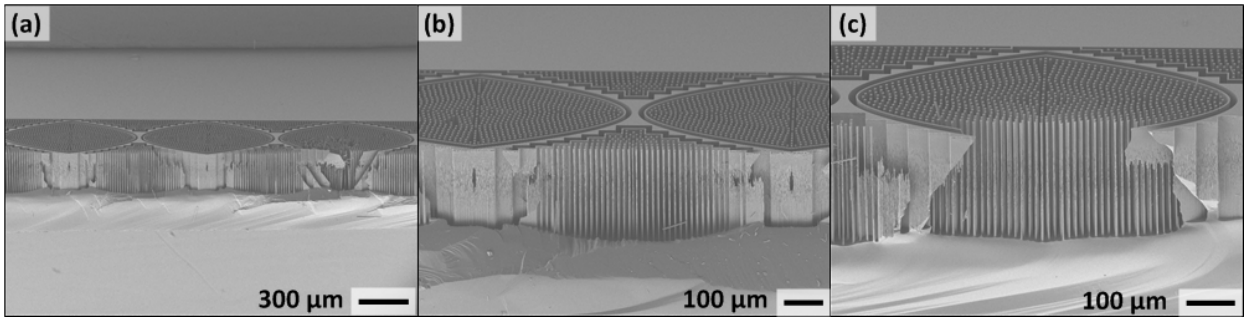

Figure 6.38. Scanning electron micrographs of cross-sections of deep reactive ion etched kinoform x-ray lenses before sacrificial structure removal. (a) Extended view. (b) and (c) Close-ups with different lines of cleavage. The view angles are 60°.

Figure 6.39(a) shows a top view of a kinoform lenslet after DRIE and Figure 6.39(b) after the complete removal of sacrificial structures by thermal oxidation and bHF etching. The compensation of silicon consumption was effective, resulting in kinoforms close to their nominal dimensions. Figure 6.40 shows a section of the CRL composed of 60 lenslets without any notable defects. No breakthrough occurred at the corners of the steps. The visible bright shades indicate that the silicon is locally thin and that the sidewalls are slightly bowed.

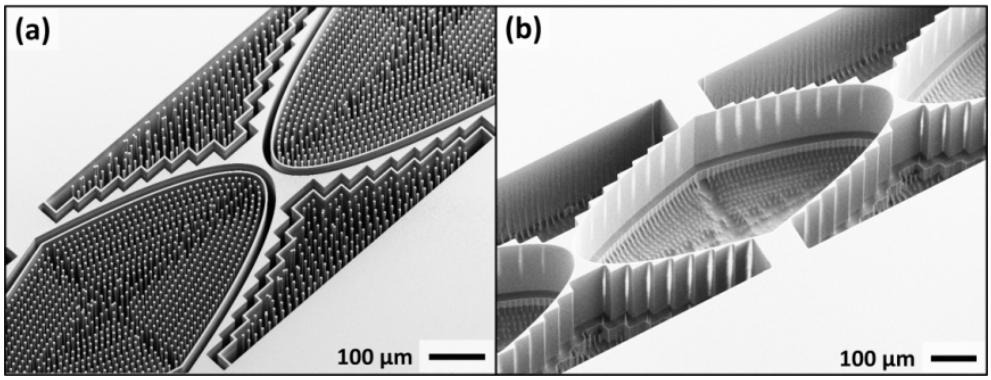

Figure 6.39. Top view kinoform lenses (a) before and (b) after removal of sacrificial structures. The view tilt angle is 30°.

A top view of the steps (cf. inset in Figure 6.40) reveals sharp convex and rounded concave corners, which are due to the physics of the oxidation [411]. The rounded corners clearly affect the lens shape and will locally cause additional refraction. The length of the kinoform steps is 44.4 ± 0.7 µm and deviates up to 3 % from the nominal value. For optimal focusing and a maximum wavefront distortion of λ/4, this deviation should be less than 0.3 %. The bridge thickness *b* is 7.2 µm. Hence, not enough silicon was consumed relatively to the original design. However, additional thermal oxidation would most likely have caused partial breakthrough of the sidewalls and we accepted these minor shape deviations for an optical test.

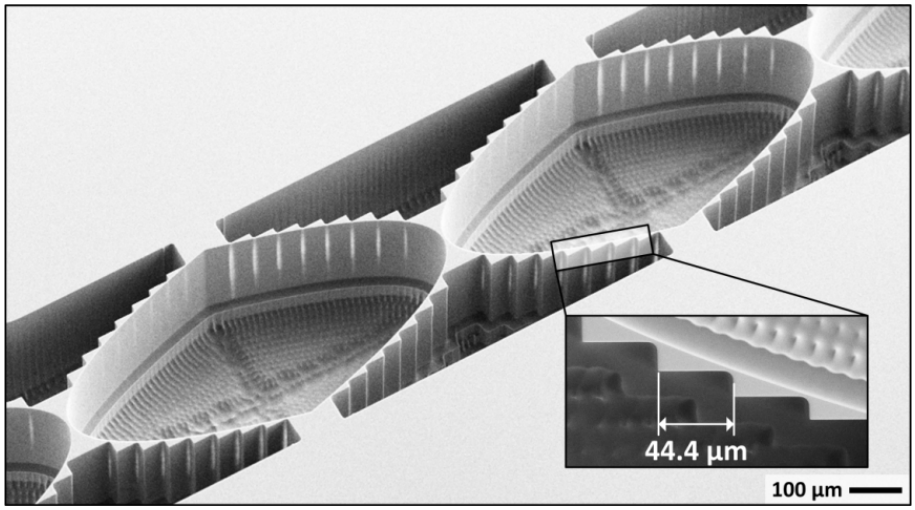

Figure 6.40. SEM image of deep reactive ion etched kinoform x-ray lenses after the removal of sacrificial structures. Note the bright vertical stripes indicating the thinness of the sidewalls at the step boundaries. The view tilt angle is 30°. The inset shows a top view of the kinoform steps.

6.4.3 Optical performance

The x-ray optical performance of a kinoform CRL was tested on 16th – 17th April 2015 at the beamline ID06 at the ESRF (cf. Chapter 5.6.5). Two types of experiments were performed. The first sought to determine how different regions across the lens aperture shaped the incoming beam, whereas the second specifically concerned the achieved spot size (i.e., beam waist) as a function of the lens depth. The lenses were aligned for optimal transmission, i.e., parallel to the incoming beam direction, and the detector was placed at twice the focal length $2f$ = 430 mm (cf. Figure 6.41). A horizontal slit was adapted to the depth of the lenses (d = 200 µm) and a vertical slit with an opening of ~5 µm was scanned across the aperture of the lens in steps of 2.5 µm. Figure 6.42 shows the transmitted beam monitored on the CCD as a function of the slit positions, whereas the beam intensity was summed in the direction of the lens depth.[31] The diagonal line indicates correct optical performance of the lens, i.e., rays impinging on a certain position at the lens aperture got refracted, pass the focal plane at a common focal position, and strike the detector at their conjugate positions.

[31] See ftp://ftp.aip.org/epaps/journ_vac_scitech_b/E-JVTBD9-33-316506 for a sequence of two dimensional radiographs (Dec 2015).

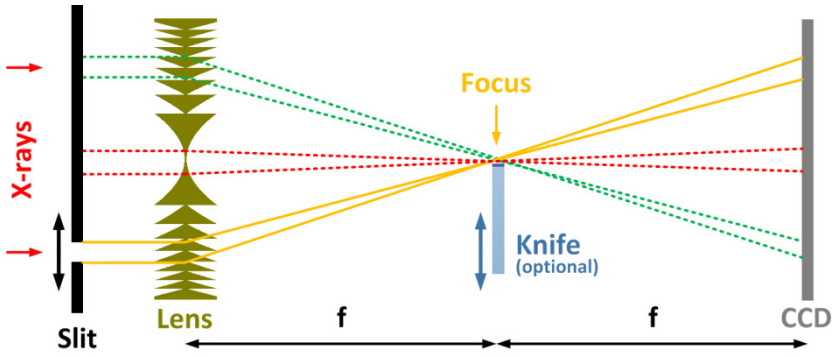

Figure 6.41. Conceptual drawing of the optical setup. A 5 µm wide slit was scanned across the lens aperture and the scattered beam recorded with a CCD detector positioned at twice the focal distance from the lens. A knife optionally inserted into the beam path is used for spot size measurements. The lens is shown as a folded kinoform for simplicity.

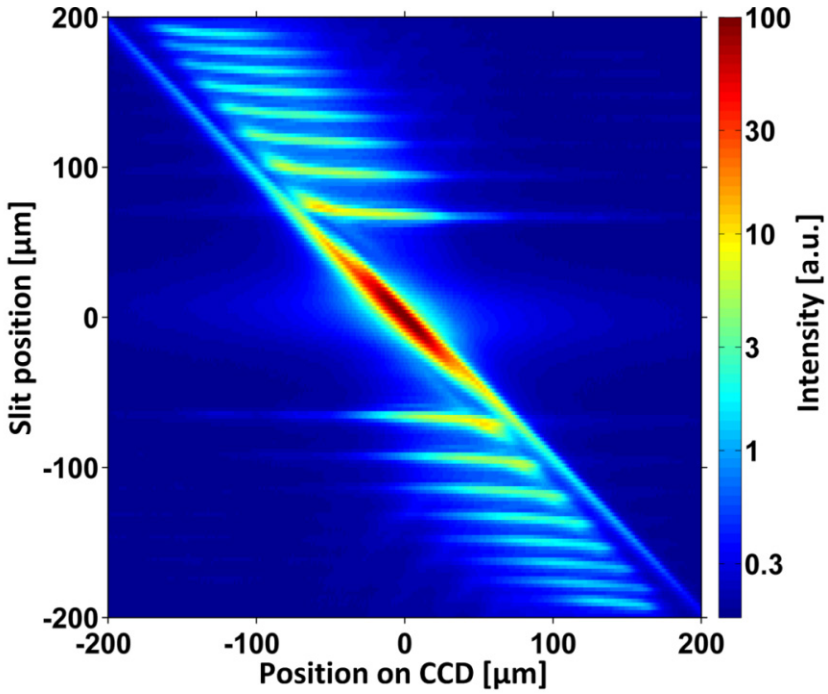

Figure 6.42. Optical transmission and refractive behavior of the silicon x-ray lenses. Surface plot of the x-ray intensity on the space resolved CCD according to the setup shown in Figure 6.41. The diagonal line indicates correct refraction of the x-ray beam. While the middle lens section is flawless, the kinoform steps scatter and reflect the beam wildly. Note the logarithmic scale.

The central, 100 µm-wide region showed flawless optical behavior and a lens transmittance of 21%, in agreement with theoretical expectations [164]. Optical performance in the regions of the kinoform steps was dominated by non-ideal x-ray scattering, i.e., departing from the bright diagonal line of intensity. We attribute this non-ideal behavior to successive total external reflection of the refracted beam at the sidewalls of the kinoform steps. Because the lens was composed of multiple elements, the beam converged inside the lens, which was intended to be compensated for by the adiabatic lens design. However, the beam converged faster than expected, which was to some extent caused by the additional curvature at the concave corners of the steps. Future lens designs thus need to take potential total reflection into account.

Additionally, dynamical diffraction need to be considered in the future [205]. The transmission at the kinoform steps was negligible relative to transmission at the central region. A total lens transmittance of 14.3% was expected, while a transmittance of 7.3% was measured. The gain in transmission compared to a non-kinoform lens was 1.3% and generally did not contribute to the focus.

Spot size measurements were performed by inserting an absorbing sample into the light path and taking knife-edge scans (cf. Figure 6.41). Figure 6.43(a) shows the result from such a scan. Calculating the derivative of the envelope of the raw data yields a waist of 430 nm (FWHM) of the focused ~180 µm long line beam. No notable difference in spot size was observed between illuminating the full aperture of the lens or only its central part. Figure 6.43(b) shows the center of the intensity profile of the transmitted beam. The transmission profile of the aperture is Gaussian with a $1/e^2$-width of ~60 µm, but with broad tails originating from the kinoform steps. The gain in photon flux density of the central part was 50. The uniformity of the beam intensity along the lens depth is ~94%, whereas the slight maximum at a depth of ~45 µm is most likely due to the aforementioned sidewall bowing and the cause for the variation at a depth of ~120 µm remains unknown.

The spatially resolved CCD detector allowed the focusing behavior along the lens depth direction to be measured. Therefore, the beam intensity on the CCD was divided into 50 µm long sections, which were analyzed separately. Knife-edge scans were performed at different positions along the optical axis around the focal position to obtain information pertaining to the depth-of-focus (cf. Figure 6.44). Focused beams from individual sections are close to Gaussian in profile. A minimum beam waist of 250 nm was measured for the top 50 µm section, which matches the ideally expected spot size (considering the diffraction limit and source demagnification). Generally, the topmost lens section outperformed the lowermost, and stronger focusing was observed at the bottom section of the lens. This decrease of the focal length from the top to the bottom of the lens can be attributed to a non-uniform shape along its depth. More specifically, the slanted focal plane can be attributed to a steady decrease of R along the depth of a lenslet, corresponding to positively tapered sidewalls ($\alpha \approx 90.5°$). In order to guarantee a uniform line focus with minimal waist, a future iteration needs to improve the verticality of the sidewalls to ~90 ± 0.05°. The averaged beam showed a depth of focus ~2 mm, determining the necessary accuracy for sample placement.

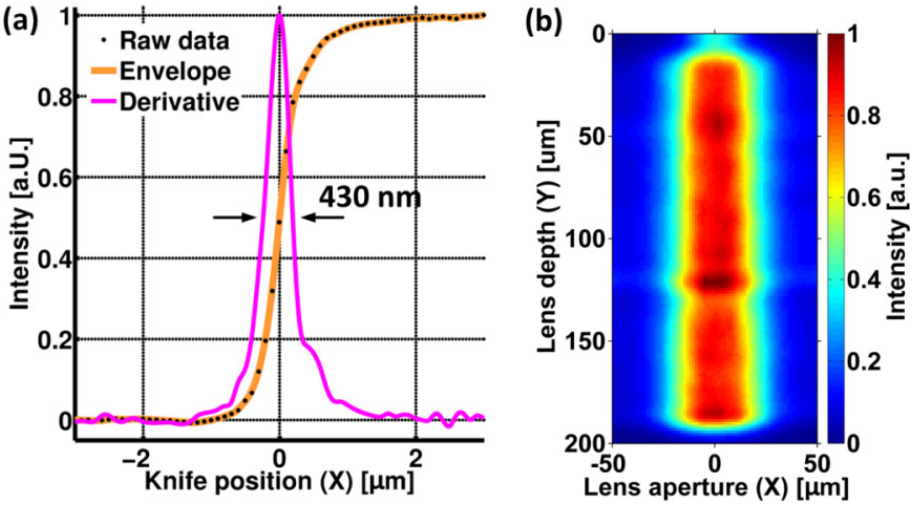

Figure 6.43. Beam focusing performance of the silicon x-ray lenses. (a) Integrated intensity on the CCD while the knife was scanned through the focal plane of the 180 µm long line beam. (b) CCD image of the projection of the same beam twice the focal length from the exit of the lens.

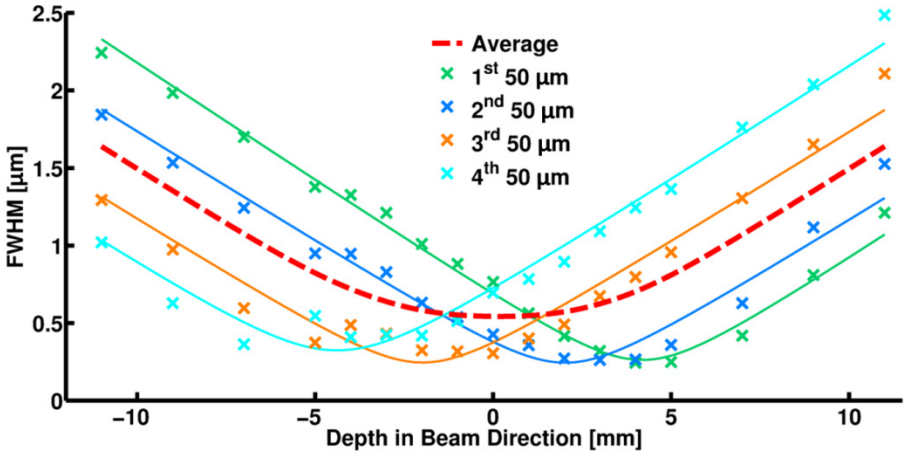

Figure 6.44. Depth of focus scans and separate analysis of different depths of the lens. The full lines are fits to the function of a Gaussian beam. The average of the individual Gaussian beams is indicated by a dashed line.

The demonstrated 180 µm-long line beam with a waist of 430 nm is remarkable and can be contrasted to the performance of similar silicon refractive optics discussed in literature [145,146,286]. Although the spot size does not reach ~50 nm, as was previously demonstrated with a 60 µm deep etched silicon lens with ~11 mm focal length [145], the lens depth achieved here is 3 times higher and the focal length of 215 mm provides ample space for sample surroundings. The over-depth uniformity of our lens was accomplished by the use of sacrificial structures. Our attempt to double the lens transmittance by a kinoform design failed due to our underestimation of the convergence of the beam inside the lens. Recent developments of kinoform x-ray lenses seem to concentrate on the fabrication of single plano-concave lens elements with relatively small radii of curvature, although some compound lenses are reported as well (cf. Chapter 2.2.7). Due to the parabolic profile, the steps of such lenses reach high aspect ratios very quickly at their apertures and the demonstrated utilization of sacrificial

structures for profile control may facilitate increasing the heights of future silicon kinoform optics.

6.5 Summary

The manufactures of four different x-ray lens systems has been presented. All systems share the novelty of utilizing sacrificial structures for improved sidewall profile control during DRIE. The structure heights of 1D-focusing silicon compound refractive lenses could be considerably increased beyond the traditional heights of 50 µm. Sub-micron focusing of a 310 µm wide beam was achieved using 56 keV x-rays. Sub-500 nm focusing of a 180 µm wide beam was achieved using 17 keV x-rays. The lenses have been designed for focal lengths >200 mm to leave ample space for sample surroundings. A prototype of a silicon x-ray objective has been demonstrated, showing acceptably low aberration and performance close to theoretical expectations. Polymer injection molded lenses have proven to be promising low-cost highly efficient x-ray optics.

7 Conclusion

The goals defined in the introduction are recapitulated and the achievements of this thesis work are summarized. Potential future improvements are outlined and this thesis is closed.

7.1 Recapitulation

7.1.1 X-ray lenses

Silicon CRLs made by lithography and DRIE are versatile x-ray optical components. They can be used for efficiently shaping high energy synchrotron radiation and are relatively easy to handle in experimental setups. Planar technology enables the parallel manufacture of multiple lenslets and their compact arrangement on chips to be installed in beamlines without complicated precautions. CRLs are generally easy to align, cheap, monochromatic and easily tunable on-axis devices that can withstand high heat loads. They may be used in the primary beam, are long lasting, and stable. CRLs show competitive optical efficiencies at x-ray energies around 20 keV, and have unrivaled optical characteristics when used with x-ray energies higher than 50 keV. Crucially, they are capable to produce x-ray beam waists well below one micrometer (cf. Chapter 1, Chapter 2 and Chapter 3).

Previously, Snigirev et al. was using Si-CRLs with 50 µm structure depth for focusing 50 keV x-rays and reported a line beam with a spot size of 150 nm (FWHM) ([146], cf. Chapter 2.3.4). In this case, the focal length and flux increase were 110 mm and 150, respectively. 1D focusing has also been demonstrated by lenses made in SU-8 by rarely available deep x-ray lithography with structure heights of 500 µm ([245], cf. Chapter 2.3.3). A spot size of 105 nm (FWHM) was reported, but it was not explicitly stated how long the measured line beam actually was – the test structure used was 120 µm in length. In this case the x-ray energy was 16 keV, the focal length 75 mm and the intensity gain 410. CRLs made by embossing are optically thick, expensive, and limited by the plasticity of the lens material; however, they enjoy a widespread use in synchrotron beamlines (cf. Chapter 2.3.2). Multi-prism lenses manufactured by e.g. anisotropically wet etching of silicon approximate the ideal refracting profile by multiple wedges and may deliver millimeter wide line beams, but face technological challenges if sub-micrometer focusing is required ([195,301,323], cf. Chapter 2.3.5). KB-Mirrors, Fresnel zone plates and multilayer Laue lenses are valuable alternative x-ray optical components, which, briefly speaking, are delicate with respect to their alignment, inefficient at high x-ray energies, or currently under development (cf. Chapter 1).

7.1.2 Microfabrication

Lithographic techniques allow defining the required parabolic shapes with high precision and repeatability (cf. Chapter 3). Furthermore, lithography supports great freedom in lens design and the realization of radii of curvature in the single micrometer range. DRIE is a popular industrial practice, capable of producing high-aspect ratio microstructures. It is a complex process, which requires the passivation and etching phases to be accurately balanced. Ionic species generated in the plasma play a crucial role. The directional bombardment of these species perpendicular to the substrate surface is affected by their thermal motion, collisions with other species and ion deflection at the etched sidewalls. Tuning of relevant process parameters such as the timing of phases, plasma density and composition can guarantee pure directional etching only to a limited extent. The exact geometries of the patterns to be transferred into the silicon substrate also have a significant effect on the etching.

7.1.3 Requirements

Planar CRLs etched into silicon require strictly parallel sidewalls (cf. Chapter 2.4). The exact tolerances heavily depend on the lens specifications, most importantly on the focal length and the x-ray energy. Non-parallel sidewalls result in a deviation from the ideal parabolic shapes and effectively cause a variation of the actual focal lengths along the height of a lens. To achieve a uniform focal line it is absolutely essential that this variation in focal length does not exceed the depth of focus. It was argued that for typical lenses the deviation of the sidewall profile from a strict vertical must be less than 200 nm, corresponding to sidewall angles of 0.1° for 300 µm high lenses. These are stringent requirements and may explain why Si-CRLs have usually been limited in height by ~50 µm. A highly precise fabrication asks in turn for adequate characterization procedures. Since the three-dimensional shape determines the device characteristics, the qualitative inspection of micro-features and their cross-sections by scanning electron or optical microscopy is not sufficient and must be complemented by more quantitative techniques such as optical profilometry or atomic force microscopy.

The primary aim of this thesis work is to increase the heights of Si-CRLs substantially and eventually pave the way towards fabricating 1 mm high lenses that allow creating low divergent x-ray line beams with waists in the order of 200 nm, which would have a significant impact on x-ray analytical techniques such as three dimensional x-ray diffraction microscopy.

7.2 Achievements

7.2.1 Design strategies

As a consequence of stringent requirements on the sidewall parallelism of planar CRLs and inherent limitations of merely optimizing processing parameters during DRIE, the problem of increasing lens heights was addressed by modifying the pattern that needs to be transferred into the silicon substrate (cf. Chapter 4).

Two different strategies were conceived, whereat both are based on defining the bi-parabolic cavities to be etched at their perimeter by trenches of uniform width. The two strategies differ in the way the unwanted material inside the cavities is removed subsequent to DRIE. Strategy A

utilizes wafer-through etching for releasing the sacrificial portions, whereas Strategy B relies on thin sacrificial structures that can be completely oxidized within a reasonable amount of time and removed by selective etching in hydrofluoric acid. Both strategies have proven to be equally successful in achieving a substantial increase of the heights of Si-CRLs. Both strategies facilitate accurate sidewall profile control necessary for uniform x-ray focusing. They are both relatively simple as only one lithography step is needed and single crystalline wafers may be used, i.e. no SOI wafers are required.

Strategy A can result in 350 µm high lenses without much difficulty, if the wafer is designed to guarantee its integrity over the whole manufacture (cf. Chapter 6.1). Through-wafer etching results in relatively fragile wafers and a final adhesive bonding step was found to efficiently stabilize the lenses, thereby enabling their safe handling. Strategy B is more versatile as it allows realizing more complicated structures such as kinoform lenses that are characterized by sharp and thin features (cf. Chapter 6.4). No additional process steps are needed, since thermal oxidation followed by wet etching is typically used anyway for smoothing the etched sidewalls and stabilizing wafer bonding is superfluous. The heights of lenses manufactured by Strategy B are limited by the achievable aspect ratio of the sacrificial structures. Aspect ratios of 50 and structure heights of 200 µm could readily be obtained.

Strategy A requires the optimization of DRIE only with respect to one simple feature – a trench of constant width – and is therefore conceptually simple. Strategy B includes relatively complex sacrificial structures in the form of thin walls and pillars with small diameters, whose dimensions and relative distances need to be matched to the lens shape-defining trench width. A respective systematic study has been performed, which allows optimal combinations to be chosen (cf. Chapter 4.3.3).

7.2.2 Metrology

A mix of characterization methods, including imaging the 2D top parabolic shape, optical profilometry of the etched sidewalls and tactile profiling the region around the apex using a large-range atomic force microscope (AFM), were used to obtain reliable information about the three dimensional shape of the lenses (cf. Chapter 5). Inverse replica molding was established as an effective way to circumvent limitations due to the finite lengths of AFM probes (cf. Chapter 5.5). A statistical analysis proved the method reproducible and reliable. Therefore, means have been found to accurately measure the deviations from the ideal parabolic shape, the sidewall verticality, sidewall straightness, magnitudes of sidewall striations, the general 3D shape uniformity, the shape fidelity at the apex, and the surface roughness.

Quantitative measurements are generally consistent with measurements of the optical performance of the lenses in the beamline. Small deviations from the parabolic shape at the lens apexes could be identified, which had a severe and adverse effect on the focusing behavior (cf. Chapter 6.1). Measured tapering or bowing of the sidewalls clearly corresponded to measured variations in focal lengths along the heights of lenses (cf. Chapter 6.1 and Chapter 6.4). The applied characterization procedures were found to be adequate for facilitating the manufacture by enabling process control and making inferences from optical experiments to potential improvements of the lenses.

7.2.3 High-energy Si 1D-CRLs

Applying Strategy A yielded a set of line-focusing silicon CRLs (cf. Chapter 6.1). A test of the optical performance showed focusing of a 56 keV x-ray beam into a 310 µm wide line and a waist of 980 nm (FWHM) at a focal length of 1.3 m, which leaves plenty space for sample surroundings. The signal-to-noise ratio is remarkable (cf. Figure 6.12). Observed non-uniformities of the focused x-ray beam were discussed and are in agreement with the lens shape measurements. Limiting factors for x-ray focusing were found to be a slight bowing of the lens cavity sidewalls and an insufficiently uniform definition of the lens apex.

With this particular lens, a minimum beam waist of 660 nm (FWHM) for the top 50 µm top most section was measured, while it increased to 930 nm for the bottom most section. Surface roughness in the form of vertical striations most probably originating from passivation built-up during DRIE was identified as the cause for this beam broadening. The variation in focal length spanned ±10 mm and needs to be reduced in the future to ±2.5 mm for optimal focusing. This means that the sidewall parallelism from now ±400 nm maximal deviation from a strict vertical needs to be improved to ±100 nm maximal deviation. Notably this stringent requirement must be met over the full height of the lens, which in the case presented here is 300 µm. Referring to Figure 4.6, this target can be met, given a sufficiently stable etching tool, a right choice of the shape defining trench width, and extensive DRIE parameter optimization.

The observed non-uniformity of the shape at the lens apex, i.e. the deviation from the ideal parabolic shape, suggests that the trench width needs to be reduced. The lenses had a nominal radius of 20 µm and the width of the trench was also chosen to be 20 µm. To allow a uniform definition of the lens shape the trench width should be reduced to ≤15 µm (cf. Chapter 6.3.2). The total transmission of the lens was in agreement with expectations (32%), the transmission was reasonably uniform over the full width of the beam and the gain in intensity was 97.

Despite the observed non-uniformities, the tested lens created the widest x-ray beam with a sub-micrometer waist produced with a Si-CRL at the time of submission of this thesis. Further improvements in lens design and processing are feasible and will eventually allow diffraction limited focusing of beams that are wider than 50 µm. The lenses have been commissioned at the beamline ID11 at the ESRF and are ready for use.[32]

7.2.4 Kinoform Si 1D-CRLs

By applying Strategy B it was sought to produce kinoform lenses meant to minimize x-ray absorption, thereby doubling the intensity in the focus, increasing the numerical aperture and potentially decreasing the beam waist (cf. Chapter 6.4). Their test showed correct refractive behavior, but also large detrimental scattering, which annihilated the potential merit of doubling the transmission compared to a standard CRL. However, the use of sacrificial structures generally allowed the focusing of 17 keV x-rays into a 180 µm-wide line with a waist of 430 nm (FWHM), which is a substantial improvement to what was available at the start of this thesis work. The focal length was 215 mm and the gain in intensity was 75. The lenses are currently

[32] Internal discussions have identified the variations of the transmission profile as a minor hurdle for applying the lenses without further considerations as condensers for 3DXRD or DCT. The apparent intensity variation may be corrected during the data analysis or even offer extra information for a reconstruction of grain positions.

available for use at the beamline ID06 at the ESRF and will facilitate x-ray microscopy of condensed materials.

Previous developments of CRLs at Diamond in the UK or Brookhaven National Laboratory in the US concentrated on kinoforms with single plano-concave silicon refractive lenses with radii substantially smaller than 1 µm [194,200]. It is anticipated that arrays of kinoforms must be used for improving the resolution [189,200]. As was recognized earlier, diffraction at the steep edges of the kinoform steps "distorts the desired converging wave field and degrades the focusing performance of a lens" [205]. Therefore, kinoform CRLs must be carefully designed in order to compensate "[…] possible aberrations due to highly distorted front wave incident on lenses […]" and "[…] follow the curvature of the wave refracted by the previous lens in the array" [200]. Until today, experiments have been performed with kinoforms with up to ten lenslets [186,189,195,206]. Most recent experiments using an array of four plano-concave lenses showed a clear discrepancy between theoretical and measured spot size and transmission, which was attributed to "[…] stringent demands on the fabricated structure's quality that were not met, resulting in a significant portion of the intercepted radiation not being delivered into the focal spot" [195]. Given this experiences and insights, it was maybe too ambitious to manufacture a CRL comprising 60 individual kinoform lenslets. The framework of geometrical optics used to design the kinoforms in this thesis does not account for diffraction and is probably inappropriate to evaluate its optical performance [205]. It was found that the CRL needs to be arranged in an adiabatic fashion to enable x-ray transmission additionally to the lens central part. However, other effects were detrimental with respect to delivering these additional x-rays into a common focus. It could not be elucidated what actually caused the observed scattering. Most probably it was caused by total external reflection at the sidewalls of the kinoform steps. Maybe, however, it was caused by diffraction and wavefront distortion. Future studies may shed light on this issue.[33]

7.2.5 Si 2D-objective

The challenge of making objectives in silicon by the interdigitation of lenslets alternately focusing in the vertical and horizontal directions was addressed (cf. Chapter 6.2). A functioning 2D silicon objective for use in a bright-field hard x-ray microscope was demonstrated. Applying Strategy A for the fabrication of 1D-CRLs yielded silicon slices that could readily be aligned using an optical microscope and a micromanipulator. The results are promising; showing acceptably low aberration and performance close to theoretical expectations. A resolution of 300 nm was achieved at E = 17 keV and $f \approx 300$ mm. By harnessing the potential for making more compact objectives and avoiding shape defects, one could significantly improve the focusing power, transmission and numerical aperture at hard energies, potentially realizing hard-XRM with sub-100 nm resolution. Furthermore, the improved focal power available to these lenses would enable shorter imaging distances that are both more mechanically stable and practically achievable in modest synchrotron beamline hutches or laboratories.

[33] The efforts necessary for optimizing the lens design and its manufacture need to be outweighed by the potential merit, which here is a doubling of the transmission relative to a standard x-ray lens.

The encountered variation in image contrast, making the same kind of features appear sometimes dark and sometimes bright, was attributed to defects in the lenses in the form of vertical striations caused by micro masking during DRIE (cf. Figure 6.20). These defects could be largely reduced by using a silica instead of the alumina mask, as was done for fabricating the latest version of 1D-focusing CRLs (cf. Figure 6.7), which would significantly improve the imaging homogeneity.

An slight astigmatism was observed [152], i.e. a difference between the focal positions in horizontal and vertical direction. It could be remedied by the addition of corrective focusing elements [269]. This highlights an important advantage of interdigitated geometries in the ability to incorporate optimized and aberration-corrected geometries. The relative alignment of the two 1D-CRL slices focusing in the horizontal and vertical direction, respectively, could readily be controlled and measured using SEM or an optical microscope. It was greatly facilitated by the length of the slices (~6 cm) and the perpendicularity of the steal block the lenses where mounted onto. The quest for "miniaturization", i.e. more compact lenses for decreasing the focal length and thus increasing the numerical aperture and improving the achievable resolution, must consider requirements on the lens alignment accuracy. Detailed investigations of the required alignment accuracy and the effect of potential misalignments remain to be performed for interdigitated lenses [228]. In this thesis, respective tolerances were based on experience from aligning 1D-CRLs in the beamline – the achieved accuracy of 0.01° was considered to be sufficiently good for a first demonstration of the concept.

7.2.6 Injection molded polymeric lenses

Polymer injection molding was explored as a novel route for x-ray lens manufacture (cf. Chapter 6.3). Injection molded lenses made of polyethylene have proven to be promising highly efficient x-ray optics. A 55 µm long line focus with a minimal waist of 770 nm (FWHM) at a focal length of ~350 mm was obtained with 17 keV x-ray synchrotron radiation. The total lens transmittance was 32% (absorption limited), yielding a gain of ~50 at the intensity peak.

The proposed manufacturing route including fully automated injection molding allowed to produce lens chips comprising multiple CRLs with a final production rate of >10 pieces per hour. This indicates the economic value of injection molded x-ray lenses, which may have applications not only at synchrotron radiation facilities, but also in more readily available small laboratory x-ray instruments or medical devices.

Discrepancies to the theoretically expected optical performance have been discussed. Deformed lens shapes, warpage of the polymeric chip and high-Z contaminants in the thermoplastic have been identified as limiting factors. Potential improvements have been discussed, including a redesign of the tool used to hold the nickel mold insert to guarantee a gentler release of the polymeric part. Degradation of the polymer in the x-ray beam and its effects on the economic value of the lenses remain to be investigated. The practicability of lenses with limited life-times depends on whether quick lens replacement routines can be established.

7.3 Outlook

7.3.1 Lens design

Immediate improvements in the manufacture of Si-CRLs are possible through either the lens design or the processing. In terms of lens design, a better control of the lens shape is needed. This may be accomplished by narrowing the shape defining trenches, which would allow the parabolic shapes to be defined more uniformly, especially at the apex of the parabola. However, a narrower trench will reduce the etch rate and impede reaching larger depths due to an increased aspect ratio. A compromise must be therefore struck between the desired structure heights, the trench widths and the etch rates. Alternatively, the apex could be defined more uniformly by increasing the radius of curvature, which in turn necessitates adjusting the number of single lens elements. Design improvements must also include more accurate compensation of the structure widening caused by the surface smoothing step.

The precision with which CRLs may be manufactured using Strategy A could be increased by using thinner silicon wafers. The heights of the lenses could be increased by using thicker silicon wafers. Hence, a compromise must be struck between the height and the precision of the manufacture. In a long term perspective both may be accomplished.

The manufacture following Strategy B could benefit from using different sacrificial structures. The small diameters of sacrificial pillars resulted in high aspect ratios, which promoted their collapse before to the end of DRIE. For example meshes with thin beam widths may be used instead, which would guarantee a mutual support [403]. Alternatively, sacrificial thin walls arranged in an onion-like fashion inside the lens cavities could be used. In any case, respective systematic studies are required to allow a uniform etching and a successful removal of the structures in final devices.

7.3.2 Processing

In terms of processing, DRIE must be optimized in order to increase the parallelism of the sidewalls and to reduce any sidewall bow or tapering. The mechanism of local passivation breakthrough needs to be investigated. Previously it was suggested that it is caused by facetted edges of the masking material [347]. Strategies to avoid this faceting are not available; however, it is known to have its origin in ion sputtering during DRIE and to worsen with etch time. Minimizing the ion bombardment could therefore reduce local passivation breakthrough and sidewall defects.

Ion bombardment is necessary during DRIE for removal of the passivation layer at the bottom of etched structures. If this removal is not sufficient, silicon etching would essentially stop. However, since silicon etching with fluorine is spontaneous, ion bombardment is not required. Therefore, the ion bombardment, i.e. applying an additional power at the wafer platen, may be limited to small time windows subsequent to the passivation phase. Such processes are known as advanced or modified Bosch processes and are supported by modern plasma etching systems allowing more flexible tuning of the whole etching process [396–398,499,500]. Preliminary experiments were performed in this thesis work, showing exceptional mask selectivities. Generally speaking, a better understanding of the actual etching process, combined with the

possibilities to tailor individual processes to the point where every single parameter outlined in Chapter 3.5.3 can be precisely controlled, is key for meeting the stringent requirements for high-quality silicon CRL manufacture [345].

For obtaining very deep etchings, the Bosch process could further be supplemented by regular hard passivation steps, meaning that every 100 µm depth or so, the etched sidewalls are passivated by thin thermally grown SiO_2, alumina deposited by ALD, or SiO_2 formed by intermittent O_2 plasma treatments inside the DRIE system [501–504]. Plasma monitoring by fluoresce or secondary ion mass spectrometers would facilitate reaching stable etching tool conditions from day to day and during prolonged etchings. Thereby, e.g. onset of sidewall passivation breakthrough could be identified.

Processing steps prior to DRIE may be improved as well. The sidewall roughness of the masking layer was not critical in terms of final sidewall quality. However, Figure 3.4 suggests it could be substantially improved, which eventually would reduce surface defects such as vertical striations. In particular, if very deep etchings (>300 µm) are required, the oxide mask must be reasonably thick and mask roughness could turn out to be a more severe issue. Patterning thick oxide layers using RIE requires sufficiently thick masking materials. For this purpose, photoresist may not be adequate and stronger materials such as chromium need to be used, necessitating additional process steps and precautions. For a more accurate definition of lens patterns, lithography projection systems could be a viable alternative. However, as this technique is more time and cost expensive its use needs to be justified by potential merits.

Generally, a reduction of any shape non-uniformity encountered in this study would allow designing silicon lenses with shorter focal lengths that would create wider line foci with narrower waists closer to the diffraction limit.

7.3.3 Alternative strategies

Here, two alternative strategies for increasing the heights of Si-CRLs with enhanced sidewall profile control are proposed. Strategy C would use silicon-on-insulator (SOI) wafers in combination with patterns from Strategy A or Strategy B [402]. SOI wafers are expensive, so the use must be justified by potential merits. Potential merits may include flexible lens heights in conjunction with Strategy A; e.g. 50 µm thin silicon wafers are difficult to handle, but may be beneficial for realizing highly miniaturized interdigitated Si objectives. Using SOI wafers instead with 50 µm thin device layers on top of 500 µm handle wafers would ease the manufacture. Inversely, the thicker handle wafer may be patterned using Strategy A, while the thinner device layer stabilizes the structures, thereby making subsequent adhesive wafer bonding superfluous. The sacrificial portions may be released by selectively etching the buried oxide layer using e.g. HF vapor etching.

Strategy D would use pre-patterned wafers combined with fusion or anodic bonded wafers [418]. Handle wafers coated with a grown SiO_2 film would be pattered with cavities slightly larger than the targeted CRLs. Then these wafers would be bonded to blank device wafers. Device wafers would be pattered as usual and preferably with the design form Strategy A, while ensuring that the lens patterns are well aligned with the cavities of the handle wafer. DRIE would be performed and reach the cavities, thereby releasing the sacrificial portions. After

unloading the wafer from the DRIE reactor, sacrificial portions may easily be removed by turning the wafers upside down. The advantage to Process C is the avoidance of the release step by etching the buried oxide layer, while neither resulting in fragile wafers (contrary to Strategy A), nor being limited by the achievable aspect ratio of sacrificial pillars or walls (contrary to Strategy B).

Additionally to efforts in increasing the heights of Si-CRLs, two or multiple structured wafers may be wafer bonded, thereby effectively doubling or multiplying the lens heights [284]. The challenge is the proper alignment of the wafer pairs. Rotations can be well controlled by alignment marks at the rims of the wafers. Longitudinal offsets may be tolerated as long as they do not exceed the depth of focus. Most critically are offsets normal to the optical axis. According to internal discussions, such offsets cannot be tolerated. As line foci with sub-micrometer waists are targeted, offsets must not exceed ~100 nm. However, tricks may be found to relax the difficulty in high accuracy wafer bonding and without many efforts, lens heights may be increased substantially.

7.3.4 Shape characterization

A good agreement between the shape characterization and the measurements of the optical performance was found. The procedures presented in this thesis allow guiding the manufacture and measuring the shapes with sufficiently high accuracy. The measurements of the lens sidewalls by optical profilometry and AFM relied on inspecting cross sections, and hence on a destruction of the devices. Methods for non-destructive testing are rare and may include computed tomography or custom-made stylus profilers (cf. Chapter 5). The resolution in 3D, reliability and the throughput need to be considered. Ideally, respective equipment is available in the cleanroom to allow online optimization work.

The inspections by AFM could substantially be improved by scanners with larger ranges, namely in all directions, whereat the accuracy must not necessarily lie in the single nanometer range. An accuracy of 10 nm would be just fine, thereby bridging the gap between tactile stylus profilers and AFMs. However, tapping or intermittent mode is still necessary to avoid a deformation of the soft PDMS inverse replicas.

7.3.5 Optical performance

New beam characterization techniques need to be established. The knife edge scans performed in this thesis were sufficiently accurate. However, they approached their limits. Potential alternatives have been discussed in Chapter 5.6 and advanced techniques such as ptychography could be adapted for characterizing wide and narrow line beams.

7.3.6 New techniques, processes or materials

Advanced silicon structuring techniques are attractive for CRL manufacture. It is well known that x-ray absorption limits the ultimate optical performance of these devices. An early proposal for using PMMA CRL templates made by LIGA to electro plate lithium or beryllium has apparently not been pursued [254]. Also, injection molding or vacuum casting of lithium has been considered in 1999. Now it is time to reconsider these options, since miniaturized lithium

or beryllium CRLs would clearly result in a tremendous step forward. Safety precautions ensured, experimental setups need to be built to cast lithium in an inert atmosphere at >179ºC (i.e. the melting point of lithium) [505]. Silicon masters manufactured by the strategies demonstrated in this thesis can be used. Diffusion of lithium into silicon need to be considered and may be avoided by dense metal coatings. Strategies need to be found to release lithium lenses mechanically in dry atmosphere. The manufacture of lithium lenses with 100 µm radii by embossing was demonstrated at the Argonne National Laboratory [232].

Beryllium can be electroplated using non-aqueous solutions [506–508]. The silicon master may be selectively etched using fluorine plasma. Beryllium is known to be toxic and may be inhaled in the form of powder. Required safety needs to be investigated for beryllium dissolved in solutions.

Recently, an innovative way for defining parabolic profiles of CRLs was demonstrated [288]. Instead of etching bi-parabolic cavities into silicon, thin lamellas of constant thickness mimic individual lenslets. This has the technological advantage that low-*Z* materials may be coated onto the lamellas, eventually replacing the silicon, thereby yielding more efficient CRLs. While techniques such as chemical vapor deposition result in coatings of limited uniformity [298], atomic layer deposition (ALD) is known for its exceptional characteristics in serving such purposes [509,510]. Depositing beryllium oxide by ALD may be a good alternative to previously used aluminum oxide [511]. However, although conceptually simple, lamellas result in non-uniform patterns in the context of DRIE (cf. Chapter 4.1) and unless the pattern is made more uniform, lenses will be limited in height.

7.3.7 New functionalities

Silicon is the material of contemporary electronics and silicon optical components may be supplemented by taking advantage of various developments. Far-fetched possibilities are to utilize MEMS and construct compact versions of transfocators [229], or systems that allow minute adjustments in focal lengths by translating individual lenslets along the optical axis. Silicon CRLs may readily be doped such that they can simultaneously function as photo diodes, which would enable in-line x-ray beam monitoring. Generally speaking, possibilities to utilize established technologies are vast. In terms of x-ray microscopy, any advancement in miniaturizing functional optics would be another step forward towards more powerful analytical techniques. Combined with more compact x-ray sources and detectors this would result in an increased availability of cutting edge characterization techniques for the materials of tomorrow.

7.4 Final remarks

In times like these, where governments have realized that economic growth strongly depends on innovation, public funding seems secured given that well prepared research plans are submitted. Sharing resources internationally may additionally guarantee an efficient progress in research and development. This is even more important in areas where applications are limited and the direct economic value is not as clear. X-ray optics and especially x-ray optics designed for synchrotron sources is such an area. At the time of submitting this thesis a minimum of five international groups were independently working on silicon lens development. Commercial

supply of embossed metal lenses in the form of a university spin-off exists and other institutions pursue similar developments. Lenses made by DXRL is a separate branch of intense development similar to those of Fresnel zone plates, multilayer Laue lenses or KB mirrors. Mutual exchange and competition heat up innovation and is indispensable for the life of a researcher. However, closer collaborations may speed up developments, especially those which are just a matter of time as is the race to x-ray nano-beam science. Joint initiatives may avoid that similar inventions are made twice for the benefit of everyone.

X-ray techniques become ever more abundant, whether in medical institutions, production lines, airports, harbors, borders, recycling facilities, or wind mills. X-ray lenses could play a crucial role in making these techniques more powerful. A ready availability of such lenses would facilitate their wide distribution in various sectors. The silicon lenses fabricated in this thesis for shaping high energy x-ray beams are ready for commercialization, whereas the polymeric injection molded lenses may be produced in large quantities.

References

[1] Als-Nielsen J and McMorrow D 2011 *Elements of Modern X-ray Physics* (Chichester, West Sussex, UK: Wiley)

[2] Seeck O H and Murphy B 2014 *X-Ray Diffraction: Modern Experimental Techniques* (Boca Raton, Florida, US: CRC Press)

[3] Stangl J, Mocuta C, Chamard V and Carbone D 2014 *Nanobeam X-Ray Scattering: Probing Matter at the Nanoscale* (Weinheim, Germany: Wiley)

[4] Beckhoff B, Kanngießer B, Langhoff N, Wedell R and Wolff H 2006 *Handbook of Practical X-Ray Fluorescence Analysis* (Berlin, Heidelberg, Germany: Springer)

[5] Waseda Y, Matsubara E and Shinoda K 2011 *X-Ray Diffraction Crystallography* (Berlin, Heidelberg, Germany: Springer)

[6] Reimers W, Pyzalla A R, Schreyer A K and Clemens H 2008 *Neutrons and Synchrotron Radiation in Engineering Materials Science: From Fundamentals to Material and Component Characterization* (Weinheim, Germany: Wiley)

[7] Jenkins R 2006 X-Ray Techniques: Overview *Encycl. Anal. Chem.* 1–20

[8] Skarzynski T 2013 Collecting data in the home laboratory: evolution of X-ray sources, detectors and working practices *Acta Crystallogr. Sect. D Biol. Crystallogr.* **69** 1283–8

[9] Hemberg O, Otendal M and Hertz H M 2003 Liquid-metal-jet anode electron-impact x-ray source *Appl. Phys. Lett.* **83** 1483–5

[10] Kim K-J 1989 Characteristics of synchrotron radiation *AIP Conf. Proc.* **184** 565–632

[11] Wille K 1991 Synchrotron radiation sources *Reports Prog. Phys.* **54** 1005–67

[12] Mobilio S, Boscherini F and Meneghini C 2015 *Synchrotron Radiation* (Berlin, Heidelberg: Springer)

[13] Eriksson M, van der Veen J F and Quitmann C 2014 Diffraction-limited storage rings – a window to the science of tomorrow *J. Synchrotron Radiat.* **21** 837–42

[14] McNeil B W J and Thompson N R 2010 X-ray free-electron lasers *Nat. Photonics* **4** 814–21

[15] Altarelli M 2015 The European X-ray Free-Electron Laser: toward an ultra-bright, high repetition-rate x-ray source *High Power Laser Sci. Eng.* **3** e18

[16] Sayre D and Chapman H N 1995 X-ray microscopy *Acta Crystallogr. Sect. A* **51** 237–52

[17] Chevallier P, Populus P and Firsov a 1999 Hard X-ray microbeam production with synchrotron radiation: application to microanalysis *X-Ray Spectrom.* **28** 348–51

[18] Snigireva I and Snigirev A 2006 X-Ray microanalytical techniques based on synchrotron radiation. *J. Environ. Monit.* **8** 33–42

[19] Kirz J and Jacobsen C 2009 The history and future of X-ray microscopy *J. Phys. Conf. Ser.* **186** 012001

[20] Chapman H N and Nugent K a. 2010 Coherent lensless X-ray imaging *Nat. Photonics* **4** 833–9

[21] Sakdinawat A and Attwood D 2010 Nanoscale X-ray imaging *Nat. Photonics* **4** 840–8

[22] Kaulich B, Thibault P, Gianoncelli A and Kiskinova M 2011 Transmission and emission x-ray microscopy: operation modes, contrast mechanisms and applications. *J. Phys. Condens. Matter* **23** 083002

[23] Falcone R, Jacobsen C, Kirz J, Marchesini S, Shapiro D and Spence J 2011 New directions in X-ray microscopy *Contemp. Phys.* **52** 293–318

[24] Holt M, Harder R, Winarski R and Rose V 2013 Nanoscale Hard X-Ray Microscopy Methods for Materials Studies* *Annu. Rev. Mater. Res.* **43** 183–211

[25] Schroer C G, Meyer J, Kuhlmann M, Benner B, Gunzler T F, Lengeler B, Rau C, Weitkamp T, Snigirev a and Snigireva I 2002 Nanotomography based on hard x-ray microscopy with refractive lenses *Appl. Phys. Lett.* **81** 1527–9

[26] Chen J, Wu C, Tian J, Li W, Yu S and Tian Y 2008 Three-dimensional imaging of a complex concaved cuboctahedron copper sulfide crystal by x-ray nanotomography *Appl. Phys. Lett.* **92** 233104

[27] Schroer C G, Boye P, Feldkamp J M, Patommel J, Schropp A and Samberg D 2010 Hard X-ray Microscopy with Elemental , Chemical , and Structural Contrast **117**

[28] Andrews J C, Meirer F, Liu Y, Mester Z and Pianetta P 2011 Transmission X-ray microscopy for full-field nano imaging of biomaterials. *Microsc. Res. Tech.* **74** 671–81

[29] Andrews J C, Almeida E, van der Meulen M C H, Alwood J S, Lee C, Liu Y, Chen J, Meirer F, Feser M, Gelb J, Rudati J, Tkachuk A, Yun W and Pianetta P 2010 Nanoscale X-ray microscopic imaging of mammalian mineralized tissue *Microsc. Microanal.* **16** 327–36

[30] Bosak A, Snigireva I, Napolskii K S and Snigirev A 2010 High-resolution transmission X-ray microscopy: A new tool for mesoscopic materials. *Adv. Mater.* **22** 3256–9

[31] Simons H, King A, Ludwig W, Detlefs C, Pantleon W, Schmidt S, Stöhr F, Snigireva I, Snigirev A and Poulsen H F 2015 Dark-field X-ray microscopy for multiscale structural characterization *Nat. Commun.* **6** 6098

[32] Poulsen H F 2004 *Three-Dimensional X-Ray Diffraction Microscopy. Mapping Polycrystals and their Dynamics* (Berlin, Heidelberg: Springer)

[33] Poulsen H F, Nielsen S F, Lauridsen E M, Schmidt S, Suter R M, Lienert U, Margulies L, Lorentzen T and Juul Jensen D 2001 Three-dimensional maps of grain boundaries and the stress state of individual grains in polycrystals and powders *J. Appl. Crystallogr.* **34** 751–6

[34] Poulsen H F 2002 3DXRD microscopy - a comparison with neutron diffraction *Appl. Phys. A* **74** s1673–5

[35] Poulsen H F 2003 A six-dimensional approach to microtexture analysis *Philos. Mag.* **83** 2761–78

[36] Poulsen H F 2012 An introduction to three-dimensional X-ray diffraction microscopy *J. Appl. Crystallogr.* **45** 1084–97

[37] Jensen D J and Poulsen H F 2012 The three dimensional X-ray diffraction technique *Mater. Charact.* **72** 1–7

[38] Sørensen H O, Schmidt S, Wright J P, Vaughan G B M, Techert S, Garman E F, Oddershede J, Davaasambuu J, Paithankar K S, Gundlach C and Poulsen H F 2012 Multigrain crystallography *Zeitschrift für Krist.* **227** 63–78

[39] Sørensen H O, Hakim S S, Pedersen S, Christiansen B C, Balogh Z I, Hem C P, Pasarin I S, Schmidt S, Olsen U L, Oddershede J, Frandsen C, Feidenhans'L R and Stipp S L S 2012 Non-destructive identification of micrometer-scale minerals and their position within a bulk sample *Can. Mineral.* **50** 501–9

[40] Suter R M, Hennessy D, Xiao C and Lienert U 2006 Forward modeling method for microstructure reconstruction using x-ray diffraction microscopy: Single-crystal verification *Rev. Sci. Instrum.* **77**

[41] Lienert U, Li S F, Heffernan C M, Lind J, Suter R M, Bernier J V, Barton N R, Brandes M, Mills M J, Miller M P, Wejdemann C and Pantleon W 2011 High Energy Diffraction Microscopy at the Advanced Photon Source *Jom* **63** 70–7

[42] Li S F, Lind J, Hefferan C M, Pokharel R, Lienert U, Rollett a. D and Suter R M 2012 Three-dimensional plastic response in polycrystalline copper via near-field high-energy X-ray diffraction microscopy *J. Appl. Crystallogr.* **45** 1098–108

[43] Ludwig W, Cloetens P, Hartwig J, Baruchel J, Hamelin B and Bastie P 2001 Three-dimensional imaging of crystal defects by 'topo-tomography' *J. Appl. Crystallogr.* **34** 602–7

[44] Ludwig W, Lauridsen E M, Schmidt S, Poulsen H F and Baruchel J 2007 High-resolution three-dimensional mapping of individual grains in polycrystals by topotomography *J. Appl. Crystallogr.* **40** 905–11

[45] Ludwig W, Schmidt S, Lauridsen E M and Poulsen H F 2008 X-ray diffraction contrast tomography: a novel technique for three-dimensional grain mapping of polycrystals. I. Direct beam case *J. Appl. Crystallogr.* **41** 302–9

[46] Johnson G, King A, Honnicke M G, Marrow J and Ludwig W 2008 X-ray diffraction contrast tomography: a novel technique for three-dimensional grain mapping of polycrystals. II. The combined case *J. Appl. Crystallogr.* **41** 310–8

[47] Ludwig W, Reischig P, King a, Herbig M, Lauridsen E M, Johnson G, Marrow T J and Buffière J Y 2009 Three-dimensional grain mapping by x-ray diffraction contrast tomography and the use of Friedel pairs in diffraction data analysis. *Rev. Sci. Instrum.* **80** 033905

[48] Ludwig W, King A, Reischig P, Herbig M, Lauridsen E M, Schmidt S, Proudhon H, Forest S, Cloetens P, Roscoat S R Du, Buffière J Y, Marrow T J and Poulsen H F 2009 New opportunities for 3D materials science of polycrystalline materials at the micrometre lengthscale by combined use of X-ray diffraction and X-ray imaging *Mater. Sci. Eng. A* **524** 69–76

[49] Ludwig W, King A, Herbig M, Reischig P, Marrow J, Babout L, Lauridsen E M, Proudhon H and Buffière J Y 2010 Characterization of polycrystalline materials using synchrotron X-ray imaging and diffraction techniques *JOM* **62** 22–8

[50] Snigirev A and Snigireva I 2008 High energy X-ray micro-optics *Comptes Rendus Phys.* **9** 507–16

[51] Ice G E, Budai J D and Pang J W L 2011 The race to x-ray microbeam and nanobeam science. *Science* **334** 1234–9

[52] Guilherme a., Buzanich G and Carvalho M L 2012 Focusing systems for the generation of X-ray micro beam: An overview *Spectrochim. Acta Part B At. Spectrosc.* **77** 1–8

[53] Snigirev A and Snigireva I 2008 Hard X-Ray Microoptics *Modern Developments in X-Ray and Neutron Optics* ed A Erko, M Idir, T Krist and A G Michette (Berlin, Heidelberg, Germany: Springer) pp 255–8

[54] Schroer C and Lengeler B 2012 X-Ray Optics *Springer Handbook of Lasers and Optics* ed F Träger (Berlin, Heidelberg, Germany: Springer) pp 1461–74

[55] Martinez-Criado G, Borfecchia E, Mino L and Lamberti C 2013 Micro- and Nano-X-ray Beams *Characterization of Semiconductor Heterostructures and Nanostructures* ed C Lamberti and G Agostini (Oxford: Elsevier) pp 361–412

[56] Stangl J, Mocuta C, Chamard V and Carbone D 2014 X-Ray Focusing Elements Characterization *Nanobeam X-Ray Scattering. Probing Matter at the Nanoscale* (Weinheim, Germany: Wiley) pp 39–87

[57] Bergemann C, Keymeulen H and van der Veen J 2003 Focusing X-Ray Beams to Nanometer Dimensions *Phys. Rev. Lett.* **91** 204801

[58] Schroer C and Lengeler B 2005 Focusing Hard X Rays to Nanometer Dimensions by Adiabatically Focusing Lenses *Phys. Rev. Lett.* **94** 054802

[59] Schroer C 2006 Focusing hard x rays to nanometer dimensions using Fresnel zone plates *Phys. Rev. B* **74** 033405

[60] Yan H, Maser J, Macrander A, Shen Q, Vogt S, Stephenson G B and Kang H 2007 Takagi-Taupin description of x-ray dynamical diffraction from diffractive optics with large numerical aperture *Phys. Rev. B* **76** 115438

[61] Handa S, Kimura T, Mimura H, Yumoto H, Matsuyama S, Sano Y, Tamasaku K, Nishino Y, Yabashi M, Ishikawa T and Yamauchi K 2010 Extended knife-edge method for characterizing sub-10-nm X-ray beams *Nucl. Instruments Methods Phys. Res. Sect. A Accel. Spectrometers, Detect. Assoc. Equip.* **616** 246–50

[62] Kirkpatrick P and Baez A V. 1948 Formation of Optical Images by X-Rays *J. Opt. Soc. Am.* **38** 766

[63] Baez A V 1990 Some reflections on x-ray optics *Proc. SPIE* **1333** 94–105

[64] Baez A V 1997 Anecdotes about the Early Days of X-Ray Optics *J. Xray. Sci. Technol.* **7** 90–7

[65] Liu W, Ice G E, Tischler J Z, Khounsary A, Liu C, Assoufid L and Macrander A T 2005 Short focal length Kirkpatrick-Baez mirrors for a hard x-ray nanoprobe *Rev. Sci. Instrum.* **76** 113701

[66] Mimura H, Yumoto H, Matsuyama S, Sano Y, Yamamura K, Mori Y, Yabashi M, Nishino Y, Tamasaku K, Ishikawa T and Yamauchi K 2007 Efficient focusing of hard x rays to 25 nm by a total reflection mirror *Appl. Phys. Lett.* **90** 051903

[67] Mimura H, Morita S, Kimura T, Yamakawa D, Lin W, Uehara Y, Yumoto H, Matsuyama S, Nishino Y, Tamasaku K, Ohashi H, Yabashi M, Ishikawa T, Ohmori H and Yamauchi K 2008 Fabrication of a 400-mm-long mirror for focusing X-ray free-electron lasers to sub-100 nm ed S Goto, A M Khounsary and C Morawe *Proc. SPIE* **7077** 70770R

[68] Mimura H, Morita S, Kimura T, Yamakawa D, Lin W, Uehara Y, Matsuyama S, Yumoto H, Ohashi H, Tamasaku K, Nishino Y, Yabashi M, Ishikawa T, Ohmori H and Yamauchi K 2008 Focusing mirror for x-ray free-electron lasers *Rev. Sci. Instrum.* **79** 083104

[69] Yumoto H, Mimura H, Koyama T, Matsuyama S, Tono K, Togashi T, Inubushi Y, Sato T, Tanaka T, Kimura T, Yokoyama H, Kim J, Sano Y, Hachisu Y, Yabashi M, Ohashi H, Ohmori H, Ishikawa T and Yamauchi K 2012 Focusing of X-ray free-electron laser pulses with reflective optics *Nat. Photonics* **7** 43–7

[70] Matsuyama S, Emi Y, Kino H, Sano Y, Kohmura Y, Tamasaku K, Yabashi M, Ishikawa T and Yamauchi K 2013 Development of achromatic full-field x-ray microscopy with compact imaging mirror system ed B Lai *Proc. SPIE* **8851** 885107

[71] Matsuyama S, Emi Y, Kino H, Kohmura Y, Yabashi M, Ishikawa T and Yamauchi K 2015 Achromatic and high-resolution full-field X-ray microscopy based on total-reflection mirrors *Opt. Express* **23** 9746

[72] Störmer M, Siewert F and Gaudin J 2011 Development of x-ray optics for advanced research light sources ed T Tschentscher and D Cocco *Proc. SPIE* **8078** 80780G

[73] Hignette O, Rostaing G, Cloetens P, Rommeveaux A, Ludwig W and Freund A 2001 Submicron focusing of hard X-rays with reflecting surfaces at the ESRF *Proc. SPIE* **4499** 105–16

[74] Dabin Y, Rostaing G, Hignette O, Rommeveaux A and Freund A K 2002 The present state of KirkpatrickBaez mirror systems at the ESRF *Proc. SPIE* **4782** 235–45

[75] Hignette O, Cloetens P, Rostaing G, Bernard P and Morawe C 2005 Efficient sub 100 nm focusing of hard x rays *Rev. Sci. Instrum.* **76** 1–5

[76] Morawe C, Hignette O, Cloetens P, Ludwig W, Borel C, Bernard P and Rommeveaux A 2006 Graded multilayers for focusing hard x-rays below 50 nm *Proc. SPIE* **6317** 63170F

[77] Hignette O, Cloetens P, Morawe C, Borel C, Ludwig W, Bernard P, Rommeveaux a. and Bohic S 2007 Nanofocusing at ESRF Using Graded Multilayer Mirrors *AIP Conf. Proc.* **879** 792–5

[78] Morawe C and Osterhoff M 2010 Curved graded multilayers for X-ray nano-focusing optics *Nucl. Instruments Methods Phys. Res. Sect. A* **616** 98–104

[79] Osterhoff M, Morawe C, Ferrero C and Guigay J-P 2012 Wave-optical theory of nanofocusing x-ray multilayer mirrors. *Opt. Lett.* **37** 3705–7

[80] Kimura T, Handa S, Mimura H, Yumoto H, Yamakawa D, Matsuyama S, Inagaki K, Sano Y, Tamasaku K, Nishino Y, Yabashi M, Ishikawa T and Yamauchi K 2009 Wavefront Control System for Phase Compensation in Hard X-ray Optics *Jpn. J. Appl. Phys.* **48** 072503

[81] Mimura H, Handa S, Kimura T, Yumoto H, Yamakawa D, Yokoyama H, Matsuyama S, Inagaki K, Yamamura K, Sano Y, Tamasaku K, Nishino Y, Yabashi M, Ishikawa T and Yamauchi K 2010 Breaking the 10 nm barrier in hard-X-ray focusing *Nat. Phys.* **6** 122–5

[82] Yamauchi K, Mimura H, Kimura T, Yumoto H, Handa S, Matsuyama S, Arima K, Sano Y, Yamamura K, Inagaki K, Nakamori H, Kim J, Tamasaku K, Nishino Y, Yabashi M and Ishikawa T 2011 Single-nanometer focusing of hard x-rays by Kirkpatrick-Baez mirrors. *J. Phys. Condens. Matter* **23** 394206

[83] Preda I, Vivo A, Demarcq F, Berujon S, Susini J and Ziegler E 2013 Ion beam etching of a flat silicon mirror surface: A study of the shape error evolution *Nucl. Instruments Methods Phys. Res. Sect. A* **710** 98–100

[84] Berujon S, Wang H, Alcock S and Sawhney K 2014 At-wavelength metrology of hard X-ray mirror using near field speckle. *Opt. Express* **22** 6438–46

[85] Howells M, Jacobsen C, Warwick T and Van den Bos A 2007 Principles and Applications of Zone Plate X-Ray Microscopes *Science of Microscopy* ed P W Hawkes and J C H Spence (New York, USA: Springer) pp 835–926

[86] Chu Y S, Yi J M, De Carlo F, Shen Q, Lee W-K, Wu H J, Wang C L, Wang J Y, Liu C J, Wang C H, Wu S R, Chien C C, Hwu Y, Tkachuk a., Yun W, Feser M, Liang K S, Yang C S, Je J H and Margaritondo G 2008 Hard-x-ray microscopy with Fresnel zone plates reaches 40 nm Rayleigh resolution *Appl. Phys. Lett.* **92** 103119

[87] Lai B, Yun W B, Legnini D, Xiao Y, Chrzas J, Viccaro P J, White V, Bajikar S, Denton D, Cerrina F, Di Fabrizio E, Gentili M, Grella L and Baciocchi M 1992 Hard x-ray phase zone plate fabricated by lithographic techniques *Appl. Phys. Lett.* **61** 1877–9

[88] Di Fabrizio E 1994 High-performance multilevel blazed x-ray microscopy Fresnel zone plates: Fabricated using x-ray lithography *J. Vac. Sci. Technol. B* **12** 3979

[89] Chen Z, Vladimirsky Y, Brown M, Leonard Q, Vladimirsky O, Moore F, Cerrina F, Lai B, Yun W and Gluskin E 1997 Design and fabrication of Fresnel zone plates with large numbers of zones *J. Vac. Sci. Technol. B* **15** 2522

[90] Yun W, Lai B, Cai Z, Maser J, Legnini D, Gluskin E, Chen Z, Krasnoperova a. a., Vladimirsky Y, Cerrina F, Di Fabrizio E and Gentili M 1999 Nanometer focusing of hard x rays by phase zone plates *Rev. Sci. Instrum.* **70** 2238

[91] Yun W, Lai B, Krasnoperova a. a., Fabrizio E Di, Cai Z, Cerrina F, Chen Z, Gentili M, Gluskin E and Di Fabrizio E 1999 Development of zone plates with a blazed profile for hard x-ray applications *Rev. Sci. Instrum.* **70** 3527

[92] Di Fabrizio E, Romanato F, Gentili M, Cabrini S, Kaulich B, Susini J and Barrett R 1999 High-efficiency multilevel zone plates for keV X-rays *Nature* **401** 895–8

[93] Di Fabrizio E and Gentili M 1999 X-ray multilevel zone plate fabrication by means of electron-beam lithography: Toward high-efficiency performances *J. Vac. Sci. Technol. B* **17** 3439

[94] Altissimo M, Romanato F, Vaccari L, Businaro L, Cojoc D, Kaulich B, Cabrini S and Di Fabrizio E 2002 X-ray lithography fabrication of a zone plate for X-rays in the range from 15 to 30 keV *Microelectron. Eng.* **61-62** 173–7

[95] Lindblom M, Hertz H M and Holmberg A 2006 Pulse reverse plating for uniform nickel height in zone plates *J. Vac. Sci. Technol. B* **24** 2848

[96] Lo T N, Chen Y T, Chiu C W, Liu C J, Wu S R, Lin I K, Su C I, Chang W D, Hwu Y, Shew B Y, Chiang C C, Je J H and Margaritondo G 2007 E-beam lithography and electrodeposition fabrication of thick nanostructured devices *J. Phys. D. Appl. Phys.* **40** 3172–6

[97] Chen Y-T, Lo T-N, Chu Y S, Yi J, Liu C-J, Wang J-Y, Wang C-L, Chiu C-W, Hua T-E, Hwu Y, Shen Q, Yin G-C, Liang K S, Lin H-M, Je J H and Margaritondo G 2008 Full-field hard x-ray microscopy below 30 nm: a challenging nanofabrication achievement. *Nanotechnology* **19** 395302

[98] Gorelick S, Guzenko V a, Vila-Comamala J and David C 2010 Direct e-beam writing of dense and high aspect ratio nanostructures in thick layers of PMMA for electroplating. *Nanotechnology* **21** 295303

[99] Gorelick S, Vila-Comamala J, Guzenko V a., Barrett R, Salomé M and David C 2011 High-efficiency Fresnel zone plates for hard X-rays by 100 keV e-beam lithography and electroplating *J. Synchrotron Radiat.* **18** 442–6

[100] Mohacsi I, Karvinen P, Vartiainen I, Diaz A, Somogyi A, Kewish C M, Mercere P and David C 2013 High efficiency x-ray nanofocusing by the blazed stacking of binary zone plates ed B Lai *Proc. SPIE* **8851** 88510Z

[101] Mohacsi I, Karvinen P, Vartiainen I, Guzenko V a., Somogyi A, Kewish C M, Mercere P and David C 2014 High-efficiency zone-plate optics for multi-keV X-ray focusing *J. Synchrotron Radiat.* **21** 497–501

[102] David C, Nöhammer B, Ziegler E and Hignette O 2001 Tunable diffractive optical elements for hard x-rays *Proc. SPIE* **4499** 96–104

[103] David C, Nöhammer B and Ziegler E 2002 Wet etching of linear Fresnel zone plates for hard X-rays *Microelectron. Eng.* **61-62** 987–92

[104] Nöhammer B, David C, Burghammer M and Riekel C 2005 Coherence-matched microfocusing of hard x rays *Appl. Phys. Lett.* **86** 163104

[105] Stein A, Jacobsen C, Evans-Lutterodt K, Tennant D M, Bogart G, Klemens F, Ocola L E, Choi B J and Sreenivasan S V. 2003 Diffractive x-ray optics using production fabrication methods *J. Vac. Sci. Technol. B* **21** 214

[106] Snigireva I, Snigirev A, Kohn V, Yunkin V, Grigoriev M, Kuznetsov S, Vaughan G and Di Michiel M 2007 Hard X-ray focusing by stacked Fresnel zone plates ed A M Khounsary, C Morawe and S Goto *Proc. SPIE* **6705** 67050G

[107] Snigireva I, Snigirev A, Kohn V, Yunkin V, Grigoriev M, Kuznetsov S, Vaughan G and Di Michiel M 2007 Focusing high energy X-rays with stacked Fresnel zone plates *Phys. Status Solidi* **204** 2817–23

[108] David C, Gorelick S, Rutishauser S, Krzywinski J, Vila-Comamala J, Guzenko V a, Bunk O, Färm E, Ritala M, Cammarata M, Fritz D M, Barrett R, Samoylova L, Grünert J and Sinn H 2011 Nanofocusing of hard X-ray free electron laser pulses using diamond based Fresnel zone plates. *Sci. Rep.* **1** 57

[109] Nilsson D, Uhlén F, Reinspach J, Hertz H M, Holmberg a, Sinn H and Vogt U 2012 Thermal stability of tungsten zone plates for focusing hard x-ray free-electron laser radiation *New J. Phys.* **14** 043010

[110] Uhlén F, Nilsson D, Holmberg A, Hertz H M, Christian G, Seiboth F, Patommel J, Meier V, Hoppe R, Lee H J, Nagler B, Galtier E, Krzywinski J, Sinn H and Vogt U 2013 Damage investigation on tungsten and diamond diffractive optics at a hard x-ray free-electron laser **21** 8051–61

[111] Tiberio R C, Rooks M J, Chang C, F. Knollenberg C, Dobisz E a. and Sakdinawat A 2014 Vertical directionality-controlled metal-assisted chemical etching for ultrahigh aspect ratio nanoscale structures *J. Vac. Sci. Technol. B* **32** 06FI01

[112] Chang C and Sakdinawat A 2014 Ultra-high aspect ratio high-resolution nanofabrication for hard X-ray diffractive optics. *Nat. Commun.* **5** 4243

[113] Vila-Comamala J, Jefimovs K, Raabe J, Pilvi T, Fink R H, Senoner M, Maaßdorf A, Ritala M and David C 2009 Advanced thin film technology for ultrahigh resolution X-ray microscopy *Ultramicroscopy* **109** 1360–4

[114] Vila-Comamala J, Gorelick S, Guzenko V a, Färm E, Ritala M and David C 2010 Dense high aspect ratio hydrogen silsesquioxane nanostructures by 100 keV electron beam lithography. *Nanotechnology* **21** 285305

[115] Vila-Comamala J, Diaz A, Guizar-Sicairos M, Mantion A, Kewish C M, Menzel A, Bunk O and David C 2011 Characterization of high-resolution diffractive X-ray optics by ptychographic coherent diffractive imaging. *Opt. Express* **19** 21333–44

[116] Vila-Comamala J, Gorelick S, Färm E, Kewish C M, Diaz A, Barrett R, Guzenko V a, Ritala M and David C 2011 Ultra-high resolution zone-doubled diffractive X-ray optics for the multi-keV regime. *Opt. Express* **19** 175–84

[117] Mohacsi I, Vartiainen I, Guizar-Sicairos M, Karvinen P, Guzenko V a, Muller E, Farm E, Ritala M, Kewish C M, Somogyi a and David C 2015 High resolution double-sided diffractive optics for hard X-ray microscopy *Opt. Express* **23** 776–86

[118] Kamijo N, Suzuki Y, Takano H, Tamura S, Yasumoto M, Takeuchi A and Awaji M 2003 Microbeam of 100 keV x ray with a sputtered-sliced Fresnel zone plate *Rev. Sci. Instrum.* **74** 5101

[119] Döring F, Robisch A L, Eberl C, Osterhoff M, Ruhlandt A, Liese T, Schlenkrich F, Hoffmann S, Bartels M, Salditt T and Krebs H U 2013 Sub-5 nm hard x-ray point focusing by a combined Kirkpatrick-Baez mirror and multilayer zone plate *Opt. Express* **21** 19311–23

[120] Keskinbora K, Robisch A-L, Mayer M, Grévent C, Szeghalmi A V., Knez M, Weigand M, Snigireva I, Snigirev A, Salditt T and Schütz G 2013 Recent advances in use of atomic layer deposition and focused ion beams for fabrication of Fresnel zone plates for hard x-rays *Proc. SPIE* **8851** 885119

[121] Keskinbora K, Robisch A-L, Mayer M, Sanli U T, Grévent C, Wolter C, Weigand M, Szeghalmi A, Knez M, Salditt T and Schütz G 2014 Multilayer Fresnel zone plates for high energy radiation resolve 21 nm features at 1.2 keV. *Opt. Express* **22** 18440–53

[122] Yan H, Conley R, Bouet N and Chu Y S 2014 Hard x-ray nanofocusing by multilayer Laue lenses *J. Phys. D. Appl. Phys.* **47** 263001

[123] Maser J, Stephenson G B, Vogt S, Yun W, Macrander A, Kang H C, Liu C and Conley R 2004 Multilayer Laue lenses as high-resolution x-ray optics *Proc. SPIE* **5539** 185–94

[124] Kang H C, Stephenson G B, Liu C, Conley R, Macrander A T, Maser J, Bajt S and Chapman H N 2004 Synchrotron x-ray study of multilayers in Laue geometry *Proc. SPIE* **5537** 127–32

[125] Kang H, Maser J, Stephenson G, Liu C, Conley R, Macrander a. and Vogt S 2006 Nanometer Linear Focusing of Hard X Rays by a Multilayer Laue Lens *Phys. Rev. Lett.* **96** 127401

[126] Conley R, Liu C, Qian J, Kewish C M, Macrander A T, Yan H, Kang H C, Maser J and Stephenson G B 2008 Wedged multilayer Laue lens. *Rev. Sci. Instrum.* **79** 053104

[127] Kang H C, Stephenson G B, Liu C, Conley R, Khachatryan R, Wieczorek M, Macrander A T, Yan H, Maser J, Hiller J and Koritala R 2007 Sectioning of multilayers to make a multilayer Laue lens. *Rev. Sci. Instrum.* **78** 046103

[128] Kang H C, Yan H, Winarski R P, Holt M V., Maser J, Liu C, Conley R, Vogt S, Macrander A T and Stephenson G B 2008 Focusing of hard x-rays to 16 nanometers with a multilayer Laue lens *Appl. Phys. Lett.* **92** 221114

[129] Yan H, Kang H C, Conley R, Liu C, Macrander A T, Stephenson G B and Maser J 2010 Multilayer Laue Lens: A Path Toward One Nanometer X-Ray Focusing *X-Ray Opt. Instrum.* **2010** 1–10

[130] Yan H, Rose V, Shu D, Lima E, Kang H C, Conley R, Liu C, Jahedi N, Macrander A T, Stephenson G B, Holt M, Chu Y S, Lu M and Maser J 2011 Two dimensional hard x-ray nanofocusing with crossed multilayer Laue lenses. *Opt. Express* **19** 15069–76

[131] Yan H and Chu Y S 2013 Optimization of multilayer Laue lenses for a scanning X-ray microscope. *J. Synchrotron Radiat.* **20** 89–97

[132] Huang X, Yan H, Nazaretski E, Conley R, Bouet N, Zhou J, Lauer K, Li L, Eom D, Legnini D, Harder R, Robinson I K and Chu Y S 2013 11 nm hard X-ray focus from a large-aperture multilayer Laue lens. *Sci. Rep.* **3** 3562

[133] Ruhlandt a., Liese T, Radisch V, Krüger S P, Osterhoff M, Giewekemeyer K, Krebs H U and Salditt T 2012 A combined Kirkpatrick-Baez mirror and multilayer lens for sub-10 nm x-ray focusing *AIP Adv.* **2** 012175

[134] Braun S, Kubec A, Menzel M, Niese S, Krüger P, Seiboth F, Patommel J and Schroer C 2013 Multilayer Laue Lenses with Focal Length of 10 mm *J. Phys. Conf. Ser.* **425** 052019

[135] Kubec A, Braun S, Niese S, Krüger P, Patommel J, Hecker M, Leson A and Schroer C G 2014 Ptychography with multilayer Laue lenses. *J. Synchrotron Radiat.* **21** 1122–7

[136] Eberl C, Döring F, Liese T, Schlenkrich F, Roos B, Hahn M, Hoinkes T, Rauschenbeutel A, Osterhoff M, Salditt T and Krebs H U 2014 Fabrication of laser deposited high-quality multilayer zone plates for hard X-ray nanofocusing *Appl. Surf. Sci.* **307** 638–44

[137] Niese S, Krüger P, Kubec A, Laas R, Gawlitza P, Melzer K, Braun S and Zschech E 2014 Fabrication of customizable wedged multilayer Laue lenses by adding a stress layer *Thin Solid Films* **571** 321–4

[138] Niese S, Krüger P, Kubec A, Braun S, Patommel J, Schroer C G, Leson A and Zschech E 2014 Full-field X-ray microscopy with crossed partial multilayer Laue lenses. *Opt. Express* **22** 20008–13

[139] Morgan A J, Prasciolu M, Andrejczuk A, Krzywinski J, Meents A, Pennicard D, Graafsma H, Barty A, Bean R J, Barthelmess M, Oberthuer D, Yefanov O, Aquila A, Chapman H N and Bajt S 2015 High numerical aperture multilayer Laue lenses. *Sci. Rep.* **5** 9892

[140] Prasciolu M, Leontowich a. F G, Krzywinski J, Andrejczuk a., Chapman H N and Bajt S 2015 Fabrication of wedged multilayer Laue lenses *Opt. Mater. Express* **5** 748

[141] Liese T, Radisch V and Krebs H-U 2010 Fabrication of multilayer Laue lenses by a combination of pulsed laser deposition and focused ion beam. *Rev. Sci. Instrum.* **81** 073710

[142] Liu C, Conley R, Qian J, Kewish C M, Macrander A T, Maser J, Kang H C, Yan H and Stephenson G B 2007 Bonded Multilayer Laue Lens for focusing hard X-rays *Nucl. Instruments Methods Phys. Res. Sect. A* **582** 123–5

[143] Snigireva I I, Kohn V G and Snigirev A A 2004 Hard x-ray focusing with extremely long compound refractive lens **5539** 218–25

[144] Schropp A, Hoppe R, Meier V, Patommel J, Seiboth F, Lee H J, Nagler B, Galtier E C, Arnold B, Zastrau U, Hastings J B, Nilsson D, Uhlén F, Vogt U, Hertz H M and Schroer C G 2013 Full spatial characterization of a nanofocused x-ray free-electron laser beam by ptychographic imaging. *Sci. Rep.* **3** 1633

[145] Schroer C G, Kurapova O, Patommel J, Boye P, Feldkamp J, Lengeler B, Burghammer M, Riekel C, Vincze L, van der Hart A and Küchler M 2005 Hard x-ray nanoprobe based on refractive x-ray lenses *Appl. Phys. Lett.* **87** 124103

[146] Snigirev A, Snigireva I, Grigoriev M, Yunkin V, Di Michiel M, Kuznetsov S and Vaughan G 2007 Silicon planar lenses for high-energy x-ray nanofocusing *Proc. SPIE* **6705** 670506–11

[147] Yunkin V, Grigoriev M, Kuznetsov S, Snigirev A and Snigireva I 2004 Planar parabolic refractive lenses for hard x-rays. technological aspects of fabrication *Proc. SPIE* **5539** 226–34

[148] Stöhr F, Michael-lindhard J, Simons H, Poulsen H F, Hübner J, Hansen O, Garnaes J and Jensen F 2015 Three-dimensional nanometrology of microstructures by replica molding and large-range atomic force microscopy *Microelectron. Eng.* **141** 6–11

[149] Stöhr F, Wright J, Simons H, Michael-Lindhard J, Hübner J, Jensen F, Hansen O and Poulsen H F 2015 Optimizing shape uniformity and increasing structure heights of deep reactive ion etched silicon x-ray lenses *J. Micromechanics Microengineering* **25** 125013

[150] Stöhr F, Michael-Lindhard J, Hübner J, Jensen F, Simons H, Jakobsen A C, Poulsen H F and Hansen O 2015 Sacrificial structures for deep reactive ion etching of high-aspect ratio kinoform silicon X-ray lenses *J. Vac. Sci. Technol. B* **33** 062001

[151] Stöhr F, Simons H, Jakobsen A C, Nielsen C H, Michael-Lindhard J, Jensen F, Poulsen H F, Hansen O and Hübner J 2015 Injection molded polymeric hard X-ray lenses *Opt. Mater. Express* **5** 2804–11

[152] Simons H, Stöhr F, Michael-Lindhard J, Jensen F, Hansen O, Detlefs C and Poulsen H F 2016 Full-field hard x-ray microscopy with interdigitated silicon lenses. *Opt. Commun.* **359** 460–4

[153] Röntgen W 1896 Über eine neue Art von Strahlen *Sitzungsberichte der Phys. Gesellschaft zu Würzbg.*

[154] Röntgen W 1896 On a New Kind of Rays *Nature* **53**

[155] Einstein A 1918 Lassen sich Brechungsexponenten der Körper für Röntgenstrahlen experimentell ermitteln? *Verhandlungen der Dtsch. Phys. Gesellschaft* **20** 86–7

[156] Kirkpatrick P and Baez A V 1948 Formation of optical images by X-rays. *J. Opt. Soc. Am.* **38** 766–74

[157] Kirkpatrick P 1949 X-Ray Images by Refractive Focusing *J. Opt. Soc. Am.* **39** 796

[158] Suehiro S, Miyaji H and Hayashi H 1991 Refractive lens for X-ray focus *Nature* **352** 385–6

[159] Michette A G 1991 No X-ray lens *Nature* **353** 510–510

[160] Yang B X 1993 Fresnel and refractive lenses for X-rays *Nucl. Instruments Methods Phys. Res. Sect. A* **328** 578–87

[161] Tomie T 1997 X-ray lens, US Patent: US5684852 A

[162] Tomie T 2010 The birth of the X-ray refractive lens *Spectrochim. Acta Part B At. Spectrosc.* **65** 192–8

[163] Snigirev A, Kohn V, Snigireva I and Lengeler B 1996 A compound refractive lens for focusing high-energy X-rays *Nature* **384** 49–51

[164] Lengeler B, Schroer C G, Benner B, Günzler T F, Kuhlmann M, Tümmler J, Simionovici A S, Drakopoulos M, Snigirev A and Snigireva I 2001 Parabolic refractive X-ray lenses: a breakthrough in X-ray optics *Nucl. Instruments Methods Phys. Res. Sect. A* **467-468** 944–50

[165] Fredenberg E, Cederström B, Åslund M, Nillius P and Danielsson M 2009 An efficient pre-object collimator based on an x-ray lens *Med. Phys.* **36** 626

[166] Cremer J T 2012 *Introduction to Neutron and X-ray Optics. Advances in Imaging and Electron Physics Vol 172.* (Elsevier)

[167] Snigirev a, Kohn V, Snigireva I, Souvorov a and Lengeler B 1998 Focusing high-energy x rays by compound refractive lenses. *Appl. Opt.* **37** 653–62

[168] Protopopov V V and Valiev K A 1998 Theory of an ideal compound X-ray lens 297–312

[169] Lengeler B, Tümmler J, Snigirev A, Snigireva I and Raven C 1998 Transmission and gain of singly and doubly focusing refractive x-ray lenses *J. Appl. Phys.* **84** 5855

[170] Lengeler B, Schroer C, Tümmler J, Benner B, Richwin M, Snigirev A, Snigireva I and Drakopoulos M 1999 Imaging by parabolic refractive lenses in the hard X-ray range *J. Synchrotron Radiat.*

[171] Kohn V G 2002 On the theory of X-ray refractive optics: Exact solution for a parabolic medium *J. Exp. Theor. Phys. Lett.* **76** 600–3

[172] Kohn V G 2003 An exact theory of imaging with a parabolic continuously refractive X-ray lens *J. Exp. Theor. Phys.* **97** 204–15

[173] Kohn V, Snigireva I and Snigirev a. 2003 Diffraction theory of imaging with X-ray compound refractive lens *Opt. Commun.* **216** 247–60

[174] Kohn V G 2009 Semianalytical theory of focusing synchrotron radiation by an arbitrary system of parabolic refracting lenses and the problem of nano-focusing *J. Surf. Investig. X-ray, Synchrotron Neutron Tech.* **3** 358–64

[175] Pantell R H, Feinstein J, Beguiristain H R, Piestrup M a, Gary C K and Cremer J T 2003 Characteristics of the thick, compound refractive lens. *Appl. Opt.* **42** 719–23

[176] Poulsen S O and Poulsen H F 2014 Efficient Analytical Approaches to the Optics of Compound Refractive Lenses for Use with Synchrotron X-rays *Metall. Mater. Trans. A* **45** 4772–9

[177] Schroer C G, Lengeler B, Benner B, G T F, Kuhlmann M, Simionovici A S, Bohic S, Drakopoulos M, Snigirev A, Snigireva I and Schr W H 2001 Microbeam Production Using Compound Refractive Lenses : Beam Characterization and Applications **4499** 52–63

[178] Schroer C G and Falkenberg G 2014 Hard X-ray nanofocusing at low-emittance synchrotron radiation sources *J. Synchrotron Radiat.* **21** 996–1005

[179] Henke B L, Gullikson E M and Davis J C 1993 X-Ray Interactions. Photoabsorption, Scattering, Transmission, and Reflection at E = 50 - 30000 eV, Z = 1-92 *At. Data Nucl. Data Tables* **54** 181–342

[180] Sanchez del Rio M and Alianelli L 2012 Aspherical lens shapes for focusing synchrotron beams. *J. Synchrotron Radiat.* **19** 366–74

[181] Evans-Lutterodt K, Ablett J, Stein A, Kao C-C, Tennant D, Klemens F, Taylor A, Jacobsen C, Gammel P, Huggins H, Bogart G, Ustin S and Ocola L 2003 Single-element elliptical hard x-ray micro-optics. *Opt. Express* **11** 919–26

[182] Lengeler B, Schroer C G, Richwin M, Tümmler J, Drakopoulos M, Snigirev a. and Snigireva I 1999 A microscope for hard x rays based on parabolic compound refractive lenses *Appl. Phys. Lett.* **74** 3924

[183] Lipson A, Lipson S G and Lipson H 2010 *Optical Physics* (Cambridge University Press)

[184] Polikarpov M, Snigireva I and Snigirev A 2014 X-ray harmonics rejection on third-generation synchrotron sources using compound refractive lenses. *J. Synchrotron Radiat.* **21** 484–7

[185] Aristov V, Grigoriev M, Kuznetsov S, Shabelnikov L, Yunkin V, Weitkamp T, Rau C, Snigireva I, Snigirev a., Hoffmann M and Voges E 2000 X-ray refractive planar lens with minimized absorption *Appl. Phys. Lett.* **77** 4058

[186] Aristov V, Grigoriev M, Kuznetsov S, Shabelnikov L, Yunkin V, Rau C, Snigirev a., Snigireva I, Weitkamp T, Hoffmann M and Voges E 2001 Silicon planar refractive lenses with the optimized design *Nucl. Instruments Methods Phys. Res. Sect. A Accel. Spectrometers, Detect. Assoc. Equip.* **470** 131–4

[187] Snigireva I, Snigirev a., Rau C, Weitkamp T, Aristov V, Grigoriev M, Kuznetsov S, Shabelnikov L, Yunkin V, Hoffmann M and Voges E 2001 Holographic X-ray optical elements: transition between refraction and diffraction *Nucl. Instruments Methods Phys. Res. Sect. A Accel. Spectrometers, Detect. Assoc. Equip.* **467-468** 982–5

[188] Evans-Lutterodt K, Ablett J M, Stein A, Tennant D M, Klemens F and Taylor A 2004 Energy-dependent focusing properties of a kinoform Fresnel lens ed A A Snigirev and D C Mancini *Proc. SPIE* **5539** 73–9

[189] Evans-Lutterodt K, Stein A, Ablett J, Bozovic N, Taylor A and Tennant D 2007 Using Compound Kinoform Hard-X-Ray Lenses to Exceed the Critical Angle Limit *Phys. Rev. Lett.* **99** 134801

[190] Jark W 2008 Comment on 'Using Compound Kinoform Hard-X-Ray Lenses to Exceed the Critical Angle Limit' *Phys. Rev. Lett.* **101** 219501

[191] Evans-Lutterodt K, Stein A, Bozovic N, Taylor A and Tennant D 2008 Evans-Lutterodt et al. Reply: *Phys. Rev. Lett.* **101** 219502

[192] Stein A, Evans-Lutterodt K, Bozovic N and Taylor A 2008 Fabrication of silicon kinoform lenses for hard x-ray focusing by electron beam lithography and deep reactive ion etching *J. Vac. Sci. Technol. B* **26** 122

[193] Isakovic A F, Stein A, Warren J B, Narayanan S, Sprung M, Sandy A R and Evans-Lutterodt K 2009 Diamond kinoform hard X-ray refractive lenses: design, nanofabrication and testing. *J. Synchrotron Radiat.* **16** 8–13

[194] Sandy A R, Narayanan S, Sprung M, Su J-D, Evans-Lutterodt K, Isakovic A F and Stein A 2010 Kinoform optics applied to X-ray photon correlation spectroscopy. *J. Synchrotron Radiat.* **17** 314–20

[195] Shastri S D, Evans-Lutterodt K, Sheffield R L, Stein A, Metzler M and Kenesei P 2014 Kinoform lens focusing of high-energy x-rays (50 - 100 keV) *Proc. SPIE* **9207** 920704

[196] Alianelli L, Sawhney K J S, Loader I M, Jenkins D W K, Stevens R, Snigirev A and Snigireva I 2007 Development of refractive X-ray focusing optics at diamond light *Proc. SPIE* **6705** 670507

[197] Alianelli L, Sawhney K J S, Tiwari M K, Dolbnya I P, Stevens R, Jenkins D W K, Loader I M, Wilson M C and Malik a 2009 Germanium and silicon kinoform focusing lenses for hard x-rays *J. Phys. Conf. Ser.* **186** 012062

[198] Tiwari M K, Alianelli L, Dolbnya I P and Sawhney K J S 2010 Application of kinoform lens for X-ray reflectivity analysis *J. Synchrotron Radiat.* **17** 237–42

[199] Alianelli L, Sawhney K J S, Snigireva I, Snigirev A, Garrett R, Gentle I, Nugent K and Wilkins S 2010 Focusing Kinoform Lenses: Optical Design and Experimental Validation **633** 633–6

[200] Alianelli L, Sawhney K J S, Barrett R, Pape I, Malik a and Wilson M C 2011 High efficiency nano-focusing kinoform optics for synchrotron radiation. *Opt. Express* **19** 11120–7

[201] David C, Weitkamp T, Nöhammer B and van der Veen J F 2004 Diffractive and refractive X-ray optics for microanalysis applications *Spectrochim. Acta Part B At. Spectrosc.* **59** 1505–10

[202] Chen Z, Xie H, Deng B and Du G 2014 Toward one nanometer X-ray focusing: a complex refractive lens design *CHINESE Opt. Lett.* **12** 123401

[203] Nazmov V, Shabel'nikov L, Pantenburg F-J, Mohr J, Reznikova E, Snigirev A, Snigireva I, Kouznetsov S and DiMichiel M 2004 Kinoform X-ray lens creation in polymer materials by deep X-ray lithography *Nucl. Instruments Methods Phys. Res. Sect. B* **217** 409–16

[204] Nazmov V, Reznikova E, Snigirev a., Snigireva I, DiMichiel M, Grigoriev M, Mohr J, Matthis B and Saile V 2005 LIGA fabrication of X-ray Nickel lenses *Microsyst. Technol.* **11** 292–7

[205] Yan H 2010 X-ray nanofocusing by kinoform lenses: A comparative study using different modeling approaches *Phys. Rev. B* **81** 075402

[206] Fukui H, Simon M, Nazmov V, Mohr J, Evans-Lutterodt K, Stein A and Baron A Q R 2013 Large-aperture refractive lenses for momentum-resolved spectroscopy with hard X-rays. *J. Synchrotron Radiat.* **20** 591–5

[207] Chubar O, Berman L, Chu Y S, Fluerasu A, Hulbert S, Idir M, Kaznatcheev K, Shapiro D, Shen Q and Baltser J 2011 Development of partially-coherent wavefront propagation simulation methods for 3rd and 4th generation synchrotron radiation sources ed M Sanchez del Rio and O Chubar *Proc. SPIE* **8141** 814107–814107 – 10

[208] Kaznatcheev K, Idir M and Chubar O 2013 Novel approaches in the SR beamline design *Nucl. Instruments Methods Phys. Res. Sect. A Accel. Spectrometers, Detect. Assoc. Equip.* **710** 161–5

[209] Chubar O, Fluerasu a, Chu Y S, Berman L, Wiegart L, Lee W-K and Baltser J 2013 Experimental characterization of X-ray transverse coherence in the presence of beam transport optics *J. Phys. Conf. Ser.* **425** 052028

[210] Chubar O, Fluerasu a, Berman L, Kaznatcheev K and Wiegart L 2013 Wavefront propagation simulations for beamlines and experiments with 'Synchrotron Radiation Workshop' *J. Phys. Conf. Ser.* **425** 162001

[211] Chubar O 2014 Recent updates in the 'Synchrotron Radiation Workshop' code, on-going developments, simulation activities, and plans for the future *Proc. SPIE* **9209** 920907

[212] Osterhoff M, Karkoulis D and Ferrero C 2013 A wave-optical toolbox for multiple CRL transfocators *J. Phys. Conf. Ser.* **425** 162005

[213] Knudsen E B, Prodi A, Willendrup P, Lefmann K, Baltser J, Gundlach C, Sanchez del Rio M, Ferrero C and Feidenhans'l R 2011 McXtrace: a modern ray-tracing package for x-ray instrumentation *Proc. SPIE* **8141** 1–7

[214] Baltser J, Bergbäck Knudsen E, Vickery A, Chubar O, Snigirev A, Vaughan G, Feidenhans'l R and Lefmann K 2011 Advanced simulations of x-ray beam propagation through CRL transfocators using ray-tracing and wavefront propagation methods *Proc. SPIE, Int. Soc. Opt. Eng.* **8141** 814111–8

[215] Bergbäck Knudsen E, Prodi A, Baltser J, Thomsen M, Kjær Willendrup P, Sanchez Del Rio M, Ferrero C, Farhi E, Haldrup K, Vickery A, Feidenhans'l R, Mortensen K, Meedom Nielsen M, Friis Poulsen H, Schmidt S and Lefmann K 2013 McXtrace: A

Monte Carlo software package for simulating X-ray optics, beamlines and experiments *J. Appl. Crystallogr.* **46** 679–96

[216] Alianelli L, Sánchez del Río M and Sawhney K J S 2007 Ray-tracing simulation of parabolic compound refractive lenses *Spectrochim. Acta Part B At. Spectrosc.* **62** 593–7

[217] Río M S Del 2013 New challenges in ray tracing simulations of X-ray optics *J. Phys. Conf. Ser.* **425** 162003

[218] Moreno I, Ferreira C and Sánchez-López M M 2006 Ray matrix analysis of anamorphic fractional Fourier systems *J. Opt. A Pure Appl. Opt.* **8** 427–35

[219] Poulsen S O and Poulsen H F 2014 Efficient Analytical Approaches to the Optics of Compound Refractive Lenses for Use with Synchrotron X-rays *Metall. Mater. Trans. A* **45** 4772–9

[220] Elleaume P 1998 Optimization of compound refractive lenses for X-rays **412**

[221] Baron a Q R, Kohmura Y, Krishnamurthy V V, Shvyd'ko Y V and Ishikawa T 1999 Beryllium and aluminum refractive collimators for synchrotron radiation *J. Synchrotron Radiat.* **6** 953–6

[222] Cremer J T, Piestrup M a, Beguiristain H R, Gary C K, Pantell R H and Tatchyn R 1999 Cylindrical compound refractive x-ray lenses using plastic substrates *Rev. Sci. Instrum.* **70** 3545–8

[223] Baron A Q R, Kohmura Y, Ohishi Y and Ishikawa T 1999 A refractive collimator for synchrotron radiation *Appl. Phys. Lett.* **74** 1492–4

[224] Lengeler B, Schroer C G, Benner B, Gerhardus A, Günzler T F, Kuhlmann M, Meyer J and Zimprich C 2002 Parabolic refractive X-ray lenses. *J. Synchrotron Radiat.* **9** 119–24

[225] Lengeler B, Schroer C G, Kuhlmann M, Benner B and Günzler T F 2004 Beryllium parabolic refractive x-ray lenses

[226] Beguiristain H R, Cremer J T, Piestrup M a., Gary C K and Pantell R H 2002 X-ray focusing with compound lenses made from beryllium *Opt. Lett.* **27** 778–80

[227] Andrejczuk A, Nagamine M, Sakurai Y and Itou M 2014 A planar parabolic refractive nickel lens for high-energy X-rays *J. Synchrotron Radiat.* **21** 57–60

[228] Andrejczuk A, Krzywiński J, Sakurai Y and Itou M 2010 The role of single element errors in planar parabolic compound refractive lenses. *J. Synchrotron Radiat.* **17** 616–23

[229] Vaughan G B M, Wright J P, Bytchkov A, Rossat M, Gleyzolle H, Snigireva I and Snigirev A 2011 X-ray transfocators: focusing devices based on compound refractive lenses. *J. Synchrotron Radiat.* **18** 125–33

[230] Pereira N R, Dufresne E M, Clarke R and Arms D a 2004 Parabolic lithium refractive optics for x rays *Rev. Sci. Instrum.* **75** 37

[231] Pereira N R, Dufresne E M, Arms D a and Clarke R 2004 Large-aperture x-ray refractive lens from lithium *Proc. SPIE* **5539** 174–84

[232] Khounsary A, Dufresne E M, Young K, Kewish C M and Jansen A N 2006 Beryllium and lithium x-ray lenses at the APS *Proc. SPIE* **6317** 63170Q – 63170Q – 9

[233] Beguiristain H R, Cremer J T, Piestrup M a, Pantell R H, Gary C K and Feinstein J 2000 Compound x-ray refractive lenses made of polyimide *SPIE Proc.* **4144** 155–64

[234] Piestrup M a., Cremer J T, Beguiristain H R, Gary C K and Pantell R H 2000 Two-dimensional x-ray focusing from compound lenses made of plastic *Rev. Sci. Instrum.* **71** 4375

[235] Piestrup M, Pantell R, Cremer J T and Beguiristain H 2001 Compound refractive lens for x-rays *US 6269145 B1*

[236] Cremer J T, Piestrup M, Gary C K and Pantell R H 2004 Large-aperture compound refractive lenses ed R O Tatchyn, Z Chang, J-C Kieffer and J B Hastings *Proc. SPIE* **5194** 62–89

[237] Gary C K, Park H, Lombardo L W, Piestrup M a., Cremer J T, Pantell R H and Dudchik Y I 2007 High resolution x-ray microscope *Appl. Phys. Lett.* **90** 181111

[238] Schroer C G, Tümmler J, Lengeler B, Drakopoulos M, Snigirev A and Snigireva I 2001 Compound refractive lenses. High Quality Imaging Optics for the XFEL *Proc. SPIE* **4143** 60–8

[239] Schroer C G, Benner B, Kuhlmann M, Kurapova O, Lengeler B, Zontone F, Snigirev A a., Snigireva I and Schulte-Schrepping H 2004 Focusing hard x-ray FEL beams with parabolic refractive lenses ed S G Biedron, W Eberhardt, T Ishikawa and R O Tatchyn *Proc. SPIE* **5534** 116–24

[240] Hedayat A, Khounsary A and Mashayek F 2012 Thermo-mechanical properties of silicon, germanium, diamond, beryllium and silicon carbide for high heat load x-ray optics applications ed S Goto, C Morawe and A M Khounsary **8502** 85020O

[241] Schroer C 2004 *Hard x-ray microscopy and microanalysis with refractive x-ray Lenses* (Habilitation treatise: RWTH Aachen)

[242] Kuhlmann M 2004 *Hard X-Ray Microanalysis with Parabolic Refractive Lenses* (PhD Thesis: RWTH Aachen)

[243] Last A 2008 Refractive X-Ray Lenses Produced by X-Ray Lithography *LIGA and Its Applications* Advanced Micro and Nanosystems ed V Saile, U Wallrabe, O Tabata and J G Korvink (Weinheim, Germany: Wiley-VCH Verlag GmbH & Co. KGaA) pp 233–42

[244] Nazmov V, Reznikova E, Mohr J, Snigirev A, Snigireva I, Achenbach S and Saile V 2004 Fabrication and preliminary testing of X-ray lenses in thick SU-8 resist layers *Microsyst. Technol.* **10** 716–21

[245] Nazmov V, Reznikova E, Mohr J, Saile V, Vincze L, Vekemans B, Bohic S and Somogyi A 2011 Parabolic crossed planar polymeric x-ray lenses *J. Micromechanics Microengineering* **21** 015020

[246] Nazmov V, Simon R, Reznikova E, Mohr J and Saile V 2012 Polymer refractive crossed long lens: a new optical component for nanoimaging and nanofocussing in the hard X-ray region *J. Instrum.* **7** P07019–P07019

[247] Nazmov V, Mohr J, Greving I, Ogurreck M and Wilde F 2015 Modified x-ray polymer refractive cross lens with adiabatic contraction and its realization *J. Micromechanics Microengineering* **25** 055010

[248] Kupka R K, Bouamrane F, Cremers C and Megtert S 2000 Microfabrication: LIGA-X and applications *Appl. Surf. Sci.* **164** 97–110

[249] Jackson M 2007 *Micro and Nanomanufacturing* (Boston, MA: Springer)

[250] Kahn Malek C and Saile V 2004 Applications of LIGA technology to precision manufacturing of high-aspect-ratio micro-components and -systems: a review *Microelectronics J.* **35** 131–43

[251] Makarova O V, Mancini D C, Moldovan N, Divan R, Tang C M, Ryding D G and Lee R H 2003 Microfabrication of freestanding metal structures using graphite substrate *Sensors Actuators, A Phys.* **103** 182–6

[252] Cheng Y, Shew B Y, Chyu M K and Chen P H 2001 Ultra-deep LIGA process and its applications *Nucl. Instruments Methods Phys. Res. Sect. A Accel. Spectrometers, Detect. Assoc. Equip.* **467-468** 1192–7

[253] Rötting O, Röpke W, Becker H and Gärtner C 2002 Polymer microfabrication technologies *Microsyst. Technol.* **8** 32–6

[254] Kupka R K, Bouamrane F, Roulliay M and Megtert S 1999 X-ray transmission lenses by deep x-ray lithography and LIGA technique: first results and fundamental limits ed B Courtois, S B Crary, W Ehrfeld, H Fujita, J M Karam and K W Markus *Proc. SPIE* **3680** 508–17

[255] Mancini D C, Moldovan N A, Divan R, DeCarlo F and Yaeger J 2002 X-ray lenses fabricated by deep x-ray lithography ed D C Mancini *Proc. SPIE* **4783** 28–36

[256] Lee K Y 1995 Micromachining applications of a high resolution ultrathick photoresist *J. Vac. Sci. Technol. B Microelectron. Nanom. Struct.* **13** 3012

[257] Lorenz H, Despont M, Fahrni N, Brugger J, Vettiger P and Renaud P 1998 High-aspect-ratio, ultrathick, negative-tone near-UV photoresist and its applications for MEMS *Sensors Actuators A Phys.* **64** 33–9

[258] Schenk R, Halle O, Müllen K, Ehrfeld W and Schmidt M 1997 Highly sensitive resist material for deep X-ray lithography *Microelectron. Eng.* **35** 105–8

[259] Cremers C, Bouamrane F, Singleton L and Schenk R 2001 SU-8 as resist material for deep X-ray lithography *Microsyst. Technol.* **7** 11–6

[260] Singleton L, Bogdanova A L, Peredkova S S, Wilhelmia O, Cremersc C, Megtert S, Schmidt A, Mainz M, Mainz D-, Universitet L, Lund S-, Cmf C and Oqx O X 2001 Deep X-ray Lithography with the SU-8 Resist **4343** 182–92

[261] Khan Malek C G 2002 SU-8 resist for low-cost X-ray patterning of high-resolution, high-aspect-ratio MEMS *Microelectronics J.* **33** 101–5

[262] Peele a. G, Shew B Y, Vora K D and Li H C 2005 Overcoming SU-8 stiction in high aspect ratio structures *Microsyst. Technol.* **11** 221–4

[263] Del Campo A and Greiner C 2007 SU-8: a photoresist for high-aspect-ratio and 3D submicron lithography *J. Micromechanics Microengineering* **17** R81–95

[264] Pérennès F, Matteucci M, Jark W and Marmiroli B 2005 Fabrication of refractive X-ray focusing lenses by deep X-ray lithography *Microelectron. Eng.* **78-79** 79–87

[265] Saile V, Wallrabe U, Tabata O and Korvink J G 2009 *LIGA and Its Applications* (Weinheim, Germany: Wiley)

[266] Simon M 2010 *Röntgenlinsen mit großer Apertur* (PhD Thesis: Karlsruhe Institute of Technology)

[267] Marschall F 2014 *Entwicklung eines Röntgenmikroskops für Photonenenergien von 15 keV bis 30 keV* (PhD Thesis: Karlsruhe Institute of Technology)

[268] Nazmov V, Reznikova E and Mohr J 2011 Investigation of the radiation-induced thermal flexure of an x-ray lithography mask during a tilted exposure *J. Vac. Sci. Technol. B Microelectron. Nanom. Struct.* **29** 011007

[269] Marschall F, Last a, Simon M, Kluge M, Nazmov V, Vogt H, Ogurreck M, Greving I and Mohr J 2014 X-ray Full Field Microscopy at 30 keV *J. Phys. Conf. Ser.* **499** 012007

[270] Snigirev A, Snigireva I, Michiel M Di, Honkimaki V and Grigoriev M 2004 Sub-micron focusing of high energy X-rays with Ni refractive lenses . **5539** 244–50

[271] Nazmov V, Reznikova E, Last A, Mohr J, Saile V, Simon R and DiMichiel M 2007 X-ray Lenses Fabricated by LIGA Technology *AIP Conf. Proc.* **879** 770–3

[272] Snigirev A, Snigireva I, Drakopoulos M, Nazmov V, Reznikova E, Kuznetsov S, Grigoriev M, Mohr J and Saile V 2003 Focusing properties of x-ray polymer refractive lenses from SU-8 resist layer ed T Ishikawa, A T Macrander and J L Wood *Proc. SPIE* **5195** 21–31

[273] Nazmov V, Reznikova E, Somogyi a, Mohr J and Saile V 2004 Planar sets of cross X-ray refractive lenses from SU-8 polymer *Proc. SPIE* **5539** 235–43

[274] Hilhorst J, Marschall F, Tran Thi T N, Last a. and Schülli T U 2014 Full-field X-ray diffraction microscopy using polymeric compound refractive lenses *J. Appl. Crystallogr.* **47** 1882–8

[275] Reznikova E, Weitkamp T, Nazmov V, Simon M, Last A and Saile V 2009 Transmission hard X-ray microscope with increased view field using planar refractive objectives and condensers made of SU-8 polymer *J. Phys. Conf. Ser.* **186** 012070

[276] Nazmov V, Reznikova E, Mohr J, Schulz J and Voigt A 2015 Development and characterization of ultra high aspect ratio microstructures made by ultra deep X-ray lithography *J. Mater. Process. Technol.* **225** 170–7

[277] Koch F, Marschall F, Meiser J, Márkus O, Faisal A, Schröter T, Meyer P, Kunka D, Last A and Mohr J 2015 Increasing the aperture of x-ray mosaic lenses by freeze drying *J. Micromechanics Microengineering* **25** 075015

[278] Aristov V V, Grigoriev M V, Kuznetsov S M, Shabelnikov L G, Yunkin V A, Hoffmann M and Voges E 2000 X-ray focusing by planar parabolic refractive lenses made of silicon *Opt. Commun.* **177** 33–8

[279] Aristov V, Grigoriev M, Kuznetsov S, Shabelnikov L, Yunkin V, Rau C, Snigirev A, Snigireva I, Weitkamp T, Hoffmann M and Voges E 2001 Silicon planar parabolic lenses *Proc. SPIE* **4145** 285–93

[280] Grigoriev M, Shabelnikov L, Yunkin V, Snigirev A, Snigireva I, Di Michiel M, Kuznetsov S, Hoffmann M and Voges E 2001 Planar parabolic lenses for focusing high-energy x-rays *Proc. SPIE* **4501** 185–92

[281] Snigireva I, Grigoriev M, Shabel'nikov L, Yunkin V, Snigirev a, Kuznetsov S, Di Michiel M, Hoffmann M and Voges E 2002 An X-ray refractive collimator based on planar silicon lens. *Proc. SPIE* **4783** 19–27

[282] Snigireva I, Yunkin V, Kuznetsov S, Grigoriev M, Chukalina M, Shabel'nikov L, Snigirev A, Hoffman M and Voges E 2003 Focusing properties of silicon refractive lenses: comparison experimental results with the computer simulation. *Proc. SPIE* **5195** 32–9

[283] Snigireva I, Snigirev A, Yunkin V, Drakopoulos M, Grigoriev M, Kuznetsov S, Chukalina M, Hoffmann M, Nuesse D and Voges E 2004 X-ray Si-based Integrated Lens System for Wide Range of Hard Synchrotron Radiation *AIP Conf. Proc.* **705** 708–11

[284] Yunkin V, Grigoriev M, Kuznetsov S, Snigirev A and Snigireva I 2004 Mechanical bonding of two identical silicon planar refractive lenses *Proc. SPIE* **5539** 251–8

[285] Schroer C G, Kuhlmann M, Hunger U T, Günzler T F, Kurapova O, Feste S, Frehse F, Lengeler B, Drakopoulos M, Somogyi a., Simionovici a. S, Snigirev a., Snigireva I, Schug C and Schröder W H 2003 Nanofocusing parabolic refractive x-ray lenses *Appl. Phys. Lett.* **82** 1485

[286] Kurapova O, Lengeler B, Schroer C G, Küchler M, Gessner T and van der Hart A 2007 Optimized fabrication of silicon nanofocusing x-ray lenses using deep reactive ion etching *J. Vac. Sci. Technol. B* **25** 1626

[287] Boye P, Feldkamp J M, Patommel J, Schwab A, Stephan S, Hoppe R, Schroer C G, Burghammer M, Riekel C, Hart A Van Der and Küchler M 2009 Nanofocusing refractive X-ray lenses: Fabrication and modeling *J. Phys. Conf. Ser.* **186** 012063

[288] Seiboth F, Scholz M, Patommel J, Hoppe R, Wittwer F, Reinhardt J, Seidel J, Knaut M, Jahn A, Richter K, Bartha J W, Falkenberg G, Schroer C G, Seiboth F, Scholz M, Patommel J, Hoppe R, Wittwer F, Reinhardt J and Seidel J 2014 Hard x-ray nanofocusing by refractive lenses of constant thickness *Appl. Phys. Lett.* **131110**

[289] Patommel J, Hönig S, Ritter S, Scholz M, Seiboth F, Schroer C G, Kubec A, Niese S and Jahn A 2012 Adiabatically Focusing Lenses (AFL) 'http://photon-science.desy.de/annual_report/files/2012/20122257.pdf' *DESY Annu. Rep.*

[290] Snigirev A, Yunkin V, Snigireva I, Di Michiel M, Drakopoulos M, Kouznetsov S, Shabelnikov L, Grigoriev M, Ralchenko V, Sychov I, Hoffmann M and Voges E 2002 Snigirev 2002 - Diamond refractive lens for hard x-ray focusing *Proc. SPIE* **4783** 1–9

[291] Kurapova O, Feste S, Gather M, Gunzler T F, Hunger U T, Kuhlmann M, Patommel J, Schroer C G, Lengeler B and van der Hart A 2004 Fabrication of parabolic nanofocusing x-ray lenses ed A A Snigirev and D C Mancini *Proc. SPIE* **5539** 38–47

[292] Kurapova O 2005 *Development of Nanofocusing Refractive X-Ray Lenses* (PhD Thesis: Technical University Dresden)

[293] Boye P 2009 *Nanofocusing Refractive X-Ray Lenses* (PhD Thesis: Technical University Dresden)

[294] Nöhammer B, David C, Rothuizen H, Hoszowska J and Simionovici A 2003 Deep reactive ion etching of silicon and diamond for the fabrication of planar refractive hard X-ray lenses *Microelectron. Eng.* **68** 453–60

[295] Nöhammer B, Hoszowska J, Freund A K and David C 2003 Diamond planar refractive lenses for third- and fourth-generation X-ray sources *J. Synchrotron Radiat.* **10** 168–71

[296] Fox O J L 2011 *Deposition of nanocrystalline diamond films by MW plasma CVD* (PhD Thesis: University of Bristol)

[297] Alianelli L, Sawhney K J S, Malik A, Fox O J L, May P W, Stevens R, Loader I M and Wilson M C 2010 A planar refractive x-ray lens made of nanocrystalline diamond *J. Appl. Phys.* **108** 123107

[298] Malik a M, Fox O J L, Alianelli L, Korsunsky a M, Stevens R, Loader I M, Wilson M C, Pape I, Sawhney K J S and May P W 2013 Deep reactive ion etching of silicon moulds for the fabrication of diamond x-ray focusing lenses *J. Micromechanics Microengineering* **23** 125018

[299] Fox O J L, Alianelli L, Malik a. M, Pape I, May P W and Sawhney K J S 2014 Nanofocusing optics for synchrotron radiation made from polycrystalline diamond *Opt. Express* **22** 7657

[300] Cederstrom B, Cahn R, Danielsson M, Lundqvist M and Nygren D 2000 Focusing hard X-rays with old LPs *Nature* **404** 951

[301] Cederström B, Lundqvist M and Ribbing C 2002 Multi-prism x-ray lens *Appl. Phys. Lett.* **81** 1399

[302] Cederström B, Ribbing C and Lundqvist M 2002 Saw-tooth refractive x-ray optics with sub-micron resolution *Proc. SPIE* **4783** 37–48

[303] Cederström B 2002 *A multi-prism lens for hard x-rays* (PhD Thesis: Institute of Technology - Stockholm)

[304] Cederström B, Lundqvist M and Ribbing C 2002 Multi-prism x-ray lens *Appl. Phys. Lett.* **81** 1399

[305] Ribbing C 2003 Microstructured diamond X-ray source and refractive lens **12** 1793–9

[306] Shastri S D, Almer J, Ribbing C and Cederström B 2007 High-energy X-ray optics with silicon saw-tooth refractive lenses. *J. Synchrotron Radiat.* **14** 204–11

[307] Jark W 2004 A simple x-ray monochromator based on an alligator lens *X-Ray Spectrom.* **33** 455–61

[308] Said a H and Shastri S D 2010 Silicon saw-tooth refractive lens for high-energy X-rays made using a diamond saw. *J. Synchrotron Radiat.* **17** 425–7

[309] Jark W H, Perennes F, Matteucci M, Mancini L, Montanari F, Rigon L, Tromba G, Somogyi A, Tucoulou R and Bohic S 2004 Focusing hard x-rays with large kinoform lenses of mm size ed A A Snigirev and D C Mancini *Proc. SPIE* **5539** 59–72

[310] Jark W, Pérennès F, Matteucci M, Mancini L, Montanari F, Rigon L, Tromba G, Somogyi A, Tucoulou R and Bohic S 2004 Focusing X-rays with simple arrays of prism-like structures. *J. Synchrotron Radiat.* **11** 248–53

[311] Jark W, Pérennès F and Matteucci M 2006 On the feasibility of large-aperture Fresnel lenses for the microfocusing of hard X-rays. *J. Synchrotron Radiat.* **13** 239–52

[312] Jark W, Matteucci M and Menk R H 2008 On the use of clessidra prism arrays in long-focal-length X-ray focusing. *J. Synchrotron Radiat.* **15** 411–3

[313] Nazmov V, Mohr J and Simon R 2013 Mosaic-like micropillar array for hard x-ray focusing—one-dimensional version *J. Micromechanics Microengineering* **23** 095015

[314] Cederström B, Ribbing C and Lundqvist M 2005 Generalized prism-array lenses for hard X-rays. *J. Synchrotron Radiat.* **12** 340–4

[315] Karvinen P, Grolimund D, Willimann M, Meyer B, Birri M, Borca C, Patommel J, Wellenreuther G, Falkenberg G, Guizar-Sicairos M, Menzel A and David C 2014 Kinoform diffractive lenses for efficient nano-focusing of hard X-rays *Opt. Express* **22** 16676

[316] Dufresne E M, Arms D a., Clarke R, Pereira N R, Dierker S B and Foster D 2001 Lithium metal for x-ray refractive optics *Appl. Phys. Lett.* **79** 4085

[317] Fredenberg E, Cederström B, Åslund M, Ribbing C and Danielsson M 2008 A Tunable Energy Filter for Medical X-Ray Imaging *X-Ray Opt. Instrum.* **2008** 1–8

[318] Simon M, Reznikova E, Nazmov V, Grund T and Last a. 2010 A new type of X-ray condenser lenses with large apertures fabricated by rolling of structured films *AIP Conf. Proc.* **1221** 85–90

[319] Nillius P, Karlsson S, Cederström B, Fredenberg E and Danielsson M 2011 Large-aperture focusing of high-energy x rays with a rolled polyimide film. *Opt. Lett.* **36** 555–7

[320] Tibbelin S, Nillius P and Danielsson M 2012 Simulation of HyperSPECT: a high-resolution small-animal system with in-line x-ray optics *Phys. Med. Biol.* **57** 1617–29

[321] Vogt H, Eisenhower R, Last A, Mettendorf K U, Mohr J, Nazmov V and Simon M 2011 Advances in the development of x-ray refractive large aperture rolled prism lenses ed R Hudec and L Pina *Proc. SPIE* **8076** 80760I

[322] Jark W 2011 High spatial resolution with zoomable saw-tooth refractive lenses? *Proc. SPIE* **8139** 81390W – 1

[323] Jark W 2011 On aberrations in saw-tooth refractive X-ray lenses and on their removal *J. Synchrotron Radiat.* **18** 198–211

[324] Antimonov M a., Khounsary A M and Shastri S D 2013 Aberrations in saw-tooth refractive lenses in short focal length x-ray focusing *Proc. SPIE* **8848** 88480A

[325] Antimonov M a. and Khounsary A M 2014 Saw-tooth refractive lens for high energy x-ray focusing *Proc. SPIE* **9207** 92070Z

[326] Katoh T, Nishi N, Fukagawa M, Ueno H and Sugiyama S 2001 Direct writing for three-dimensional microfabrication using synchrotron radiation etching *Sensors Actuators, A Phys.* **89** 10–5

[327] Zhang Y P, Katoh T, Kagoshima Y, Matui J and Tsusaka Y 2001 Focusing hard X-ray with a single lens *Jpn. J. Appl. Phys.* **40** L75–7

[328] Katoh T, Zhang Y, Kagoshima Y, Tsusaka Y and Matsui J 2002 Direct microfabrication using an X-ray micro-beam *Sensors Actuators, A Phys.* **97-98** 725–8

[329] Aristov V V, Starkov V V, Shabel L G, Kuznetsov S M, Ushakova A P, Grigoriev M V and Tseitlin V M 1999 Short-focus silicon parabolic lenses for hard X-rays 203–8

[330] Artemiev a., Snigirev a., Kohn V, Snigireva I, Artemiev N, Grigoriev M, Peredkov S, Glikin L, Levtonov M, Kvardakov V, Zabelin a. and Maevskiy a. 2006 X-ray parabolic lenses made from glassy carbon by means of laser *Rev. Sci. Instrum.* **77** 063113

[331] Polikarpov M, Snigireva I, Morse J, Yunkin V, Kuznetsov S and Snigirev A 2015 Large-acceptance diamond planar refractive lenses manufactured by laser cutting *J. Synchrotron Radiat.* **22** 23–8

[332] Terentyev S, Blank V, Polyakov S, Zholudev S, Snigirev A, Polikarpov M, Kolodziej T, Qian J, Zhou H and Shvyd'ko Y 2015 Parabolic single-crystal diamond lenses for coherent x-ray imaging *Appl. Phys. Lett.* **107** 111108

[333] Dudchik Y ., Kolchevsky N ., Komarov F ., Kohmura Y, Awaji M, Suzuki Y and Ishikava T 2000 Glass capillary X-ray lens: fabrication technique and ray tracing calculations *Nucl. Instruments Methods Phys. Res. Sect. A* **454** 512–9

[334] Dudchik Y I, Kolchevsky N N, Komarov F F, Piestrup M a., Cremer J T, Gary C K, Park H and Khounsary a. M 2004 Microspot x-ray focusing using a short focal-length compound refractive lenses *Rev. Sci. Instrum.* **75** 4651

[335] Dudchik Y I, Komarov F F, Piestrup M a., Gary C K and Cremer J T 2005 Microcapillary refractive lens as a possible optical element for focusing free-electron laser x-rays ed S B Dabagov *Proc. SPIE* **5974** 597417–1

[336] Dudchik Y I, Gary C K, Park H, Pantell R H and Piestrup M a. 2007 Projection-type X-ray microscope based on a spherical compound refractive X-ray lens ed A M Khounsary, C Morawe and S Goto *Proc. SPIE* **6705** 670509

[337] Pavlov G, Snigireva I, Snigirev a., Sagdullin T and Schmidt M 2012 Refractive X-ray shape memory polymer 3D lenses with axial symmetry *X-Ray Spectrom.* **41** 313–5

[338] Dekker J, Kolari K and Puurunen R L 2006 Inductively coupled plasma etching of amorphous Al2O3 and TiO2 mask layers grown by atomic layer deposition *J. Vac. Sci. Technol. B* **24** 2350

[339] Plummer J, Deal M and Griffin P 2001 *Silicon VLSI technolgy* (Prentice Hall)

[340] Franssila S 2010 *Introduction to Microfabrication* (West Sussex: Wiley)

[341] Ramsden J 2010 *Handbook of Silicon Based MEMS Materials and Technologies* (Oxford: William Andrew)

[342] Layadi N, Colonell J and Lee J 1999 An introduction to plasma etching for VLSI circuit technology *Bell Labs Tech. J.* **July-Septe** 155–71

[343] Wilkinson C D W and Rahman M 2004 Dry etching and sputtering. *Philos. Trans. A* **362** 125–38

[344] Coburn J W and Winters H F 1979 Ion- and electron-assisted gas-surface chemistry—An important effect in plasma etching *J. Appl. Phys.* **50** 3189

[345] Jansen H V, de Boer M J, Unnikrishnan S, Louwerse M C and Elwenspoek M C 2009 Black silicon method: X. A review on high speed and selective plasma etching of silicon with profile control: an in-depth comparison between Bosch and cryostat DRIE processes as a roadmap to next generation equipment *J. Micromechanics Microengineering* **19** 033001

[346] Maruyama T, Narukage T, Onuki R and Fujiwara N 2010 High-aspect-ratio deep Si etching in SF6/O2 plasma. I. Characteristics of radical reactions with high-aspect-ratio patterns *J. Vac. Sci. Technol. B Microelectron. Nanom. Struct.* **28** 854

[347] Maruyama T, Narukage T, Onuki R and Fujiwara N 2010 High-aspect-ratio deep Si etching in SF6/O2 plasma. II. Mechanism of lateral etching in high-aspect-ratio features *J. Vac. Sci. Technol. B Microelectron. Nanom. Struct.* **28** 862

[348] Dussart R, Tillocher T, Lefaucheux P and Boufnichel M 2014 Plasma cryogenic etching of silicon: from the early days to today's advanced technologies *J. Phys. D* **47** 123001

[349] Jensen S 2004 *Inductively Coupled Plasma Etching for Microsystems* (PhD Thesis: Technical University of Denmark)

[350] Laermer F and Schilp A 1996 Method of anisotropically etching silicon, US Patent: US5501893 A

[351] Laermer F, Schilp A, Funk K and Offenberg M 1999 Bosch deep silicon etching: improving uniformity and etch rate for advanced MEMS applications *IEEE* 211–6

[352] Laermer F and Urban A 2003 Challenges, developments and applications of silicon deep reactive ion etching *Microelectron. Eng.* **67-68** 349–55

[353] Laermer F and Urban A 2005 Milestones in deep reactive ion etching *IEEE* 1118–21

[354] Wu B, Kumar A and Pamarthy S 2010 High aspect ratio silicon etch: A review *J. Appl. Phys.* **108** 051101

[355] Barnett R, Thomas D, Song Y, Tossell D, Barrass T and Ansell O 2010 A new plasma source for next generation MEMS deep SI etching: Minimal tilt, improved profile uniformity and higher etch rates *Proceedings - Electronic Components and Technology Conference* pp 1056–9

[356] Chutani R K, Hasegawa M, Maurice V, Passilly N and Gorecki C 2014 Single-step deep reactive ion etching of ultra-deep silicon cavities with smooth sidewalls *Sensors Actuators A* **208** 66–72

[357] McNie M E, Pickering C, Rickard A, Young I, Hopkins J, Ashraf H, Mcauley S, Nicholls G, Barnett R, Roozeboom F, Kemmeren A, van den Heuvel E, Verhoeven J, Gromley C, Schina P, Di Luciano C and Kiihamäki J 2003 Performance enhancement and evaluation of deep dry etching on a production cluster platform *Proc. SPIE* **4979** 34–42

[358] Pugh C J 2013 *End Point Detection in Reactive Ion Etching* (Doctoral thesis, University College London)

[359] Ullal S J, Singh H, Daugherty J, Vahedi V and Aydil E S 2002 Maintaining reproducible plasma reactor wall conditions: SF[sub 6] plasma cleaning of films deposited on chamber walls during Cl[sub 2]/O[sub 2] plasma etching of Si *J. Vac. Sci. Technol. A* **20** 1195

[360] Wasilik M and Chen N 2004 Deep reactive ion etch conditioning recipe *Proc. SPIE* **5342** 103–10

[361] Cunge G, Pelissier B, Joubert O, Ramos R and Maurice C 2005 New chamber walls conditioning and cleaning strategies to improve the stability of plasma processes *Plasma Sources Sci. Technol.* **14** 599–609

[362] Labelle C B, Donnelly V M, Bogart G R, Opila R L and Kornblit A 2004 Investigation of fluorocarbon plasma deposition from c-C4F for use as passivation during deep silicon etching *J. Vac. Sci. Technol. A* **22** 2500–7

[363] Yunkin V A, Fischer D and Voges E 1994 Highly anisotropic selective reactive ion etching of deep trenches in silicon *Microelectron. Eng.* **23** 373–6

[364] Ayón A A, Braff R, Lin C C, Sawin H H and Schmidt M A 1999 Characterization of a Time Multiplexed Inductively Coupled Plasma Etcher **146** 339–49

[365] Ayón A A 1999 Influence of Coil Power on the Etching Characteristics in a High Density Plasma Etcher *J. Electrochem. Soc.* **146** 2730–6

[366] Blauw M A, Zijlstra T and van der Drift E 2001 Balancing the etching and passivation in time-multiplexed deep dry etching of silicon *J. Vac. Sci. Technol. B* **19** 2930

[367] Chen K, Ayón A A, Member S, Zhang X and Spearing S M 2002 Effect of Process Parameters on the Surface Morphology and Mechanical Performance of Silicon Structures After Deep Reactive Ion Etching (DRIE) **11** 264–75

[368] Boufnichel M, Aachboun S, Grangeon F, Lefaucheux P and Ranson P 2002 Profile control of high aspect ratio trenches of silicon. I. Effect of process parameters on local bowing *J. Vac. Sci. Technol. B* **20** 1508

[369] Boufnichel M, Aachboun S, Lefaucheux P and Ranson P 2003 Profile control of high aspect ratio trenches of silicon. II. Study of the mechanisms responsible for local bowing formation and elimination of this effect *J. Vac. Sci. Technol. B* **21** 267

[370] Rangelow I W 2003 Critical tasks in high aspect ratio silicon dry etching for microelectromechanical systems *J. Vac. Sci. Technol. A* **21** 1550

[371] Anderson H, Merson J and Light R 1986 A Kinetic Model for Plasma Etching Silicon in a SF6.O2 RF Discharge *IEEE* **PS-14** 156–64

[372] Chung C K, Lu H C and Jaw T H 2000 High aspect ratio silicon trench fabrication by inductively coupled plasma *Microsyst. Technol.* **6** 106–8

[373] Adam T N, Kim S, Lv P-C, Xuan G, Ray S K, Troeger R T, Prather D and Kolodzey J 2007 Cyclic deep reactive ion etching with mask replenishment *J. Micromechanics Microengineering* **17** 1773–80

[374] Arnold J C, Gray D R and Sawin H H 1993 Influence of reactant transport on fluorine reactive ion etching of deep trenches in silicon *J. Vac. Sci. Technol. B* **11** 2071

[375] Jurgensen C W 1989 Kinetic theory of bombardment induced interface evolution *J. Vac. Sci. Technol. B* **7** 1488

[376] Liu J, Huppert G L and Sawin H H 1990 Ion bombardment in rf plasmas *J. Appl. Phys.* **68** 3916–34

[377] Economou D J 1988 Effect of Potential Field on Ion Deflection and Shape Evolution of Trenches during Plasma-Assisted Etching *J. Electrochem. Soc.* **135** 941

[378] Ingram S G 1990 The influence of substrate topography on ion bombardment in plasma etching *J. Appl. Phys.* **68** 500–4

[379] Arnold J C and Sawin H H 1991 Charging of pattern features during plasma etching *J. Appl. Phys.* **70** 5314–7

[380] Kim D and Economou D J 2003 Plasma molding over deep trenches and the resulting ion and energetic neutral distributions *J. Vac. Sci. Technol. B* **21** 1248

[381] Kim D, Economou D J, Woodworth J, Miller P, Shul R, Aragon B, Hamillton T and Willison C 2003 Plasma Molding Over Surface Topography: Simulation of Ion Flow, and Energy and Angular Distributions Over Steps in RF High-Density Plasmas *IEEE* **31** 691–702

[382] Davis R J 1991 Image potentials and the dry etching of submicron trenches with low-energy ions *Appl. Phys. Lett.* **59** 1717–9

[383] Shaqfeh E S G and Jurgensen C W 1989 Simulation of reactive ion etching pattern transfer *J. Appl. Phys.* **66** 4664

[384] Gottscho R a. 1992 Microscopic uniformity in plasma etching *J. Vac. Sci. Technol. B Microelectron. Nanom. Struct.* **10** 2133

[385] Jansen H, de Boer M, Wiegerink R, Tas N, Smulders E, Neagu C and Elwenspoek M 1997 RIE lag in high aspect ratio trench etching of silicon *Microelectron. Eng.* **35** 45–50

[386] Yeom J, Wu Y, Selby J C and Shannon M a. 2005 Maximum achievable aspect ratio in deep reactive ion etching of silicon due to aspect ratio dependent transport and the microloading effect *J. Vac. Sci. Technol. B Microelectron. Nanom. Struct.* **23** 2319

[387] Lai S L, Johnson D and Westerman R 2006 Aspect ratio dependent etching lag reduction in deep silicon etch processes *J. Vac. Sci. Technol. A* **24** 1283

[388] Kiihamäki J and Franssila S 1999 Pattern shape effects and artefacts in deep silicon etching *J. Vac. Sci. Technol. A* **17** 2280

[389] Mogab C J 1977 The Loading Effect in Plasma Etching *J. Electrochem. Soc.* **124** 1262

[390] Hedlund C 1994 Microloading effect in reactive ion etching *J. Vac. Sci. Technol. A* **12** 1962

[391] Karttunen J, Kiihamäki J and Franssila S 2000 Loading effects in deep silicon etching *Proc. SPIE* **4174** 90–7

[392] Jensen S and Hansen O 2004 Characterization of the microloading effect in deep reactive ion etching of silicon *Proc. SPIE* **5342** 111–8

[393] Jung K, Song W, Lim H W and Lee C S 2010 Parameter study for silicon grass formation in Bosch process *J. Vac. Sci. Technol. B Microelectron. Nanom. Struct.* **28** 143

[394] Jansen H, de Boer M, Legtenberg R and Elwenspoek M 1995 The black silicon method: a universal method for determining the parameter setting of a fluorine-based reactive ion etcher in deep silicon trench etching with profile control *Microelectron. Eng.* **5** 115–20

[395] Jansen H, de Boer M, Burger J, Legtenberg R and Elwenspoek M 1995 The black silicon method II. The effect of mask material and loading on the reactive ion etching of deep silicon trenches *Microelectron. Eng.* **27** 475–80

[396] Abdolvand R and Ayazi F 2008 An advanced reactive ion etching process for very high aspect-ratio sub-micron wide trenches in silicon *Sensors Actuators A Phys.* **144** 109–16

[397] Blauw M A, Craciun G, Sloof W G, French P J and van der Drift E 2002 Advanced time-multiplexed plasma etching of high aspect ratio silicon structures *J. Vac. Sci. Technol. B* **20** 3106

[398] Panda S, Ranade R and Mathad G S 2003 Etching High Aspect Ratio Silicon Trenches *J. Electrochem. Soc.* **150** G612

[399] Saraf I, Goeckner M, Goodlin B, Kirmse K and Overzet L 2011 Mask undercut in deep silicon etch *Appl. Phys. Lett.* **98** 161502

[400] Volland B E, Heerlein H, Kostic I and Rangelow I W 2001 The application of secondary effects in high aspect ratio dry etching for the fabrication of MEMS *Microelectron. Eng.* **57-58** 641–50

[401] Docker P T, Kinnell P K and Ward M C L 2004 Development of the one-step DRIE dry process for unconstrained fabrication of released MEMS devices *J. Micromechanics Microengineering* **14** 941–4

[402] Seok S, Lee B, Kim J, Kim H and Chun K 2005 A new compensation method for the footing effect in MEMS fabrication *J. Micromechanics Microengineering* **15** 1791–6

[403] Haobing L and Chollet F 2006 Layout Controlled One-Step Dry Etch and Release of MEMS Using Deep RIE on SOI Wafer **15** 541–7

[404] Wasilik M and Pisano A 2001 Low-frequency process for silicon-on-insulator deep reactive ion etching *Proc. SPIE* **4592** 462–72

[405] Mcauley S A, Ashraf H, Atabo L, Chambers A, Hall S, Hopkins J, Nicholls G, Systems S T, Park I and Np N 2001 Silicon micromachining using a high-density plasma source **34** 2769–74

[406] Volland B, Shi F, Hudek P, Heerlein H and Rangelow I W 1999 Dry etching with gas chopping without rippled sidewalls *J. Vac. Sci. Technol. B Microelectron. Nanom. Struct.* **17** 2768

[407] Liu H-C, Lin Y-H and Hsu W 2003 Sidewall roughness control in advanced silicon etch process *Microsyst. Technol.* **10** 29–34

[408] Gao F, Ylinen S, Kainlauri M and Kapulainen M 2014 Smooth silicon sidewall etching for waveguide structures using a modified Bosch process *J. Micro/Nanolithography, MEMS, MOEMS* **13** 013010

[409] Juan W H 1996 Controlling sidewall smoothness for micromachined Si mirrors and lenses *J. Vac. Sci. Technol. B* **14** 4080

[410] Matthews B, Member S, Judy J W and Member S 2006 Design and Fabrication of a Micromachined Planar Patch-Clamp Substrate With Integrated Microfluidics for Single-Cell Measurements **15** 214–22

[411] Kao D-B, McVittie J P, Nix W D and Saraswat K C 1987 Two-dimensional thermal oxidation of silicon - I. Experiments *IEEE Trans. Electron Devices* **34** 1008–17

[412] Lee M-C M and Wu M C 2006 Thermal Annealing in Hydrogen for 3-D Profile Transformation on Silicon-on-Insulator and Sidewall Roughness Reduction *J. Microelectromechanical Syst.* **15** 338–43

[413] Marty F, Rousseau L, Saadany B, Mercier B, Français O, Mita Y and Bourouina T 2005 Advanced etching of silicon based on deep reactive ion etching for silicon high aspect ratio microstructures and three-dimensional micro- and nanostructures *Microelectronics J.* **36** 673–7

[414] Mita Y, Kubota M, Harada T, Marty F, Saadany B, Bourouina T and Shibata T 2006 Contour lithography methods for DRIE fabrication of nanometre–millimetre-scale coexisting microsystems *J. Micromechanics Microengineering* **16** 135–41

[415] Ikehara T and Maeda R 2005 Fabrication of an accurately vertical sidewall for optical switch applications using deep RIE and photoresist spray coating *Microsyst. Technol.* **12** 98–103

[416] Kiihamäki J, Kattelus H, Karttunen J and Franssila S 2000 Depth and profile control in plasma etched MEMS structures *Sensors and Actuators* **82** 234–8

[417] Le N C H, Dao D V, Yokokawa R, Wells J C and Sugiyama S 2009 Fabrication of optically smooth, through-wafer silicon molds for PDMS total internal reflection-based devices *Microsyst. Technol.* **15** 1845–53

[418] Agarwal R, Samson S and Bhansali S 2007 Fabrication of vertical mirrors using plasma etch and KOH:IPA polishing *J. Micromechanics Microengineering* **17** 26–35

[419] Rao M P, Aimi M F and MacDonald N C 2004 Single-mask, three-dimensional microfabrication of high-aspect-ratio structures in bulk silicon using reactive ion etching lag and sacrificial oxidation *Appl. Phys. Lett.* **85** 6281–3

[420] Khanna R, Zhang X, Protz J and Ayón A A 2001 Microfabrication Protocols for Deep Reactive Ion Etching and Wafer-Level Bonding *Sensors Mag.* **18** 51–60

[421] Chabloz M, Sakai Y, Matsuura T and Tsutsumi K 2000 Improvement of sidewall roughness in deep silicon etching **6** 86–9

[422] Hopkins J, Ashraf H, Bhardwaj J K, Hynes A M, Johnston I and Shepherd J N 1998 The Benefits of Process Parameter Ramping During The Plasma Etching of High Aspect Ratio Silicon Structures *MRS Proc.* **546**

[423] Simon M, Reznikova E, Nazmov V and Last A 2008 Measurement of side walls of high aspect ratio microstructures *Microsyst. Technol.* **14** 1727–9

[424] Schroer C G, Lengeler B, Benner B, Kuhlmann M, Guenzler T F, Tuemmler J, Rau C, Weitkamp T, Snigirev A A and Snigireva I 2001 Parabolic compound refractive lenses for hard x rays ed A K Freund, T Ishikawa, A M Khounsary, D C Mancini, A G Michette and S Oestreich *Proc. SPIE* **4145** 274–84

[425] Kruth J P, Bartscher M, Carmignato S, Schmitt R, De Chiffre L and Weckenmann A 2011 Computed tomography for dimensional metrology *CIRP Ann. - Manuf. Technol.* **60** 821–42

[426] Engelhardt M, Baumann J, Schuster M, Kottler C, Pfeiffer F, Bunk O and David C 2007 Inspection of refractive x-ray lenses using high-resolution differential phase contrast imaging with a microfocus x-ray source *Rev. Sci. Instrum.* **78** 1–5

[427] Rutishauser S, Zanette I, Weitkamp T, Donath T and David C 2011 At-wavelength characterization of refractive x-ray lenses using a two-dimensional grating interferometer *Appl. Phys. Lett.* **99** 221104

[428] Nilsson D, Uhlén F, Holmberg A, Hertz H M, Schropp A, Patommel J, Hoppe R, Seiboth F, Meier V, Schroer C G, Galtier E, Nagler B, Lee H J and Vogt U 2012 Ronchi test for characterization of nanofocusing optics at a hard x-ray free-electron laser. *Opt. Lett.* **37** 5046–8

[429] Uhlén F, Rahomäki J, Nilsson D, Seiboth F, Sanz C, Wagner U, Rau C, Schroer C G and Vogt U 2014 Ronchi test for characterization of X-ray nanofocusing optics and beamlines *J. Synchrotron Radiat.* **21** 1105–9

[430] Hansen H N, Carneiro K, Haitjema H and De Chiffre L 2006 Dimensional Micro and Nano Metrology *CIRP Ann. - Manuf. Technol.* **55** 721–43

[431] Whitehouse D J 2008 Nanometrology *Contemp. Phys.* **49** 351–74

[432] Leach R 2014 *Fundamental Principles of Engineering Nanometrology* (Oxford: Elsevier)

[433] Ali S H R 2012 Advanced Nanomeasuring Techniques for Surface Characterization *ISRN Opt.* 859353

[434] Bariani P, De Chiffre L, Hansen H N and Horsewell a. 2005 Investigation on the traceability of three dimensional scanning electron microscope measurements based on the stereo-pair technique *Precis. Eng.* **29** 219–28

[435] Marinello F, Bariani P, Savio E, Horsewell A and De Chiffre L 2008 Critical factors in SEM 3D stereo microscopy *Meas. Sci. Technol.* **19** 065705

[436] Carli L, Genta G, Cantatore a, Barbato G, De Chiffre L and Levi R 2011 Uncertainty evaluation for three-dimensional scanning electron microscope reconstructions based on the stereo-pair technique *Meas. Sci. Technol.* **22** 035103

[437] Carli L 2010 *3D-SEM Metrology for Coordinate Measurements at the Nanometer Scale* (PhD Thesis: Technical University of Denmark)

[438] Leach R 2011 *Optical Measurement of Surface Topography* (Berlin, Heidelberg: Springer)

[439] Leach R K, Boyd R, Burke T, Danzebrink H-U, Dirscherl K, Dziomba T, Gee M, Koenders L, Morazzani V, Pidduck A, Roy D, Unger W E S and Yacoot A 2011 The European nanometrology landscape. *Nanotechnology* **22** 062001

[440] Leach R K, Claverley J, Giusca C, Jones C W, Nimishakavi L, Sun W, Tedaldi M and Yacoot A 2012 Advances in engineering nanometrology at the National Physical Laboratory *Meas. Sci. Technol.* **23** 074002

[441] Kramar J a 2005 Nanometre resolution metrology with the Molecular Measuring Machine *Meas. Sci. Technol.* **16** 2121–8

[442] Eves B J 2009 Design of a large measurement-volume metrological atomic force microscope (AFM) *Meas. Sci. Technol.* **20** 084003

[443] Kim J-A, Kim J W, Kang C-S and Eom T B 2010 Metrological atomic force microscope using a large range scanning dual stage *Int. J. Precis. Eng. Manuf.* **10** 11–7

[444] Hausotte T, Percle B and Jäger G 2009 Advanced three-dimensional scan methods in the nanopositioning and nanomeasuring machine *Meas. Sci. Technol.* **20** 084004

[445] Manske E, Jäger G, Hausotte T and Füßl R 2012 Recent developments and challenges of nanopositioning and nanomeasuring technology *Meas. Sci. Technol.* **23** 074001

[446] Hausotte T, Vorbringer-Dorozhovets N, Shen J C, Manske E and Jager G 2013 Dimensional metrology in the macroscopic range with sub-nanometre resolution *Proc. Inst. Mech. Eng. Part B J. Eng. Manuf.* **227** 657–61

[447] Canny J 1986 A computational approach to edge detection *IEEE* **PAMI-8** 679–714

[448] Artigas R 2011 Imaging Confocal Microscopy *Optical Measurement of Surface TopographyTopography* ed R Leach (Berlin, Heidelberg: Springer Berlin Heidelberg) pp 237–86

[449] Helmi F 2011 Focus variation instruments *Optical Measurement of Surface TopographyTopography* ed R Leach (Berlin, Heidelberg) pp 131–66

[450] Marinello F, Bariani P, Pasquini a, Chiffre L De, Bossard M and Picotto G B 2007 Increase of maximum detectable slope with optical profilers, through controlled tilting and image processing *Meas. Sci. Technol.* **18** 384–9

[451] Dai G, Wolff H, Pohlenz F, Danzebrink H-U and Wilkening G 2006 Atomic force probe for sidewall scanning of nano- and microstructures *Appl. Phys. Lett.* **88** 171908

[452] Marinello F, Savio E, Bariani P and Carmignato S 2009 Coordinate metrology using scanning probe microscopes *Meas. Sci. Technol.* **20** 084002

[453] Martin Y and Wickramasinghe H K 1994 Method for imaging sidewalls by atomic force microscopy *Appl. Phys. Lett.* **64** 2498

[454] Dai G, Häßler-Grohne W, Hüser D, Wolff H, Danzebrink H-U, Koenders L and Bosse H 2011 Development of a 3D-AFM for true 3D measurements of nanostructures *Meas. Sci. Technol.* **22** 094009

[455] Garnaes J, Hansen P-E, Agersnap N, Holm J, Borsetto F and Kühle a 2006 Profiles of a high-aspect-ratio grating determined by spectroscopic scatterometry and atomic-force microscopy. *Appl. Opt.* **45** 3201–12

[456] Hussain M M, Gondran C F H and Michelson D K 2007 Atomic force microscope study of three-dimensional nanostructure sidewalls *Nanotechnology* **18** 335303

[457] Cho S-J, Ahn B-W, Kim J, Lee J-M, Hua Y, Yoo Y K and Park S 2011 Three-dimensional imaging of undercut and sidewall structures by atomic force microscopy. *Rev. Sci. Instrum.* **82** 023707

[458] Hansen H N, Hocken R J and Tosello G 2011 Replication of micro and nano surface geometries *CIRP Ann. - Manuf. Technol.* **60** 695–714

[459] Rana N and Goldfarb D 2012 Bridging CD metrology gaps of advanced patterning with assistance of nanomolding *Proc. SPIE* **83241M** 1–13

[460] Gasparin S 2012 *Verification of Tolerance Chains in Micro Manufacturing* (PhD Thesis: Technical University of Denmark)

[461] Xia Y and Whitesides G 1998 Soft lithography *Annu. Rev. Mater. Sci.* **28** 153–84

[462] Johnston I D, McCluskey D K, Tan C K L and Tracey M C 2014 Mechanical characterization of bulk Sylgard 184 for microfluidics and microengineering *J. Micromechanics Microengineering* **24** 035017

[463] Ye X, Liu H, Ding Y, Li H and Lu B 2009 Research on the cast molding process for high quality PDMS molds *Microelectron. Eng.* **86** 310–3

[464] Madsen M, Feidenhans'l N, Garnaes J, Kai D and Hansen P-E 2014 Accounting for PDMS shrinkage when replicating structures. Accepted in *J. Micromechanics Microengineering*

[465] Schroer C G, Hönig S, Goldschmidt A, Hoppe R, Patommel J, Samberg D, Schropp A, Seiboth F, Stephan S, Schöder S, Burghammer M, Denecke M, Wellenreuther G and Falkenberg G 2011 Hard x-ray nano-beam characterization by ptychographic imaging *Proc. SPIE* **8141** 814103

[466] Patommel J 2010 *Hard X-Ray Scanning Microscope Using Nanofocusing Parabolic Refractive Lenses* (Dissertation, Technische Universität Dresden)

[467] McBrayer J D, Swanson R and Sigmon T 1986 Diffusion of Metals in Silicon Dioxide *J. Electrochem. Soc.* **133** 12421246

[468] Shacham-Diamand Y, Dedhia a., Hoffstetter D and Oldham W 1993 Copper Transport in Thermal SiO *J. Electrochem. Soc.* **140** 2427–32

[469] Guizar-Sicairos M, Evans-Lutterodt K, Isakovic A F, Stein A, Warren J B, Sandy A R, Narayanan S and Fienup J R 2010 One-dimensional hard x-ray field retrieval using a moveable structure. *Opt. Express* **18** 18374–82

[470] Suzuki Y, Takeuchi A, Takano H and Takenaka H 2005 Performance test of fresnel zone plate with 50 nm outermost zone width in hard X-ray region *Jpn. J. Appl. Phys.* **44** 1994–8

[471] Mimura H, Yumoto H, Matsuyama S, Handa S, Kimura T, Sano Y, Yabashi M, Nishino Y, Tamasaku K, Ishikawa T and Yamauchi K 2008 Direct determination of the wave field of an x-ray nanobeam *Phys. Rev. A* **77** 015812

[472] Faulkner H and Rodenburg J 2004 Movable Aperture Lensless Transmission Microscopy: A Novel Phase Retrieval Algorithm *Phys. Rev. Lett.* **93** 023903

[473] Rodenburg J M and Faulkner H M L 2004 A phase retrieval algorithm for shifting illumination *Appl. Phys. Lett.* **85** 4795

[474] Rodenburg J, Hurst a., Cullis a., Dobson B, Pfeiffer F, Bunk O, David C, Jefimovs K and Johnson I 2007 Hard-X-Ray Lensless Imaging of Extended Objects *Phys. Rev. Lett.* **98** 034801

[475] Huang X, Wojcik M, Burdet N, Peterson I, Morrison G R, Vine D J, Legnini D, Harder R, Chu Y S and Robinson I K 2012 Quantitative X-ray wavefront measurements of Fresnel zone plate and K-B mirrors using phase retrieval. *Opt. Express* **20** 24038–48

[476] Maiden A M and Rodenburg J M 2009 An improved ptychographical phase retrieval algorithm for diffractive imaging. *Ultramicroscopy* **109** 1256–62

[477] Maiden A M, Humphry M J, Zhang F and Rodenburg J M 2011 Superresolution imaging via ptychography. *J. Opt. Soc. Am. A. Opt. Image Sci. Vis.* **28** 604–12

[478] Thibault P, Dierolf M, Menzel A, Bunk O, David C and Pfeiffer F 2008 High-resolution scanning x-ray diffraction microscopy. *Science* **321** 379–82

[479] Takahashi Y, Suzuki A, Zettsu N, Kohmura Y, Senba Y, Ohashi H, Yamauchi K and Ishikawa T 2011 Towards high-resolution ptychographic x-ray diffraction microscopy *Phys. Rev. B* **83** 214109

[480] Schropp a, Boye P, Goldschmidt a, Hönig S, Hoppe R, Patommel J, Rakete C, Samberg D, Stephan S, Schöder S, Burghammer M and Schroer C G 2011 Non-destructive and quantitative imaging of a nano-structured microchip by ptychographic hard X-ray scanning microscopy. *J. Microsc.* **241** 9–12

[481] Schropp a., Hoppe R, Patommel J, Samberg D, Seiboth F, Stephan S, Wellenreuther G, Falkenberg G and Schroer C G 2012 Hard x-ray scanning microscopy with coherent radiation: Beyond the resolution of conventional x-ray microscopes *Appl. Phys. Lett.* **100** 253112

[482] Kewish C M, Thibault P, Dierolf M, Bunk O, Menzel A, Vila-Comamala J, Jefimovs K and Pfeiffer F 2010 Ptychographic characterization of the wavefield in the focus of reflective hard X-ray optics. *Ultramicroscopy* **110** 325–9

[483] Schropp A, Boye P, Feldkamp J M, Hoppe R, Patommel J, Samberg D, Stephan S, Giewekemeyer K, Wilke R N, Salditt T, Gulden J, Mancuso a. P, Vartanyants I a., Weckert E, Schöder S, Burghammer M and Schroer C G 2010 Hard x-ray nanobeam characterization by coherent diffraction microscopy *Appl. Phys. Lett.* **96** 091102

[484] Hönig S, Hoppe R, Patommel J, Schropp A, Stephan S, Schöder S, Burghammer M and Schroer C G 2011 Full optical characterization of coherent x-ray nanobeams by ptychographic imaging. *Opt. Express* **19** 16324–9

[485] Schroer C G, Brack F-E, Brendler R, Hönig S, Hoppe R, Patommel J, Ritter S, Scholz M, Schropp A, Seiboth F, Nilsson D, Rahomäki J, Uhlén F, Vogt U, Reinhardt J and Falkenberg G 2013 Hard x-ray nanofocusing with refractive x-ray optics: full beam characterization by ptychographic imaging *Proc. SPIE* **8848** 884807

[486] Schropp A, Hoppe R, Patommel J, Seiboth F, Uhlén F, Vogt U, Lee H J, Nagler B, Galtier E C, Zastrau U, Arnold B, Heimann P, Hastings J B and Schroer C G 2013 Scanning coherent x-ray microscopy as a tool for XFEL nanobeam characterization ed A Klisnick and C S Menoni **8849** 88490R

[487] Dzhigaev D, Lorenz U, Kurta R P, Seiboth F, Stankevic T, Mickevicius S, Singer a, Shabalin a, Yefanov O M, Strikhanov M N, Falkenberg G, Schroer C G, Feidenhans'l R and Vartanyants I a 2014 Ptychographical imaging of the phase vortices in the x-ray beam formed by nanofocusing lenses *J. Phys. Conf. Ser.* **499** 012020

[488] Guizar-Sicairos M, Narayanan S, Stein A, Metzler M, Sandy A R, Fienup J R and Evans-Lutterodt K 2011 Measurement of hard x-ray lens wavefront aberrations using phase retrieval *Appl. Phys. Lett.* **98** 111108

[489] Liu J M 1982 Simple technique for measurements of pulsed Gaussian-beam spot sizes. *Opt. Lett.* **7** 196–8

[490] Chalupský J, Juha L, Kuba J, Cihelka J, Hájková V, Koptyaev S, Krása J, Velyhan a, Bergh M, Caleman C, Hajdu J, Bionta R M, Chapman H, Hau-Riege S P, London R a, Jurek M, Krzywinski J, Nietubyc R, Pelka J B, Sobierajski R, Meyer-Ter-Vehn J, Tronnier a, Sokolowski-Tinten K, Stojanovic N, Tiedtke K, Toleikis S, Tschentscher T, Wabnitz H and Zastrau U 2007 Characteristics of focused soft X-ray free-electron laser beam determined by ablation of organic molecular solids. *Opt. Express* **15** 6036–43

[491] Chalupský J, Krzywinski J, Juha L, Hájková V, Cihelka J, Burian T, Vysín L, Gaudin J, Gleeson a, Jurek M, Khorsand a R, Klinger D, Wabnitz H, Sobierajski R, Störmer M, Tiedtke K and Toleikis S 2010 Spot size characterization of focused non-Gaussian X-ray laser beams. *Opt. Express* **18** 27836–45

[492] Roth T, Detlefs C, Snigireva I and Snigirev A 2015 X-ray diffraction microscopy based on refractive optics *Opt. Commun.* **340** 33–8

[493] Vaughan G B M, Wright J P, Bytchkov A, Curfs C, Gundlach C, Orlova M, Erra L, Gleyzolle H, Buslaps T, Götz A, Suchet G, Petitdemange S, Rossat M, Margulies L, Ludwig W, Snigirev A, Snigireva I, Schmidt S, Sørensen H O, Lauridsen E M, Olsen U

L, Oddershede J and Poulsen H F 2010 The extension of ID11 for nanoscale and hierarchical characterization *Risoe Int. Symp. Mater. Sci. Proc.* **31** 457–76

[494] Martin T and Koch A 2006 Recent developments in X-ray imaging with micrometer spatial resolution *J. Synchrotron Radiat.* **13** 180–94

[495] Labiche J-C, Mathon O, Pascarelli S, Newton M a, Ferre G G, Curfs C, Vaughan G, Homs A and Carreiras D F 2007 Invited article: the fast readout low noise camera as a versatile x-ray detector for time resolved dispersive extended x-ray absorption fine structure and diffraction studies of dynamic problems in materials science, chemistry, and catalysis. *Rev. Sci. Instrum.* **78** 091301

[496] Kobrin B, Chinn J, Nowak R and Yi R 2007 Functional organic based vapor deposited coatings adhered by an oxide layer US Patent Application 2007/0020392 A1

[497] Cech J and Taboryski R 2012 Stability of FDTS monolayer coating on aluminum injection molding tools *Appl. Surf. Sci.* **259** 538–41

[498] Persson P and Strang G 2004 A simple mesh generator in MATLAB *SIAM Rev.* **46** 329–45

[499] Jo S-B, Lee M-W, Lee S-G, Lee E-H, Park S-G and O B-H 2005 Characterization of a modified Bosch-type process for silicon mold fabrication *J. Vac. Sci. Technol. A* **23** 905

[500] Ashraf H, Hopkins J and Lea L M 2010 Advanced Materials and Technologies for Micro/Nano-Devices, Sensors and Actuators ed E Gusev, E Garfunkel and A Dideikin 157–65

[501] Ohara J, Kano K, Takeuchi Y, Ohya N, Otsuka Y and Akita S A new deep reactive ion etching process by dual sidewall protection layer 277–82

[502] Ohara J, Kano K, Takeuchi Y and Otsuka Y 2001 Improvement of Si/SiO2 mask etching selectivity in the new D-RIE process *IEEE* 76–9

[503] Ohara J, Takeuchi Y and Sato K 2009 Improvement of high aspect ratio Si etching by optimized oxygen plasma irradiation inserted DRIE *J. Micromechanics Microengineering* **19** 095022

[504] Ohara J, Takeuchi Y and Sato K 2011 Development of Si DRIE process allowing simultaneous etching from narrow and wide mask openings *Electron. Commun. Japan* **94** 36–43

[505] Maksimovich G G, Drozd N P, Shevchuk M I and Baranetskii V S 1967 Universal apparatus for melting and casting lithium *Sov. Mater. Sci.* **22** 285–6

[506] Wood G B and Brenner A 1957 Electrodeposition of Metals from Organic Solutions. IV. Electrodeposition of Beryllium and Beryllium Alloys *J. Electrochem. Soc.* **104** 29–37

[507] Takai T 1979 Studies on the electrodeposition from organic solutions of metals that are difficult to deposit from aqueous solutions *Surf. Technol.* **9** 285–302

[508] Jayakrishnan S, Pushpavanam M and Shenoi B A 1981 Electrodeposition from organic solutions of metals that are difficult to deposit from aqueous solutions *Surf. Technol.* **13** 225–40

[509] Miikkulainen V, Leskelä M, Ritala M and Puurunen R L 2013 Crystallinity of inorganic films grown by atomic layer deposition: Overview and general trends *J. Appl. Phys.* **113** 021301

[510] Johnson R W, Hultqvist A and Bent S F 2014 A brief review of atomic layer deposition: from fundamentals to applications *Mater. Today* **17** 236–46

[511] Yum J H, Akyol T, Lei M, Ferrer D a., Hudnall T W, Downer M, Bielawski C W, Bersuker G, Lee J C and Banerjee S K 2011 A study of highly crystalline novel beryllium oxide film using atomic layer deposition *J. Cryst. Growth* **334** 126–33

A Publications based on this thesis

Parts of this thesis have been published in peer-reviewed journals:

Stöhr F, Michael-Lindhard J, Hübner J, Jensen F, Simons H, Jakobsen A C, Poulsen H F and Hansen O. 2015 Sacrificial structures for deep reactive ion etching of high-aspect ratio kinoform silicon X-ray lenses. *Journal of Vacuum Science and Technology B* **33**(6), 062001 LINK

Stöhr F, Michael-Lindhard J, Simons H, Poulsen H F, Hübner J, Hansen O, Garnaes J and Jensen F. 2015 Three-dimensional nanometrology of microstructures by replica molding and large-range atomic force microscopy. *Microelectronic Engineering* **141**, 6–11 LINK

Stöhr F, Wright J, Simons H, Michael-Lindhard J, Hübner J, Jensen F, Hansen O and Poulsen H F. 2015 Optimizing shape uniformity and increasing structure heights of deep reactive ion etched silicon X-ray lenses. *Journal of Micromechanics and Microengineering* **25**(12), 125013 LINK

Stöhr F, Simons H, Jakobsen A C, Nielsen C H, Michael-Lindhard J, Jensen F, Poulsen H F, Hansen O and Hübner J. 2015 Injection molded polymeric hard X-ray lenses. *Optical Materials Express* **5**(12), 2804-2811 LINK

Simons H, Stöhr F, Michael-Lindhard J, Jensen F, Hansen O, Detlefs C and Poulsen H F. 2015 Full-field hard x-ray microscopy with interdigitated silicon lenses. *Optics Communications* **359**, 460-464 LINK

Simons H, King A, Ludwig W, Detlefs C, Pantleon W, Schmidt S, Stöhr F, Snigireva I, Snigirev A and Poulsen H F. 2015 Dark-field X-ray microscopy for multiscale structural characterization. *Nature Communications* **6**, 6098 LINK

In addition, several papers are in preparation related to the use of the lens technology presented. This work, however, is outside the scope of this thesis.

B Conferences and workshops

Parts of this thesis have been presented at workshops and international conferences:

F. Stöhr, J. Michael-Lindhard, H. Simons, A.C. Jakobsen, J. Hübner, F. Jensen, O. Hansen, H.F. Poulsen. Polymer injection molding of hard X-ray refractive optics. Oral presentation. *41st International Conference on Micro and Nano Engineering (MNE 2015)*. The Hague (Netherlands), 21-24 September 2015.

F. Stöhr, H. Simons, A. C. Jakobsen, F. Jensen, O. Hansen, H.F. Poulsen. Polymer injection molding of hard X-ray refractive optics. Poster presentation. *23rd International Congress on X-Ray Optics and Microanalysis (ICXOM23)*. Upton, New York (USA), 14-18 September 2015.

H. Simons, F. Stöhr, J. Michael-Lindhard, F. Jensen, O. Hansen, C. Detlefs, H.F. Poulsen. Interdigitated silicon CRLs: A route to full-field x-ray microscopy at hard energies. Oral presentation. *23rd International Congress on X-Ray Optics and Microanalysis (ICXOM23)*. Upton, New York (USA), 14-18 September 2015.

H. Simons, A. C. Jakobsen, S.R. Ahl, F. Stöhr, W. Ludwig, C. Detlefs, H.F. Poulsen. Multi-scale 3D characterization with dark-field x-ray microscopy. Poster presentation. *23rd International Congress on X-Ray Optics and Microanalysis (ICXOM23)*. Upton, New York (USA), 14-18 September 2015.

S.R. Ahl, H. Simons, A. C. Jakobsen, Y. Zhang, F. Stöhr, D. Juul Jensen, H.F. Poulsen. Dark field X-ray microscopy for studies of recrystallization. Oral presentation. *36th Risø International Symposium on Materials Science*. Roskilde (Denmark), 7-11 September 2015.

F. Stöhr, J. Michael-Lindhard, H. Simons, J. Hübner, F. Jensen, O. Hansen, J. Garnaes, H.F. Poulsen. X-ray refractive optics. Manufacture, shape characterization and optical performance. Poster presentation. *Myfab and NorFab User Meeting 2015*. Lund (Sweden). 21-22 April 2015.

F. Stöhr, J. Michael-Lindhard, H. Simons, J. Hübner, F. Jensen, O. Hansen, J. Garnaes, A. Snigirev, H.F. Poulsen. Three-dimensional characterization of X-Ray refractive optics. Poster presentation. *Conference on Micro and Nano Engineering (MNE 2014)*. Lausanne (Switzerland). 22-26 September 2015.

H.F. Poulsen, H. Simons, A. King, W. Ludwig, W. Pantleon, F. Stöhr, S. Schmidt, E.M. Lauridsen, I. Snigireva, A. Snigirev, C. Detlefs. Hard X-Ray Microscopy: multiscale structural mapping. Invited Talk. *TMS 2014 143rd Annual meeting and exhibition*. San Diego, California (USA). 16-20 February 2014.

F. Stöhr, J. Michael-Lindhard, H. Simons, J. Hübner, F. Jensen, O. Hansen, A. Snigirev, H.F. Poulsen. Manufacturing and Characterization of Silicon Compound Refractive Lenses for Focusing of Hard X-Rays. Poster presentation. *22nd International Congress on X-Ray Optics and Microanalysis (ICXOM22)*. Hamburg (Germany). 2-6 September 2013.

C Abbreviations

1D	One dimension
2D	Two dimensions
$2R_0$	Physical lens aperture (cf. Figure 2.5)
3D	Three dimensions
3DXRD	Three-dimensional x-ray diffraction
A	Molar mass
AFM	Atomic force microscopy
Al	Aluminum
Al_2O_3	Alumina, aluminum oxide
ALD	atomic layer deposition
Ar	Argon
ARDE	Aspect ratio dependent etching
α	Sidewall angle (cf. Figure 2.16)
Å	Ångström (10^{-10} m)
B	Spot size (cf. Equation 26)
BARC	bottom-anti-reflective coating
B_{demag}	Size of the demagnified source (cf. Equation 22)
B_{diff}	Diffraction limited spot size (cf. Equation 13)
Be	Beryllium
bHF	Buffered hydrofluoric acid
β	Extinction coefficient
°C	Degree Celsius
C	Carbon
C_4F_8	Octafluorocyclobutane
CAD	Computer Assisted Drafting
CIF	File extension
cm	Centimeter (10^{-2} m)
CRL	Compound refractive lens
DCT	Diffraction contrast tomography
D_{eff}	Absorption limited CRL aperture (cf. Equation 17)
DOF	Depth of focus (cf. Equation 27)
DTU	Technical University of Denmark
d_{source}	Source size

DXF	File extension
DRIE	Deep reactive ion etching
DXRL	Deep x-ray lithography
δ	Refractive index decrement ($\delta = 1 - n$)
E	Energy
e.g.	exempli gratia (for example)
eV	Electron-volt
f	Focal length (measured from middle of the CRL, cf. Equation 13)
f_0	Focal length (measured from middle of the CRL, cf. Equation 11)
f_S	Focal length of a single lens element (cf. Equation 9)
FWHM	Full width at half maximum
FZP	Fresnel zone plates
g	Gram
H	Hydrogen
HF	Hydrofluoric acid
HMDS	Hexamethyldisilazane
I	Intensity
i.e.	Id est (that is)
IAD	Ion angular distribution
ID	Ion deflection
IF	Image force
KB	Kirkpatrick-Baez
keV	Kiloelectron-volt (10^3 eV)
KOH	Potassium hydroxide
kW	Kilowatt
Li	Lithium
LIGA	German acronym for lithography, electro plating and molding
λ	Wavelength
m	Meter
mBar	Millibar
MFC	Mass flow controller
MHz	Megahertz
min	Minutes
MLL	Multilayer Laue lenses
mrad	Milliradian
μ^{-1}	Attenuation length or penetration depth
µrad	Microradian
µm	Micrometer (10^{-6} m)
n	Refractive index
N	Newton

N	Number of lenslets
NA	Numerical aperture
N_A	Avogadro's number (6.022×10^{23} mol^{-1})
NFL	Nano-focusing lens
Ni	Nickel
nm	Nanometer (10^{-9} m)
O	Oxygen
OP	Optical profilometry
OSA	Order selecting aperture
p	Dot diameter (cf. Figure 4.2)
PE	Polyethylene
PECVD	Plasma-enhanced chemical vapor deposition
PDMS	Polydimethylsiloxane
PMMA	Poly(methyl methacrylate), acrylic glass
PP	Polypropylene
π	Pi (3.14159265)
R	Radius of curvature (cf. Figure 2.5)
r_0	Classical electron radius ($r_0 = 2.818\times10^{-15}$ m)
RF	Radiofrequency
RIE	Reactive ion etching
ρ	mass density
s	Inter-pillar spacing (cf. Figure 4.2)
SEM	Scanning electron microscopy
SF_6	Sulfur hexafluoride
Si	Silicon
SiO_2	Silica, silicon dioxide
SOI	Silicon-on-insulator
σ	RMS surface roughness
t	Trench width (cf. Figure 4.2)
T	Total CRL thickness
T_0	Thickness of the web of a lenslet (cf. Figure 2.5)
TX	Total transmission through a CRL (cf. Equation 13)
u	"Undercut", compensation for shape widening (cf. Chapter 2.4)
UV	Ultraviolet
w	Wall thickness (cf. Figure 4.2)
W	Watt
XRM	X-ray microscopy
Z	Atomic number